

Study of Identified Hadron Spectra and Yields  
at Mid-rapidity in  $\sqrt{s_{\text{NN}}} = 200 \text{ GeV}$   
Au+Au Collisions

Akio KIYOMICHI

January 2005



Study of Identified Hadron Spectra and Yields  
at Mid-rapidity in  $\sqrt{s_{\text{NN}}} = 200 \text{ GeV}$   
Au+Au Collisions

Akio KIYOMICHI

Submitted to the Graduate School of  
Pure and Applied Sciences  
in Partial Fulfillment of the Requirements  
for the Degree of Doctor of Philosophy in  
Science

at the  
University of Tsukuba



## Abstract

Heavy ion collisions at relativistic energy offer the possibility of producing highly compressed strongly interacting matter, which may form the quark-gluon plasma (QGP). We present the results of identified hadron spectra and yields in Au+Au collisions at the energy of  $\sqrt{s_{\text{NN}}} = 200$  GeV by the PHENIX experiment using the Relativistic Heavy Ion Collider (RHIC) at Brookhaven National Laboratory (BNL).

The PHENIX is one of the major experiments at RHIC to detect a variety of signals from quark-gluon plasma. It is designed to perform a broad study of  $A + A$ ,  $p + A$ , and  $p + p$  collisions to investigate nuclear matter under extreme condition. The detector consists of a large number of subsystems. It comprises two central arms, two forward muon arms, and three global detectors. For the systematic studies of identified hadron productions in relativistic heavy-ion collisions, we have constructed a high resolution time-of-flight detector and installed in PHENIX central arm. It is designed for good hadron identification capability in a broad momentum range. Pions and kaons are identified up to  $3 \text{ GeV}/c$  and  $2 \text{ GeV}/c$  in  $p_T$ , respectively, and protons and anti-protons can be identified up to  $4.5 \text{ GeV}/c$ .

For single particle analysis, we have measured the transverse momentum spectra and yields for  $\pi^\pm$ ,  $K^\pm$ ,  $p$  and  $\bar{p}$  at mid-rapidity in  $\sqrt{s_{\text{NN}}} = 200$  GeV Au+Au collisions over a broad momentum range with various centrality selections. We have observed a clear particle mass dependence of the shapes of transverse momentum spectra in Au+Au central collisions below  $\sim 2 \text{ GeV}/c$  in  $p_T$ . We also measured particle ratios of  $\pi^-/\pi^+$ ,  $K^-/K^+$ ,  $\bar{p}/p$ ,  $K/\pi$ ,  $p/\pi$  and  $\bar{p}/\pi$  as a function of  $p_T$  and collision centrality. The ratios of equal mass particle yields are independent of  $p_T$  and centrality within the experimental uncertainties. The ratios in central Au+Au collisions are well reproduced by the statistical thermal model with a baryon chemical potential of  $\mu_B = 29 \text{ MeV}$  and a chemical freeze-out temperature of  $T_{\text{ch}} = 177 \text{ MeV}$ .

Motivated by this observation that the single particle spectra are well fitted with a hydrodynamic-inspired parameterization, termed the “blast-wave” model, to extract freeze-out temperature and radial flow velocity of the particle source. Since the experimental data include the decay of resonance, we have taken into account decays of mesonic ( $\rho$ ,  $\eta$ ,  $\omega$ ,  $K^*$ , , ,) and baryonic ( $\Delta$ ,  $\Lambda$ ,  $\Sigma$ , , ,) resonances whose abundances are determined by the chemical parameters. From this analysis, we have obtained freeze-out temperature  $T_{\text{fo}} = 108 \text{ MeV}$  and average flow velocity  $\langle \beta_T \rangle = 0.57$  in Au + Au central collisions at

## II

$\sqrt{s_{\text{NN}}} = 200 \text{ GeV}$ . It is found that  $T_{\text{fo}}$  decreases and  $\beta_{\text{T}}$  increases from the most peripheral to mid-central collisions, and appears to saturate in the central collisions.

Another motivation is that the suppression of high- $p_{\text{T}}$  hadron as a probe of QGP formation. The binary collision scaling behavior of identified charged hadrons has been measured and compared with that of neutral pions. The central-to-peripheral ratio,  $R_{\text{CP}}$ , approaches unity for  $(\bar{p} + p)/2$  from  $p_{\text{T}} = 1.5$  up to  $4.5 \text{ GeV}/c$ . Meanwhile, charged and neutral pions are suppressed. The  $p/\pi$  and  $\bar{p}/\pi$  ratios in central events both increase with  $p_{\text{T}}$  up to  $3 \text{ GeV}/c$  and approach unity at  $p_{\text{T}} \approx 2 \text{ GeV}/c$ . However, in peripheral collisions these ratios saturate at the value of  $0.3 - 0.4$  around  $p_{\text{T}} = 1.5 \text{ GeV}/c$ . The observed  $R_{\text{CP}}$  and  $p/\pi$  ratios in intermediate  $p_{\text{T}}$  region are not explained by the hydrodynamic model alone, but some of theoretical model qualitatively agree with data. These observations can be explained by the hydrodynamical model with jet fragmentation (hydro + jet model) and the parton recombination at intermediate  $p_{\text{T}}$  (recombination model). Both theoretical models reproduce the binary collision scaling observed in the data. We have extended our identified hadron studies to include the  $\phi$  vector meson. The observed  $R_{\text{CP}}$  for  $\phi$  is similar to other mesons despite the fact that they are more massive than protons. This scaling with quark content favors recombination models.

# Contents

<b>1</b>	<b>Introduction</b>	<b>1</b>
1.1	Relativistic Heavy-Ion Collisions . . . . .	1
1.1.1	Physics of High Energy Heavy-Ion Collisions . . . . .	1
1.1.2	Signatures of the Quark-Gluon Plasma . . . . .	4
1.1.3	Collision Geometry of Heavy-Ion Collisions . . . . .	6
1.2	Particle Production in Heavy-Ion Collisions . . . . .	7
1.2.1	Single Particle Spectra . . . . .	8
1.2.2	Collective Expansion . . . . .	9
1.2.3	Particle Ratios and Chemical Equilibrium . . . . .	11
1.3	Hard Scattering as a Probe of QGP . . . . .	13
1.3.1	Hard Scattering in $N - N$ Collisions . . . . .	13
1.3.2	Hard Scattering in Heavy-Ion Collisions . . . . .	15
1.3.3	Reference Experiment: $d + \text{Au}$ Collisions . . . . .	17
1.4	Thesis Motivation . . . . .	18
1.5	Contributions of the Author . . . . .	19
<b>2</b>	<b>The PHENIX Experiment</b>	<b>20</b>
2.1	RHIC : Collider Facility . . . . .	20
2.2	PHENIX Detector Overview . . . . .	23
2.3	PHENIX Magnet System . . . . .	25
2.4	PHENIX Global Detectors . . . . .	26
2.4.1	Zero Degree Calorimeter . . . . .	26
2.4.2	Beam-Beam Counter . . . . .	28
2.5	Central Arm Spectrometers . . . . .	31
2.5.1	Drift Chamber . . . . .	32
2.5.2	Pad Chamber . . . . .	34
2.5.3	Time-of-Flight Counter . . . . .	35

2.6	Other Detectors . . . . .	38
2.6.1	Time Expansion Chamber . . . . .	38
2.6.2	Ring-Imaging Cherenkov Detector . . . . .	39
2.6.3	Electromagnetic Calorimeter . . . . .	40
2.6.4	Muon Arm Spectrometer . . . . .	42
<b>3</b>	<b>Data Analysis</b>	<b>46</b>
3.1	Event Selection . . . . .	46
3.1.1	Minimum Bias Trigger . . . . .	46
3.1.2	Centrality Determination . . . . .	48
3.1.3	Glauber Model Calculation . . . . .	50
3.2	Track Reconstruction . . . . .	53
3.2.1	Track Selection . . . . .	53
3.2.2	Momentum Determination . . . . .	54
3.2.3	Track Association . . . . .	55
3.3	Particle Identification . . . . .	56
3.4	Cut Conditions . . . . .	58
3.4.1	Fiducial Cut . . . . .	59
3.4.2	Energy Loss Cut . . . . .	59
3.5	Correction . . . . .	61
3.5.1	Comparison of Data with Simulation . . . . .	61
3.5.2	Corrections of Acceptance, Decay and Multiple Scattering . . . . .	65
3.5.3	Correction of Multiplicity Dependence . . . . .	66
3.5.4	Weak Decay Correction . . . . .	67
3.5.5	Invariant Yield . . . . .	69
3.6	Systematic Uncertainties . . . . .	69
<b>4</b>	<b>Experimental Results</b>	<b>71</b>
4.1	Transverse Momentum Distributions . . . . .	71
4.2	Mean Transverse Momentum and Particle Yields . . . . .	74
4.3	Particle Ratios . . . . .	77
<b>5</b>	<b>Discussions</b>	<b>81</b>
5.1	Particle Productions . . . . .	81
5.1.1	Particle Ratios . . . . .	81
5.1.2	Features of Chemical Equilibrium . . . . .	82

5.1.3	Comparison with Theoretical Phase Boundary . . . . .	83
5.2	Transverse Distributions . . . . .	84
5.2.1	$p_T$ Spectra of $\pi, K, p$ . . . . .	84
5.2.2	$p/\pi$ ratios . . . . .	85
5.2.3	Feature of Thermal Equilibrium: $m_T$ Spectra . . . . .	87
5.3	Collective Expansion Model . . . . .	90
5.3.1	Blast-wave Parametrization . . . . .	90
5.3.2	Previous Studies . . . . .	91
5.3.3	Proposed Analysis and Results . . . . .	91
5.4	Beyond the Thermal Behavior: Hard Component . . . . .	99
5.4.1	Suppression of High $p_T$ Hadrons . . . . .	99
5.4.2	Comparison with Theoretical Models: hydro+jet and recombination	101
<b>6</b>	<b>Conclusions</b>	<b>107</b>
<b>A</b>	<b>Numerical Supplement</b>	<b>109</b>
A.1	Relativistic Kinematics and Variables . . . . .	109
A.2	Transverse Expansion . . . . .	110
<b>B</b>	<b>Time-of-flight Detector</b>	<b>113</b>
B.1	Detector Design . . . . .	113
B.2	The TOF Scintillator and Photomultiplier Tubes . . . . .	117
B.3	Front End Electronics . . . . .	118
B.4	TOF Detector Performance . . . . .	120
<b>C</b>	<b>Data Tables</b>	<b>126</b>
C.1	$p_T$ Spectra Data Tables . . . . .	126
C.2	Particle Ratio Data Tables . . . . .	141
<b>D</b>	<b>PHENIX Collaboration List</b>	<b>147</b>

# Acknowledgments

I would like to express my great appreciation to Prof. Y. Miake for providing me the exciting field of physics. His appropriate and valuable advice show me the way to promote the present work, and I could learn a lot from him as an experimental physicist. I express my thanks to Prof. K. Yagi for introducing me to this fascinating field of nuclear physics. Their draft of book, Quark-Gluon Plasma (K. Yagi, T. Hatsuda and Y. Miake, will be pressed from Cambridge University Press), is helpful to learn this field.

I wish to express my thanks to Dr. H. Sako for leading me to the PHENIX experiment. His appropriate and kind advice have helped me a lot to work at BNL. I appreciate Dr. S. Sato for his advice and discussions on the detector construction and operation. I could learn from him as a way of experimentalist. I express my thanks to Dr. T. Chujo for his useful advice and discussions in the data analysis. I am much obliged to Dr. S. Esumi for his advice and discussions in the data analysis and manuscript of this thesis.

I wish to acknowledge all the collaborators of the PHENIX experiment. I am grateful to the spokesperson Prof. W. A. Zajc for his various arrangements for my activity at BNL, and hurtful encouragement. I would also like to thank the previous spokesperson Prof. S. Nagamiya for his guidance, precious advice and encouragement since I joined the PHENIX experiment. I would like to express my appreciation to Dr. H. En'yo for his continuous encouragement to complete this work. I express my thanks to Prof. H. Hamagaki, Prof. T. Sugitate and Prof. J. Chiba for their stimulate advice, supports and encouragement. I appreciate Dr. Y. Akiba and Prof. K. Kurita for their useful advice and discussions in the data analysis. I express my special thanks to Prof. K. Shigaki, Dr. H. Ohnishi, Dr. M. Kaneta and Dr. T. Sakaguchi for their helpful advice on this work and their friendship at BNL. I would like to appreciate Dr. S. Sawada, Dr. K. Homma, and Dr. K. Ozawa for their advice and discussion. I appreciate Prof. N. Saito, Dr. Y. Goto, Dr. Y. Watanabe, Dr. T. Ichihara, Dr. A. Taketani, Dr. S. Yokkaichi, Dr. J. Murata, Dr. K. Okada and Dr. O. Jinnouchi for their encouragement and useful discussion. I'd like to thanks to Dr. K. Oyama, Dr. H. Torii, Dr. H. D. Sato, Dr. T. Kohama, Dr. J. Tojo, Dr. A. Enoki-

zono, Mr. T. Matsumoto, Mr. T. Hachiya, Mr. T. Nakamura and Mr. S. Kametani for fruitful discussions and friendship on BNL life.

I acknowledge the colleagues at BNL for detector construction, data taking and analysis. I would like to appreciate to Dr. C.Y. Chi and Dr. M. Chiu for TOF front-end electronics and to Prof. J. H. Kang, Dr. Y. H. Shin and Mr. D. J. Lim for developing the TOF online systems together. I appreciate all of the technical staff on BNL, especially M. Van Lith, W. E. Lenz, J. Labounty and K. Johnes for their helps in detector construction. I would like to express my appreciation to Prof. B. V. Jacak, Prof. C. Ogilvie, Prof. J. Velkovska, Dr. A. Franz, Dr. J.M. Burward-Hoy, Dr. J. Jia, Dr. F. Matathias for their useful advice and discussions in the data analysis. I appreciate Prof. C. Maguire, Dr. J. T. Mitchell, and Dr. D. P. Morrison for their computing supports and discussions in the analysis. I express my thanks to Dr. Y. Nara, Dr. T. Hirano and Dr. C. Nonaka for their theoretical advice and discussions.

Here I acknowledge all the members of the high energy nuclear experiment group at University of Tsukuba. I express my thanks Dr. S. Nishimura, Dr. M. Kurata-Nishimura, Mr. S. Kato, Dr. K. Enosawa, Mr. K. Kanoh, Mr. Y. Yokota, Mr. Y. Ohkuma, Ms. R. Higuchi and Ms. Y. Miyamoto for their friendship and discussions. I appreciate Ms. S. Urasawa, Mr. D. Miura and Mr. T. Ishibashi for their encouragement and continuous friendship from undergraduate. I appreciate Dr. M. Inaba, Mr. T. Hirano, Mr. T. Shimada, Mr. H. Hayashi, Ms. M. Suzuki-Nara, Mr. K. Koseki, Ms. M. Aizawa, Mr. M. Ono, Mr. H. Tsuruoka, Mr. H. Masui, Mr. S. Sakai, Mr. Y. Kuroki, Mr. S. Takagi, Mr. M. Konno and Ms. M. Shiomomura for their friendship and kindness.

I acknowledge the member of the RIKEN Radiation Laboratory. I express my thanks Ms. N. Kiyama, Ms. M. Muroi and Ms. K. Sakuma for their heartful support by the secretaries. I appreciate Dr. R. Vladimir, Dr. M. Okamura and Dr. Y. Ohtake for their encouragement. I'd like to thanks to Dr. K. Sudo, Dr. M. Hirai, Dr. M. Ohtani, Mr. T. Tabaru, Dr. N. Fukuda, Dr. K. Tanida, Dr. T. Ohnishi, Dr. H. Takeda, Dr. H. Kano, Ms. M. Naruki, Mr. R. Muto, Mr. F. Sakuma and Mr. N. Kamihara for their encouragement and friendship. I am grateful to all my colleagues and friends.

Finally, I would like to express my great appreciation to my parents, Yoshiharu Kiyomichi and Fumiko Kiyomichi, for their support and encouragement to accomplish this work. I would like to express my sincere gratitude to late grandfather Mamoru Kitamura for his comprehension and encouragement to my ambitious. I really wish my grandfather find pleasure in my success from the heaven.



# Chapter 1

## Introduction

In this chapter, the relativistic heavy-ion collisions are introduced. We describe interpretations of particle production in heavy-ion collisions and review the experimental probes. Finally, we present the thesis motivation.

### 1.1 Relativistic Heavy-Ion Collisions

#### 1.1.1 Physics of High Energy Heavy-Ion Collisions

Heavy-ion collisions at high energies ( $E/m \gg 1$ ) offer a unique opportunity to probe highly excited dense nuclear matter in the laboratory. The driving force for such studies both on experimental and theoretical side, is the expectation that a entirely new form of nuclear matter may be created from relativistic heavy-ion reactions. That form of matter is called the quark-gluon plasma (QGP), which is quantum chromodynamics (QCD) analogue of the plasma phase of ordinary atomic matter.

According to the lattice QCD calculations [1], it is predicted that the phase transition from a hadronic phase to QGP phase takes place at a temperature of approximately  $T \approx 170$  MeV ( $\approx 10^{12}$  K) as shown in Figure 1.1. This transition temperature corresponds to an energy density  $\varepsilon \approx 1$  GeV/fm<sup>3</sup>, nearly an order of magnitude larger than that of normal nuclear matter. This value is plausible based on dimensional grounds, since such densities correspond to the total overlap of several (light) hadrons within a typical hadron volume of 1–3 fm<sup>3</sup>. Lattice calculations also indicate that this significant change in the behavior of the system occurs over a small range in temperature ( $\sim 20$  MeV) indicating that it is the phase transition, and suggest that the change of phase includes the restoration of approximate chiral symmetry resulting from greatly reduced or vanishing quark constituent masses.

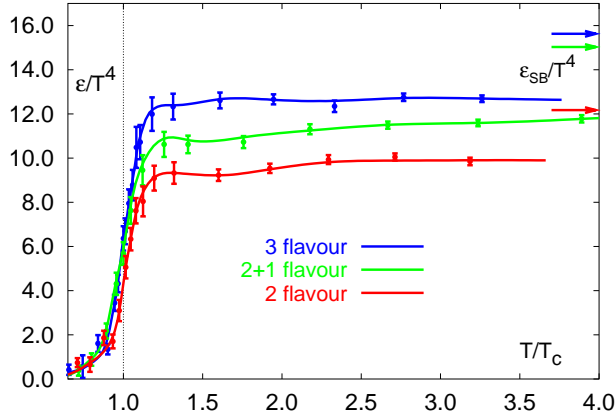


Figure 1.1: Lattice QCD results [1] for the energy density /  $T^4$  as a function of the temperature scaled by the critical temperature  $T_c$ . Note the arrows on the right side indicating the values for the Stefan-Boltzmann limit. [1]

A schematic version of the phase diagram for an idealized form of nuclear matter with vanishing light quark (up and down) masses and infinite strange quark mass is presented in Figure 1.2. For sufficiently large values of the baryon chemical potential  $\mu$  this system is considered to exhibit a first order phase transition between hadronic matter and QGP, along with a tricritical point below which the transition becomes second order. However, non-zero values of the light quark masses dramatically alter this simple picture: The second order phase transition denoted by the dashed line in Figure 1.2 becomes a smooth crossover, and the tricritical point correspondingly becomes a critical point designating the end of the first order transition found at higher values of  $\mu$ .

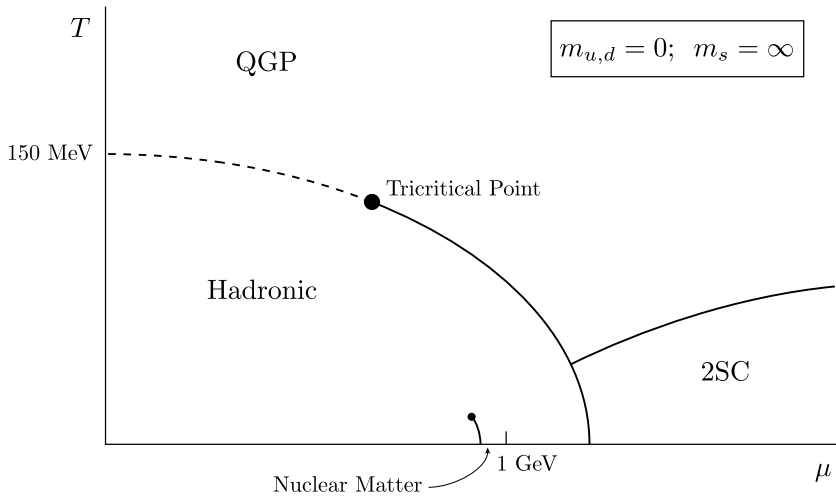


Figure 1.2: Theoretical phase diagram of nuclear matter for two massless quarks as a function of temperature  $T$  and baryon chemical potential  $\mu$ .

In order to understand the properties of the nuclear matter under the extreme conditions and hopefully to capture the signal of QGP formation, various experiments have been taken

Accelerator	Location	Ion beam	Momentum	$\sqrt{s}$	Commissioning date
			[A · GeV/c]	[GeV]	
AGS	BNL	$^{16}\text{O}, ^{28}\text{Si}$	14.6	5.4	Oct.1986
		$^{197}\text{Au}$	11.4	4.8	Apr.1992
SPS	CERN	$^{16}\text{O}, ^{32}\text{S}$	200	19.4	Sep.1986
		$^{208}\text{Pb}$	158	17.4	Nov.1994
RHIC	BNL	$^{197}\text{Au} + ^{197}\text{Au}$	65	130	2000
		$^{197}\text{Au} + ^{197}\text{Au}$	100	200	2001
		d + $^{197}\text{Au}$	100	200	2003
		$^{197}\text{Au} + ^{197}\text{Au}$	31.2	62.4	2004
		$^{63}\text{Cu} + ^{63}\text{Cu}$	100	200	2005
LHC	CERN	$^{208}\text{Pb} + ^{208}\text{Pb}$	2800	5600	2007 (project)

Table 1.1: List of heavy-ion accelerator facilities with the ion beams, the corresponding beam momentum and the center of mass energy.

place both at the Alternating Gradient Synchrotron (AGS) at Brookhaven National Laboratory (BNL), and the Super Proton Synchrotron (SPS) at CERN. The Relativistic Heavy Ion Collider (RHIC) at BNL has been operated from June 2000. This new machine provides collisions of Au nucleus at the center of mass energy per nucleon ( $\sqrt{s_{\text{NN}}}$ ) up to 200 GeV.

The hot and dense matter produced in relativistic heavy-ion collisions may evolve through the following scenario: pre-equilibrium, thermal (or chemical) equilibrium of partons, possible formation of QGP or a QGP-hadron gas mixed state, a gas of hot interacting hadrons, and finally, a freeze-out state when the produced hadrons no longer strongly interact with each other. Figure 1.3 shows the space-time evolution of the medium created in heavy-ion collisions. Since produced hadrons carry information about the collision dynamics and the entire space-time evolution of the system from the initial to the final stage of collisions, a precise measure of the transverse momentum ( $p_T$ ) distributions and yields of identified hadrons as a function of collision geometry is essential for the understanding of the collision dynamics and properties of the created matter.

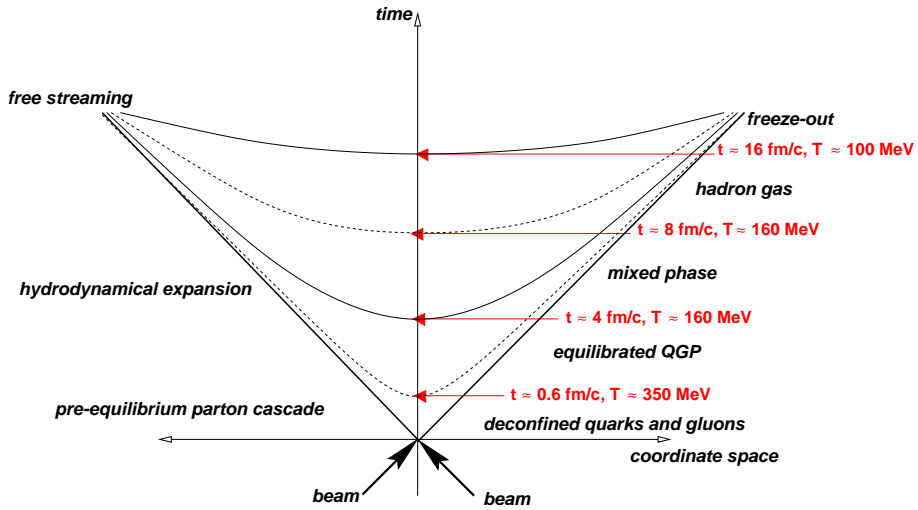


Figure 1.3: Space-time picture of a nucleus-nucleus collision.

### 1.1.2 Signatures of the Quark-Gluon Plasma

It is generally recognized that there is no clear signals of the quark-gluon plasma phase. In order to catch the signals of QGP formation, a variety of probes are proposed. As the distinct signature of the existence of QGP is still under the study, the best way to prove the presence of a QGP phase is to measure several signatures simultaneously.

#### Deconfinement

Suppression of heavy quarkonia has been proposed as a signature of deconfinement. The suppression mechanism follows directly from the Debye screening expected in the medium, which reduces the range of the potential between charm quark and anti-quark pairs [2, 3]. If radius of a meson is larger than the Debye radius, which is determined by the plasma temperature and density, the meson cannot survive in the plasma. It is proposed that  $J/\Psi$  meson made of  $c\bar{c}$  quarks is suitable for the detection of Debye screening effect because of the following reasons; 1) as  $J/\Psi$  measured in leptonic decay, decay products do not interact strongly with other hadrons, thus it is expected a penetrative probe for the early stage of the collisions, 2)  $J/\Psi$ 's are produced in the very early stage of the collision, 3) hadronic interaction of  $J/\Psi$  is expected to be not too high ( $\sigma_{\Psi N} \sim 6 \text{ mb}$ ), thus it has the information of initial state condition of the collisions.

### Strangeness enhancement

The most often proposed signature for the possible observation of QGP are enhancements in strangeness and anti-baryon production. In the  $q\bar{q}$  pair production at high energy nucleon-nucleon collisions, heavy flavors are suppressed due to their masses. The  $s\bar{s}$  yields is about  $0.1 \sim 0.2$  compared to  $u\bar{u}$  or  $d\bar{d}$  yields. This situation may change in heavy-ion collisions. If the hadronic matter is deconfined during the heavy-ion collision, the production of  $u$  and  $d$  quarks will be suppressed by Pauli blocking. Therefore, the enhancements of strangeness might be one of signals of QGP. [5]

### Collision dynamics and equation of state

Study of collective motion of produced hadrons in final state is expected to provide information on the dynamics of heavy ion collisions. With a hydrodynamical view of collisions, collective motion is governed by a pressure gradient of compressed nuclear matter at the early stage of collision. In the case of a phase transition from the ordinal nuclear to the quark-gluon plasma, it is expected that the equation of state should exhibit a corresponding softening due to the increased number of degrees of freedom [4]. Thus, the observation of collective motion is crucially important to validate the hydrodynamical description of dynamics.

If the phase transition is the first order, the equation of state will be “softest” at the critical temperature  $T_c$ . Such softening is expected to affect the dynamic evolution of the system because the internal pressure drops at  $T_c$ . Thus an observation of excitation function of the transverse collective flow can be a probe for the QGP formation; drop in the excitation function of collective flow indicates threshold energy of the QGP formation.

### Parton energy loss

Another possible way of probing the quark-gluon plasma is by the energy loss of a fast parton (quark or gluon). The mechanisms are similar to those responsible for the electromagnetic energy loss of a fast charged particle in matter, i.e. energy may be lost either by excitation of the penetrated medium or by radiation.

The fast parton may produce the high- $p_T$  hadron, the measurement of high- $p_T$  hadron production is a good probe for studying the parton energy loss. The more details are described in Section 1.3

### 1.1.3 Collision Geometry of Heavy-Ion Collisions

#### Participant-Spectator Picture

Nuclei are extended objects, and therefore their geometry aspects in heavy-ion collisions plays an important role in collision dynamics. There are two groups of nucleons; the *participants* which are in the overlapped region and the *spectators* which proceed with little perturbation along the original direction. Figure 1.4 shows a schematic view of reaction at a high energy between symmetric Lorentz contracted nuclei in the center of mass frame. As is shown in figure, the size of the participant/spectator is determined by the impact parameter  $b$  and there is anti-correlation between the size of the participant and that of spectator. The number of participants can be calculated by simple geometrical considerations, Glauber model.

Based on participant-spectator picture, the centralities of the Au+Au collision are defined by combined information on the energy deposition of spectator neutrons by the calorimeter located at zero-degree and charge sum information measured by beam-line detector (see Section 3.1).

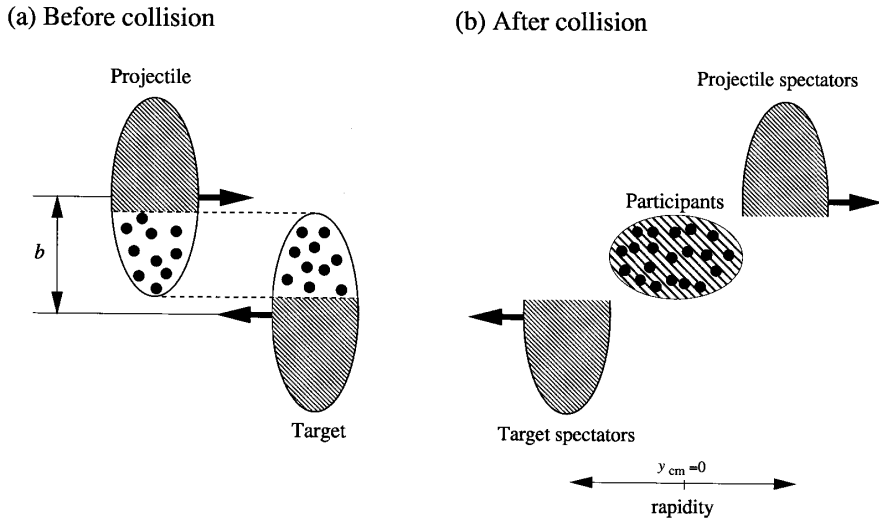


Figure 1.4: Participant-Spectator picture of a high energy heavy-ion collision with impact parameter  $b$ . On the left (a), the two incoming nuclei in the center of mass frame are shown. On the right (b), after the collision, the nucleons are separated to participants, projectile spectators and target spectators.

### Glauber Model

The Glauber model [6] is based on a simple geometrical picture of a nucleus-nucleus collision. It is a semi-classical model treating the nucleus-nucleus collisions as multiple nucleon-nucleon interactions: a nucleon of incident nucleus interacts with target nucleons with a given density distribution. Nucleons are assumed to travel on straight line trajectories and are not deflected even after the collisions, which should hold as a good approximation at very high energies. Another assumption is that nucleon-nucleon inelastic cross section  $\sigma_{NN}^{\text{in}}$  to be the same as that in the vacuum.

The nucleons are randomly distributed according to Woods-Saxon distribution, the density profile  $\rho(r)$  is defined as

$$\rho(r) = \rho_0 \cdot \frac{1}{1 + \exp(\frac{r-R}{a})} \quad (1.1)$$

where  $R$  is radius of nucleus and  $a$  is surface diffuseness parameter. The density profile for Au is shown in Figure 1.5. For the Au ion, the parameters are  $R = 6.38 \text{ fm}$ ,  $a = 0.54 \text{ fm}$  and  $\rho_0 = 0.169 \text{ fm}^{-3}$ . The inelastic nucleon-nucleon cross section  $\sigma_{NN} = 42 \text{ mb}$  is used on Au+Au collisions at  $\sqrt{s_{NN}} = 200 \text{ GeV}$ .

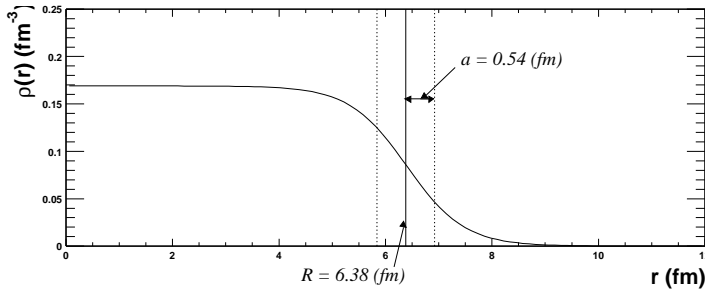


Figure 1.5: Woods-Saxon nuclear density profile for Au.

## 1.2 Particle Production in Heavy-Ion Collisions

To understand the high energy hadron-hadron collisions, Fermi proposed a statistical method [7] as follows. Because of saturation of the phase space, the multi particle production resulting from the high energy elementary collisions is consistent with a thermal description [7, 8, 9].

In heavy-ion collisions, hydrodynamical behavior, that is, local thermal equilibrium and collective motion, may be expected because of the large number of secondary scatterings. The final state hadrons are the most abundant and dominant source of information of the early stage of the collisions. Hadron momentum spectra and rapidity densities are affected

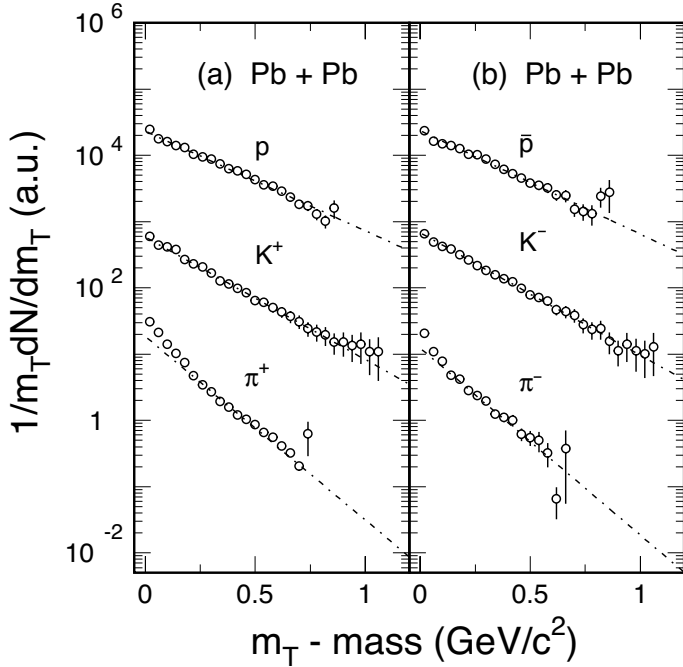


Figure 1.6: Transverse mass distributions for pions, kaons, and protons from 158 A GeV Pb + Pb central collisions. The dashed lines represent the exponential fits. This figure is taken from [11].

by thermal freeze-out and collective flow. The particle ratios are sensitive to the chemical properties of the system and particle production mechanism. The recent review of the existing data obtained mainly from CERN-SPS can be found in the literature [10].

### 1.2.1 Single Particle Spectra

Single particle spectra, i.e., transverse momentum ( $p_T$ ) distributions with single particle inclusive measurements are one of the most common tools used in studying high energy collisions. This is because the transverse motion is totally generated during the collision and hence is sensitive to the collision dynamics.

Transverse momentum spectra are presented in terms of the invariant differential cross section,

$$\begin{aligned} E \frac{d^3 \sigma}{dp^3} &= \frac{d^3 \sigma}{p_T dp_T dy d\phi} = \frac{d^3 \sigma}{m_T dm_T dy d\phi} \\ &= \frac{1}{2\pi p_T} \frac{d^2 \sigma}{dp_T dy} = \frac{1}{2\pi m_T} \frac{d^2 \sigma}{dm_T dy}, \end{aligned} \quad (1.2)$$

where  $p_T$  is the transverse momentum,  $y$  is the rapidity,  $m_T = \sqrt{p_T^2 + m_0^2}$  is the transverse mass and  $m_0$  is the rest mass of the particle. Figure 1.6 shows inclusive  $m_T$  distribution in 158 A GeV ( $\sqrt{s_{NN}} = 17.2$  GeV) Pb + Pb collisions measured by SPS-NA44 experiment [11]. Invariant cross sections are shown to be exponential in  $m_T$ . The dashed lines in

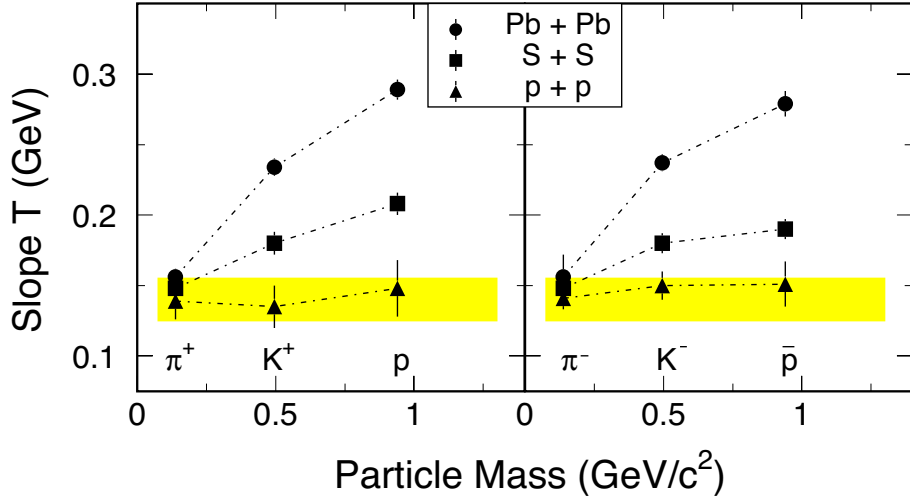


Figure 1.7: Inverse slope parameter  $T$  as a function of particle mass. They are compared at mid-rapidity in  $p + p$ , S+S and Pb+Pb collisions. This figure is taken from [11].

Figure 1.6 are fit to the function

$$\frac{1}{m_T} \frac{dN}{dm_T} = A \exp\left(-\frac{m_T}{T}\right), \quad (1.3)$$

where  $A$  is a constant and  $T$  is the inverse slope parameter of the distribution. Because of decay products from the resonances, steeper component are exist for low- $m_T$  region of pions. One may notice that proton and anti-proton distributions look flatter than those for pions and kaons.

The slope parameters for pions, kaons and protons are obtained and plotted as a function of particle mass in Figure 1.7, where they are compared in  $p + p$  ( $\sqrt{s_{NN}} = 23$  GeV), S+S ( $\sqrt{s_{NN}} = 19.4$  GeV) and Pb+Pb ( $\sqrt{s_{NN}} = 17.2$  GeV) collisions at mid-rapidity. While for  $p + p$  collision the slope parameters are independent of particle species, these parameters increase with increasing mass for heavy-ion collisions. This effect becomes larger in Pb+Pb than that in S+S; larger the collision system, the effect becomes larger. While the parameters of pions are similar to those in  $p + p$ , slopes of heavier particles become flatter in  $A + A$ .

## 1.2.2 Collective Expansion

Most successful description of the different slope parameters and the change of shape observed in  $m_T$  spectra in  $A + A$  collisions is given by the model including the common transverse expanding velocity field together with a moderate temperature of a thermalized sys-

tem. With the presence of the transverse velocity field, the mass dependence of inverse slope parameters can be understood qualitatively as follows [12].

In case of a purely thermal motion, all particles (irrespective of their mass) would move with the same average kinetic energy determined by the temperature, i.e.,

$$\langle E_{\text{kine}} \rangle \sim T_{\text{thermal}}. \quad (1.4)$$

On the other hand, in case of a purely collective motion, all particles would move with the same velocity  $\beta_T$  and consequently, the average kinetic energy would increase proportional to their mass  $m_0$ , since

$$\langle E_{\text{collective}} \rangle \sim \frac{m_0 \beta_T^2}{2}. \quad (1.5)$$

Under the assumption of complete decoupling between the thermal and collective motion of the particle, superposition of both types of motion will give the mass dependence of;

$$\begin{aligned} \langle E_{\text{kine}} \rangle &= \langle E_{\text{thermal}} \rangle + \langle E_{\text{collective}} \rangle \\ &= T_{\text{thermal}} + \frac{m_0 \langle \beta_T \rangle^2}{2}, \end{aligned} \quad (1.6)$$

where  $\langle \beta_T \rangle$  is the averaged collective velocity for all particle species. The inverse slope parameter  $T_0$  is proportional to the average transverse kinetic energy and is given as,

$$T_0 \propto T_{\text{thermal}} + m_0 \cdot \langle \beta_T \rangle^2. \quad (1.7)$$

Furthermore, because of this velocity dependence, for heavier collision system, which presumably stronger collective transverse flow, the value of  $T_0$  is expected to be larger. The above observations are thus qualitatively consistent with the hypothesis of transverse hydrodynamic flow produced in the heavy-ion collisions. Quantitatively, the phenomenological hydrodynamical model proposed by Schnedermann *et. al.* [13] can be applied to the single particle spectra for the extraction of transverse velocity and temperature at freeze-out. In this model, termed the “blast-wave” model, collective expansion effects are incorporated into transverse mass spectra as following:

$$\frac{d\sigma}{m_T dm_T} \propto \int_0^R r dr m_T I_0\left(\frac{p_T \sinh \rho}{T_{\text{fo}}}\right) K_1\left(\frac{m_T \cosh \rho}{T_{\text{fo}}}\right), \quad (1.8)$$

where  $I_0$  and  $K_1$  represent modified Bessel functions with  $\rho$  being the transverse boost which depends on the radial position according to  $\rho = \tanh^{-1} \beta_r(r)$ . The detail of this expression is described in Appendix A.2. Here  $T_{\text{fo}}$  is the freeze-out temperature and  $R$  is

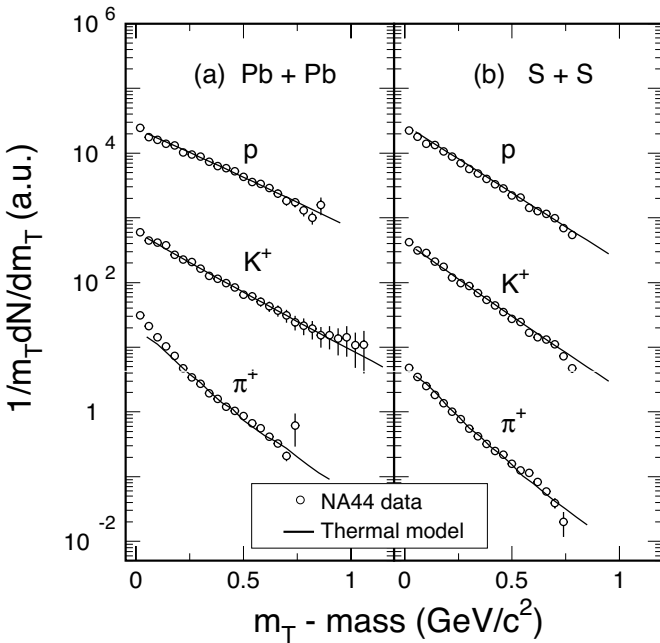


Figure 1.8: Transverse mass distributions for pions, kaons, and protons compared with results of a hydrodynamical model calculation. Resonance decays are included in the pion spectra, and resonance effects on kaon and proton spectra are neglected. This figure is taken from [11].

the maximum radius of the expanding source at freeze-out. The transverse velocity profile  $\beta_r(r)$  is parameterized as  $\beta_r(r) = \beta_T(r/R)^n$ , with the surface velocity  $\beta_T$ . We can vary the form of velocity profile with index  $n$ , for example,  $n = 0.5, 1, 2$ . The average of transverse velocity is defined as

$$\langle \beta_T \rangle = \frac{\int_0^R \beta_r(r) r dr}{\int_0^R r dr} = \left( \frac{2}{2+n} \right) \beta_T. \quad (1.9)$$

From the fitting results, the average of transverse velocity is independent of velocity profile [14].

Figure 1.8 shows the fitting results by the hydrodynamical flow model in central Pb + Pb and S+S collisions at mid-rapidity region [11]. Solid lines are the spectra of a source at  $T_{fo} = 140$  MeV and  $\beta_T = 0.6$  ( $\langle \beta_T \rangle = 0.4$ ) for Pb+Pb, and a source at  $T_{fo} = 140$  MeV and  $\beta_T = 0.41$  ( $\langle \beta_T \rangle = 0.27$ ) for S+S. As shown in Figure 1.8, all the particle spectra from pions to protons are shown to be reproduced very well with two parameters,  $T_{fo}$  and  $\beta_T$ .

### 1.2.3 Particle Ratios and Chemical Equilibrium

Hadron multiplicities and their correlations are observables in heavy-ion collisions. We can evaluate particle abundances by integrating particle yields over the complete phase space, Unlike the momentum distributions, particle ratios are expected to be non-sensitive to the underlying processes. It is found that the ratios of produced hadrons are well described by the simple statistical model [15].

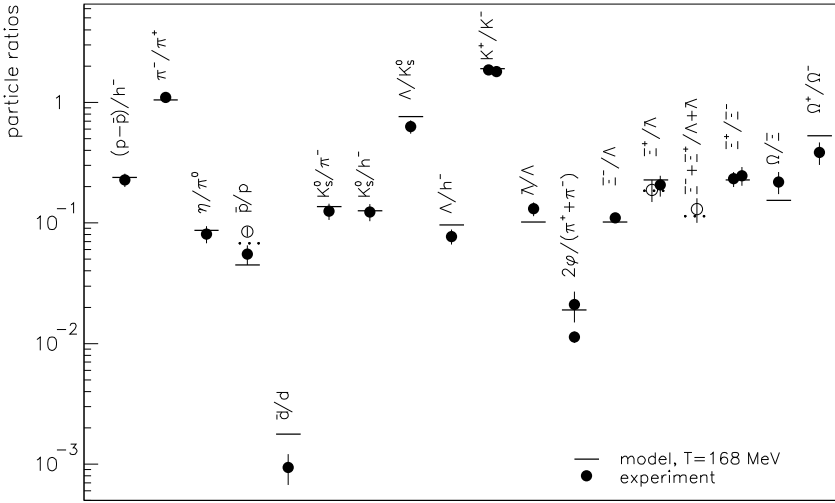


Figure 1.9: Hadron abundance ratios. Comparison between statistical model (horizontal bars) and experimental ratios (filled circles) [15].

The statistical model is based on the use of a grand canonical ensemble to describe the partition function and hence the density of the particles of species  $i$  in an equilibrated fireball:

$$n_i = \frac{g_i}{2\pi^2} \int_0^\infty \frac{p^2 dp}{\exp[(E_i - \mu_i)/T_{ch}] \pm 1} \quad (1.10)$$

with particle density  $n_i$ , spin degeneracy  $g_i$ , momentum  $p$ , total energy  $E$  and chemical potential  $\mu_i = \mu_B B_i - \mu_S S_i - \mu_{I_3} I_i^3$ . The quantities  $B_i$ ,  $S_i$  and  $I_i^3$  are the baryon, strangeness and three-component of the isospin quantum numbers of the particle of species  $i$ . With this model, only two parameters, the temperature  $T_{ch}$  and a baryon chemical potential  $\mu_B$  are independent and it has been shown that ratios of particle production can be well fitted.

Figure 1.9 show the comparison of the measured particle ratios and the model calculation. The model calculation include the effect of resonance decay and excluded volume corrections. As seen in the figure, this simple model can fit the the experimental ratios reasonably well and the temperature of  $T_{ch} \sim 170$  MeV at baryon chemical potential of  $\mu_B \sim 270$  MeV are obtained. Thus, chemical equilibrium seems to hold. It is very intriguing that abundances of the multi-strange particles also show the chemical equilibrium. Because they are supposed to decouple early from the fireball, they do not have enough time to reach the chemical equilibrium if they are produced in hadronic interactions.

## 1.3 Hard Scattering as a Probe of QGP

The spectra of high transverse momentum ( $p_T$ ) hadrons resulting from the fragmentation of hard-scattered partons potentially provide a direct probe of the properties of the initial state. In a high-energy nuclear collision, hard scattering will occur at the earliest time during the collision, well before the QGP is expected to form, and thus the scattered partons will subsequently experience the strongly interacting medium created in the collision. These partons are expected to lose energy [16] in hot and dense nuclear matter through gluon bremsstrahlung, effectively quenching jet production. This would have many observable consequences, of which the most directly measurable would be a depletion in the yield of high- $p_T$  hadrons [17]. It has been suggested that the energy loss is larger in a medium of deconfined color charges than in hadronic matter [18, 19], making “jet quenching” a potential signature for QGP formation. Therefore, a detailed analysis of high- $p_T$  hadron production may reveal information on the properties of the dense medium created early in the collisions [19, 20, 21].

### 1.3.1 Hard Scattering in $N - N$ Collisions

At the energies reached at the Relativistic Heavy Ion Collider (RHIC), high- $p_T$  hadrons are abundantly produced. In nucleon-nucleon collisions, it has been well established that hadrons with  $p_T \geq 2 \text{ GeV}/c$  result primarily from the fragmentation of hard-scattered partons, and that the  $p_T$  spectra of these hadrons can be calculated using perturbative QCD (pQCD) [22, 23]. For high- $p_T$  particles, hard scattering is described by the lowest-order subprocesses which corresponds to a convolution of two-body scattering. Figure 1.10 shows a schematic view of the factorization in  $1 + 2 \rightarrow 3 + X$  reaction. The corresponding expression for the inclusive particle production cross section in nucleon-nucleon collisions can be written as,

$$\begin{aligned} \sigma_{1,2}^3 &= \sum_{i,j,k} \int dx_i dx_j dz_k \cdot f_1^i(x_i, \mu_F) \cdot f_2^j(x_j, \mu_F) \\ &\quad \times \sigma_{i,j}^k(p_i, p_j, p_k, \alpha_s(\mu_R), Q^2/\mu_R, Q^2/\mu_F) \times D_k^3(z_k, \mu_F), \end{aligned} \quad (1.11)$$

where  $f_1^i(x_i, \mu_F)$  and  $f_2^j(x_j, \mu_F)$  are parton distribution function (PDF),  $D_k^3(z_k, \mu_F)$  is fragmentation function (FF), and  $\sigma_{i,j}^k(\dots)$  represents the cross section from two partons ( $i$  and  $j$ ) into a parton ( $k$ ).

The pQCD calculations are rather successful in describing high- $p_T$  particle production in high-energy  $N + N$  collisions. As an example, Figure 1.11 shows the invariant

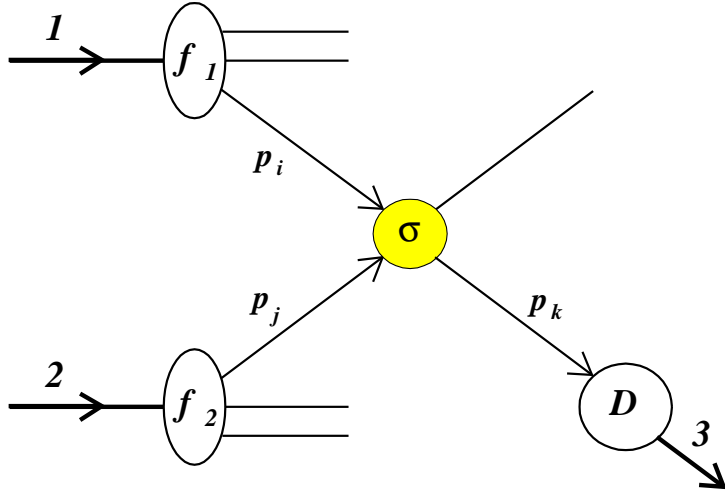


Figure 1.10: Schematic diagram for a hadron reaction ( $1 + 2 \rightarrow 3 + X$ ) factorized into parton distribution functions ( $f$ ), parton fragmentation functions ( $D$ ), and cross section ( $\sigma$ ) from two partons to parton.

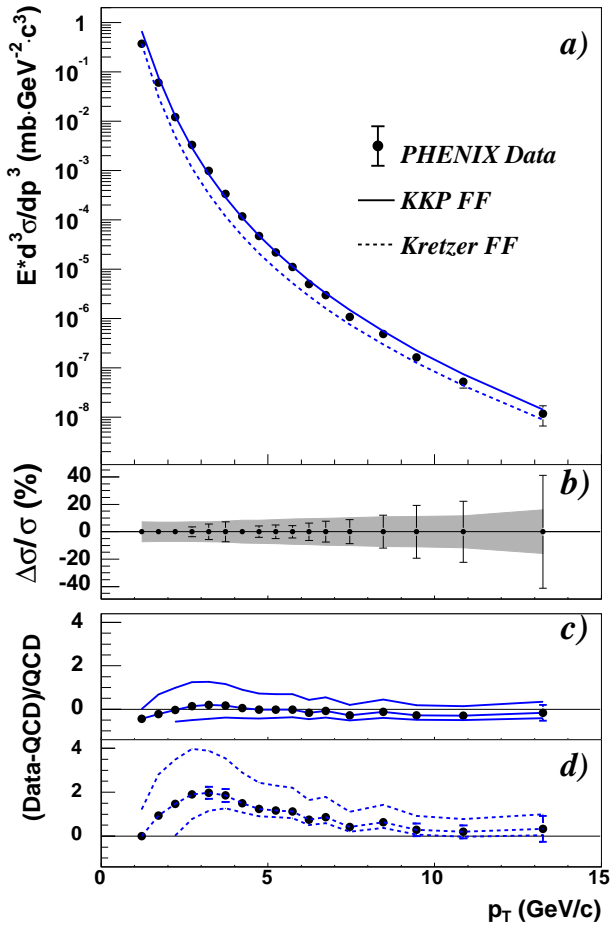


Figure 1.11: a) The invariant differential cross section for inclusive  $\pi^0$  production (points) at mid-rapidity in  $p + p$  collisions at  $\sqrt{s_{NN}} = 200$  GeV, and the results from NLO pQCD calculations with equal renormalization and factorization scales of  $p_T$  using the “Kniehl-Kramer-Pötter” [24] (solid line) and “Kretzer” [25] (dashed line) sets of fragmentation functions. b) The relative statistical (points) and point-to-point systematic (band) errors. c,d) The relative difference between the data and the theory using KKP (c) and Kretzer (d) fragmentation functions with scales of  $p_T/2$  (lower curve),  $p_T$ , and  $2p_T$  (upper curve). This figure is taken from [23].

cross section for the  $\pi^0$  production measured by PHENIX in  $p + p$  collisions at  $\sqrt{s} = 200$  GeV/c [23]. The results are compared with a next-to-leading order (NLO) pQCD calculation [24, 25] based on the factorization theorem. These calculations are consistent with the data down to  $p_T \sim 2$  GeV/c, indicating that the particle production is dominated by the fragmentation of hard-scattered partons and the production rate is well calibrated.

### 1.3.2 Hard Scattering in Heavy-Ion Collisions

In heavy-ion collision, the inclusive cross section for high- $p_T$  particle production is given by single hard parton-parton two-body scattering. The factorization theorem can be directly extrapolated to heavy-ion collisions. Naively, the hard-scattering cross section is proportional to the number of binary scaled  $N + N$  collisions,  $\langle N_{\text{coll}} \rangle$ ,

$$\frac{dN^{AA}}{dyd^2p_T} = \langle N_{\text{coll}} \rangle \frac{dN^{NN}}{dyd^2p_T} \quad (1.12)$$

Thus, the total hard-scattering cross-section for minimum bias A-A collisions is related to that for  $N + N$  collisions (Eq. 1.12) by,

$$\frac{1}{\sigma_{\text{inel}}^{AA}} \frac{d\sigma^{AA}}{dyd^2p_T} = \frac{\langle N_{\text{coll}} \rangle}{\sigma_{\text{inel}}^{NN}} \frac{d\sigma^{NN}}{dyd^2p_T}. \quad (1.13)$$

At the energy reached at RHIC, a bulk medium spanning a few hundred of fm<sup>3</sup> with energy density exceeding several GeV/fm<sup>3</sup> can be created 0.3-1 fm/c after the colliding nuclei pass through each other. This matter will leave its footprint on the properties of the experimentally observed particles. To quantify such modifications we need a baseline expectation for spectra from nuclear ( $A + A$ ) collisions in the absence of nuclear medium effects. Given that hard parton scatterings have small cross sections, one can regard the nuclei as an incoherent superposition of partons (“point-like scaling”). We approximate this by modeling the  $A + A$  collision as a sum of independent nucleon-nucleon ( $N + N$ ) collisions (“binary scaling”). For a given class of  $A + A$  collisions, we can determine  $\langle N_{\text{coll}} \rangle$  the average number of inelastic  $N + N$  collisions per event and then define the *nuclear modification factor* as the ratio,

$$R_{AA}(p_T) = \frac{(1/N_{\text{evt}}) d^2N^{AA}/dp_T d\eta}{(\langle N_{\text{coll}} \rangle / \sigma_{\text{inel}}^{NN}) d^2\sigma^{NN}/dp_T d\eta}. \quad (1.14)$$

In the absence of nuclear modifications to hard scattering, the ratio  $R_{AA}$  will be unity; thus departures from  $R_{AA} = 1$  indicate nuclear medium effects. For  $p_T$  above 2 GeV/c, particle production in  $p + A$  collisions is enhanced compared to binary scaling, commonly

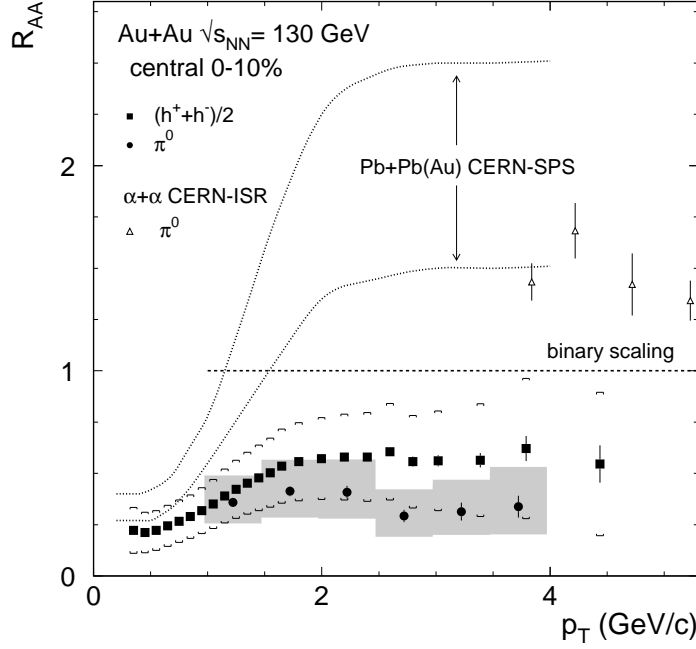


Figure 1.12: The ratio  $R_{AA}$  for charged hadrons and neutral pions (weighted average of PbSc and PbGl results) in central Au+Au collisions. The error bars indicate the statistical errors on the measurement. The surrounding bands [shaded for  $\pi^0$ 's, brackets for  $(h^+ + h^-)/2$ ] are the quadrature sums of (i) the systematic errors on the measurement, (ii) the uncertainty in the  $N+N$  reference, and (iii) the uncertainty in  $\langle N_{\text{coll}} \rangle$ . Also shown are the ratio of inclusive cross sections in  $\alpha + \alpha$  compared to  $p + p$  at  $\sqrt{s_{NN}}=31$  GeV [34], and spectra from central Pb + Pb, Pb + Au compared to  $p + p$  collisions at  $\sqrt{s_{NN}}=17$  GeV [35] shown as a band indicating the range of uncertainty. This figure is taken from [30].

referred to as the “Cronin effect” [27, 28]. It is observed and studied in  $p+A$  collisions up to 400GeV. This effect is consistent with the power law form of the jet production cross section and with the picture of multiple parton scattering in  $p+A$  collisions, a random walk of partons in transverse momentum enhances the production of high- $p_T$  hadrons. This Cronin effect is observed at lower beam energy  $A+A$  collisions as below; namely at CERN-ISR  $\alpha+\alpha$  collisions at  $\sqrt{s_{NN}}=31$  GeV [34] and CERN-SPS Pb + Pb, Pb + Au collisions at  $\sqrt{s_{NN}}=17$  GeV [35].

At RHIC-PHENIX experiment, we have studied and reported the high- $p_T$   $\pi^0$  and charged hadron production from Au+Au collisions at  $\sqrt{s_{NN}} = 130$ GeV [30, 31] and 200GeV [32, 33]. Figure 1.12 show the ratio  $R_{AA}$  for central collisions. For the charged spectrum  $R_{AA}$

rises up to  $2 \text{ GeV}/c$ , as expected; but above  $2 \text{ GeV}/c$ ,  $R_{AA}$  remains significantly below unity for both spectra. The suppression in central collisions is in qualitative agreement with the predictions of energy loss by scattered partons traversing a dense medium.

### 1.3.3 Reference Experiment: $d+\text{Au}$ Collisions

Theoretical studies of parton propagation in high density matter suggest that partons lose a significant fraction of their energy through gluon bremsstrahlung[16], reducing the parton momentum and depleting the yield of high  $p_T$  hadrons [17, 21]. This is a final-state effect in the spatially extended medium created in  $A+A$  collisions. Initial-state effects include nuclear modifications to the parton momentum distributions (structure functions), and soft scatterings of the incoming parton prior to its hard scattering. These should be present in  $p+A$ ,  $d+A$  and  $A+A$ .

Interpretations of Au+Au collisions based on initial-state parton saturation effects [36] or final-state hadronic interactions [37] also predict a considerable suppression of the hadron production at high- $p_T$ . It is therefore of paramount interest to determine experimentally the modification, if any, of high- $p_T$  hadron yields due to initial state nuclear effects for a system in which a hot, dense medium is not produced in the final state. To consider the initial-state effect or final-state effect, we have measured charged hadron and  $\pi^0$  production at mid-rapidity in  $d+\text{Au}$  collisions at  $\sqrt{s_{\text{NN}}} = 200 \text{ GeV}$  [38].

The *nuclear modification factor* for  $d+\text{Au}$  collisions is defined as the ratio of invariant yield in  $d+\text{Au}$  to that of  $p+p$ , scaled by the number of binary collisions,

$$R_{dA}(p_T) = \frac{(1/N_{\text{evt}}) d^2N^{dA} / dp_T d\eta}{(\langle N_{\text{coll}} \rangle / \sigma_{\text{inel}}^{NN}) d^2\sigma^{NN} / dp_T d\eta}. \quad (1.15)$$

The top panel of Figure 1.13 shows  $R_{dA}$  for inclusive charged particles  $(h^+ + h^-)/2$ , again compared with  $R_{AA}$  observed in central Au+Au collisions, while the lower panel compares  $(h^+ + h^-)/2$  with  $\pi^0$ .

The data clearly indicate that there is no suppression of high- $p_T$  particles in  $d+\text{Au}$  collisions. We do, however, observe an enhancement in inclusive charged particle production at  $p_T > 2 \text{ GeV}/c$ . A similar enhancement was observed in  $p+A$  fixed-target experiments [28] and is generally referred to as the “Cronin effect”. The  $\pi^0$  data suggest a smaller enhancement for pions than for inclusive charged particles at  $p_T = 2\text{-}4 \text{ GeV}/c$ . We note that the charged spectrum includes baryons and anti-baryons, which may have a different nuclear enhancement than the mesons [28].

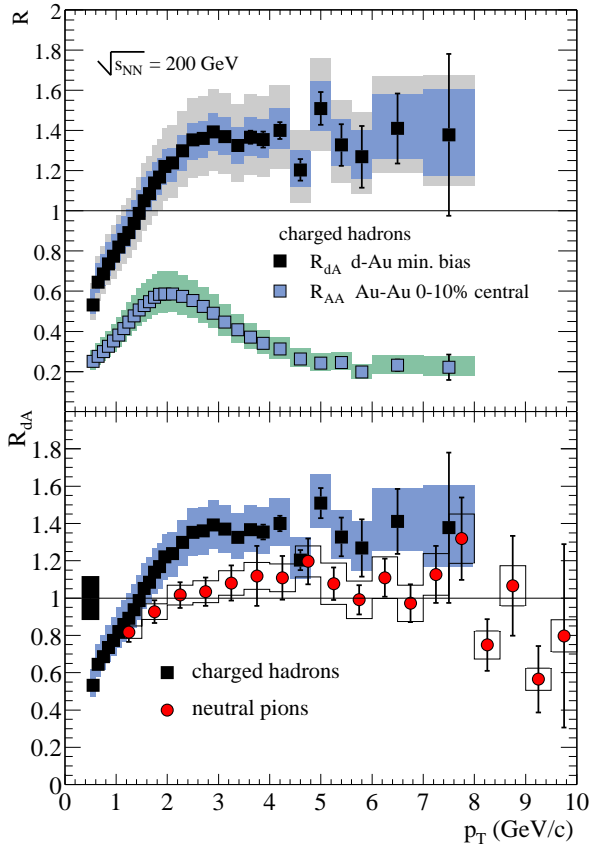


Figure 1.13: Top: Nuclear modification factor  $R_{dA}$  for  $(h^+ + h^-)/2$  in minimum bias d+Au compared to  $R_{AA}$  in the 10% most central Au+Au collisions. Inner bands show systematic errors which can vary with  $p_T$ , and outer bands include also the normalization uncertainty. Bottom: Comparison of  $R_{dA}$  for  $(h^+ + h^-)/2$  and the average of the  $\pi^0$  measurements in d+Au. The bar at the left indicates the systematic uncertainty in common for the charged and  $\pi^0$  measurements. This figure is taken from [38].

The observation of an enhancement of high- $p_T$  hadron production in both the minimum bias  $d+Au$  and the neutron tagged sample of  $p+Au$  collisions indicates that the suppression in central Au+Au collisions is not an initial state effect. Nor does it arise from modification of parton structure functions in nuclei. The data suggest, instead, that the suppression of high- $p_T$  hadrons in Au+Au is more likely a final state effect of the produced dense medium.

## 1.4 Thesis Motivation

In this thesis, we present the results of identified hadron spectra and yields in Au+Au collisions at the energy of  $\sqrt{s_{NN}} = 200$  GeV by the PHENIX experiment using the Relativistic Heavy Ion Collider (RHIC).

As reviewed in this chapter, hydrodynamic models that include radial flow successfully describe the measured  $p_T$  distributions in heavy-ion collisions at AGS and SPS. Particle ratios have been shown to be well reproduced by two parameters: a baryon chemical potential  $\mu_B$  and a chemical freeze-out temperature  $T_{ch}$ . We study the hydrodynamic behavior at RHIC energy. Especially, we like to study the  $p_T$  range where the hydrodynamical anal-

ysis can be applicable by taking into account the decay effects.

On the other hand, one of the most interesting observations at RHIC is that the yield of high- $p_T$  neutral pions and non-identified charged hadrons in central Au+Au collisions at RHIC are below the expectation of the scaling with the number of nucleon-nucleon binary collisions,  $N_{\text{coll}}$ . It has also been observed that the yield of neutral pions is more strongly suppressed than that for non-identified charged hadrons in central Au+Au collisions at RHIC. These observations suggest that a detailed study of particle composition at high- $p_T$  is very important to understand hadron production and collision dynamics at RHIC.

## 1.5 Contributions of the Author

The author participated RHIC-PHENIX experiment and contributed as following,

- Construction of the Time-of-Fight counter.
- Installation of the Time-of-Fight counter in PHENIX detector system.
- Operation of the Time-of-Fight counter during run period.
- Development of the detector simulation for the Time-of-Fight counter.
- Programming of the reconstruction software for the Time-of-Fight counter.
- Timing calibration for the Time-of-Fight counter.
- Analysis of the identified hadron spectra and yields in Au+Au collisions at  $\sqrt{s_{\text{NN}}} = 200 \text{ GeV}$  and publish the results to Phys. Rev. C **69** 034909 (2004) [40].

# Chapter 2

## The PHENIX Experiment

In this chapter, the RHIC collider complex and the PHENIX detector system overview are described. The detail description of PHENIX detector system are described in section 2.2 to 2.6.

### 2.1 RHIC : Collider Facility

The Relativistic Heavy Ion Collider (RHIC) [41] at Brookhaven National Laboratory is capable of accelerating a wide variety of nuclei and ions from protons to Au ions. The top energy for heavy ion beams (e.g., for Au ions) is 100 GeV per nucleon and that for protons is 250GeV. The design luminosity are  $2 \times 10^{26} \text{cm}^{-2}\text{sec}^{-1}$  for Au beams and  $1.4 \times 10^{31} \text{cm}^{-2}\text{sec}^{-1}$  for proton beams.

The schematic diagram of the RHIC collider facility is shown in Figure 2.1. The RHIC complex consists of Tandem Van de Graff, Alternating Gradient Synchrotron (AGS) and RHIC main rings. The collider consists of two quasi-circular concentric accelerator/storage rings on a common horizontal plane, one ("Blue Ring") for clockwise and the other ("Yellow Ring") for counter-clockwise beams. Rings are oriented to intersect with one another at six locations along their 3.8 km circumference. [42]

Procedure of the RHIC acceleration for Au ion beams is as follow. Negatively charged Au ions generated by pulsed sputter ion source are injected to the Tandem Van de Graaffs. The ions are partially stripped off their electrons with a foil at the Tandem's high voltage terminal, and then accelerated to the energy of 1 MeV per nucleon by the second stage of the Tandem. After further stripping at the exit of the Tandem and a charge selection by bending magnets, beams of Au ions with the charge state of +32 are delivered to the

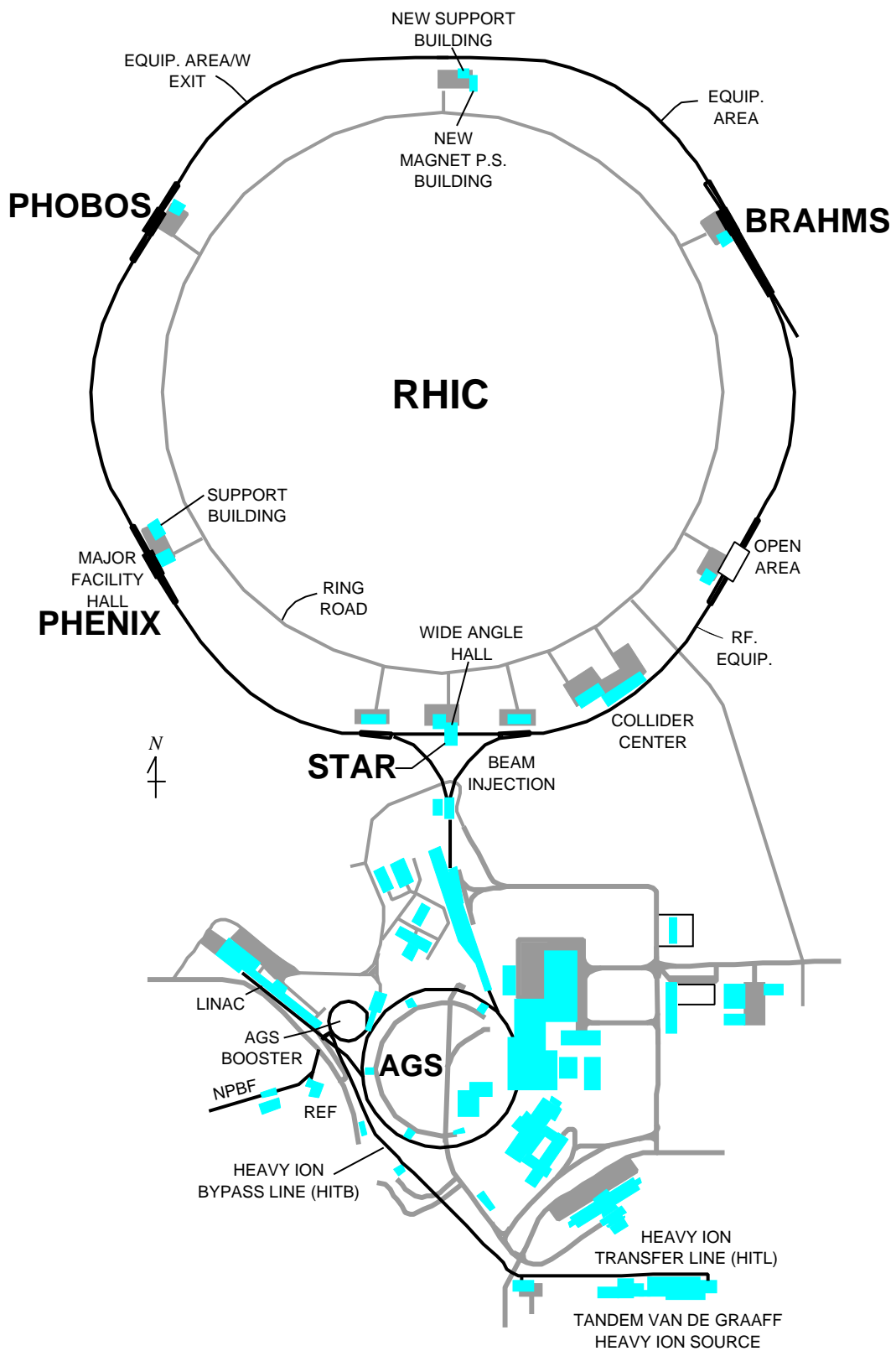


Figure 2.1: Layout of the AGS–RHIC complex

Booster Synchrotron and accelerated to 95 MeV per nucleon. Then the ions are stripped again at the exit from the Booster to reach the charge state of +77, a helium-like ion, and injected to the AGS. The AGS accelerates the Au beams to the RHIC injection energy of 10.8 GeV per nucleon. The Au ions, injected into the AGS in 24 bunches, are de-bunched and then re-bunched to four bunches at the injection from porch prior to the acceleration. These four bunches are ejected at the top energy, one bunch at a time, and transferred to RHIC through the AGS-to-RHIC Beam Transfer Line. The Au ions are fully stripped to the charge state of +79 at the exit from the AGS. The stacking in the RHIC rings is done in a boxcar fashion.

Acceleration and storage of beam bunches at RHIC uses two RF systems; i.e., one operating at 28 MHz to capture the AGS bunches and accelerates to the top energy, and the other operating at 197 MHz to provide short-collision diamond ( $\sigma_L \sim 25$  cm) for a more reasonable detector design. The synchrotron phase transition of the RHIC lattice is at  $\gamma_T = 24.7$ ; thus all ions, except protons, must go through this transition. The RHIC collider, indeed, is the first super-conducting accelerator (hence slow ramp rate) that passes through the synchrotron phase transition and associated beam instability. It is important to cross this transition rapidly in order to minimize the beam loss and the emittance growth. This can be accomplished either by rapid acceleration through it with resultant orbit jump to a larger radius or by a " $\gamma_T$ -jump", where sets of quadrupole are pulsed to change the tune of the machine and thus move the transition energy momentarily. For the year 2000 operation, the former method was used due to the lack of pulsed power supplies, while for the year 2001 run, the latter method has been implemented.

## 2.2 PHENIX Detector Overview

The PHENIX [43, 44] is one of the major experiments at RHIC to detect a variety of signals from quark-gluon plasma. It is designed to perform a broad study of A-A, p-A, and p-p collisions to investigate nuclear matter under extreme condition. PHENIX measures electrons, muons, photons and hadrons with excellent energy and momentum resolution.

The detector consists of a large number of subsystems. It comprises two central arms, two forward muon arms, and three global detectors. The east and west central arms are placed at zero rapidity and instrumented to detect electrons, photons and charged hadrons. The north and south forward arms have full azimuthal coverage and are instrumented to detect muons. The global detectors measure the start time, vertex and multiplicity of the interactions. The rapidity and  $\phi$  coverage and other features of these subsystems is given in Table 2.1 and a perspective drawing of the PHENIX detector with the major subsystems labeled is shown in Figure 2.2. The details of each subsystems are described as following section.

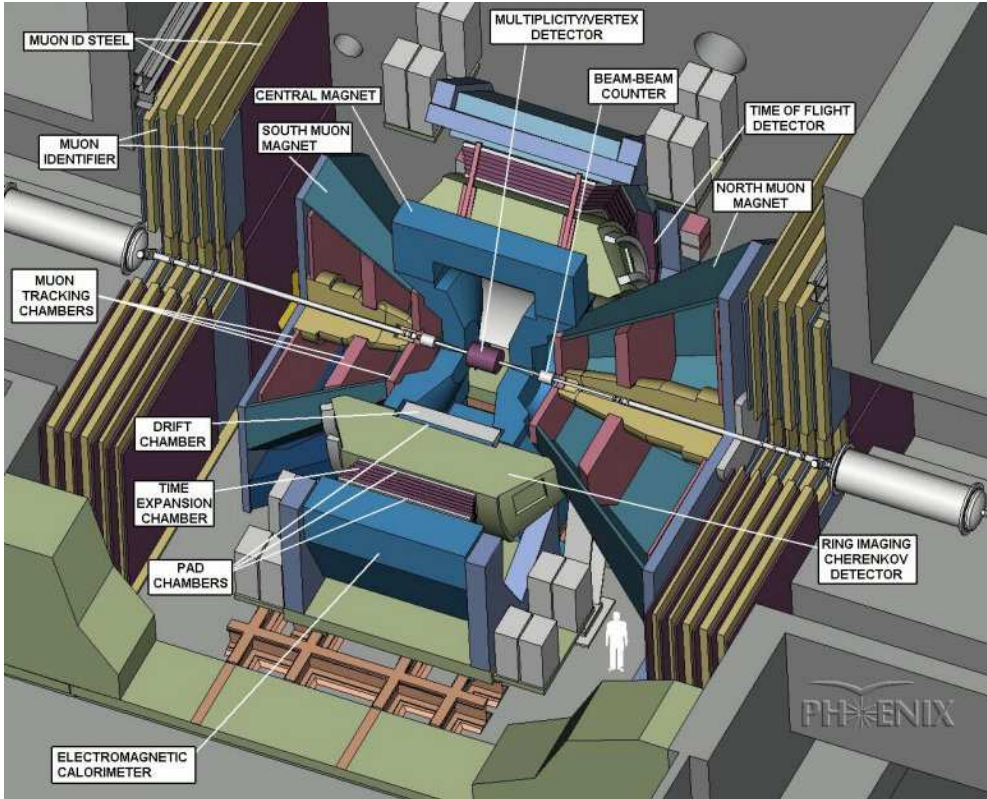


Figure 2.2: A cutaway drawing of the PHENIX detector. Labeled arrows point to the major detector subsystems.

Element	$\Delta\eta$	$\Delta\phi$	Purpose and Special Features
Magnet: Central (CM) muon (MMS) muon (MMN)	$\pm 0.35$	$360^\circ$	Up to $1.15 \text{ T}\cdot\text{m}$ .
	$-1.1 \text{ to } -2.2$	$360^\circ$	$0.72 \text{ T}\cdot\text{m}$ for $\eta = 2$
	$1.1 \text{ to } 2.4$	$360^\circ$	$0.72 \text{ T}\cdot\text{m}$ for $\eta = 2$
Silicon (MVD)	$\pm 2.6$	$360^\circ$	$d^2N/d\eta d\phi$ , precise vertex, reaction plane determination
Beam-beam (BBC)	$\pm(3.1 \text{ to } 3.9)$	$360^\circ$	Start timing, fast vertex.
NTC	$\pm(1 \text{ to } 2)$	$320^\circ$	Extend coverage of BBC for p-p and p-A.
ZDC	$\pm 2 \text{ mrad}$	$360^\circ$	Minimum bias trigger.
Drift chambers (DC)	$\pm 0.35$	$90^\circ \times 2$	Good momentum and mass resolution, $\Delta m/m = 0.4\%$ at $m = 1 \text{ GeV}$ .
Pad chambers (PC)	$\pm 0.35$	$90^\circ \times 2$	Pattern recognition, tracking for nonbend direction.
TEC	$\pm 0.35$	$90^\circ$	Pattern recognition, $dE/dx$ .
RICH	$\pm 0.35$	$90^\circ \times 2$	Electron identification.
TOF	$\pm 0.35$	$45^\circ$	Good hadron identification, $\sigma < 100 \text{ ps}$ . $K^\pm/\pi^\pm$ separation up to $2 \text{ GeV}/c$
T0	$\pm 0.35$	$45^\circ$	Improve TOF timing for p-p and p-A.
PbSc EMCal	$\pm 0.35$	$90^\circ + 45^\circ$	For both calorimeters, photon and electron detection.
PbGl EMCal	$\pm 0.35$	$45^\circ$	Good $e^\pm/\pi^\pm$ separation at $p > 1 \text{ GeV}/c$ by EM shower and $p < 0.35 \text{ GeV}/c$ by TOF. $K^\pm/\pi^\pm$ separation up to $1 \text{ GeV}/c$ by TOF.
$\mu$ tracker: ( $\mu$ TS) ( $\mu$ TN) $\mu$ identifier: ( $\mu$ IDS) ( $\mu$ IDN)	$-1.15 \text{ to } -2.25$	$360^\circ$	Tracking for muons.
	$1.15 \text{ to } 2.44$	$360^\circ$	Muon tracker north installed for year-3
	$-1.15 \text{ to } -2.25$	$360^\circ$	Steel absorbers and Iarocci tubes for
	$1.15 \text{ to } 2.44$	$360^\circ$	muon/hadron separation.

Table 2.1: Summary of the PHENIX Detector Subsystems.

## 2.3 PHENIX Magnet System

The PHENIX magnet system [45] is composed of three spectrometer magnets with iron yokes and water-cooled copper coils. The Central Magnet (CM) is energized by two pairs of concentric coils and provides a field around the interaction vertex that is parallel to the beam. This allows momentum analysis of charged particles in the polar angle range from  $70^\circ$  to  $110^\circ$ . The north and south Muon Magnets (MMN and MMS) use solenoid coils to produce a radial magnetic field for muon analysis. Each covers a pseudo-rapidity interval of 1.1 to 2.3 and full azimuth. The Main Magnet coils are wound on cylindrical surfaces at the end of large tapered pistons. Each of the three magnets provides a field integral of about 0.8 Tesla-meters. The physical and operating parameters of the magnets and their coils are given along with a description of the magnetic fields generated. The magnetic volumes of the PHENIX magnets are very large and complex, so a new technique was developed to map the fields based on surface measurements of a single field component using single axis Hall probes mounted on a rotating frame.

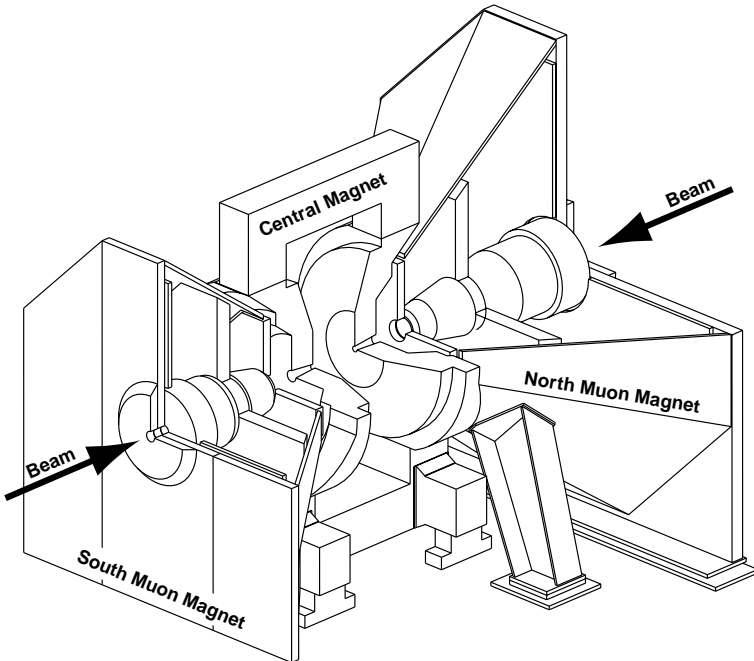


Figure 2.3: Line drawings of the PHENIX magnets, shown in perspective and cut away to show the interior structures. Arrows indicate the beam line of the colliding beams in RHIC.

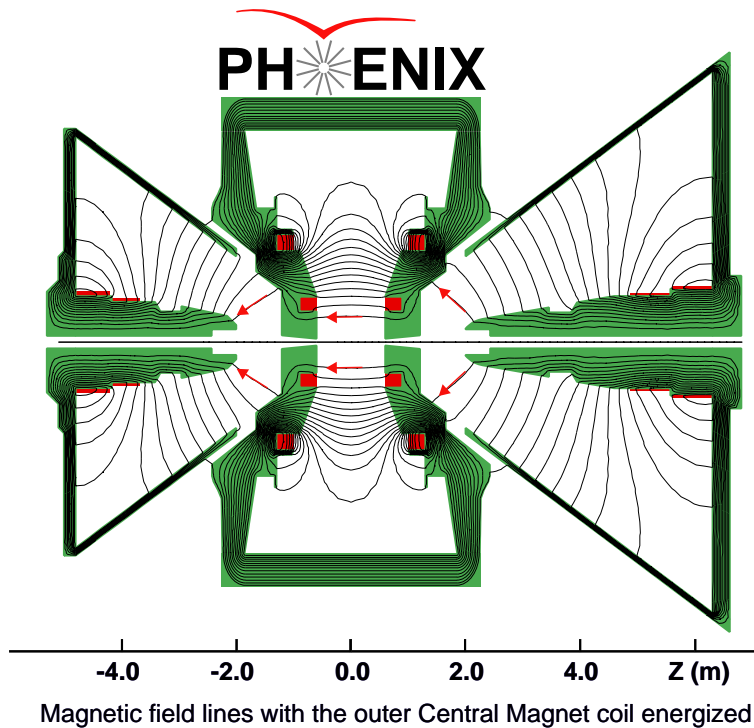


Figure 2.4: CM and MM field lines shown on a cutaway drawing of the PHENIX magnets. The beams travel along the  $z$  axis in this figure and collide at  $z = 0$ .

## 2.4 PHENIX Global Detectors

The timing, location and particle multiplicity of collision are determined by the Beam-Beam Counters (BBC), the Multiplicity/Vertex Detector (MVD) and the Zero-Degree Calorimeters (ZDC) [46, 47]. The BBC's provide both the time of interaction and position of a collision along  $z$  axis from the flight time of prompt particles. The MVD provides a measure of event particle multiplicity, collision vertex position and fluctuations in charged particle distributions. The ZDC's provide information on the collisions.

### 2.4.1 Zero Degree Calorimeter

The zero-degree calorimeters provide common event characterization in the four experiments at RHIC. The ZDC is a small hadronic calorimeter which measures the kinetic energy carried by spectator neutrons.

A single ZDC consists of three modules. Figure 2.5 shows the mechanical design of a ZDC module. Each ZDC module consists of Tungsten alloy plates and ribbons of optical fibers in the sampling layer. The depth is 2 hadronic interaction lengths. The lights are

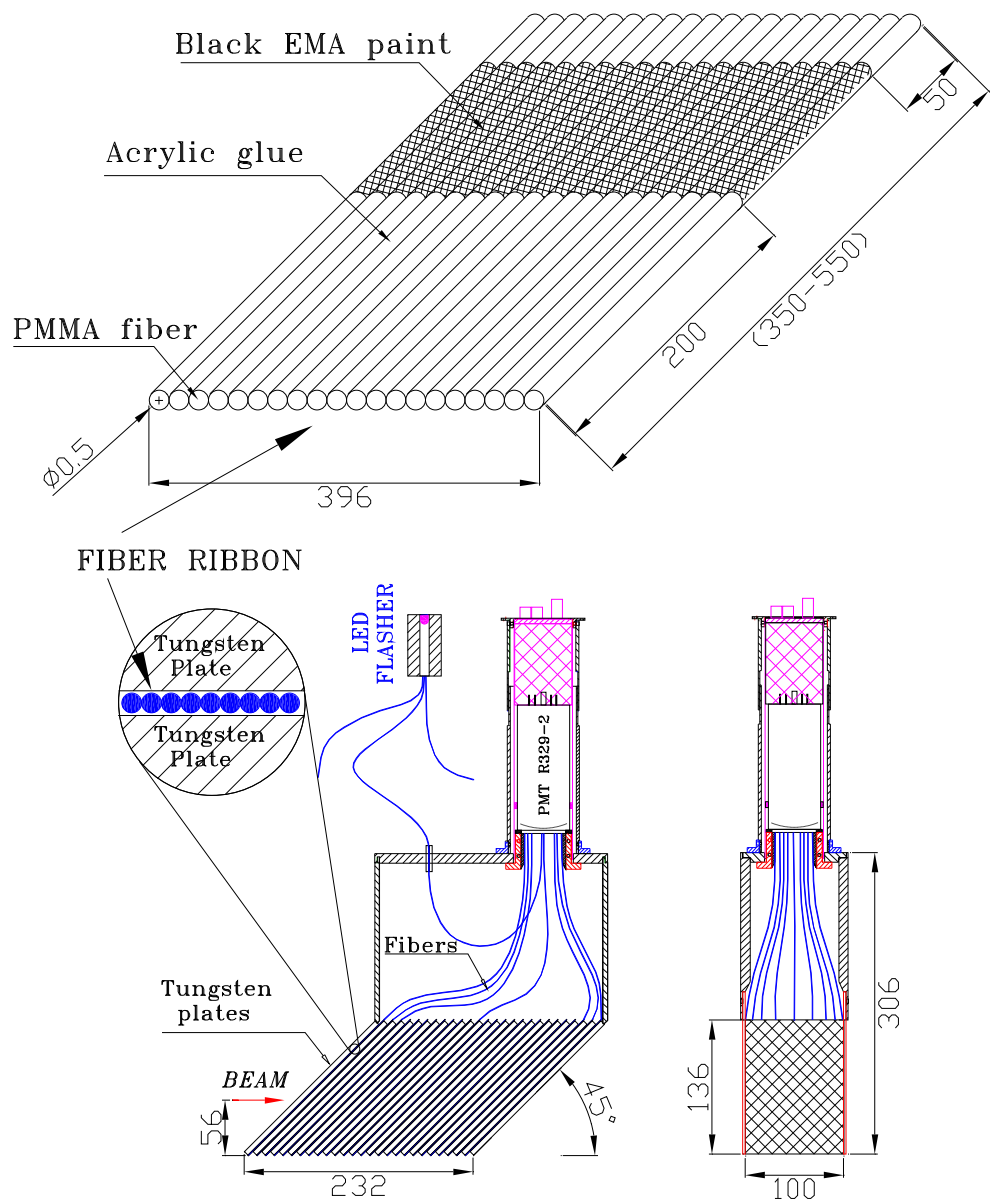


Figure 2.5: Mechanical design of a ZDC module

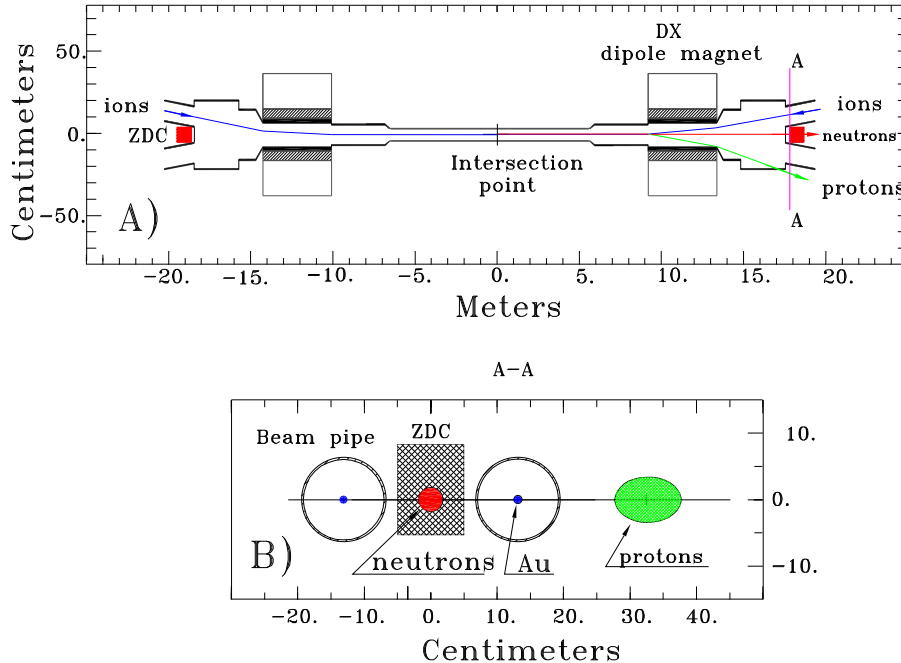


Figure 2.6: Plain view of the collision region and (section A-A) “beam’s eye” view of the ZDC location

collected into a photo-multiplier tube (PMT) via optical fibers and readout. Both time and amplitude are digitized for each PMT – as is an analog sum of the three PMT signals for each ZDC.

Figure 2.6 shows the layout of the ZDC location. They are placed 18 m up- and downstream of the interaction point along the beam line. Each ZDC covers 2 mrad of forward angular cone which corresponds to pseudo-rapidity region  $|\eta| > 6.0$ . At 11 m from the interaction point, there are the dipole magnets to align two circulating beams to match at intersection point. The Au ions beam is bended by one dipole magnet and bended again by another dipole magnet in the opposite side, then it is returned to the collider beam line. For the collision, fragment protons are swept out and only fragment neutrons emitted in the very narrow angular cone hit the ZDC.

## 2.4.2 Beam-Beam Counter

The beam-beam counters (BBC) measure the start time and the collision vertex point along the beam axis ( $z$ -axis). Since the longitudinal size of the beam bunch at RHIC for Au+Au

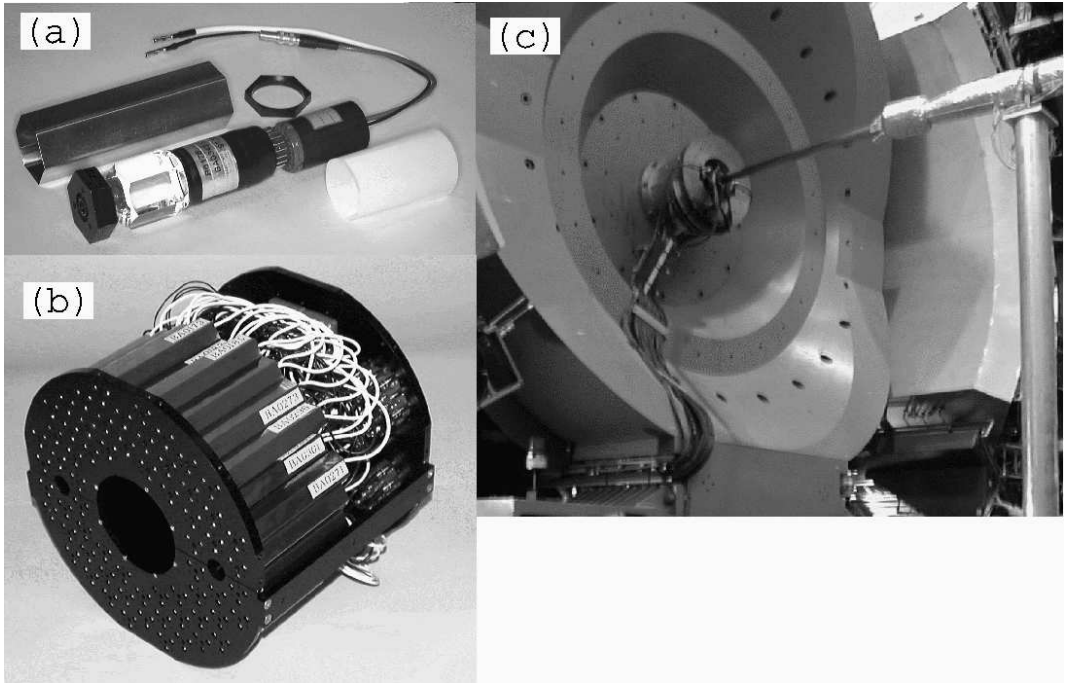


Figure 2.7: (a) A BBC element consists of one-inch mesh dynode photomultiplier tubes mounted on a 3 cm quartz radiator. (b) A BBC array comprises 64 BBC elements. (c) The BBC is mounted on the PHENIX detector. The beam pipe is seen in the middle of the picture. The BBC is installed on the mounting structure just behind the central spectrometer magnet.

collisions is designed to be 25 cm RMS, the time spread of nuclear collisions could be as much as 2 ns.

The BBC consists of two identical sets of counters, which are placed 1.44 m from the interaction point along the beam line (one on the North side and the other on the South side) surrounding the beam pipe. This corresponds to a pseudo-rapidity range from 3.0 to 3.9 over the full azimuth. Each counter consists of 64 Čerenkov telescopes, arranged radially around the beam pipe. A BBC telescope consists of one-inch mesh dynode photomultiplier tubes (HAMAMATSU R6178) mounted on a 3 cm quartz radiator. Figure 2.7 shows (a) a BBC element, (b) a BBC array and (c) the BBC mounted on the PHENIX detector.

Each BBC measures arrival times of leading charged particles from the collision. The arrival time for each BBC is defined as the average of the hit time in each BBC. The collision time is defined as the average arrival time of North and South BBCs. The time-of-flight measurement uses this information for start time.

The time difference between North and South side of BBCs provides the vertex position along the beam axis. Figure 2.8(a) shows a correlation of z-vertex calculated by BBC and ZDC, and Figure 2.8(b) shows the projection of Figure 2.8(a) on to the axis of BBC

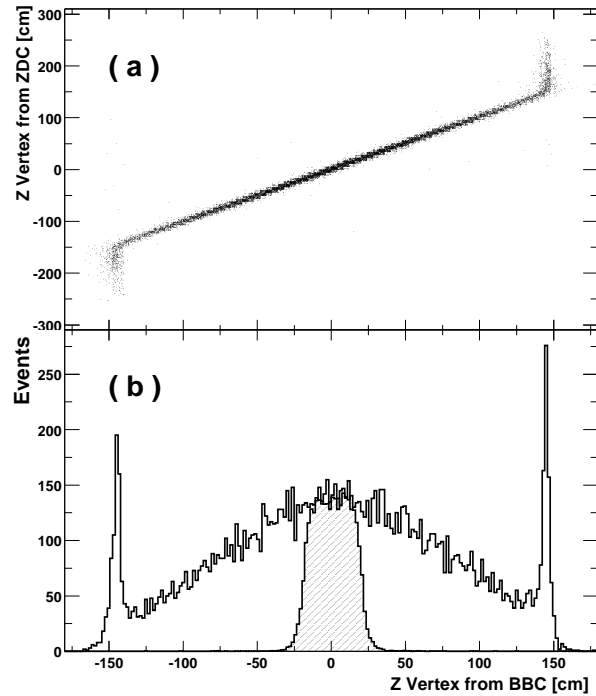


Figure 2.8: (a) Correlation of determined  $z$  vertex between BBC and ZDC. (b)  $Z$  vertex distribution from BBC. Hatched area corresponds to the events satisfying the PHENIX Local LVL1 trigger condition.

$z$ -vertex. The peak at  $\pm 144$  cm in Figure 2.8(b) corresponds to beam collisions outside of the BBC. The  $z$ -vertex position and number of PMT's hits in each BBC are also calculated online and sent to the LVL1 trigger.  $|z\text{-vertex}| < 20$  cm and two or more PMT's fired in each BBC are required as the LVL1 trigger condition. The hatched area in Figure 2.8(b) corresponds to the events selected by the LVL1 trigger. The trigger efficiency with respect to inelastic Au+Au collisions is evaluated by a PHENIX detector simulation with the HI-JING event generator to produce Au+Au collisions as input, and was found to be  $92 \pm 2\%$ . The correlation between BBC charge sum and ZDC total energy is used for centrality determination. The detail explanation of the trigger efficiency and the centrality selection is given in section 3.1.

## 2.5 Central Arm Spectrometers

PHENIX have two central arms at zero rapidity to detect electrons, photons and charged hadrons. The central arm detectors consist of tracking system for charged particles and electromagnetic calorimetry. The tracking system consists of drift chamber (DC), pad chamber (PC) and time expansion chamber (TEC) [48]. The ring imaging cherenkov (RICH) and time-of-flight (TOF) systems provide identification of charged particle [49]. The electromagnetic calorimeter (EMCal) provides measurements of both photons and energetic electrons [50]. The following sections describe the parts of the detector that are used for charged hadron measurements.

PHENIX Detector - Second Year Physics Run

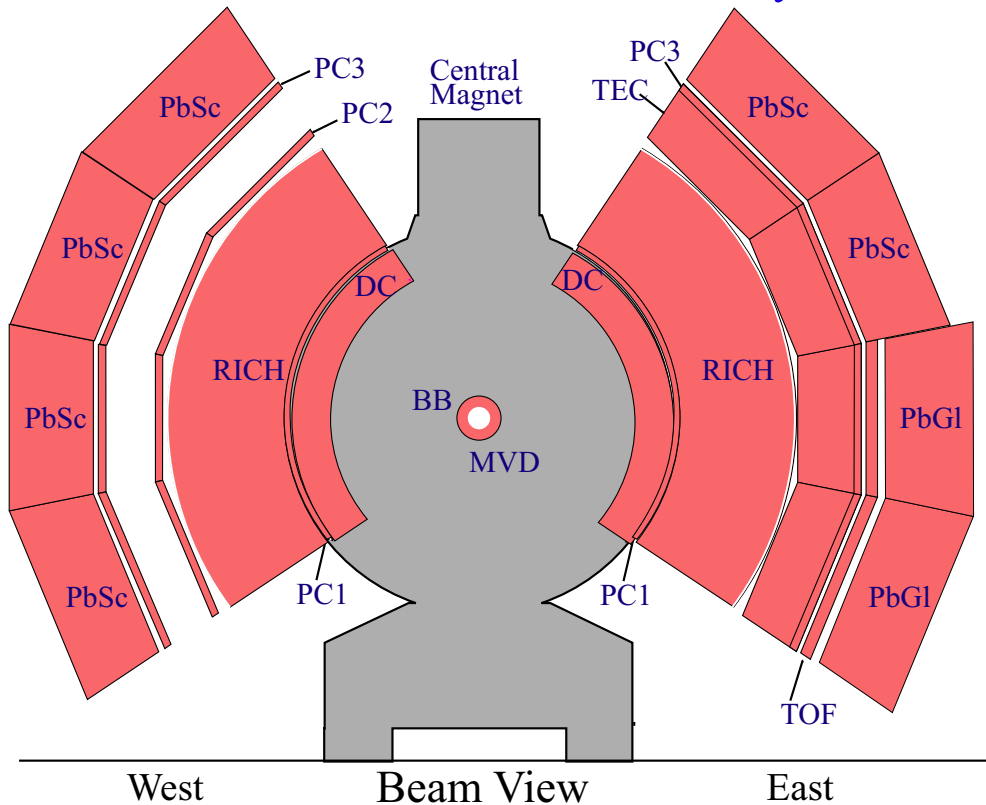


Figure 2.9: The two central spectrometer arms, viewed in a cut through the collision vertex.

### 2.5.1 Drift Chamber

The drift chambers (DC) measures charged particle trajectories in the  $r-\phi$  direction to determine the transverse momentum of charged particle. By combining the polar angle information from the first layer of the PC with the transverse momentum, the total momentum  $p$  is determined. The DC also participates in the pattern recognition at high particle track densities by providing position information that is used to link tracks through the various PHENIX detector subsystems. To measure the  $\phi \rightarrow e^+e^-$  mass with a resolution better than its natural width of 4.4 MeV and have good tracking efficiency for the highest multiplicities at RHIC, the DC was designed to have (i) single wire resolution better than  $150 \mu\text{m}$  in  $r-\phi$ , (ii) single wire two track separation better than 1.5 mm, (iii) single wire efficiency better than 99%, and (vi) spatial resolution in the  $z$  direction better than 2 mm.

The DC system consists of two independent gas volumes located in the west and east arms, respectively. The chambers in the east arm and the west arm are symmetric with respect to  $x = 0$  plane, as seen in Figure 2.9. They are located in the region from 2 to 2.4 m from the beam axis and 2 m along the beam direction. It is in a residual magnetic field with a maximum of 0.6 kG.

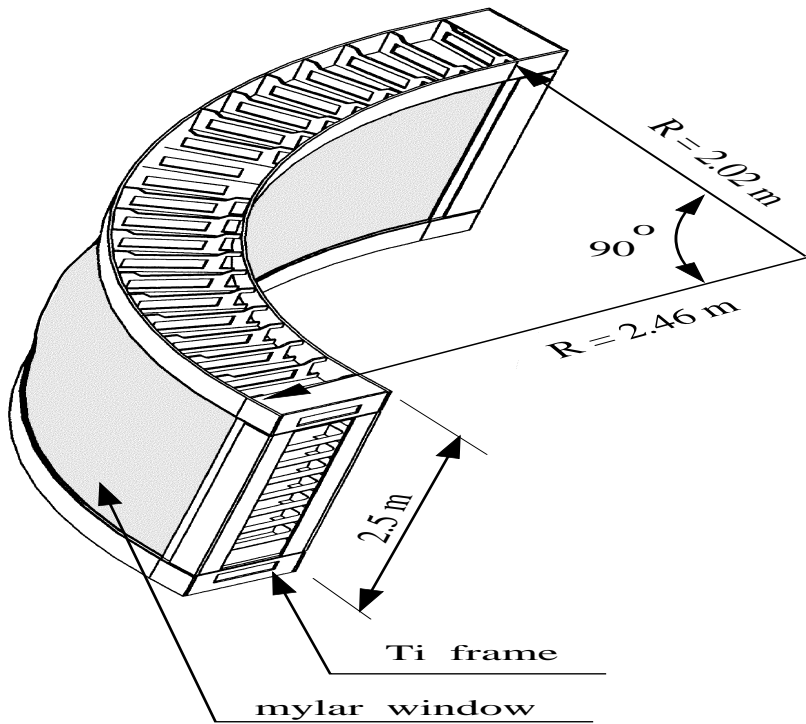


Figure 2.10: Construction of DC frame.

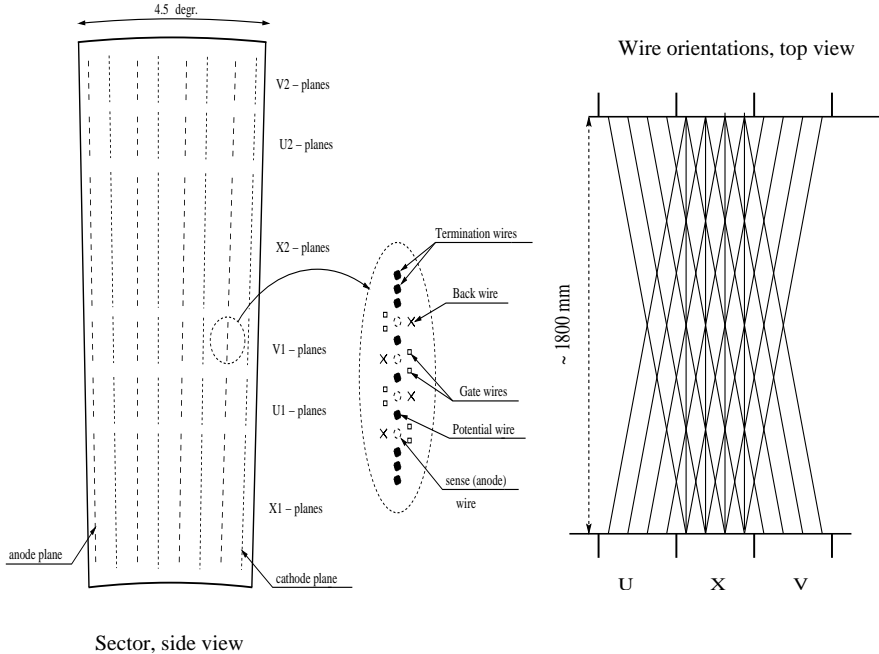


Figure 2.11: The layout of wire position within one sector and inside the anode plane (left). A schematic diagram, top view, of the stereo wire orientation (right).

Each DC volume is defined by a cylindrical titanium frame defining the azimuthal and beam-axis limits of the detector volume (Figure 2.10). 0.125 mm Al-mylar windows define the limits of the gas volume radially. Each frame is filled with drift chamber modules and is divided in 20 equal sectors covering  $4.5^\circ$  in  $\phi$ . There are six types of wire modules stacked radially in each sector: X1, U1, V1, X2, U2 and V2. Each module contains 4 sense (anode) planes and 4 cathode planes forming cells with a 2–2.5 cm drift space in the  $\phi$  direction.

The X1 and X2 wire cells run in parallel to the beam to perform precise track measurements in  $r-\phi$ . These wire cells are followed by two sets of small angle U,V wire planes used in the pattern recognition. U1, V1, U2, and V2 wires have stereo angles of about  $6^\circ$  relative to the X wires and measure the z coordinate of the track. The stereo angle was selected to minimize track ambiguities by matching the z resolution of the pad chambers.

Each of the X- and U,V-stereo cells contain 12 and 4 anode (sense) wires, respectively. As a result, there are 40 drift cells in the DC located at different radii. The layout of wires within one DC sector is shown in Figure 2.11. The stereo wires start in a sector on one side and end in a neighboring sector on the other side of the DC.

## 2.5.2 Pad Chamber

The pad chambers (PC) are multi-wire proportional chambers that form three separate layers of the PHENIX central tracking system. Each chamber contains a single plane of wires inside a gas volume bounded by two cathode planes. One cathode is finely segmented into an array of pixels. The charge induced on a number of pixels when a charged particle starts an avalanche on an anode wire, is read out through specially designed readout electronics.

The PC system determines space points along the straight line particle trajectories outside the magnetic field. Figure 2.9 shows the radial location of the PC's in the central tracking arms. The first pad chamber layer (PC1) is located at the radial outer edge of each drift chamber at a distance of 2.49 m, while the third layer (PC3) is 4.98 m from the interaction point. The second layer (PC2) is located at a radial distance of 4.19 m in the west arm only.

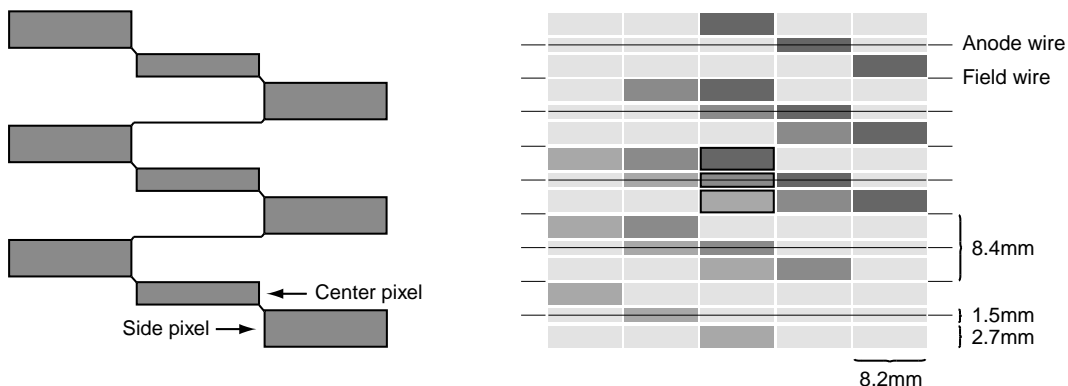


Figure 2.12: The pad and pixel geometry (left). A cell defined by three pixels is at the center of the right picture

Figure 2.12 shows the pad pattern of the PC. Each cell contains three pixels and an avalanche must be sensed by all three pixels to form a valid hit in the cell. The interleaved pixels were ganged together, nine by nine and connected to a common readout channel, such that the three pixels in a cell are always connected to different but neighboring channels and each cell is defined by its unique channel triplet. So, the information can be broken down to the cell level, by identifying the triplets.

This solution saves a factor of nine in readout channels compared to readout of every pixel and a factor of three compared to a readout pad geometry where a cell is the actual electrode connected to an electronics channel. The design goals for the position resolution were  $\pm 4$  mm. This motivated an anode wire spacing of about 8 mm. For geometrical

reasons, a spacing of 8.4 mm was chosen. Desiring a square cell geometry, a cell area of  $8.4 \times 8.4 \text{ mm}^2$  was adopted. In the  $z$  direction, this resulted in a position resolution of  $\pm 1.7 \text{ mm}$  which was substantially better than the design goals. At the positions of PC2 and PC3 it is sufficient to maintain the same angular resolution as of PC1. Thus the cells on PC3 have 4 times the area of PC1 cells since PC3 is at twice the distance from the vertex as compared to PC1.

### 2.5.3 Time-of-Flight Counter

The time-of-flight counter (TOF) serves as the primary particle identification device for charged hadrons in PHENIX. It is designed to have about 100 ps timing resolution in order to achieve clear particle separation in the high momentum region, i.e.  $\pi/K$  separation up to 2.4 GeV/c and  $K/\text{proton}$  separation up to 4.0 GeV/c.

The TOF wall is located at a radial distance of 5.06 m from the interaction point, between the pad chamber (PC3) and the electromagnetic calorimeter (EMCal) in the east central arm. It is designed to cover  $|\eta| < 0.35$  and  $\Delta\phi = 45^\circ$  in azimuthal angle. The TOF system consists of 10 panels of TOF walls. One TOF wall consists of 96 segments, each equipped with a plastic scintillator slat and photomultiplier tubes which are read out at both ends. A total 10 TOF panels, 960 slats of scintillators and 1920 channels of PMTs were installed and operated at the first year of operation. The slat is oriented along the  $r-\phi$  direction and provides time and longitudinal position information of particles that hit the slat.

Figure 2.13 shows a schematic view of one panel of the TOF detector. It consists of 96 plastic scintillation counters with photomultiplier tubes (PMT's) at both ends, light guides and mechanical supports. Scintillator rod and light guides were wrapped with thin aluminum foil and were glued on the honeycomb board. The honeycomb boards are made of paper of a honeycomb structure sandwiched between carbon fiber sheets, which provide a “massless” rigid structure. Scintillators with two different lengths (637.7 and 433.9 mm) are assembled in an alternating fashion in order to avoid geometrical conflicts between the PMTs of neighboring slats. Appendix B discusses in detail the specifications and performance of the TOF counter.

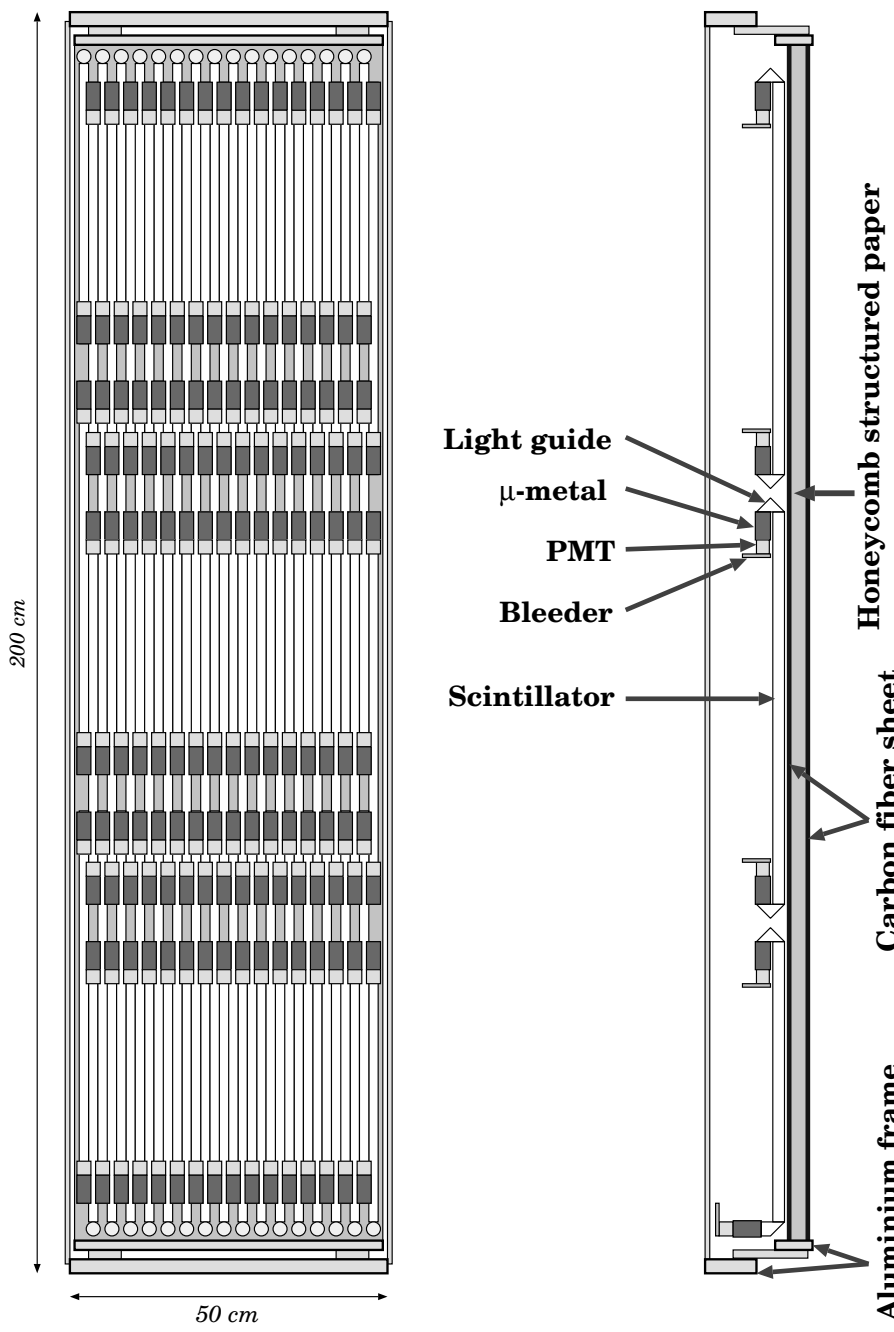


Figure 2.13: Schematic diagram of the components of a single TOF panel which consists of 96 plastic scintillation counters with photomultiplier tubes at both ends, light guides and supports.

Particle identification for charged hadrons is performed by combining the information from the DC, PC1, BBC and the TOF. Figure 2.14 shows a contour plot of time-of-flight as a function of the reciprocal momentum in minimum-bias Au+Au collisions after a momentum dependent track and TOF hits association residual cut between the track projection point and TOF hits has been taken. The flight path is also corrected for each particle species in this figure.

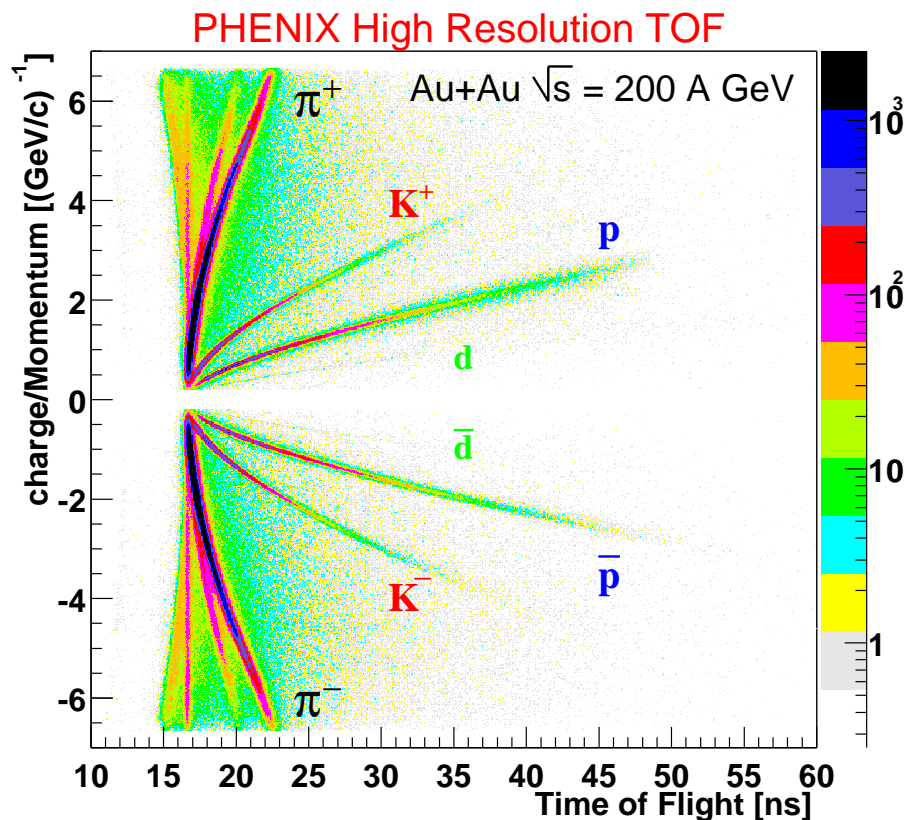


Figure 2.14: Contour plot of the time-of-flight versus reciprocal momentum in minimum bias Au+Au collisions at the energy of  $\sqrt{s_{\text{NN}}} = 200 \text{ GeV}$ . The figure clearly demonstrates the particle identification capability using the TOF detector in the year 2001 data taking period. The flight path is corrected for each track.

## 2.6 Other Detectors

These detectors are mainly used for lepton and photon measurement.

### 2.6.1 Time Expansion Chamber

The time expansion chamber (TEC) is composed of a set of 24 large multi-wire tracking chambers arranged in four, six-chamber sectors which reside in east central arm. It measures all charged particles passing through its active area, providing direction vectors that are matched to additional track information from the DC's and PC's also located in the central arm. The tracking information is used to solve the complex pattern recognition problems associated with the high particle density in relativistic heavy ion physics. It aides in background rejection for particles passing into the EMCAL and TOF wall. The detector system allows for systematic studies of tracking efficiency and background rejection versus multiplicity in coordination with the DC. The TEC also enhances the momentum resolution of the central arm at  $p_T \geq 4\text{GeV}/c$  by combining with the DC to provide a long lever arm for improved track-angle resolution. In addition the TEC measures ionization energy losses ( $dE/dx$ ) of charged tracks which enables particle identification, particularly electron/pion separation, over a momentum range important to the physics goals of the experiment.

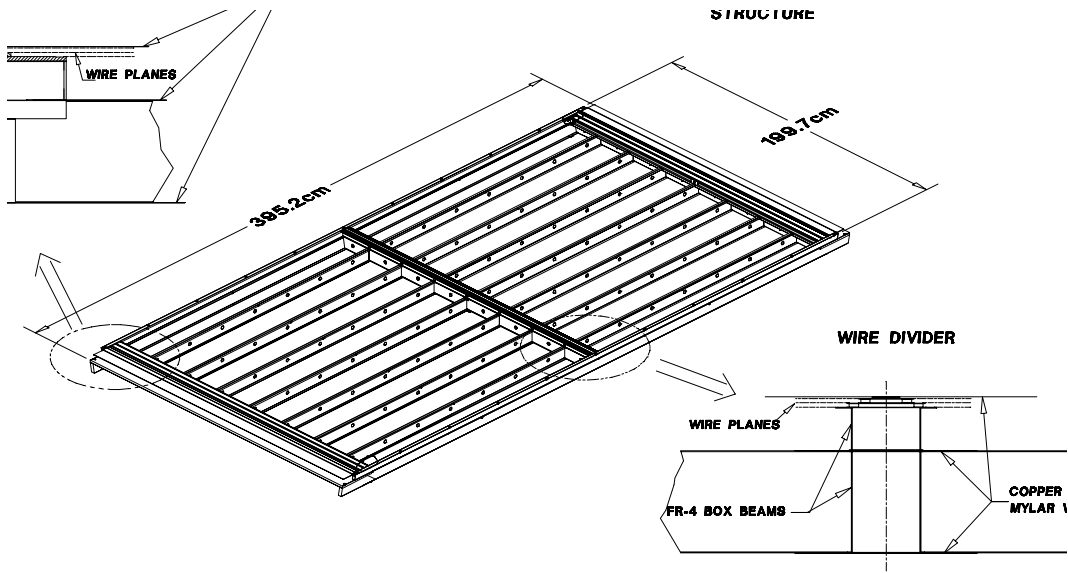


Figure 2.15: Mechanical structure of single TEC chamber. The frame skeleton, anode-cathode interface board and central wire divider are shown.

The TEC is composed of individual chambers, with six chambers stacked together to form a wedge-shaped sector. Each chamber is independent and self-supporting, made from a combination of machined graphite-composite, S2-glass and FR-4 components all epoxied together. Individual chambers have active areas varying from 3.1m x 1.7m for the smallest to 3.5m x 1.9 m for the largest TEC plane. The material in the detector's active area was minimized by using a box beam wire divider located at  $z=0$  and widely spaced I-beam window supports all made of thin FR-4. The open design results in 98% of the TEC's fiducial area being active.

Each chamber is built in two layers: a lower layer containing structural elements for window support and space for inclusion of TRD radiator foils, and an upper layer containing the active elements of the wire chamber. The upper layer is filled with P-10 gas and is composed of a Cu-mylar cathode window, 3 cm drift space, three wire planes (field, anode, field) oriented parallel to the  $z$  axis of the detector, and a final Cu-mylar cathode window (Figure 2.15). The anode wires are spaced on average 4 mm from each other (specifically 4.05 mm and 4.15 mm depending on the sector plane) and 3.0 mm from both cathode wire planes. The Cu-coated mylar windows have multiple functions. They are biased to establish the proper field shaping inside the detector, serve as the gas barrier and provide an RF shield. The wire planes are divided in half at  $z=0$  both for ease of construction and to decrease the average multiplicity per wire by a factor of two.

## 2.6.2 Ring-Imaging Cherenkov Detector

The ring imaging cherenkov (RICH) detector is designed for electron identification, and provides  $e/\pi$  discrimination below the  $\pi$  Cherenkov threshold, which is set at about 4  $GeV/c$ . In combination with the EMCAL in each arm and the TEC in one arm, the goal is to limit the false identification of hadrons as  $e^+$  and  $e^-$  to less than  $10^{-4}$ .

Figure 2.16 contains a cutaway drawing of one of the RICH detectors revealing the internal components. Each RICH detector has a volume of  $40\text{ m}^3$ , with an entrance window area of  $8.9\text{ m}^2$  and an exit window area of  $21.6\text{ m}^2$ . Each detector contains 48 composite mirror panels, forming two intersecting spherical surfaces, with a total reflecting area of  $20\text{ m}^2$ . The spherical mirrors focus Cherenkov light onto two arrays of 1280 UV photomultiplier tubes (HAMAMATSU H3171S), each located on either side of the RICH entrance window. The phototubes are fitted with 2" diameter Winston cones and have magnetic shields that allow them to operate at up to 100 Gauss. The phototube UV glass windows absorb photons of wavelengths below 200 nm. The minimum thickness of radiator gas seen

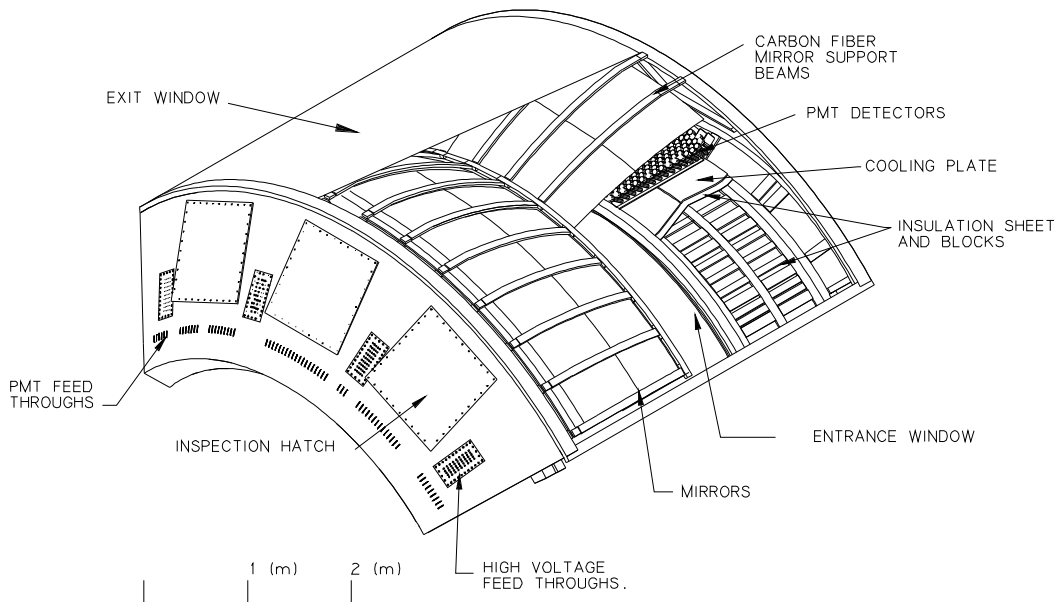


Figure 2.16: A cutaway view of one arm of the PHENIX RICH detector.

by any particle is 87 cm, the maximum is about 150 cm. The radiator gas is maintained at a pressure of 0.5" of water above ambient. The large aluminized Kapton entrance and exit windows are 125  $\mu\text{m}$  thick, and are supported against the internal pressure by graphite-epoxy beams. All gas seals are made using Goretex gaskets. There are black vinyl coated polyester light shields covering the outside of the Kapton windows. The preamplifiers for the signals from the photon detectors are mounted directly on the RICH detector.

### 2.6.3 Electromagnetic Calorimeter

The primary role of the electromagnetic calorimeter (EMCal) is to provide a measurement of the energies and spatial positions of photons and electrons produced in heavy ion collisions. It also plays a major role in particle identification and is an important part of the PHENIX trigger system. The EMCal system can trigger on rare events with high transverse momentum ( $p_T$ ) photons and electrons. Its signals are incorporated in Level-1 triggers for high multiplicity or large total transverse energy ( $E_T$ ) events. In addition the EMCal provides a good measurement of the *hadronic* energy produced at mid-rapidity and thus of the  $E_T$  produced in the reaction.

The EMCal system consists of a total of 24768 individual detector modules divided between the Pb-Scintillator calorimeter (PbSc), which provides six sectors of azimuthal coverage and the Pb-glass calorimeter (PbGl) comprised of two sectors. Both sub-detectors

are read out with photomultipliers and have good energy resolution and intrinsic timing characteristics but their design is quite different and they will be described separately.

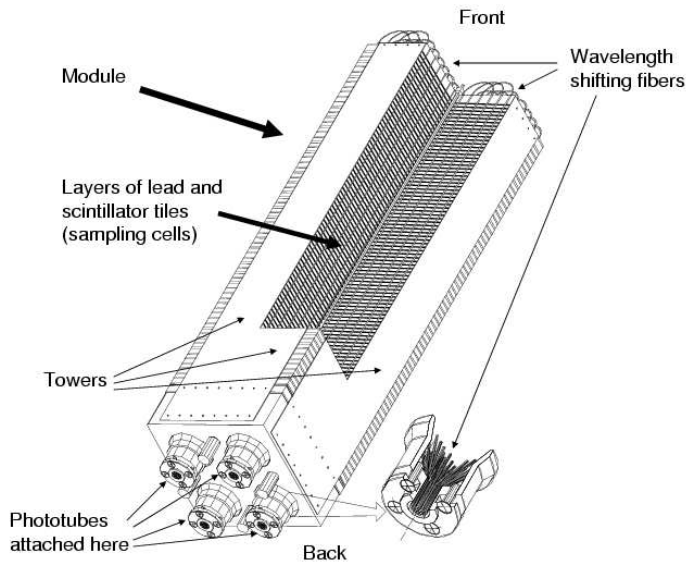


Figure 2.17: Interior view of a Pb-scintillator calorimeter module showing a stack of scintillator and lead plates, wavelength shifting fiber readout and leaky fiber inserted in the central hole.

The Pb-scintillator electromagnetic calorimeter is a shashlik type sampling calorimeter made of alternating tiles of Pb and scintillator consisting of 15552 individual towers and covering an area of approximately  $48 \text{ m}^2$ . The basic building block is a module consisting of four (optically isolated) towers which are read out individually. Each Pb-scintillator tower contains 66 sampling cells consisting of alternating tiles of Pb and scintillator. The edges of the tiles are plated with Al. These cells are optically connected by 36 longitudinally penetrating wavelength shifting fibers for light collection. Light is read out by 30 mm FEU115M phototubes at the back of the towers. Four towers are mechanically grouped together into a single structural entity called a module as shown in Fig. 2.17. The PbSc calorimeter has a nominal energy resolution of  $8.1\%/\sqrt{E}(\text{GeV}) \oplus 2.1\%$  and an intrinsic timing resolution better than 200 ps for electromagnetic showers. A high precision calibration and monitoring system has been developed to achieve an absolute energy calibration better than 5% for day one operation at RHIC, and to maintain an overall long term gain stability of the order of 1%.

The Pb-glass calorimeter array comprises 9216 elements of a system previously used in CERN experiment WA98. It has a nominal energy resolution of  $6\%/\sqrt{E}$  (GeV) and

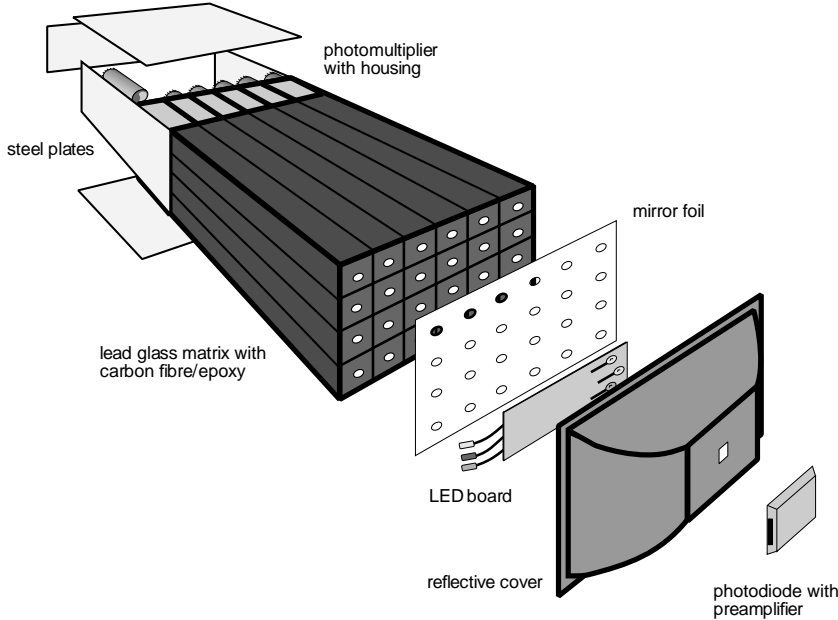


Figure 2.18: Exploded view of a lead-glass detector supermodule.

an intrinsic timing resolution of better than 300 ps for electromagnetic showers above the minimum ionizing peak energy.

The Pb-glass calorimeter occupies the two lower sectors of the East Central arm of PHENIX. The PHENIX Time-of-Flight system is located on the Pb-glass sectors. Each Pb-glass sector comprises 192 supermodules. The Pb-glass supermodule comprises 24 Pb-glass modules in an array of 6 Pb-glass modules wide by 4 modules high as shown in Figure 2.18. The size of one Pb-glass module is  $40 \text{ mm} \times 40 \text{ mm} \times 400 \text{ mm}$ . The Pb-glass modules within a supermodule are individually wrapped with aluminized mylar and shrink tube and 24 modules are glued together with carbon fiber and epoxy resin to form a self-supporting supermodule with a shared calibration system (see Figure 2.18).

## 2.6.4 Muon Arm Spectrometer

PHENIX have two forward muon arms at rapidity of  $1.2 < |y| < 2.4$  with full azimuthal acceptance to detect muon [51]. Each muon arm must track and identify muons and provide good rejection of pions and kaons ( $\sim 10^{-3}$ ). In order to accomplish this we employ a radial field magnetic spectrometer with precision tracking (Muon Tracker: MuTr) followed by a stack of absorber/low resolution tracking layers (Muon Identifier: MuID).

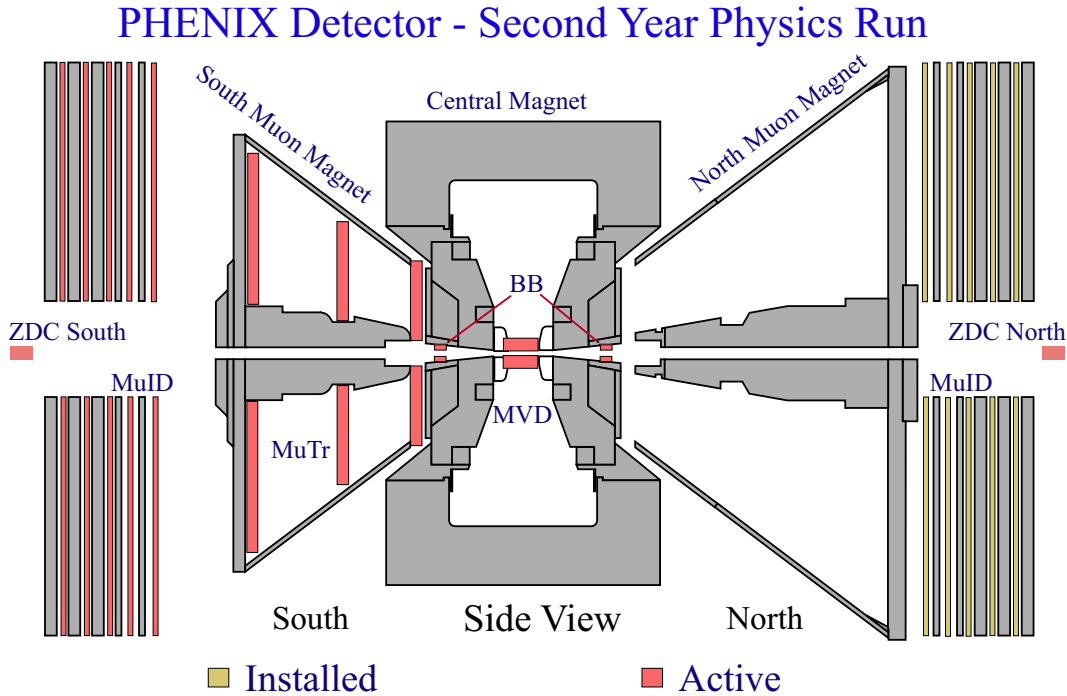


Figure 2.19:

### Muon Tracker

The muon tracker (MuTr) design specifications were driven by the requirements that it be able to (i) allow a clean separation of  $J/\psi$  from  $\psi'$ ,  $\Upsilon(1S)$  from  $\Upsilon(2S,3S)$  and  $\rho/\omega$  from  $\phi$ , (ii) provide a large enough signal-to-background and acceptance for vector mesons to be able to do statistically significant physics measurements in less than 1 year of RHIC running, (iii) have low enough occupancy to be able to reconstruct tracks efficiently in central Au+Au events and (iv) still perform well in the lower occupancy but higher event rate p-p and p-A physics programs.

The relative mass resolution is approximately given by  $\sigma(M)/M = 6\%/\sqrt{M}$ , where  $M$  is in GeV. This mass resolution enables a clear separation of the  $\rho/\omega$  peak from the  $\phi$ ,  $J/\psi$  and  $\psi'$ , with an acceptable separation of  $\Upsilon$  and  $\Upsilon'$ . This is consistent with a spacial resolution of 100 microns.

The above design requirements led to a Muon Tracker design which is comprised of three stations of cathode-strip readout tracking chambers mounted inside conical-shaped muon magnets (see Figure 2.20), with multiple cathode strip orientations and readout planes in each station. The electronics design specifications were driven by the requirement that the non-stereo cathode planes provide 100  $\mu\text{m}$  resolution measurements of the

particle trajectories and that the readout of the system be able to meet the global PHENIX readout requirements. Test-bench measurements from production chambers and electronics combined with simulations of the full muon tracker design show that the tracker should meet the design requirements outlined above.

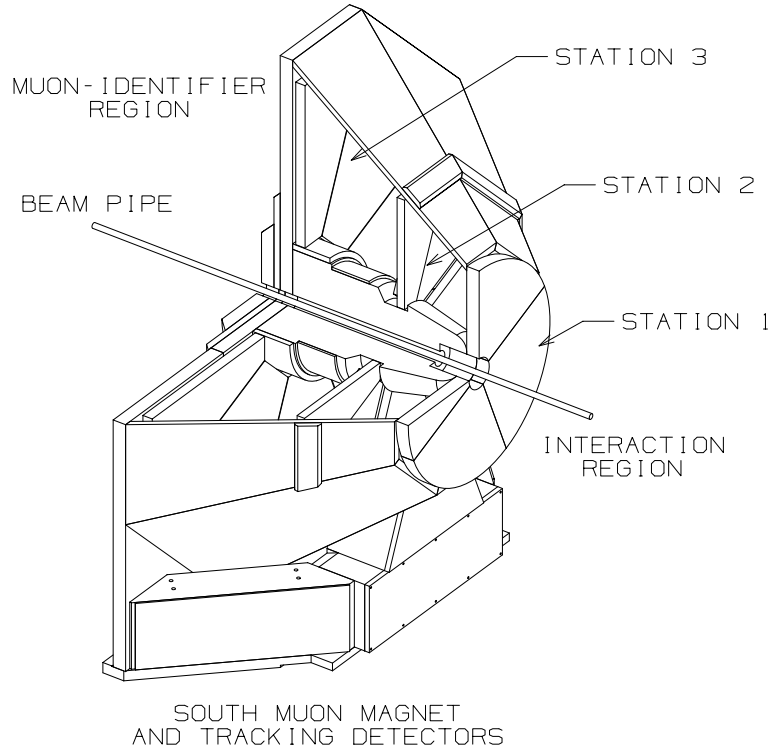


Figure 2.20: The South Muon ARM tracking spectrometer. Muons from the intersection region, to the right, intercept the station 1, 2 and 3 detectors and proceed to the muon identifier detectors to the left (not shown).

### Muon Identifier

The muon identifier (MuID) consists of five layers of chambers interleaved with steel absorbers. The MuID is used for separating muons from charged hadrons and other background as well as providing trigger for single muons and dimuons.



Figure 2.21: Muon identifier panel being flipped over during construction.



Figure 2.22: The south PHENIX Muon Identifier before installation of the shield wall.

# Chapter 3

## Data Analysis

This analysis is based on the experimental data of Au+Au collisions at  $\sqrt{s_{NN}} = 200$  GeV in the second year of running at RHIC. The Au-Au run was operated from August 2001 to November 2001.

In this chapter, we describe the event selection, track reconstruction, momentum determination, particle identification and various corrections, including geometrical acceptance, particle decay, multiple scattering and absorption effects, detector occupancy corrections and weak decay contributions from  $\Lambda$  and  $\bar{\Lambda}$  to proton and anti-proton spectra. The estimations of systematic uncertainties on the measurements are addressed at the end of this chapter.

### 3.1 Event Selection

Figure 3.1 shows the integrated luminosity which has been delivered by RHIC in the 2001 Au-Au run period. RHIC has delivered  $85 \mu\text{b}^{-1}$  of integrated machine luminosity for all  $z$  at PHENIX collision point. About  $42 \mu\text{b}^{-1}$  was within  $|z| < 45$  cm vertex cut. The PHENIX experiment recorded about  $24 \mu\text{b}^{-1}$  of integrated luminosity.

#### 3.1.1 Minimum Bias Trigger

For this analysis, we use the PHENIX minimum bias trigger events which are determined by following conditions on BBC and ZDC.

- A coincidence between the north and south BBC with at least two PMTs fired in each BBC is required. The collision vertex has to satisfy  $|z_{vtx}| < 75$  cm. These cuts are performed by the BBC Level-1 (BBLL1) trigger online. [BBLL1]>= 2]

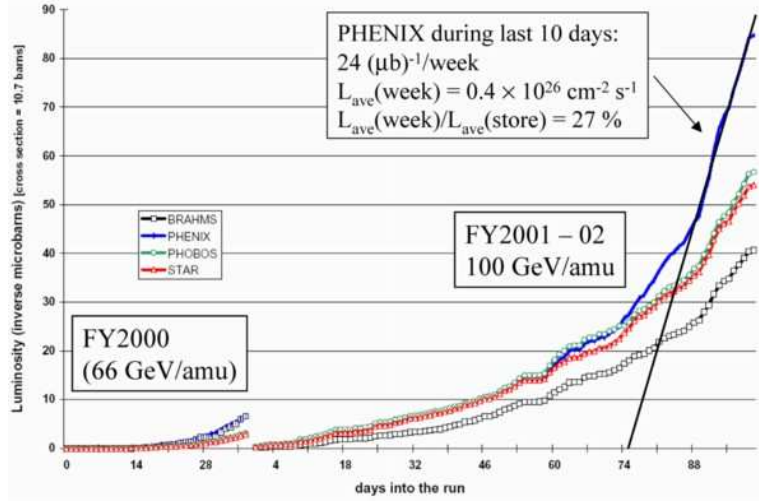


Figure 3.1: Integrated luminosity which was delivered by RHIC in first and second Au-Au run period as a function of day. The blue line is for PHENIX.

- At least one forward neutron has to be registered in each of the two ZDCs. [ZDCNS]
- An offline collision vertex cut of  $|z_{vtx}| < 30$  cm is required.

The trigger efficiency for minimum bias Au nuclear interactions related to these cuts is studied by a detailed simulation of the BBC and the ZDC. First, response for all 124 PMT tubes and the BBLL1 board logic are tuned in the simulation to match the real data. Then HIJING [55] simulated events are used to determine the BBC trigger efficiency. Figure 3.2 shows the extracted the BBC trigger efficiency as a function of  $z_{vtx}$ . The systematic errors are studied by varying the TDC (Time Digital Converter) threshold for each PMT (used by the BBLL1 trigger) and the input  $dN/dy$  and collision vertex distribution from HIJING.

The extracted BBC trigger efficiency is

$$\epsilon_{bbc}^{trigger} = 93.1\% \pm 0.4\% (stat.) \pm 1.6\% (sys.). \quad (3.1)$$

To reject the small percentage of BBC triggers that are “background” events, a ZDC coincidence with at least one neutron on both sides is required. The fraction of BBC triggers that also satisfy the ZDC condition,  $(BBLL1 \geq 2 \& \& ZDCNS) / (BBLL1 \geq 2)$ , is shown in Figure 3.3 as a function of run number.

The ratio has a maximum value around 97.5% (indicated by the horizontal line). The fact that the ratio drops to lower values in some later runs is in agreement with observations during these runs that the luminosity was high, and the BBC trigger had a higher background rate. It is also possible that the BBC had a “hot” tube in some of these runs. A

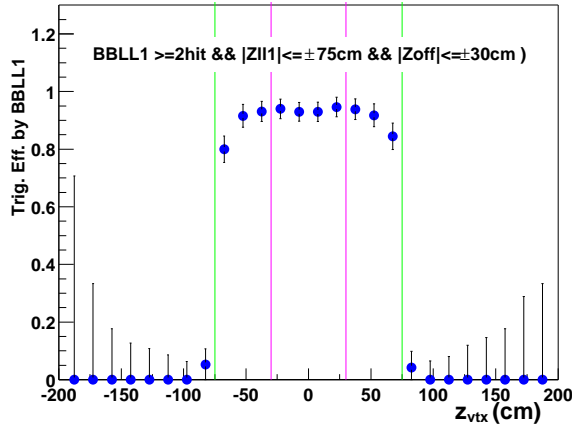


Figure 3.2: The BBC trigger efficiency as a function of  $z_{vtx}$

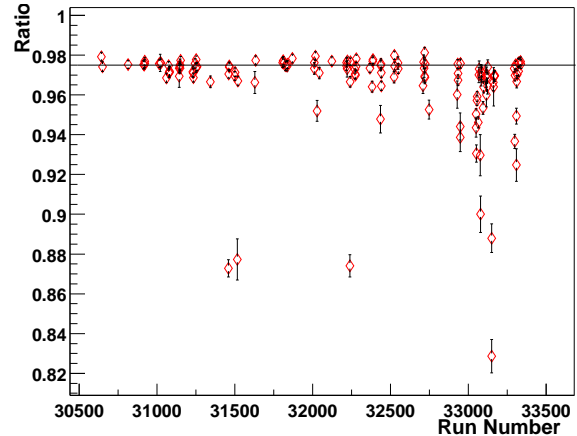


Figure 3.3: The ratio  $R = (BBLL1 \geq 2 \&\& ZDCNS) / (BBLL1 \geq 2)$  is plotted as a function of run number.

conservative estimate for the 2.5% exclusive BBC triggers is that 40% of these events are due to ZDC inefficiencies and 60% are “background” events. The ZDC trigger efficiency for events that also satisfy the BBC trigger is

$$\epsilon_{zdc|bbc}^{trigger} = 99^{+1.0}_{-1.5}\%. \quad (3.2)$$

The minimum bias trigger efficiency with the BBC and ZDC coincidence can be calculated as,

$$\epsilon_{minbias}^{trigger} = \epsilon_{bbc}^{trigger} \times \epsilon_{zdc|bbc}^{trigger} = 92.2^{+2.5}_{-3.0}\%. \quad (3.3)$$

### 3.1.2 Centrality Determination

The events are classified by centrality, which is related to the measured fraction of the total geometrical cross-section between two ions. The ZDC measure spectator neutrons that are not bound in deuterons or heavier fragments. The BBC measures the number of charged particles at forward rapidity. The centrality is determined by the combined information on spectator neutrons measured by the ZDC and the charged sum information measured by the BBC. A schematic figure is shown in Figure 3.4.

Figure 3.5 shows the correlation between the BBC charge sum and ZDC total energy for Au+Au at  $\sqrt{s_{NN}} = 200$  GeV. The lines on the plot indicate the centrality definition in the analysis. For the centrality determination, these events are subdivided into 11 bins using the BBC and ZDC correlation: 0–5%, 5–10%, 10–15%, 15–20%, 20–30%, ..., 70–80% and

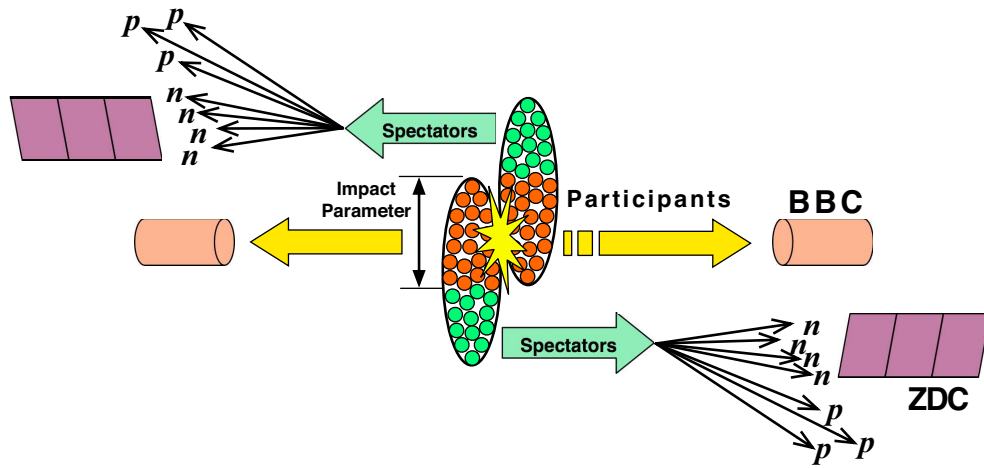


Figure 3.4: A schematic figure showing nucleus-nucleus collisions. Nucleons which have interacted with other nucleons are called “participants”. Nucleons which have not interacted go straight with initial momenta. They are called “spectators”. Protons in the spectators are swept out by accelerator dipole magnet and only neutrons are emitted in ZDC.

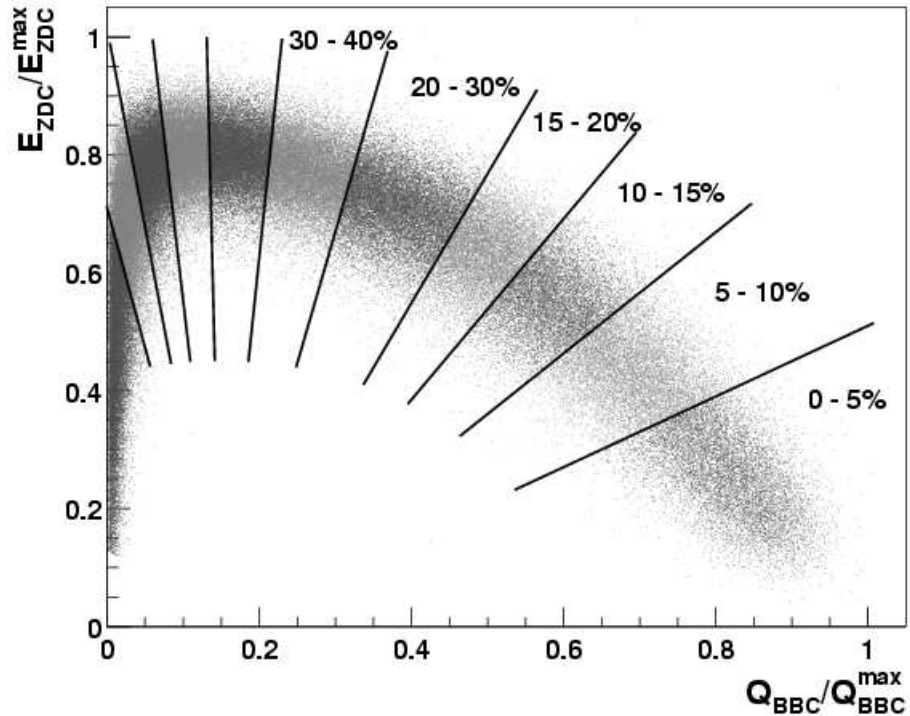


Figure 3.5: Correlation between the BBC charge sum and ZDC total energy. The lines represent the centrality cut boundaries.

80–92%. Due to the statistical limitations in the peripheral events, we also use the 60–92% centrality bin as the most peripheral bin.

### 3.1.3 Glauber Model Calculation

To estimate the number of nucleon-nucleon binary collisions  $N_{\text{coll}}$  and participating nucleons  $N_{\text{part}}$  for each centrality class, a Glauber model [6] Monte-Carlo simulation that includes the responses of the BBC and ZDC is used. A participant is defined as a nucleon which has suffered at least one inelastic nucleon-nucleon collision. The average number of binary collisions  $\langle N_{\text{coll}} \rangle$  and the geometrical nuclear overlap function  $T_{AB}$  are related quantities:

$$T_{AB} = \langle N_{\text{coll}} \rangle / \sigma_{\text{NN}} \quad (3.4)$$

where  $\sigma_{\text{NN}}$  is inelastic nucleon-nucleon cross section.

Based on a Glauber model calculation, the average nuclear overlap function  $T_{\text{AuAu}}$ , the average number of nucleon-nucleon binary collisions  $\langle N_{\text{coll}} \rangle$ , and the average number of participants  $\langle N_{\text{part}} \rangle$  are obtained with each centrality bin (Table 3.1). The systematic errors of the Glauber quantities are estimated by varying the model assumptions, e.g.:

1.  $\sigma_{\text{NN}} = 39$  mb and  $\sigma_{\text{NN}} = 45$  mb (default  $\sigma_{\text{NN}} = 42$  mb)
2. Woods-Saxon parameters,  $R = 6.65$  fm,  $a = 0.55$  fm and  $R = 6.25$  fm,  $a = 0.53$  fm.  
(defaults :  $R = 6.38$  fm,  $a = 0.54$  fm)
3. an alternative neutron loss function in the ZDC
4. a different smearing function for the BBC response.
5. Each nucleon is assumed to have a hard core of 0.4 fm, the distance between the centers of the two nucleons is always greater than 0.8 fm in the Au nucleus.

Figure 3.6 shows the systematic errors for  $\langle N_{\text{coll}} \rangle$ ,  $\langle N_{\text{part}} \rangle$ ,  $T_{\text{AuAu}}$  and impact parameter  $\langle b \rangle$ .

Figure 3.7 shows the systematic errors for the total geometric cross section. The total geometric Au + Au cross section at  $\sqrt{s_{\text{NN}}} = 200$ GeV is

$$\sigma_{\text{Au+Au}}^{\text{geo}} = 6847 \pm 542 \text{mb.} \quad (3.5)$$

### 3.1. EVENT SELECTION

51

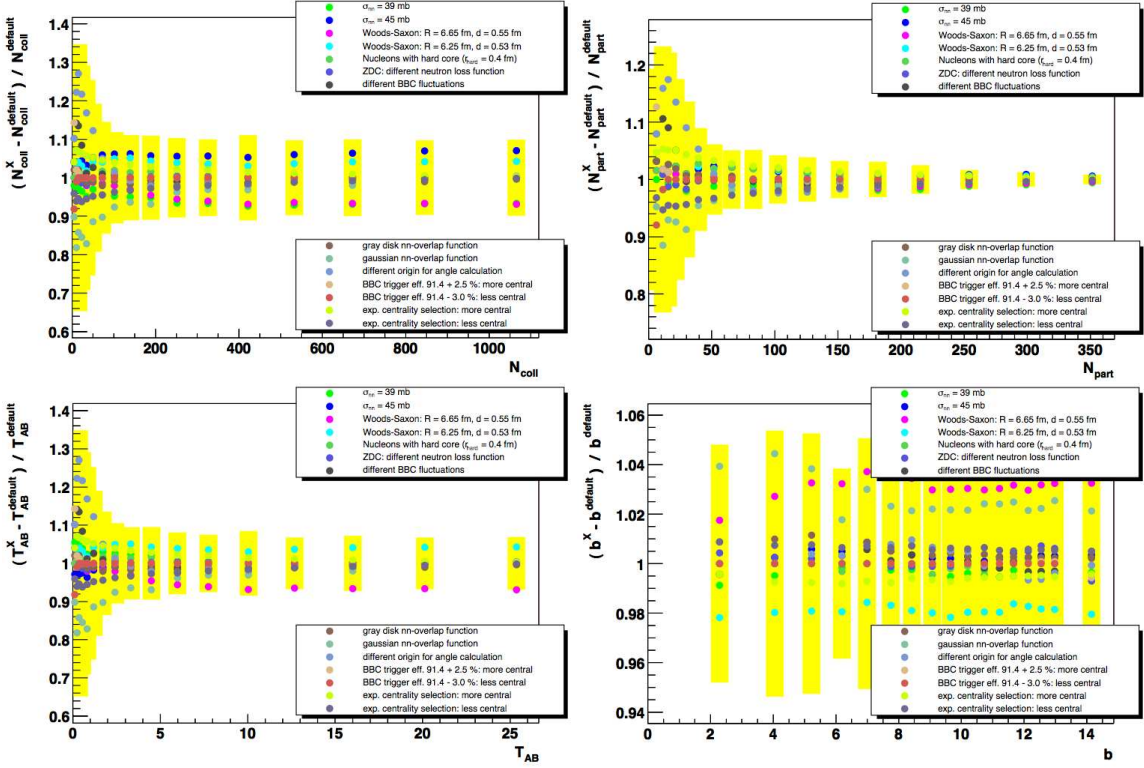


Figure 3.6: Systematic errors on  $\langle N_{\text{coll}} \rangle$ ,  $\langle N_{\text{part}} \rangle$ ,  $T_{\text{AuAu}}$  and impact parameter  $\langle b \rangle$ .

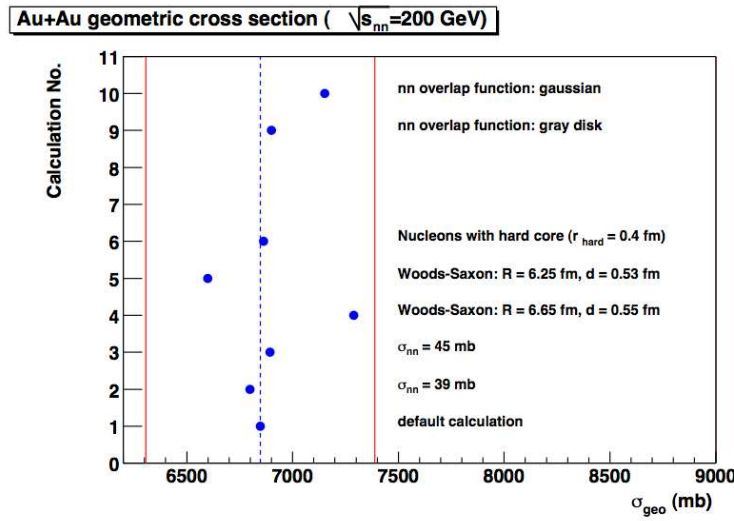


Figure 3.7: Total geometrical cross section for Glauber calculation with different parameters.

Centrality	$\langle T_{AuAu} \rangle$ (mb $^{-1}$ )		$\langle N_{coll} \rangle$		$\langle N_{part} \rangle$	
0- 5%	25.37	$\pm$	1.77	1065.4	$\pm$	105.3
0-10%	22.75	$\pm$	1.56	955.4	$\pm$	93.6
5-10%	20.13	$\pm$	1.36	845.4	$\pm$	82.1
10-15%	16.01	$\pm$	1.15	672.4	$\pm$	66.8
10-20%	14.35	$\pm$	1.00	602.6	$\pm$	59.3
15-20%	12.68	$\pm$	0.86	532.7	$\pm$	52.1
20-30%	8.90	$\pm$	0.72	373.8	$\pm$	39.6
30-40%	5.23	$\pm$	0.44	219.8	$\pm$	22.6
40-50%	2.86	$\pm$	0.28	120.3	$\pm$	13.7
50-60%	1.45	$\pm$	0.23	61.0	$\pm$	9.9
60-70%	0.68	$\pm$	0.18	28.5	$\pm$	7.6
60-80%	0.49	$\pm$	0.14	20.4	$\pm$	5.9
60-92%	0.35	$\pm$	0.10	14.5	$\pm$	4.0
70-80%	0.30	$\pm$	0.10	12.4	$\pm$	4.2
70-92%	0.20	$\pm$	0.06	8.3	$\pm$	2.4
80-92%	0.12	$\pm$	0.03	4.9	$\pm$	1.2
60-92%	0.35	$\pm$	0.10	14.5	$\pm$	4.0
min. bias	6.14	$\pm$	0.45	257.8	$\pm$	25.4
						109.1 $\pm$ 4.1

Table 3.1: The average nuclear overlap function ( $\langle T_{AuAu} \rangle$ ), the number of nucleon-nucleon binary collisions ( $\langle N_{coll} \rangle$ ), and the number of participant nucleons ( $\langle N_{part} \rangle$ ) obtained from a Glauber Monte Carlo correlated with the BBC and ZDC response for Au+Au at  $\sqrt{s_{NN}} = 200$  GeV as a function of centrality. Centrality is expressed as percentiles of  $\sigma_{AuAu} = 6.9$  barn with 0% representing the most central collisions. The last line refers to minimum bias collisions.

## 3.2 Track Reconstruction

### 3.2.1 Track Selection

Charged particle tracks are reconstructed by the DC based on a combinatorial Hough transform (CHT) [56] – which gives the angle of the track in the main bend plane. The main bend plane is perpendicular to the beam axis (azimuthal direction). PC1 is used to measure the position of the hit in the longitudinal direction (along the beam axis).

A typical track in the DC main bend plane is illustrated in Figure 3.8a. The coordinates we chose to describe tracks in the drift chamber are  $\phi$ , the azimuthal angle at the intersection of the track with a “reference radius” at the mid-radius of the drift chamber, and  $\alpha$ , the inclination of the track at that point. In principle,  $\phi$  and  $\alpha$  are equivalent to a slope and intercept; the main difference is that  $\phi$  and  $\alpha$  are limited to a given range of possible values while slope and intercept are not. Figure 3.8b shows the track in the  $r$ - $z$  plane, perpendicular to the bend plane. Because the magnetic field is along the beam direction, tracks usually have a very small bend in this plane. Therefore, it is called the non-bend plane. The coordinates used in this projection are  $z_{\text{DCH}}$  ( $zed$ ), the  $z$  coordinate of the intersection point, and  $\beta$ , the inclination of the track at the reference radius.

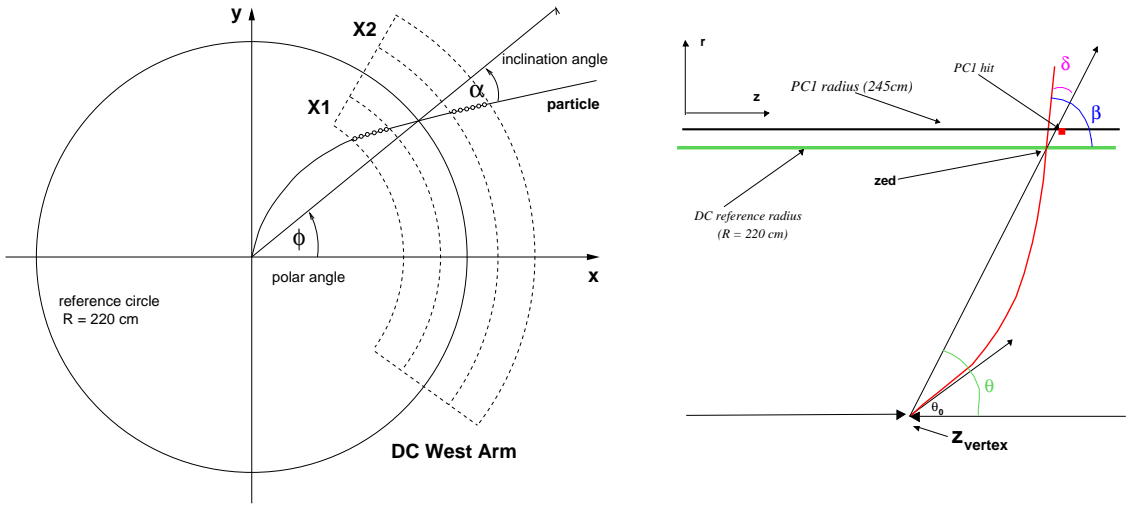


Figure 3.8: a) A schematic cutaway view of a track in the DC  $x$ - $y$  (or  $r$ - $\phi$ ) plane. The X1 and X2 hits in the drift chamber are shown as small circles within an outline of the drift chamber.  $\phi$  and  $\alpha$  are the feature space variables in the CHT transform (see text). b) A schematic cutaway view of a track in the DC  $r$ - $z$  plane. The track polar angle is  $\beta$ . The associated PC1 hit is indicated by the box marker. The track bending angle is  $\delta$ , which is small, such that the track can be approximated by the straight line linking the PC1 hit and collision vertex measured by the BBC.

The tracking is done separately in the  $r\text{-}\phi$  and the  $r\text{-}z$  plane. The track reconstruction in  $r\text{-}\phi$  is realized using a CHT technique where any pair of hits can be mapped to a point in the space defined by azimuth angle  $\phi$  and track bending angle  $\alpha$ . The basic assumption is that tracks are straight lines within the DC. In this case, all hit pairs for a given track will have the same  $\phi$  and  $\alpha$ , thus resulting in a local maximum in the feature space spanned by these variables. The DC tracking efficiency in a high multiplicity environment is estimated based on an embedding technique, which will be discussed in Section 3.5.3.

After the reconstruction of the track in the main bend plane, the direction of the track is specified by  $\phi$  and  $\alpha$ . Tracks are then reconstructed in the non-bend plane by combining the information from the PC1 reconstructed hits and the collision vertex  $z_{vtx}$  as measured by the BBC. First, PC1 candidate hits within 2 cm distance from the track in the  $r\text{-}\phi$  plane are identified. Then a straight line connecting  $z_{vtx}$  and PC1  $z$  fixes the direction of the track in  $z$ . The intersection points between the  $r\text{-}z$  plane and UV hit lines are calculated. UV1 hits are associated to the track if they are within  $\pm 5$  cm from the track in the  $r\text{-}z$  plane. If there is more than one PC1 association, the one with more associated UV hits is accepted to be the correct track.

### 3.2.2 Momentum Determination

The  $\alpha$  measured in the drift chamber is closely related to the field integral along the track trajectory. For tracks emitted perpendicular to the beam axis, this relation can be approximated by

$$\alpha \simeq \frac{K_1}{p}, \quad (3.6)$$

where  $K_1$  is the field integral,

$$K_1 = 0.3/R_{DC} \int l B dl = 87 \text{ mrad GeV}/c. \quad (3.7)$$

However, due to the small non-uniformity of the focusing magnetic field along the flight path of charged particles, an accurate analytical expression for the momentum of the particles can not be determined. A four-dimensional field integral grid was constructed within the entire radial extent of the central arm for momentum determination based on drift chamber hits. The variables in the grid are  $z_{vtx}$ , the polar angle  $\theta_0$  of the particle at the vertex, the total momentum  $p$ , and radius  $r$ , at which the field integral  $f(p, r, \theta_0, z)$  is calculated. The field integral grid is generated by explicitly swimming particles through the magnetic field map from survey measurement and numerically integrating to obtain

$f(p, r, \theta_0, z)$  for each grid point. An iterative procedure is used to determine the momentum for reconstructed tracks, using equation 3.6 as an initial guess.

### 3.2.3 Track Association

In order to associate a track with a hit on the TOF, the track is projected to its expected hit location on the TOF. The track matching residual of  $\phi$  and  $z$  on TOF plane are shown in Figure 3.9. We estimated sigma value of  $\phi$  and  $z$  as a function of momentum, [ $\sigma = a \cdot e^{-b \cdot p} + c$ ]. The offset value is also estimated from mean residual of  $\phi$  and  $z$ . Tracks are required to have a hit on the TOF within  $\pm 2\sigma$  of the expected hit location in both the azimuthal and beam directions. The flight path-length is calculated from a fit to the reconstructed track trajectory.

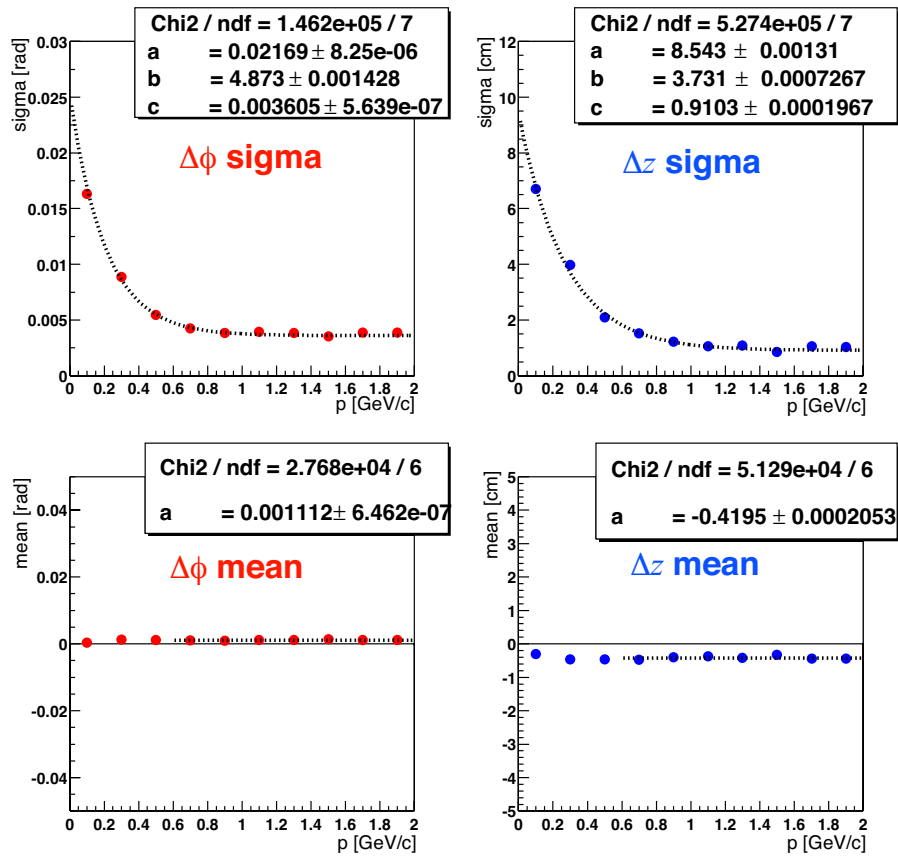


Figure 3.9: Track matching residual on TOF. Upper figures are sigma residual of  $\phi$  (left) and  $z$  (right) as a function of momentum. The dotted lines are fitted results using function  $\sigma = a \cdot e^{-b \cdot p} + c$ . Lower figures are mean residual of  $\phi$  (left) and  $z$  (right) as a function of momentum. The dotted lines are offset value.

### 3.3 Particle Identification

The charged particle identification (PID) is performed by using the combination of three measurements: time-of-flight from the BBC and TOF, momentum from the DCH, and flight path-length from the collision vertex point to the hit position on the TOF wall. The flight path-length is calculated from a fit to the reconstructed track trajectory. The square of the mass is derived from the following formula,

$$m^2 = \frac{p^2}{c^2} \left[ \left( \frac{t_{\text{TOF}}}{L/c} \right)^2 - 1 \right], \quad (3.8)$$

where  $p$  is the momentum,  $t_{\text{TOF}}$  is the time-of-flight,  $L$  is a flight path-length, and  $c$  is the speed of light. The charged particle identification is performed using cuts in  $m^2$  and momentum space.

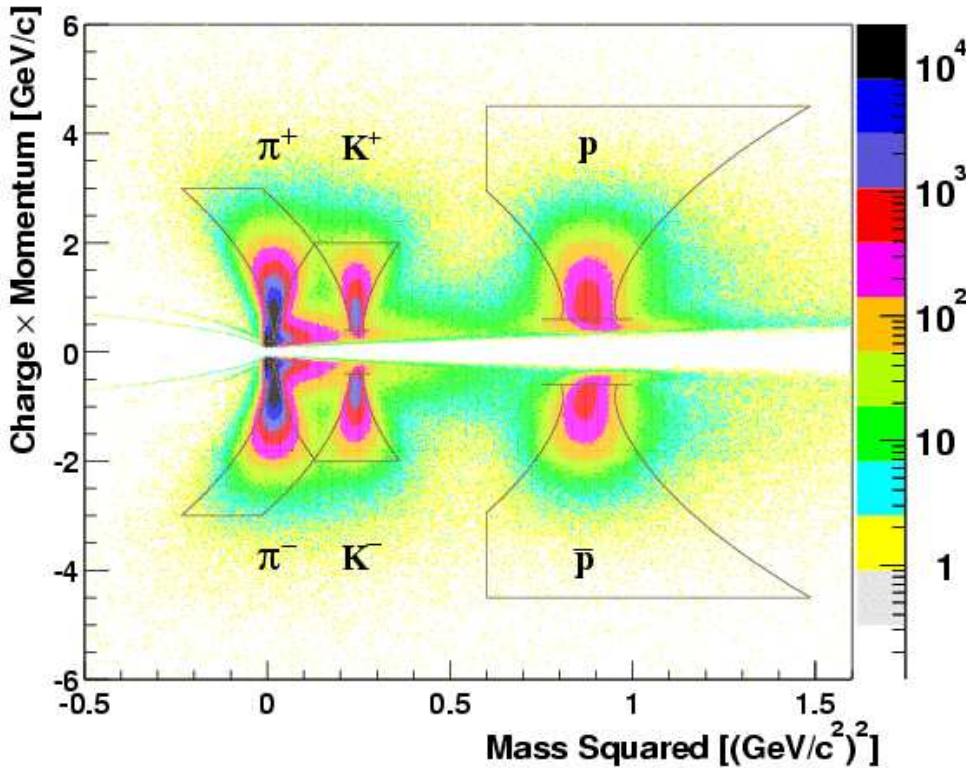


Figure 3.10: Mass squared vs. momentum · charge distribution. The lines indicate the PID cut boundaries for pions, kaons, and protons(anti-protons) from left to right, respectively.

In Figure 3.10, a plot of  $m^2$  versus momentum multiplied by charge is shown together with applied PID cuts as solid curves. We use  $2\sigma$  standard deviation PID cuts in  $m^2$  and momentum space for each particle species. Figure 3.11 show the mass squared width

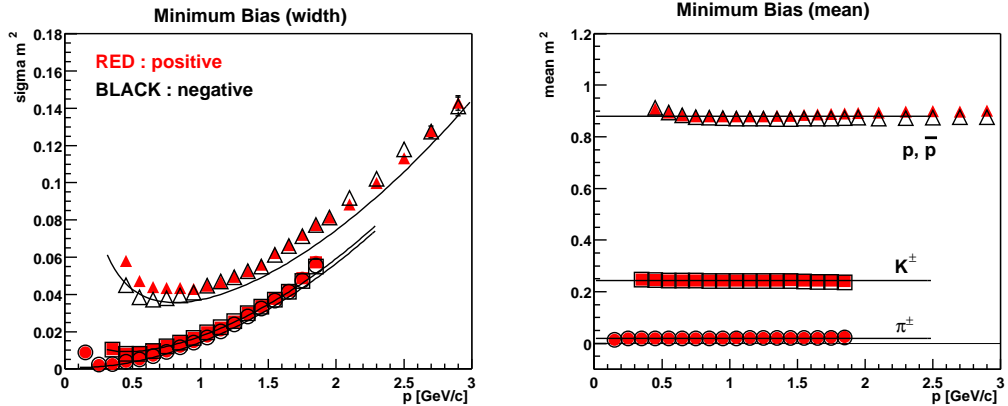


Figure 3.11: Momentum dependence of width (left) and centroid (right) of mass squared distributions for each particle species. Red symbols indicate for positively charged particle and black symbols are for negatives. The minimum bias event samples are used.

(left) and centroid (right) as a function of momentum for positives (red filled symbols) and negatives (black open symbols) for minimum bias events. The lines on the left are  $1\sigma$  PID cut boundary used in the analysis based on the following parameterization.

$$\sigma_{m^2}^2 = \frac{\sigma_\alpha^2}{K_1^2} (4m^4 p^2) + \frac{\sigma_{ms}^2}{K_1^2} \left[ 4m^4 \left( 1 + \frac{m^2}{p^2} \right) \right] + \frac{\sigma_{TOF}^2 c^2}{L^2} [4p^2 (m^2 + p^2)], \quad (3.9)$$

where  $\sigma_\alpha$  is the angular resolution,  $\sigma_{ms}$  is the multiple scattering term,  $\sigma_{TOF}$  is the overall time-of-flight resolution and  $m$  is the centroid of  $m^2$  distribution for each particle species. The parameters for PID are,  $\sigma_\alpha = 0.835$  mrad,  $\sigma_{ms} = 0.86$  mrad·GeV and  $\sigma_{TOF} = 120$  ps. Through improvements in alignment and calibrations, the momentum resolution is improved over the 130 GeV data [73]. The centrality dependence of the width and the mean position of the  $m^2$  distribution has also been checked. There is no clear difference seen between central and peripheral collisions. For pion identification above 2  $\text{GeV}/c$ , we apply an asymmetric PID cut to reduce kaon contamination of the pions. As shown by the lines in Figure 3.10, the overlap region which is within the  $2\sigma$  cuts for both pions and kaons is excluded. For kaons, the upper momentum cut-off is 2  $\text{GeV}/c$  since the pion contamination level for kaons is  $\approx 10\%$  at that momentum. The upper momentum cut-off on the pions is  $p_T = 3$   $\text{GeV}/c$  – where the kaon contamination reaches  $\approx 10\%$ . The contamination of protons by kaons reaches about 5% at 4  $\text{GeV}/c$ . Electron (positron) and decay muon background at very low  $p_T$  ( $< 0.3$   $\text{GeV}/c$ ) are well separated from the pion mass-squared peak. The contamination background on each particle species is not subtracted in the analysis.

For protons, the upper momentum cut-off is set at  $4.5 \text{ GeV}/c$  due to statistical limitations and background at high  $p_T$ . An additional cut on  $m^2$  for protons and anti-protons,  $m^2 > 0.6 (\text{GeV}/c^2)^2$ , is introduced to reduce background. The lower momentum cut-offs are  $0.2 \text{ GeV}/c$  for pions,  $0.4 \text{ GeV}/c$  for kaons, and  $0.6 \text{ GeV}/c$  for  $p$  and  $\bar{p}$ . This cut-off value for  $p$  and  $\bar{p}$  is larger than those for pions and kaons due to the large energy loss effect.

## 3.4 Cut Conditions

The cut conditions used in the analysis are summarized in Table 3.2. Most of the cuts are commonly used in the other PHENIX analysis, e.g. minimum bias event selection, BBC z-vertex cut and track quality bit selection, but there are some specific cuts in the identified charged particle analysis using Drift Chamber and Time-of-Flight detectors. In the following subsections, we explain fiducial cut and energy loss cut. The PID cut is described in Section 3.3. And also we used the same (or equivalent) cuts over the single particle Monte Carlo output to get the correction functions. See Section 3.5 for more detail about single particle Monte Carlo simulation.

Cut	Value
Trigger	Minimum Bias
BBC $z$ -vertex cut	$\pm 30 \text{ cm}$
Number of PC1 hit	$\geq 1$
Fiducial cut	(see text)
DCH Zed cut	$\pm 75 \text{ cm}$
TOF $z$ position cut	$\pm 135 \text{ cm}$
TOF slat cut	$0 \geq \text{slat ID} < 767$ (select only E1 sector)
DCH track quality	31 or 63 (X1 $\&\&$ X2 w/ and w/o unique PC1 association)
TOF Matching cut	$2\sigma$ in $\phi$ and $z$
PC3 Matching cut	None
TOF energy loss cut	beta dependent energy loss cut (see text)
PID cut	$2\sigma$ in $m^2$ vs momentum space and additional cuts (see text)

Table 3.2: Cut conditions used in the analysis.

### 3.4.1 Fiducial Cut

The geometrical acceptance is determined by detector edges in both DCH and TOF. The fiducial cut is introduced in order to avoid the distortion of the particle distribution near the edges and the dead regions thorough the runs.

We apply the fiducial cut in DCH  $z$  within  $\pm 75$  cm to avoid the edge effect. (Figure 3.12)

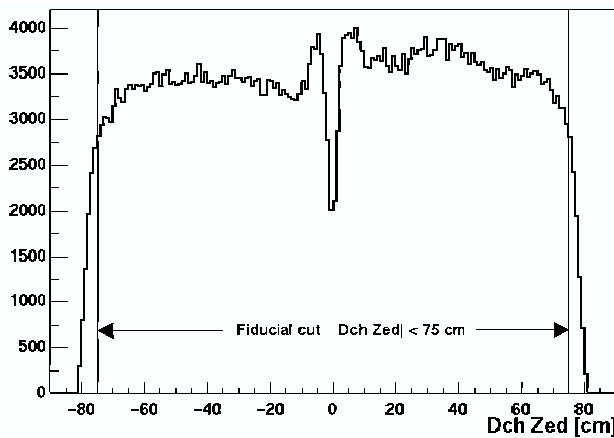


Figure 3.12: Drift chamber  $z$  distribution. In this analysis,  $|z| < 75$  cm are required for the fiducial cut. (solid line)

In order to avoid the dead region of the drift chamber, we determine the momentum dependence cuts for  $\phi_{DCH}$  in the  $\phi$  vs. *charge/p* space. This is due to the fact that the dead regions in the drift chamber increase during the run. Figure 3.13 shows the fiducial area at TOF after applying the fiducial cuts, which required TOF hit association.

### 3.4.2 Energy Loss Cut

The energy deposit in scintillator of TOF slat is useful to clean up noise hits on TOF wall. We use  $\beta = L/(TOF \cdot c)$ , where  $L$  is flight path length from vertex to hit on TOF detector,  $TOF$  is the time of flight, and  $c$  is the light velocity. The energy loss cut is defined as,

$$Eloss(cut) = a * \beta^b \quad (3.10)$$

where  $a = 0.0014$  and  $b = -1.66$ .

Figure 3.14 shows the distribution of  $\beta$  vs. energy loss, and the solid red line is the cut boundary. The dashed lines above and below the solid line are the energy loss cuts used in the systematic error estimation.

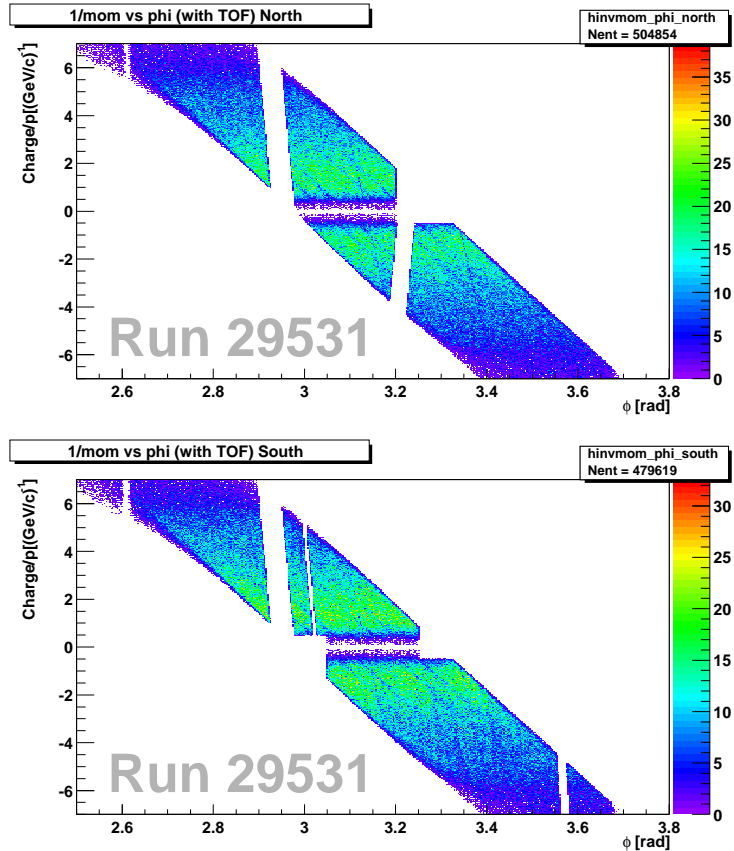


Figure 3.13: Fiducial area in TOF acceptance in all measured  $p_T$  rage. DCH  $\phi$  vs.  $charge/p$  distribution for north (top) and south side (bottom) are shown. The fiducial cuts are already applied in these plots.

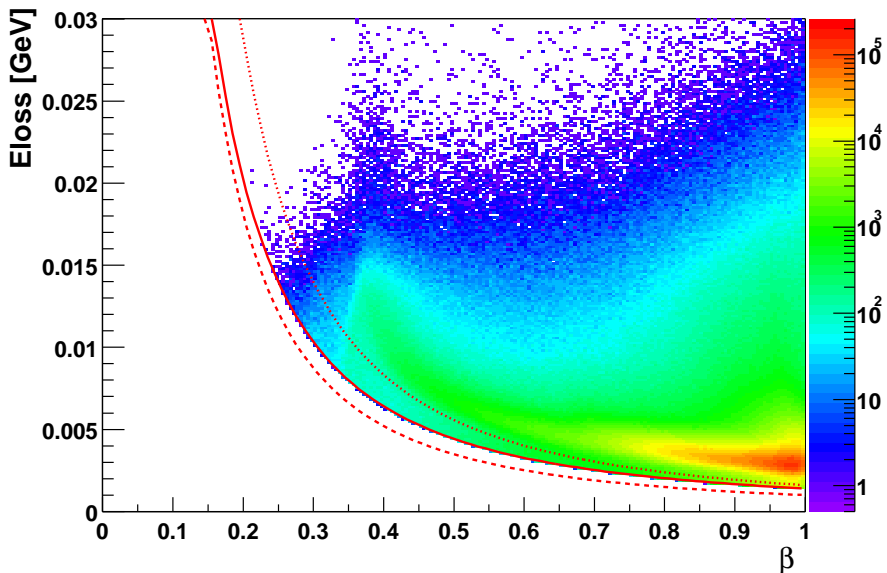


Figure 3.14:  $\beta$  vs. energy loss distributions with energy loss cut boundary (solid red line in the middle). The dashed lines above and below the solid line are only used for systematic error estimation.

## 3.5 Correction

In order to correct for 1) the geometrical acceptance, 2) in-flight decay for pions and kaons, 3) the effect of multiple scattering, and 4) nuclear interactions with materials in the detector (including anti-proton absorption), we use PISA (PHENIX Integrated Simulation Application), a GEANT [54] based Monte Carlo (MC) simulation program of the PHENIX detector. The single particle tracks are passed from GEANT through the PHENIX event reconstruction software [56].

In this section, we describe how we obtain a correction factors for the inclusive transverse momentum distributions of identified charged particles. The same procedure can be applied for all particles. We processed the following individual steps and estimated the correction factors for each particle species.

### 3.5.1 Comparison of Data with Simulation

In the Monte Carlo single particle simulation, we used following parameters in response and reconstruction chain. The DCH response chain used run2 average efficiency map. The TOF response chain used run2 typical parameter set which were used on run2 data reconstruction. This parameter files contain TOF dead channel map. The dead area is about 3%.

Since this is single particle simulation, there is no information in the BBC. We used the z coordinate of the origin of primary single particle smeared with a Gaussian distribution with sigma = 0.7 cm. We also used the time zero coordinate of the origin of GEANT value (= 0.0 ns) smeared with a Gaussian distribution with sigma = 0.04 ns. We set the intrinsic timing resolution of TOF in response chain. The value is 0.100 ns. It affects position resolution for  $\phi$  direction on TOF and time-of-flight resolution.

- Z-vertex resolution of BBC is 0.7 cm.
- Time zero resolution of BBC is 0.040 ns.
- Timing resolution of TOF is 0.100 ns.

#### Track Matching Residual

We check the track matching residual on TOF plane to compare Monte Carlo and real data. The track matching residual of  $\phi$  and  $z$  for Monte Carlo data are shown in Figure 3.15.

Comparing both Monte Carlo (Figure 3.15) and real data (Figure 3.9), we have good agreement for the sigma residual of  $\phi$  and  $z$ . We applied same sigma parameters for Monte Carlo and real data analysis. From mean residual of  $\phi$  and  $z$ , we estimated offset value and applied for Monte Carlo data.

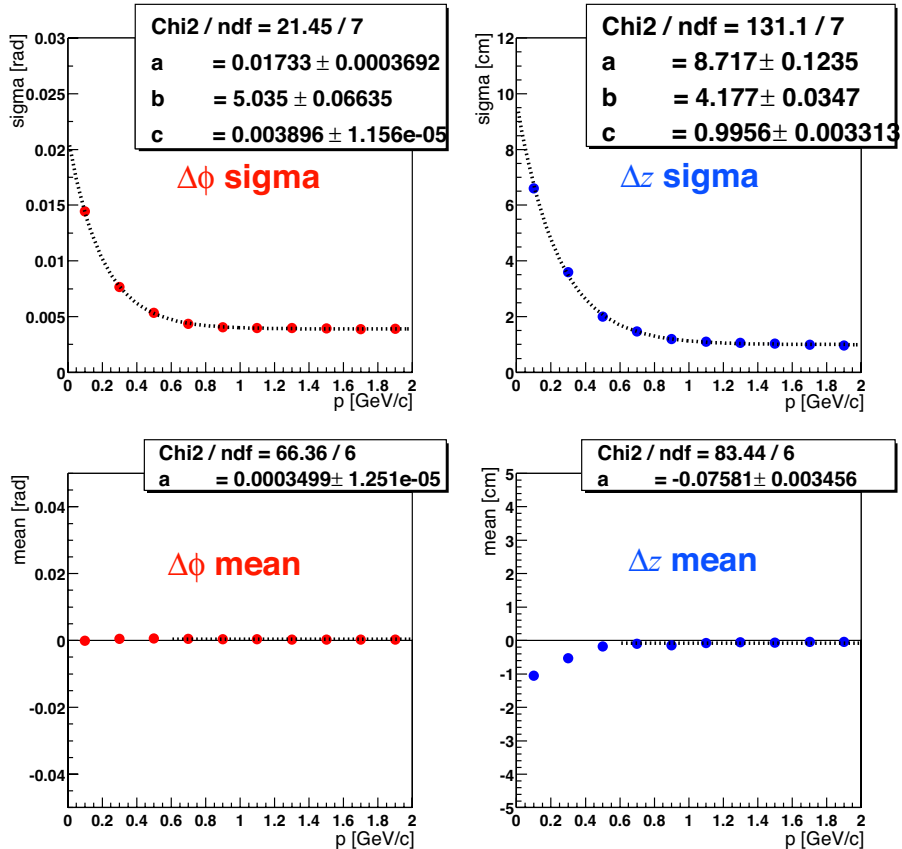


Figure 3.15: Track matching residual on TOF for Monte Carlo. Uppers are sigma residual of  $\phi$  (left) and  $z$  (right) as a function of momentum. Lowers are mean residual of  $\phi$  (left) and  $z$  (right) as a function of momentum.

### PID cut parameters

The mass squared resolution for Monte Carlo is better than for real. Figure 3.16 shows sigma and mean of mass squared for  $\pi, K, p$  as a function of momentum. We estimated PID cut parameters from sigma of mass squared distribution for each particle species. The parameters are,  $\sigma_\alpha = 0.860$  mrad,  $\sigma_{ms} = 0.550$  mrad·GeV and  $\sigma_{TOF} = 110$  ps. We applied these PID cut parameters for Monte Carlo data analysis.

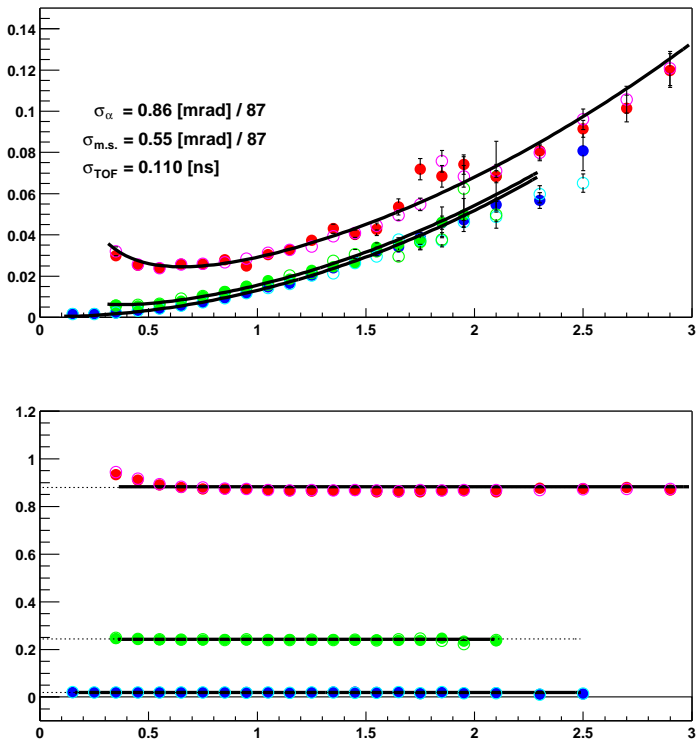


Figure 3.16: Sigma(up) and mean (down) of mass squared as a function of momentum. Blue is pion, green is kaon and red is proton. Open circle is negative.

## Fiducial Cut

The fiducial cut region is estimated by comparing Monte Carlo and real data. Section 3.4.1 describe about determination of fiducial cut region. We applied same fiducial cut for Monte Carlo and real data analysis. Figure 3.17 shows the fiducial area in TOF acceptance for Monte Carlo after applying fiducial cut. The DCH  $\phi$  vs  $charge/p$  are plotted for north (top) and south side (bottom), respectively. These fiducial area distributions show good agreement both Monte Carlo and real data.

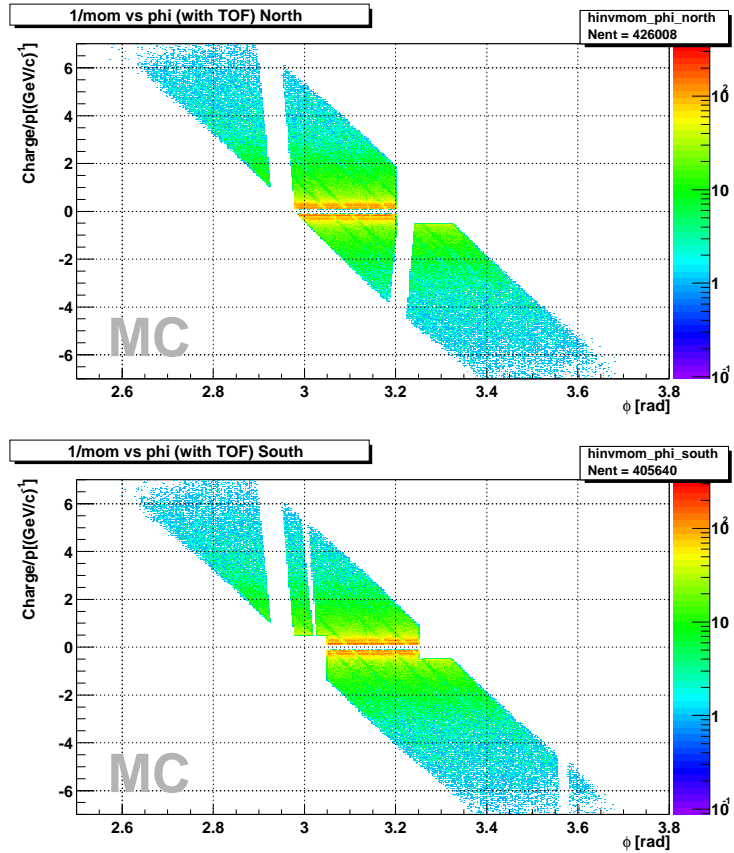


Figure 3.17: Fiducial area in TOF acceptance for Monte Carlo. The DCH  $\phi$  vs.  $charge/p$  counter plots for north (top) and south side (bottom), respectively. The fiducial cuts are already applied in these plots.

### 3.5.2 Corrections of Acceptance, Decay and Multiple Scattering

In this section, we describe how we obtain a correction factors for the inclusive transverse momentum distributions of identified charged particles. The same procedure can be applied for all particles.

We generate  $1 \times 10^7$  single particle events for each particle species ( $\pi^\pm$ ,  $K^\pm$ ,  $p$  and  $\bar{p}$ ) with low  $p_T$  enhanced ( $< 2 \text{ GeV}/c$ ) + flat  $p_T$  distributions for high  $p_T$  ( $2 - 4 \text{ GeV}/c$  for pions and kaons,  $2 - 8 \text{ GeV}/c$  for  $p$  and  $\bar{p}$ )<sup>1</sup>. The efficiencies are determined in each  $p_T$  bin by dividing the reconstructed output by the generated input as expressed as follows:

$$\epsilon_{\text{acc}}(j, p_T) = \frac{\# \text{ of reconstructed MC tracks}}{\# \text{ of generated MC tracks}}, \quad (3.11)$$

where  $j$  is the particle species. The resulting correction factors ( $1/\epsilon_{\text{acc}}$ ) are applied to the data in each  $p_T$  bin and for each individual particle species.

Figure 3.18 shows the transverse momentum distribution of generated and reconstructed MC tracks for each particle species. Figure 3.19 shows the correction factor as a function of  $p_T$  for each particle species.

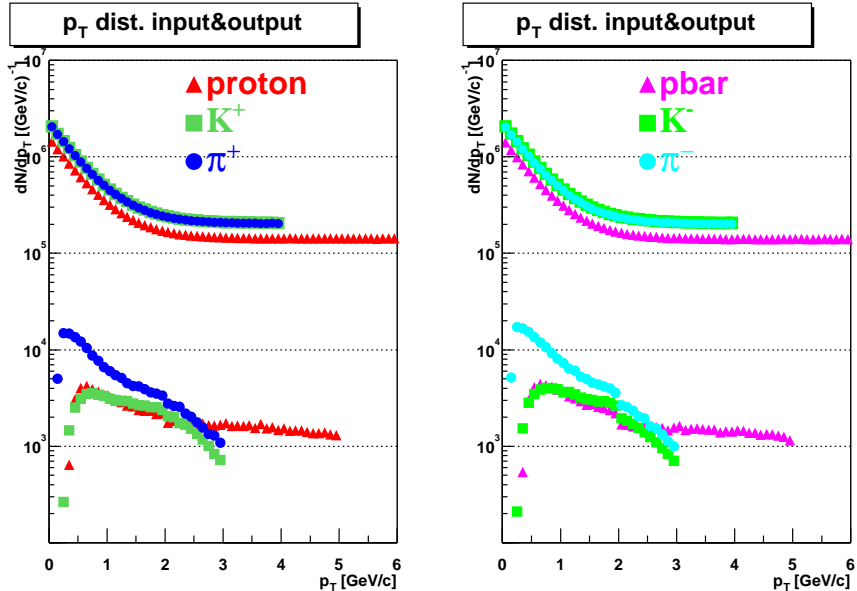


Figure 3.18:  $p_T$  distribution of Generated (top) and reconstructed (bottom) MC tracks for each particle species.

<sup>1</sup>Due to the good momentum resolution at the high  $p_T$  region, the momentum smearing effect for a steeply falling spectrum is  $< 1\%$  at  $p_T = 5 \text{ GeV}/c$ . The flat  $p_T$  distribution up to  $5 \text{ GeV}/c$  can be used to obtain the correction factors.

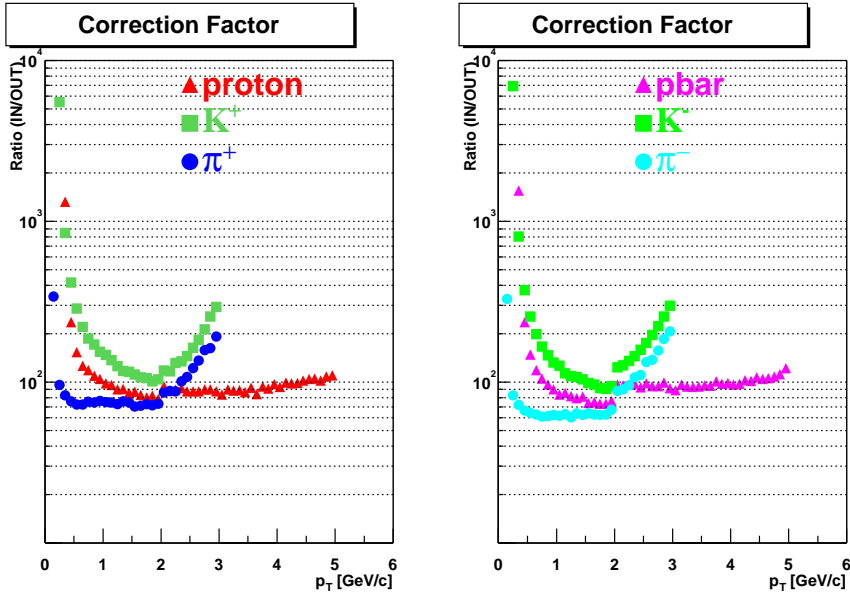


Figure 3.19: Correction factor as a function of  $p_T$  for pion (blue), kaon (green) and proton (red). Left is positive and right is negative charge.

### 3.5.3 Correction of Multiplicity Dependence

In high multiplicity environment, it is expected that the track reconstruction efficiency in central events is lower than that in peripheral events, which causes high occupancy and multiple hits on a detector cell such as scintillator slats of the TOF. The typical occupancy at TOF is less than 10% in the most central Au+Au collisions. To obtain the multiplicity dependence correction, we estimate the effect of detector occupancy by embedding single track Monte Carlo events into real events. The multiplicity dependence efficiency  $\epsilon_{\text{mult}}(i, j)$  was calculated in each centrality bin  $i$  and particle species  $j$ ,

$$\epsilon_{\text{mult}}(i, j) = \frac{\# \text{ of reconstructed embedded tracks}}{\# \text{ of embedded tracks}}. \quad (3.12)$$

This study has been performed for each particle species and each centrality bin. The track reconstruction efficiencies are factorized (into independent terms depending on centrality and  $p_T$ ) for  $p_T > 0.4$  GeV/c, since there is no  $p_T$  dependence in the efficiencies above that  $p_T$ . Figure 3.20 shows the dependence of track reconstruction efficiency for  $\pi^\pm$ ,  $K^\pm$ ,  $p$  and  $\bar{p}$  as a function of centrality expressed as  $N_{\text{part}}$ . The efficiency in the most central 0–5% events is about 80% for protons ( $\bar{p}$ ), 83% for kaons and 85% for pions. Slower particles are more likely lost due to high occupancy in the TOF because the system responds to the earliest hit. For the most peripheral 80–92% events, the efficiency for detector occupancy

effect is  $\approx 99\%$  for all particle species. The factors are applied to the spectra for each particle species and centrality bin. Systematic uncertainties on detector occupancy corrections ( $1/\varepsilon_{\text{mult}}$ ) are less than 3%.

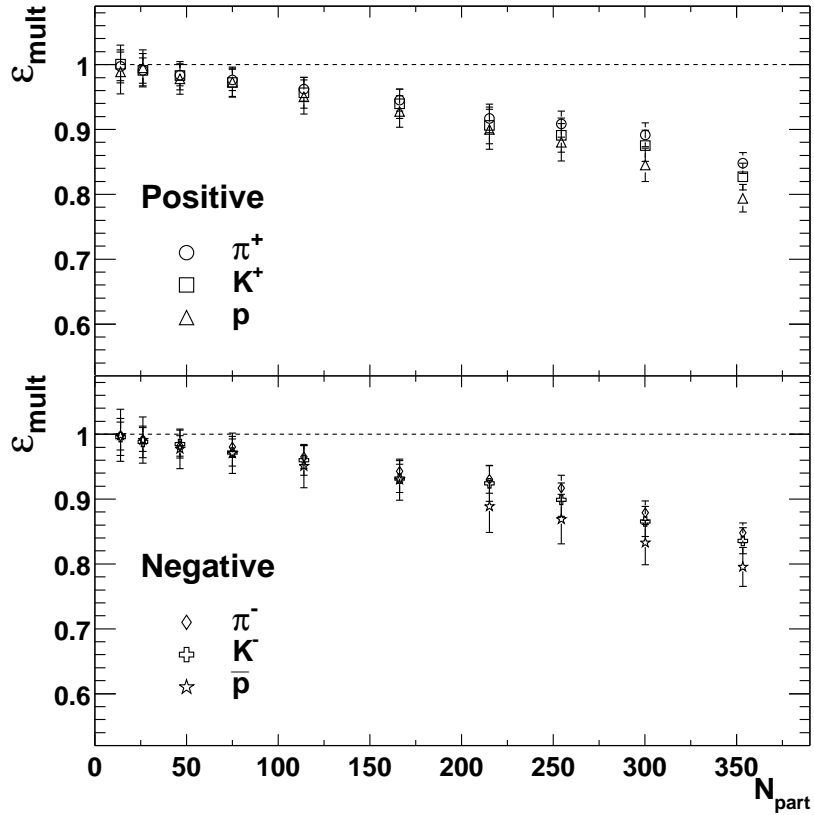


Figure 3.20: Track reconstruction efficiency (detector occupancy correction) as a function of centrality. The error bars on the plot represent the systematic errors.

### 3.5.4 Weak Decay Correction

Protons and anti-protons from weak decays (e.g. from  $\Lambda$  and  $\bar{\Lambda}$ ) can be reconstructed as tracks in the PHENIX spectrometer. The proton and anti-proton spectra are corrected to remove the feed-down contribution from weak decays using a HIJING [55] simulation. HIJING output has been tuned to reproduce the measured particle ratios of  $\Lambda/p$  and  $\bar{\Lambda}/\bar{p}$  along with their  $p_T$  dependencies in  $\sqrt{s_{\text{NN}}} = 130$  GeV Au+Au collisions [53] which include contribution from  $\Xi$  and  $\Sigma^0$ . Corrections for feed-down from  $\Sigma^\pm$  are not applied, as these yields were not measured. About  $2 \times 10^6$  central HIJING events (impact parameter  $b =$

0 – 3 fm) covering the TOF acceptance have been generated and processed through the PHENIX reconstruction software.

To calculate the feed-down corrections, the  $\bar{p}/p$  and  $\bar{\Lambda}/\Lambda$  yield ratios were assumed to be independent of  $p_T$  and centrality. The systematic error due to the feed-down correction is estimated at 6% by varying the  $\Lambda/p$  and  $\bar{\Lambda}/\bar{p}$  ratios within the systematic errors of the  $\sqrt{s_{NN}} = 130$  GeV Au+Au measurement [53] ( $\pm 24\%$ ) and assuming  $m_T$ -scaling at high  $p_T$ . This uncertainty could be larger if the  $\Lambda/p$  and  $\bar{\Lambda}/\bar{p}$  ratios change significantly with  $p_T$  and beam energy.

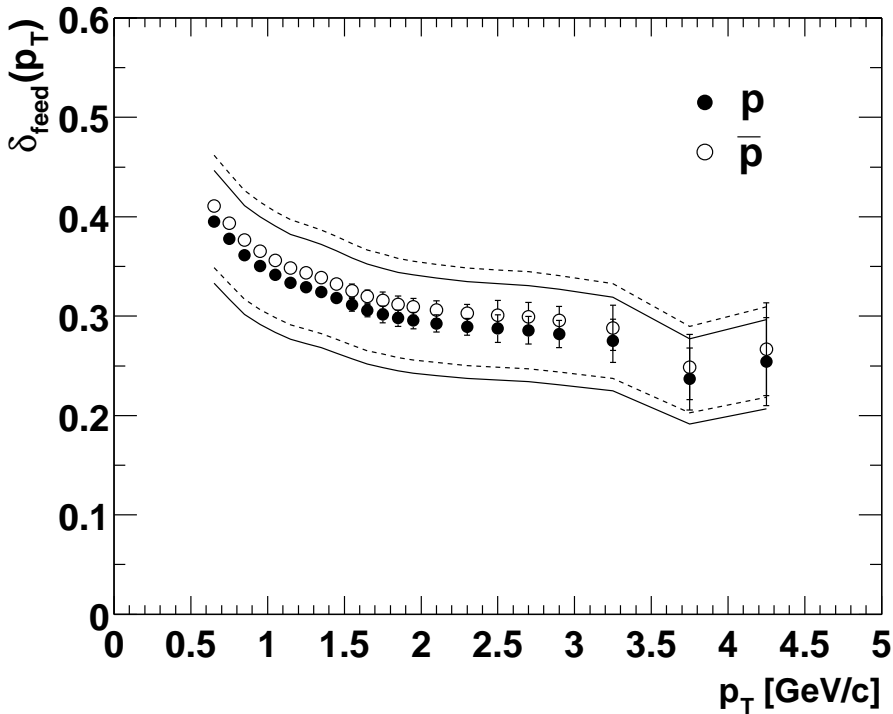


Figure 3.21: The fractional contribution of protons ( $\bar{p}$ ) from  $\Lambda(\bar{\Lambda})$  decays in all measured protons ( $\bar{p}$ ),  $\delta_{feed}(p_T)$ , as a function of  $p_T$ . The solid (dashed) lines represent the systematic errors for protons ( $\bar{p}$ ). The error bars are statistical errors.

The fractional contribution to the  $p$  ( $\bar{p}$ ) yield from  $\Lambda(\bar{\Lambda})$ ,  $\delta_{feed}(p_T)$ , is shown in Figure 3.21. The solid (dashed) lines represent the systematic errors for protons ( $\bar{p}$ ). The obtained factor is about 40% below 1 GeV/c and 30% at 4 GeV/c. We multiply the proton and anti-proton spectra by the factor,  $C_{feed}$ , for all centrality bins as a function of  $p_T$ :

$$C_{feed}(j, p_T) = 1 - \delta_{feed}(j, p_T), \quad (3.13)$$

where  $j$  is particle species ( $p, \bar{p}$ ).

### 3.5.5 Invariant Yield

Applying the data cuts and corrections discussed above, the final invariant yield for each particle species and centrality bin are derived using the following equation.

$$\frac{1}{2\pi p_T} \frac{d^2N}{dp_T dy} = \frac{1}{2\pi p_T} \cdot \frac{1}{N_{evt}(i)} \cdot C_{ij}(p_T) \cdot \frac{N_j(i, p_T)}{\Delta p_T \Delta y}, \quad (3.14)$$

where  $y$  is rapidity,  $N_{evt}(i)$  is the number of events in each centrality bin  $i$ ,  $C_{ij}(p_T)$  is the total correction factor and  $N_j(i, p_T)$  is the number of counts in each centrality bin  $i$ , particle species  $j$ , and  $p_T$ . The total correction factor is composed of:

$$C_{ij}(p_T) = \frac{1}{\epsilon_{acc}(j, p_T)} \cdot \frac{1}{\epsilon_{mult}(i, j)} \cdot C_{feed}(j, p_T). \quad (3.15)$$

## 3.6 Systematic Uncertainties

To estimate systematic uncertainties on the  $p_T$  distribution and particle ratios, various sets of  $p_T$  spectra and particle ratios were made by changing the cut parameters including the fiducial cut, PID cut, and track association windows slightly from what was used in the analysis. For each of these spectra and ratios using modified cuts, the same changes in the cuts were made in the Monte Carlo analysis. The absolutely normalized spectra with different cut conditions are divided by the spectra with the baseline cut conditions, resulting in uncertainties associated with each cut condition as a function of  $p_T$ . The various uncertainties are added in quadrature. Three different centrality bins (minimum bias, central 0–5%, and peripheral 60–92%) are used to study the centrality dependence of systematic errors. The same procedure has been applied for the following particle ratios:  $\pi^-/\pi^+$ ,  $K^-/K^+$ ,  $\bar{p}/p$ ,  $K/\pi$ ,  $p/\pi^+$ , and  $\bar{p}/\pi^-$ .

Table 3.3 shows the systematic errors of the  $p_T$  spectra for central collisions. The systematic uncertainty on the absolute value of momentum (momentum scale) are estimated as 3% in the measured  $p_T$  range by comparing the known proton mass to the value measured as protons in real data. It is found that the total systematic error on the  $p_T$  spectra is 8–14% in both central and peripheral collisions. For the particle ratios, the typical systematic error is about 6% for all particle species. The dominant source of uncertainties on the central-to-peripheral ratio scaled by  $N_{coll}$  ( $R_{CP}$ ) are the systematic errors on the nuclear overlap function,  $T_{AuAu}$  (see Table 3.4). Table 3.5 and Table 3.6 show the systematic errors on  $dN/dy$  and  $\langle p_T \rangle$ . The procedure for the determination of these quantities are discuss in Section 4.2.

$p_T$ range (GeV/c)	$\pi^+$	$\pi^-$	$K^+$	$K^-$	$p$	$\bar{p}$		
	0.2 - 3.0	0.2 - 3.0	0.4 - 2.0	0.4 - 2.0	0.6 - 3.0	3.0 - 4.5	0.6 - 3.0	3.0 - 4.5
Cuts	6.2	6.2	11.2	9.5	6.6	11.6	6.6	11.6
Momentum scale	3	3	3	3	3	3	3	3
Occupancy correction	2	2	3	3	3	3	3	3
Feed-down correction	-	-	-	-	6.0	6.0	6.0	6.0
Total	7.2	7.2	12.0	10.4	9.9	13.7	9.9	9.9

Table 3.3: Systematic errors on the  $p_T$  spectra for central events. All errors are given in percent.

Source	$(\pi^+ + \pi^-)/2$	$(K^+ + K^-)/2$	$(p + \bar{p})/2$
Occupancy correction (central)	2	3	3
Occupancy correction (peripheral)	2	3	3
$\langle T_{\text{AuAu}} \rangle$ (0–10%)	6.9	6.9	6.9
$\langle T_{\text{AuAu}} \rangle$ (60–92%)	28.6	28.6	28.6
Total	29.5	29.7	29.7

Table 3.4: Systematic errors on Central-to-Peripheral ratio ( $R_{\text{CP}}$ ). All errors are given in percent.

Source	Central 0–5%						Peripheral 60–92%					
	$\pi^+$	$\pi^-$	$K^+$	$K^-$	$p$	$\bar{p}$	$\pi^+$	$\pi^-$	$K^+$	$K^-$	$p$	$\bar{p}$
Cuts	6.2	6.2	11.2	9.5	6.6	6.6	6.2	6.2	7.7	6.6	7.7	7.7
Extrapolation	3.9	3.5	3.5	3.3	6.2	5.9	5.4	5.3	4.6	4.4	8.6	8.6
Contamination background	<1	<1	<1	<1	<1	<1	<1	<1	<1	<1	<1	<1
Feed-down	-	-	-	-	1.0	1.0	-	-	-	-	1.0	1.0
Total	7.3	7.1	13.5	10.0	9.1	8.9	8.2	8.1	8.9	7.9	11.5	11.5

Table 3.5: Systematic errors on  $\langle p_T \rangle$  for central 0–5% (top) and peripheral 60–92% (bottom) collisions. All errors are given in percent.

Source	Central 0–5%						Peripheral 60–92%					
	$\pi^+$	$\pi^-$	$K^+$	$K^-$	$p$	$\bar{p}$	$\pi^+$	$\pi^-$	$K^+$	$K^-$	$p$	$\bar{p}$
Cuts + occupancy	6.5	6.5	11.6	10.0	7.2	7.2	6.5	6.5	8.3	7.2	8.3	8.3
Extrapolation	5.4	4.8	5.7	5.6	9.6	9.2	8.4	8.0	7.4	7.5	13.6	13.6
Contamination background	<1	<1	<1	<1	<1	<1	<1	<1	<1	<1	<1	<1
Feed-down	-	-	-	-	8.0	8.0	-	-	-	-	8.0	8.0
Total	8.4	8.0	12.9	11.4	14.4	14.4	10.6	10.3	11.1	10.3	17.8	17.8

Table 3.6: Systematic errors on  $dN/dy$  for central 0–5% (top) and peripheral 60–92% (bottom) collisions. All errors are given in percent.

# Chapter 4

## Experimental Results

In this chapter, the transverse momentum spectra and yields of identified charged hadrons at mid-rapidity in  $\sqrt{s_{\text{NN}}} = 200$  GeV Au+Au collisions are shown. Also the systematic study of particle ratios are presented. In this analysis, we use the eleven centrality classes (0–5%, 5–10%, 10–15%, 15–20%, 20–30%, ..., 70–80%, 80–92%) described in Section 3.1, combined peripheral event class (60–92%) and minimum bias event class.

### 4.1 Transverse Momentum Distributions

Figure 4.1 shows the centrality dependence of the  $p_T$  spectrum for  $\pi^+$  (left) and  $\pi^-$  (right). For the comparison of the spectra shape, the data points are scaled vertically as quoted in the figures. The error bars are statistical only. The pion spectra show a concave shape for all centrality bins. The spectra become steeper (fall faster with increasing  $p_T$ ) in peripheral collisions. The comparison between charged pions and  $\pi^0$  [32] are shown in Figure 4.2.

Figure 4.3 shows the  $p_T$  spectrum for kaons. The data can be well described by an exponential in  $p_T$  for all centralities. Finally, the centrality dependence of the  $p_T$  spectra for protons (left) and anti-protons (right) are shown in Figure 4.4. As in Figure 4.4, both  $p$  and  $\bar{p}$  spectra show a strong centrality dependence below 1.5 GeV/ $c$ , i.e. they develop a shoulder at low  $p_T$  and the spectra flatten (fall more slowly with increasing  $p_T$ ) with increasing  $N_{\text{part}}$ .

The invariant yields for  $\pi^\pm$ ,  $K^\pm$ ,  $p$  and  $\bar{p}$  in Au+Au collisions at  $\sqrt{s_{\text{NN}}} = 200$  GeV at mid-rapidity are tabulated in Tables C.1 – C.20 (Appendix C.1). The data presented here are for the the minimum bias events and each centrality classes.

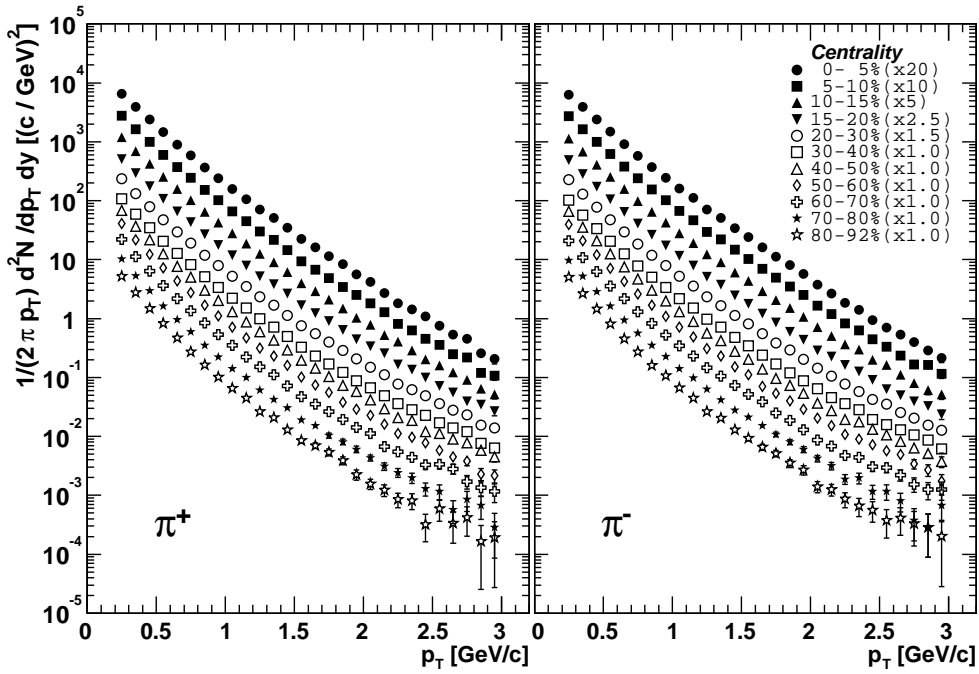


Figure 4.1: Centrality dependence of the  $p_T$  distribution for  $\pi^+$  (left) and  $\pi^-$  (right) in Au+Au collisions at  $\sqrt{s_{NN}} = 200$  GeV. The different symbols correspond to different centrality bins. The error bars are statistical only. For clarity, the data points are scaled vertically as quoted in the figure.

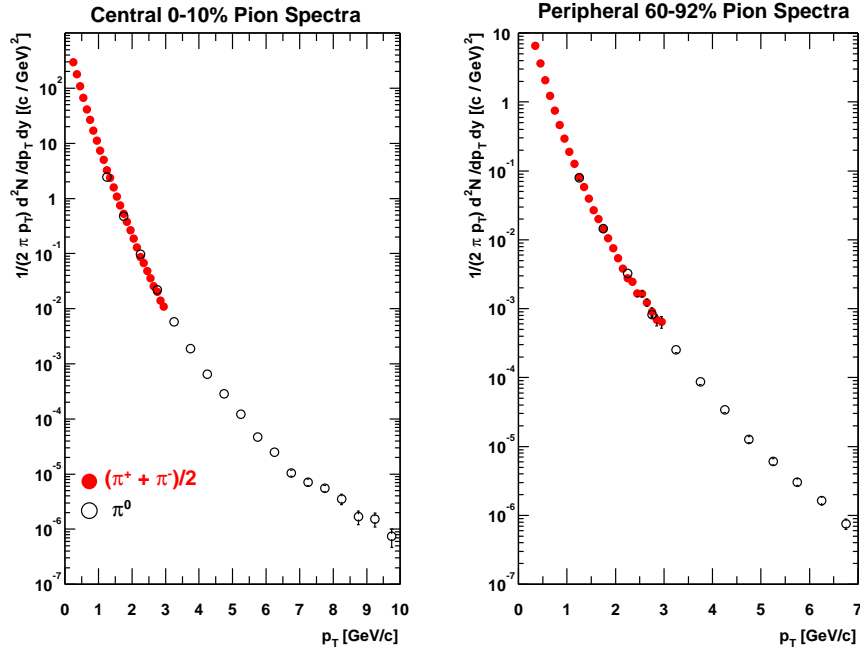


Figure 4.2: Comparison between averaged charged pion  $p_T$  spectra  $(\pi^+ + \pi^-)/2$  (red filled circle) and  $\pi^0$  (open circle) for central 0-10% (left) and peripheral 60-92% (right).

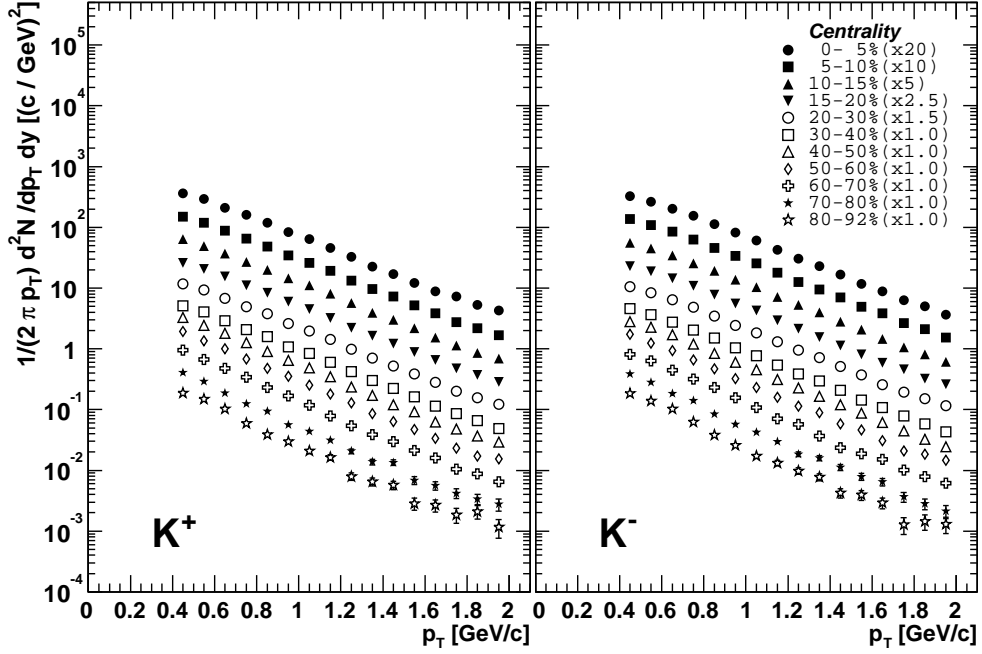


Figure 4.3: Centrality dependence of the  $p_T$  distribution for  $K^+$  (left) and  $K^-$  (right) in Au+Au collisions at  $\sqrt{s_{NN}} = 200$  GeV. The different symbols correspond to different centrality bins. The error bars are statistical only. For clarity, the data points are scaled vertically as quoted in the figure.

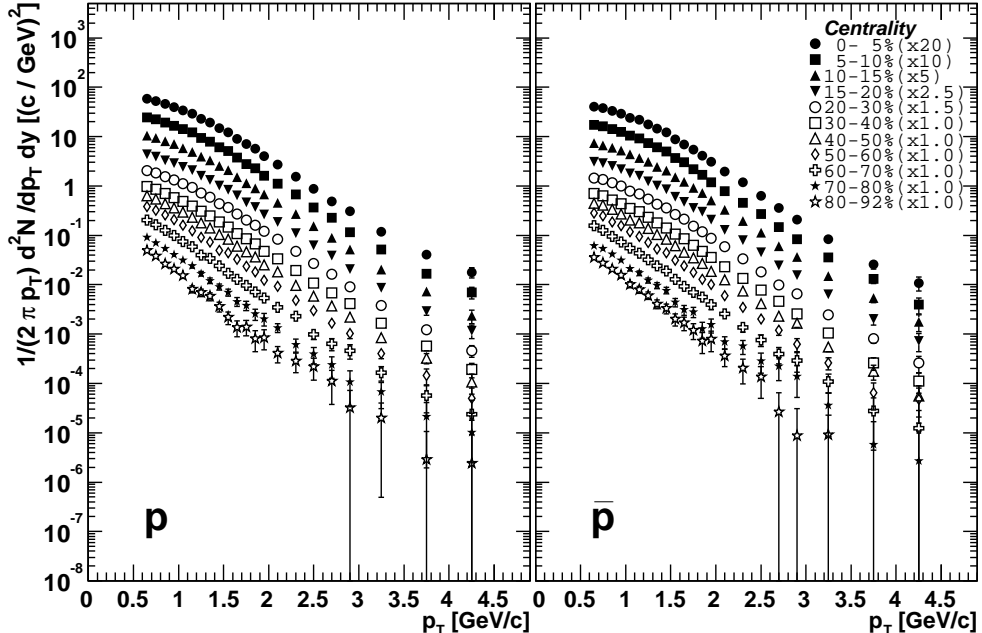


Figure 4.4: Centrality dependence of the  $p_T$  distribution for protons (left) and anti-protons (right) in Au+Au collisions at  $\sqrt{s_{NN}} = 200$  GeV. The different symbols correspond to different centrality bins. The error bars are statistical only. Feed-down corrections for  $\Lambda$  ( $\bar{\Lambda}$ ) decaying into proton ( $\bar{p}$ ) have been applied. For clarity, the data points are scaled vertically as quoted in the figure.

## 4.2 Mean Transverse Momentum and Particle Yields

By integrating a measured  $p_T$  spectrum over  $p_T$ , one can determine the mean transverse momentum,  $\langle p_T \rangle$ , and particle yield per unit rapidity,  $dN/dy$ , for each particle species. For the extrapolation of  $p_T$  spectrum, the following functional forms are used for different particle species: a power-law function and a  $p_T$  exponential for pions, a  $p_T$  exponential and an  $m_T$  exponential for kaons, and a Boltzmann function,  $p_T$  exponential, and  $m_T$  exponential for protons and anti-protons. The effects of contamination background at high  $p_T$  region for both  $\langle p_T \rangle$  and  $dN/dy$  are estimated as less than 1% for all particle species. The procedure to determine the mean  $p_T$  and  $dN/dy$  is described below:

1. Determine  $dN/dy$  and  $\langle p_T \rangle$  by integrating over the measured  $p_T$  range from the data.
2. Fit several appropriate functional forms (detailed below) to the  $p_T$  spectra. Note that all of the fits are reasonable approximations to the data. Integrate from zero to the first data point and from the last data point to infinity.
3. Sum the data yield and the two functional yield pieces together to get  $dN/dy$  and  $\langle p_T \rangle$  in each functional form.
4. Take the average between the upper and lower bounds from the different functional forms to obtain the final  $dN/dy$  and  $\langle p_T \rangle$ . The statistical uncertainties are determined from the data. The systematic errors from the extrapolation of yield are defined as half of the difference between the upper and lower bounds.
5. Determine the final systematic errors on  $dN/dy$  and  $\langle p_T \rangle$  for each centrality bin by taking the quadrature sum of the extrapolation errors, errors associated with cuts, detector occupancy corrections (for  $dN/dy$ ) and feed-down corrections (for protons).

The overall systematic uncertainties on both  $\langle p_T \rangle$  and  $dN/dy$  are about 10–15%. See Table 3.5 for the systematic errors of  $\langle p_T \rangle$  and Table 3.6 for those of  $dN/dy$ .

Figure 4.5 shows the centrality dependence of  $\langle p_T \rangle$  for  $\pi^\pm$ ,  $K^\pm$ ,  $p$  and  $\bar{p}$ . The error bars in the figure represent the statistical errors. The systematic errors from cuts conditions are shown as shaded boxes on the right for each particle species. The systematic errors from extrapolations, which are scaled by a factor of 2 for clarity, are shown in the bottom for each particle species. The data are also summarized in Table 4.1. It is found that  $\langle p_T \rangle$  for all particle species increases from the most peripheral to mid-central collisions, and appears to saturate from the mid-central to central collisions (although the  $\langle p_T \rangle$  values for  $p$  and  $\bar{p}$  may continue to rise). It should be noted that while the total systematic errors on  $\langle p_T \rangle$  listed in Table 3.5 is large, the trend shown in the figure is significant. One of the main sources of the uncertainty is the yield extrapolation in unmeasured  $p_T$  range (e.g.  $p_T < 0.6$  GeV/c

for protons and anti-protons). These systematic errors are correlated, and therefore move the curve up and down simultaneously.

Figure 4.6 shows the centrality dependence of  $dN/dy$  per participant pair ( $0.5 N_{\text{part}}$ ). The data are summarized in Table 4.2. The error bars on each point represent the quadratic sum of the statistical errors and systematic errors from cut conditions. The statistical errors are negligible. The lines represent the effect of the systematic error on  $N_{\text{part}}$  which affects all curves in the same way. The data indicate that  $dN/dy$  per participant pair increases for all particle species with  $N_{\text{part}}$  up to  $\approx 100$ , and saturates from the mid-central to the most central collisions. From  $dN/dy$  for protons and anti-protons, we obtain the net proton number at mid-rapidity for the most central 0–5% collisions,  $dN/dy|_p - dN/dy|_{\bar{p}} = 18.47 - 13.52 = 4.95 \pm 2.74$ .

$N_{\text{part}}$	$\pi^+$	$\pi^-$	$K^+$	$K^-$	$p$	$\bar{p}$
351.4	$451 \pm 33$	$455 \pm 32$	$670 \pm 78$	$677 \pm 68$	$949 \pm 85$	$959 \pm 84$
299.0	$450 \pm 33$	$454 \pm 33$	$672 \pm 78$	$679 \pm 68$	$948 \pm 84$	$951 \pm 83$
253.9	$448 \pm 33$	$453 \pm 33$	$668 \pm 78$	$676 \pm 68$	$942 \pm 84$	$950 \pm 83$
215.3	$447 \pm 34$	$449 \pm 33$	$667 \pm 78$	$670 \pm 67$	$937 \pm 84$	$940 \pm 83$
166.6	$444 \pm 35$	$447 \pm 34$	$661 \pm 77$	$668 \pm 67$	$923 \pm 85$	$920 \pm 83$
114.2	$436 \pm 35$	$440 \pm 35$	$655 \pm 77$	$654 \pm 66$	$901 \pm 83$	$892 \pm 82$
74.4	$426 \pm 35$	$429 \pm 35$	$636 \pm 54$	$644 \pm 48$	$868 \pm 88$	$864 \pm 88$
45.5	$412 \pm 35$	$416 \pm 34$	$617 \pm 53$	$621 \pm 47$	$833 \pm 86$	$824 \pm 86$
25.7	$398 \pm 34$	$403 \pm 33$	$600 \pm 52$	$606 \pm 46$	$788 \pm 84$	$777 \pm 83$
13.4	$381 \pm 32$	$385 \pm 32$	$581 \pm 51$	$579 \pm 46$	$755 \pm 82$	$747 \pm 80$
6.3	$367 \pm 30$	$371 \pm 30$	$568 \pm 51$	$565 \pm 45$	$685 \pm 78$	$708 \pm 81$

Table 4.1: Centrality dependence of  $\langle p_T \rangle$  for  $\pi^\pm, K^\pm, p$  and  $\bar{p}$  in MeV/c. The errors are systematic only. The statistical errors are negligible.

$N_{\text{part}}$	$\pi^+$	$\pi^-$	$K^+$	$K^-$	$p$	$\bar{p}$
351.4	$286.4 \pm 24.2$	$281.8 \pm 22.8$	$48.9 \pm 6.3$	$45.7 \pm 5.2$	$18.4 \pm 2.6$	$13.5 \pm 1.8$
299.0	$239.6 \pm 20.5$	$238.9 \pm 19.8$	$40.1 \pm 5.1$	$37.8 \pm 4.3$	$15.3 \pm 2.1$	$11.4 \pm 1.5$
253.9	$204.6 \pm 18.0$	$198.2 \pm 16.7$	$33.7 \pm 4.3$	$31.1 \pm 3.5$	$12.8 \pm 1.8$	$9.5 \pm 1.3$
215.3	$173.8 \pm 15.6$	$167.4 \pm 14.4$	$27.9 \pm 3.6$	$25.8 \pm 2.9$	$10.6 \pm 1.5$	$7.9 \pm 1.1$
166.6	$130.3 \pm 12.4$	$127.3 \pm 11.6$	$20.6 \pm 2.6$	$19.1 \pm 2.2$	$8.1 \pm 1.1$	$5.9 \pm 0.8$
114.2	$87.0 \pm 8.6$	$84.4 \pm 8.0$	$13.2 \pm 1.7$	$12.3 \pm 1.4$	$5.3 \pm 0.7$	$3.9 \pm 0.5$
74.4	$54.9 \pm 5.6$	$52.9 \pm 5.2$	$8.0 \pm 0.8$	$7.4 \pm 0.6$	$3.2 \pm 0.5$	$2.4 \pm 0.3$
45.5	$32.4 \pm 3.4$	$31.3 \pm 3.1$	$4.5 \pm 0.4$	$4.1 \pm 0.4$	$1.8 \pm 0.3$	$1.4 \pm 0.2$
25.7	$17.0 \pm 1.8$	$16.3 \pm 1.6$	$2.2 \pm 0.2$	$2.0 \pm 0.1$	$0.93 \pm 0.15$	$0.71 \pm 0.12$
13.4	$7.9 \pm 0.8$	$7.7 \pm 0.7$	$0.89 \pm 0.09$	$0.88 \pm 0.09$	$0.40 \pm 0.07$	$0.29 \pm 0.05$
6.3	$4.0 \pm 0.4$	$3.9 \pm 0.3$	$0.44 \pm 0.04$	$0.42 \pm 0.04$	$0.21 \pm 0.04$	$0.15 \pm 0.02$

Table 4.2: Centrality dependence of  $dN/dy$  for  $\pi^\pm, K^\pm, p$  and  $\bar{p}$ . The errors are systematic only. The statistical errors are negligible.

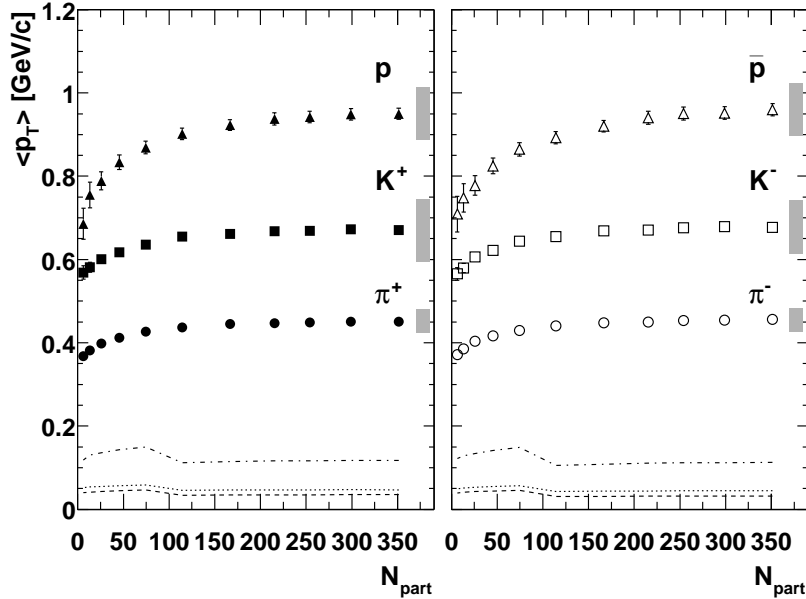


Figure 4.5: Mean transverse momentum as a function of  $N_{\text{part}}$  for pions, kaons, protons and anti-protons in Au+Au collisions at  $\sqrt{s_{\text{NN}}} = 200$  GeV. The left (right) panel shows the  $\langle p_T \rangle$  for positive (negative) particles. The error bars are statistical errors. The systematic errors from cuts conditions are shown as shaded boxes on the right for each particle species. The systematic errors from extrapolations, which are scaled by a factor of 2 for clarity, are shown in the bottom for protons and anti-protons (dashed-dot lines), kaons (dotted lines), and pions (dashed lines).

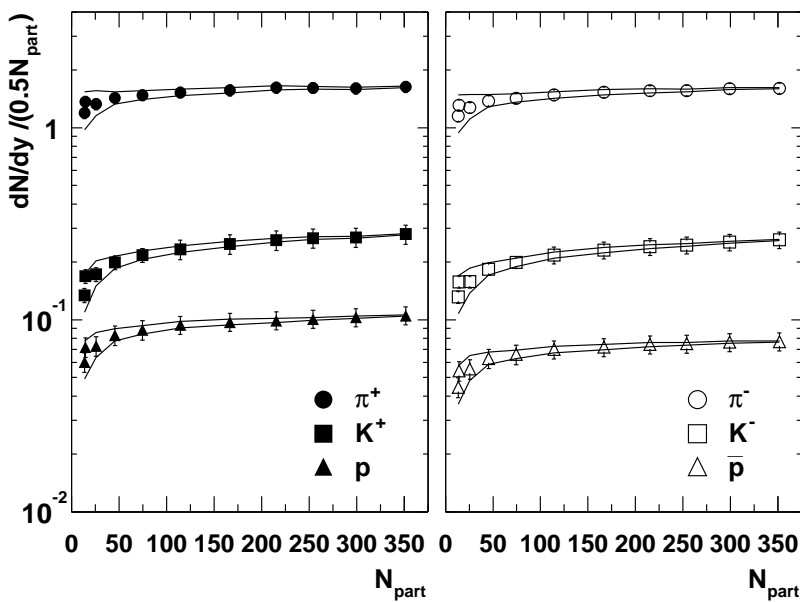


Figure 4.6: Particle yield per unit rapidity ( $dN/dy$ ) per participant pair ( $0.5 N_{\text{part}}$ ) as a function of  $N_{\text{part}}$  for pions, kaons, protons and anti-protons in Au+Au collisions at  $\sqrt{s_{\text{NN}}} = 200$  GeV. The left (right) panel shows the  $dN/dy$  for positive (negative) particles. The error bars represent the quadratic sum of statistical errors and systematic errors from cut conditions. The lines represent the effect of the systematic error on  $N_{\text{part}}$  which affects all curves in the same way.

## 4.3 Particle Ratios

The ratios of  $\pi^-/\pi^+$ ,  $K^-/K^+$ ,  $p/\bar{p}$ ,  $K/\pi$ ,  $p/\pi$  and  $\bar{p}/\pi$  measured as a function of  $p_T$  and centrality at  $\sqrt{s_{NN}} = 200$  GeV in Au+Au collisions are presented here.

Figure 4.7 shows the particle ratios of  $\pi^-/\pi^+$  (top),  $K^-/K^+$  (middle), and  $\bar{p}/p$  (bottom) as a function of  $p_T$  for central (0–5%, left) and peripheral (60–92%, right). The error bars represent statistical errors and the shaded boxes on each panel represent the systematic errors. For each of these particle species and centralities, the particle ratios are constant within the experimental errors over the measured  $p_T$  range.

In Figure 4.8, the  $p_T$  dependence of the  $K/\pi$  ratio is shown for the most central 0–5% and the most peripheral 60–92% centrality bins. The  $K^+/\pi^+$  ( $K^-/\pi^-$ ) ratios are shown on the left (right). Both ratios increase with  $p_T$  and the increase is faster in central collisions than in peripheral ones. In Figure 4.9, the  $p/\pi$  and  $\bar{p}/\pi$  ratios are shown as a function of  $p_T$  for the most central 0–5% and the most peripheral 60–92% centrality bins.

Figure 4.10 shows the centrality dependence of particle ratios for  $\pi^-/\pi^+$ ,  $K^-/K^+$  and  $\bar{p}/p$ . The ratios presented here are derived from the integrated yields over  $p_T$  (i.e.  $dN/dy$ ). The shaded boxes on each data point indicate the systematic errors. Within uncertainties, the ratios are all independent of  $N_{\text{part}}$  over the measured range.

Figure 4.11 shows the centrality dependence of  $K/\pi$  and  $p/\pi$  ratios. Both  $K^+/\pi^+$  and  $K^-/\pi^-$  ratios increase rapidly for peripheral collisions ( $N_{\text{part}} < 100$ ), and then saturate or rise slowly from the mid-central to the most central collisions. The  $p/\pi^+$  and  $\bar{p}/\pi^-$  ratios increase for peripheral collisions ( $N_{\text{part}} < 50$ ) and saturate from mid-central to central collisions – similar to the centrality dependence of  $K/\pi$  ratio (but possibly flatter).

The data tables describe in Appendix C.2.

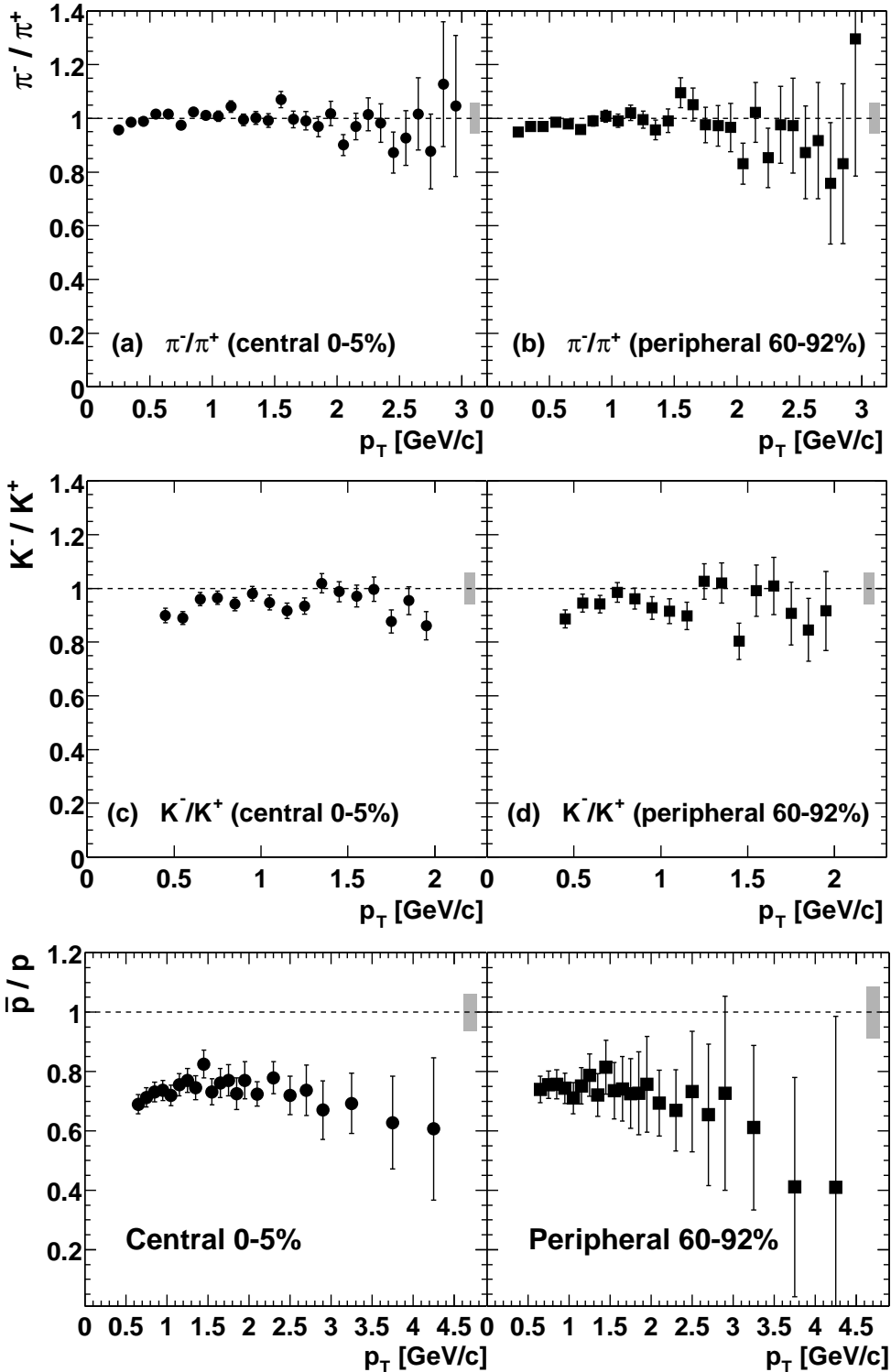


Figure 4.7: Particle ratios of  $\pi^-/\pi^+$  (top),  $K^-/K^+$  (middle), and  $\bar{p}/p$  (bottom) as a function of  $p_T$  for central 0–5% (left) and peripheral 60–92% (right) in Au+Au collisions at  $\sqrt{s_{NN}} = 200$  GeV. The error bars indicate the statistical errors and shaded boxes around unity on each panel indicate the systematic errors.

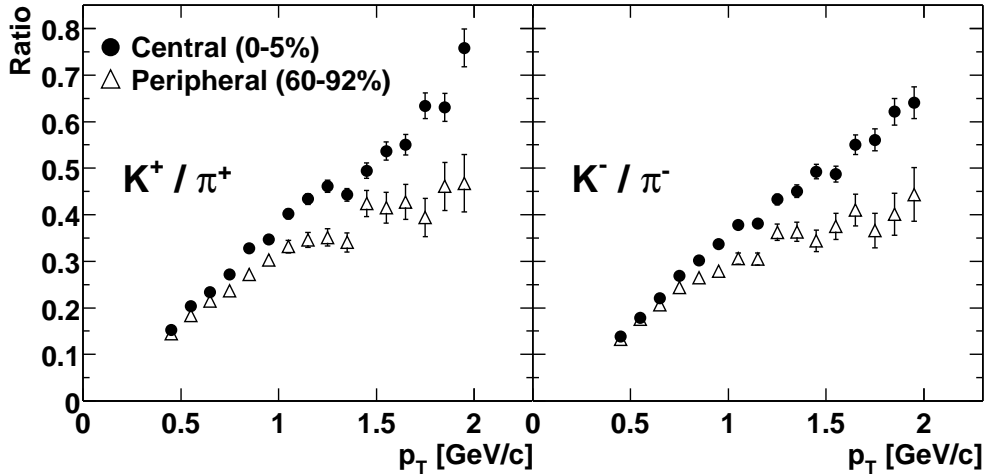


Figure 4.8:  $K/\pi$  ratios as a function of  $p_T$  for central 0–5% and peripheral 60–92% in Au+Au collisions at  $\sqrt{s_{NN}} = 200$  GeV. The left is for  $K^+/\pi^+$  and the right is for  $K^-/\pi^-$ . The error bars indicate the statistical errors.

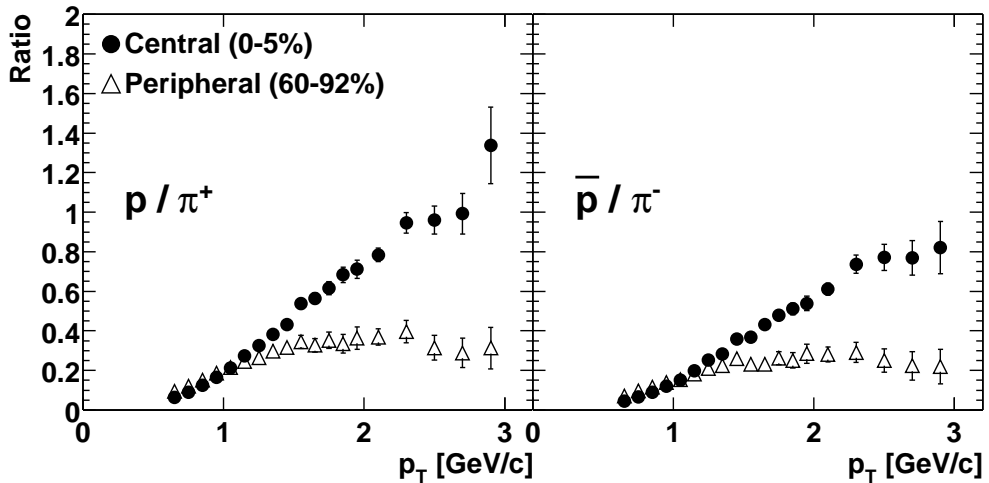


Figure 4.9:  $p/\pi^+$  (left) and  $\bar{p}/\pi^-$  (right) ratios as a function of  $p_T$  for central 0–5% and peripheral 60–92% in Au+Au collisions at  $\sqrt{s_{NN}} = 200$  GeV. The error bars indicate the statistical errors.

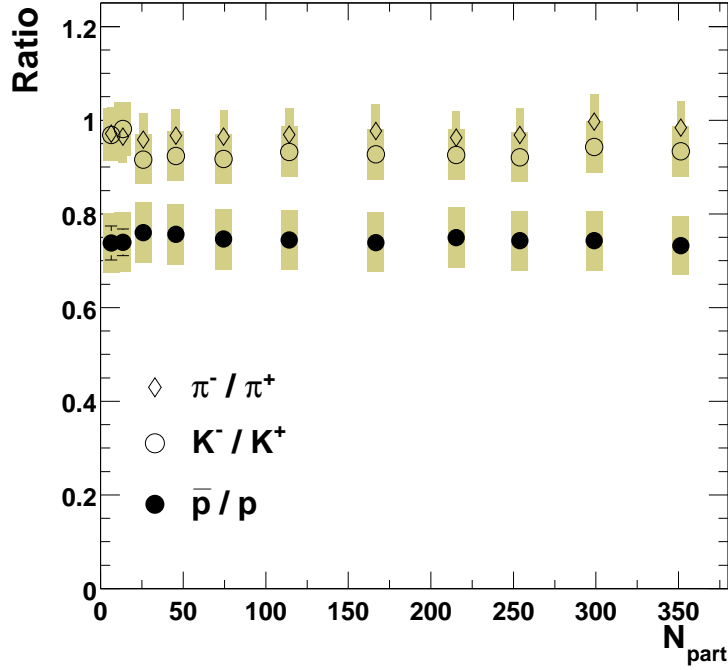


Figure 4.10: Centrality dependence of particle ratios for  $\pi^-/\pi^+$ ,  $K^-/K^+$ , and  $\bar{p}/p$  in Au+Au collisions at  $\sqrt{s_{NN}} = 200$  GeV. The error bars indicate the statistical errors. The shaded boxes on each data point are the systematic errors.

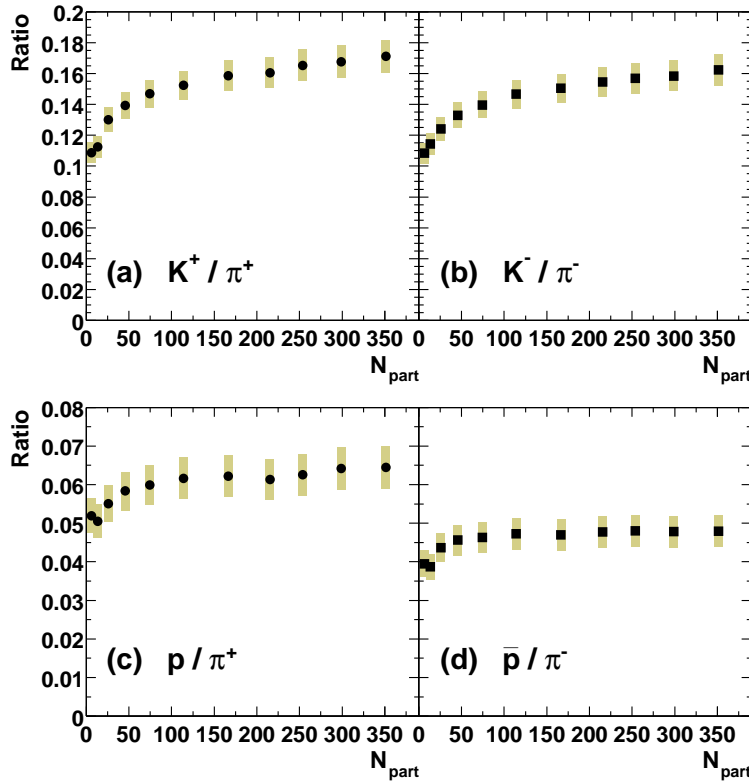


Figure 4.11: Centrality dependence of particle ratios for (a)  $K^+/\pi^+$ , (b)  $K^-/\pi^-$ , (c)  $p/\pi^+$ , and (d)  $\bar{p}/\pi^-$  in Au+Au collisions at  $\sqrt{s_{NN}} = 200$  GeV. The error bars indicate the statistical errors. The shaded boxes on each data point are the systematic errors.

# Chapter 5

## Discussions

As shown in Chapter 4, we have measured single particle spectra and yields for pions, kaons and protons in Au+Au at  $\sqrt{s_{\text{NN}}} = 200$  GeV. In this chapter, we discuss the collision dynamics using the experimental results. The particle ratios are sensitive to the chemical properties of the system and particle production mechanism, we discuss the chemical equilibrium from within statistical thermal model. The momentum spectra of pions, kaons, and protons are sensitive to the dynamical evolution of the system, we discuss the radial flow velocity  $\beta_T$  and the freeze-out temperature  $T_{\text{fo}}$  in Au + Au collisions at RHIC energies within the framework of the expansion source model. In the high- $p_T$  region, hard component is dominant. We also discuss binary collision scaling of  $p_T$  spectra to study hard component.

### 5.1 Particle Productions

#### 5.1.1 Particle Ratios

Hadron abundances reflect chemical composition of the system in heavy-ion collisions. It studied in the framework of statistical thermal model.

As is shown in Figure 4.7 and Figure 4.10 (Section 4.3), the ratios of anti-particle/particle are all independent of  $p_T$  and  $N_{\text{part}}$  over the measured range. The statistical thermal model (discussed in more detail in next section) predicted [67] a baryon chemical potential of  $\mu_B = 29$  MeV and a freeze-out temperature of  $T_{\text{ch}} = 177$  MeV for central Au+Au collisions at 200 GeV. From these, the expected  $\bar{p}/p$  ratio is  $e^{-2\mu_B/T_{\text{ch}}} = 0.72$ , which agrees with our data (0.73).

### 5.1.2 Features of Chemical Equilibrium

As is described in Section 1.2.3, the particle ratios have been studied in term of chemical equilibrium. Figure 5.1 shows a comparison of the PHENIX particle ratios with those from PHOBOS [64], BRAHMS [65], and STAR [66] in Au+Au central collisions at  $\sqrt{s_{\text{NN}}} = 200$  GeV at mid-rapidity. The PHENIX anti-particle to particle ratios are consistent with other experimental results within the systematic uncertainties.

The particle ratios in central collisions at  $\sqrt{s_{\text{NN}}} = 200$  GeV have been analyzed with statistical thermal model [67]. The thermal parameters, chemical freeze-out temperature  $T_{\text{ch}} = 177 \pm 7$  MeV and baryon chemical potential  $\mu_B = 29 \pm 8$  MeV are extracted. The comparison between the PHENIX data at 200 GeV for 0–5% central and the thermal model prediction is shown in this figure and Table 5.1. There is a good agreement between data and the model. The small  $\mu_B$  is qualitatively consistent with our measurement of the number of net protons ( $\approx 5$ , see Section 4.2) in central Au+Au collisions at  $\sqrt{s_{\text{NN}}} = 200$  GeV at mid-rapidity.

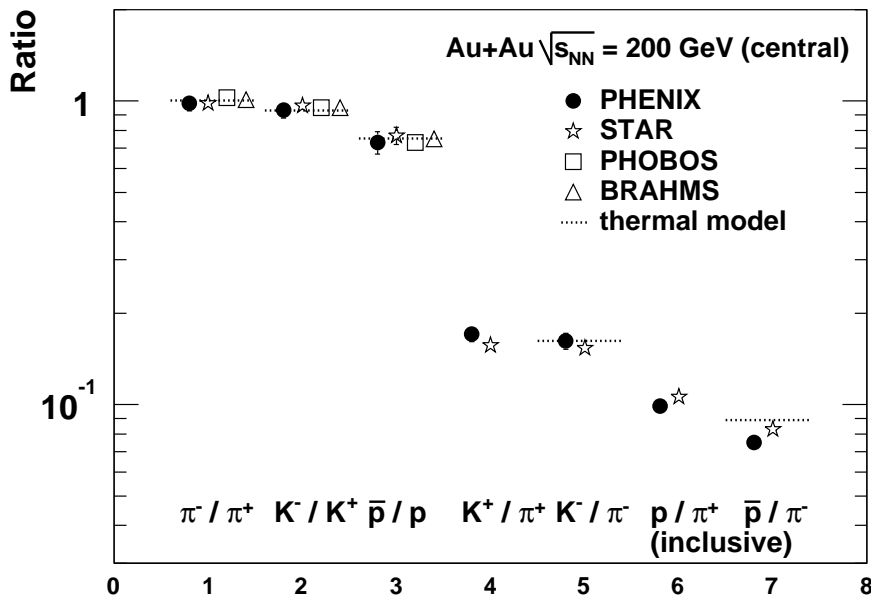


Figure 5.1: Comparison of PHENIX particle ratios with those of PHOBOS [64], BRAHMS [65], and STAR [66] results in Au+Au central collisions at  $\sqrt{s_{\text{NN}}} = 200$  GeV at mid-rapidity. The thermal model prediction [67] for 200 GeV Au+Au central collisions are also shown as dotted lines. The error bars on data indicate the systematic errors.

Particles	Ratio $\pm$ stat. $\pm$ sys.	Thermal Model
$\pi^-/\pi^+$	$0.984 \pm 0.004 \pm 0.057$	1.004
$K^-/K^+$	$0.933 \pm 0.007 \pm 0.054$	0.932
$\bar{p}/p$	$0.731 \pm 0.011 \pm 0.062$	
$\bar{p}/p$ (inclusive)	$0.747 \pm 0.007 \pm 0.046$	0.752
$K^+/\pi^+$	$0.171 \pm 0.001 \pm 0.010$	
$K^-/\pi^-$	$0.162 \pm 0.001 \pm 0.010$	0.147
$p/\pi^+$	$0.064 \pm 0.001 \pm 0.003$	
$p/\pi^+$ (inclusive)	$0.099 \pm 0.001 \pm 0.006$	
$\bar{p}/\pi^-$	$0.047 \pm 0.001 \pm 0.002$	
$\bar{p}/\pi^-$ (inclusive)	$0.075 \pm 0.001 \pm 0.004$	0.089

Table 5.1: Comparison between the data for the 0–5% central collisions and the thermal model prediction at  $\sqrt{s_{NN}} = 200$  GeV with  $T_{ch} = 177$  MeV and  $\mu_B = 29$  MeV [67].

### 5.1.3 Comparison with Theoretical Phase Boundary

A detailed analysis of experimental data in heavy ion collisions from SIS through AGS, SPS up to RHIC energy makes it clear that the statistical thermal model reproduces most of the measured hadron yields [68, 69].

The chemical freeze-out temperature, found from a thermal analysis of experimental data in Pb–Pb collisions at the SPS and in Au–Au collisions at RHIC energy is remarkably consistent with the critical temperature  $T_c \simeq 173 \pm 8$  MeV obtained [1] from lattice Monte-Carlo simulations of QCD at a vanishing net baryon density. Thus, the observed hadrons seem to be originating from a deconfined medium and the chemical composition of the system is most likely to be established during hadronization of the quark-gluon plasma. The observed coincidence of chemical and critical conditions in the QCD medium at the SPS and RHIC energy open the question if this property is also valid in heavy ion collisions at lower collision energies where the statistical order of the secondaries is phenomenologically well established.

Figure 5.2 shows the results on the position of the phase boundary that were obtained using the methods indicated above together with the freeze-out curve. The chemical freeze-out points at RHIC energy are indeed lying on the phase boundary.

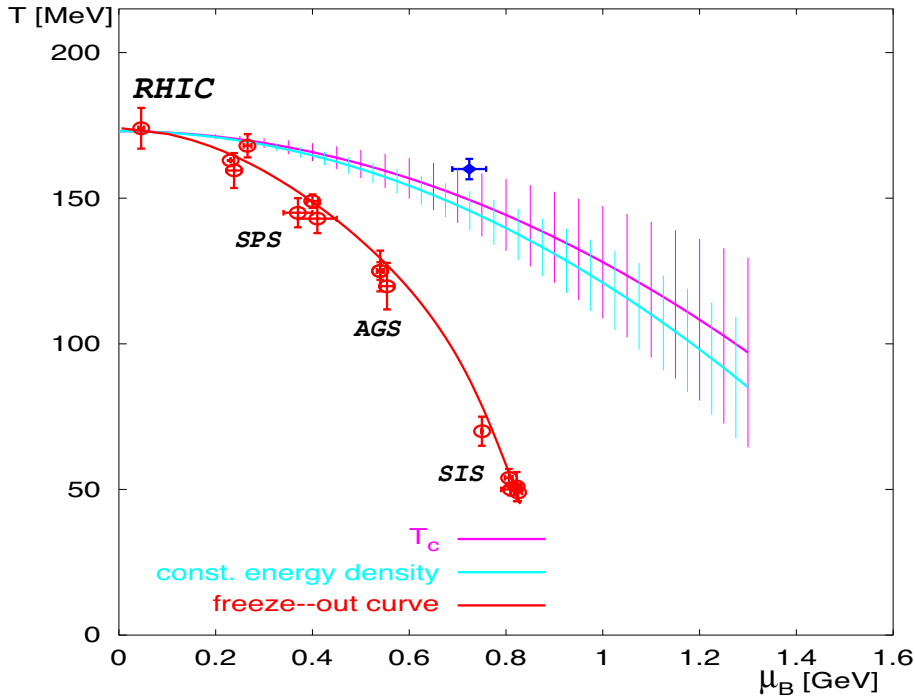


Figure 5.2: A compilation of chemical freeze-out parameters appropriate for A–A collisions at different energies with the phase boundary line. The freeze-out curve line represents the phenomenological condition of a chemical freeze-out at the fixed energy/particle  $\simeq 1.0$  GeV. The upper thin line represents the LGT results obtained in Ref. [70] and the lower thin line describes the conditions of constant energy density that was fixed at  $\mu = 0$ . The upper point with crossed error bars denotes the end-point of the crossover transition from Ref. [71]. This figure is taken from [69].

## 5.2 Transverse Distributions

### 5.2.1 $p_T$ Spectra of $\pi, K, p$

Hadron spectra reflect conditions late in the reaction, as well as the integrated effects of expansion from the beginning of the collision. Figure 5.3 shows the  $p_T$  distributions for pions, kaons, protons, and anti-protons. The top two plots are for the most central 0–5% collisions, and the bottom two are for the most peripheral 60–92% collisions. The spectra for positive particles are presented on the left, and those for negative particles on the right. For  $p_T < 1.5$  GeV/c in central events, the data show a clear mass dependence in the shapes of the spectra. The  $p$  and  $\bar{p}$  spectra have a shoulder-arm shape, the pion spectra have a concave shape, and the kaons fall exponentially. On the other hand, in the peripheral events, the mass dependences of the  $p_T$  spectra are less pronounced and the  $p_T$  spectra are more nearly parallel to each other. Another notable observation is that at  $p_T$  above

$\approx 2.0 \text{ GeV}/c$  in central events, the  $p$  and  $\bar{p}$  yields become comparable to the pion yields, which is also observed in 130 GeV Au+Au collisions [72, 73].

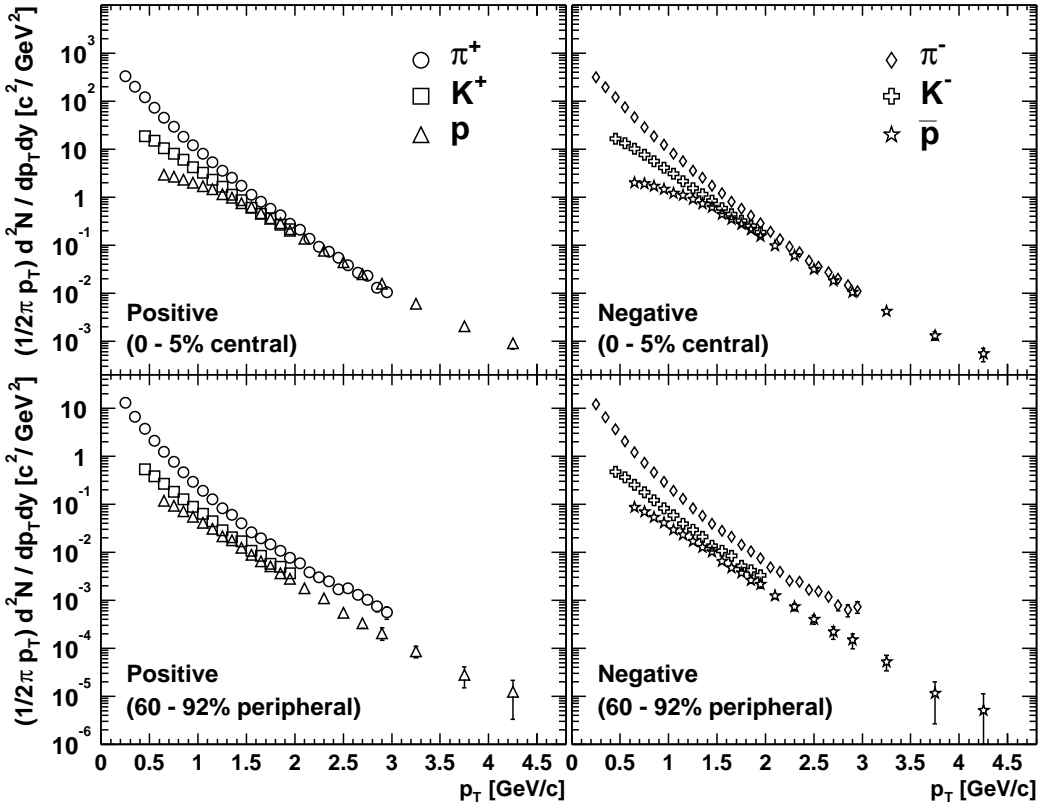


Figure 5.3: Transverse momentum distributions for pions, kaons, protons and anti-protons in Au+Au collisions at  $\sqrt{s_{\text{NN}}} = 200 \text{ GeV}$ . The top two figures show  $p_T$  spectra for the most central 0–5% collisions. The bottom two are for the most peripheral 60–92% collisions.

### 5.2.2 $p/\pi$ ratios

One of the most unexpected observations in heavy-ion collision at RHIC is the large enhancement of baryons relative to pions at intermediate  $p_T \approx 2\text{--}5 \text{ GeV}/c$ . Figure 5.4 show the  $p/\pi$  and  $\bar{p}/\pi$  ratios as a function of  $p_T$  for the 0–10%, 20–30% and 60–92% centrality bins. In this figure, the results of  $p/\pi^0$  and  $\bar{p}/\pi^0$  [32] are presented above  $1.5 \text{ GeV}/c$  and overlaid on the results of  $p/\pi^+$  and  $\bar{p}/\pi^-$ , respectively. The absolutely normalized  $p_T$  spectra of charged and neutral pions agree within 5–15%. The error bars on the PHENIX data points in the figure show the quadratic sum of the statistical errors and the point-to-point systematic errors. The ratios increase rapidly at low  $p_T$ , but saturate at different

values of  $p_T$  which increase from peripheral to central collisions. In central collisions, the yields of both protons and anti-protons are comparable to that of pions for  $p_T > 2 \text{ GeV}/c$ .

For comparison, the corresponding ratios for  $p_T > 2 \text{ GeV}/c$  observed in  $p + p$  collisions at lower energies ( $\sqrt{s_{NN}} = 53 \text{ GeV}$ ) [74], and in gluon jets produced in  $e^+ + e^-$  collisions [75], are also shown in the figure. At high- $p_T$  region, those ratios are compatible with the peripheral Au+Au collisions in the uncertainties. In hard-scattering processes described by pQCD, the  $p/\pi$  and  $\bar{p}/\pi$  ratios at high- $p_T$  are determined by the fragmentation of energetic partons, independent of the initial colliding system, which is seen as agreement between  $p + p$  and  $e^+ + e^-$  collisions.

Thus, the clear increase in the  $p/\pi$  ( $\bar{p}/\pi$ ) ratios at high  $p_T$  from  $p + p$  and peripheral to the mid-central and to the central Au+Au collisions requires ingredients other than pQCD.

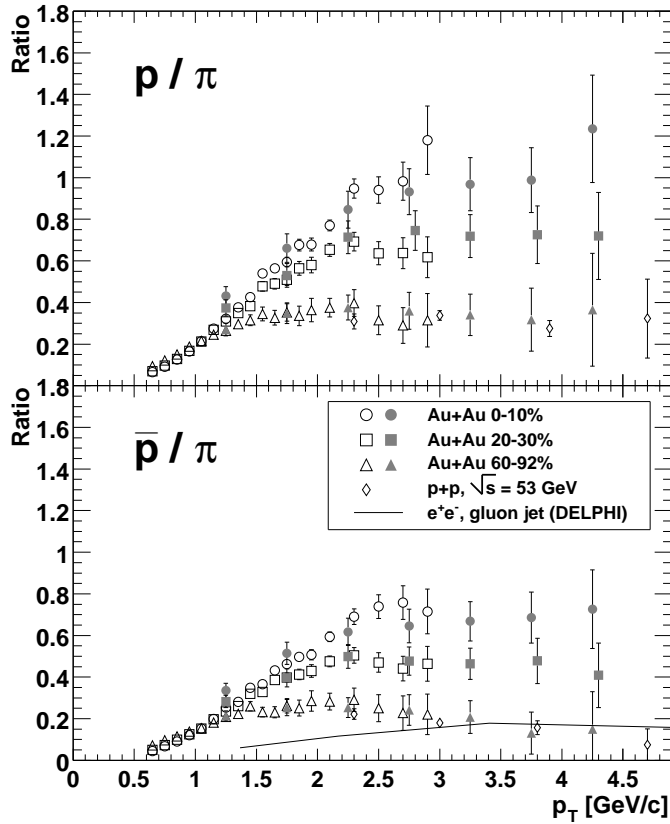


Figure 5.4: Proton/pion (top) and anti-proton/pion (bottom) ratios for central 0–10%, mid-central 20–30% and peripheral 60–92% in Au+Au collisions at  $\sqrt{s_{NN}} = 200 \text{ GeV}$ . Open (filled) points are for charged (neutral) pions. The data at  $\sqrt{s} = 53 \text{ GeV}$   $p + p$  collisions [74] are also shown. The solid line is the  $(\bar{p} + p)/(\pi^+ + \pi^-)$  ratio measured in gluon jets [75].

### 5.2.3 Feature of Thermal Equilibrium: $m_T$ Spectra

In order to quantify the observed particle mass dependence of the  $p_T$  spectra shape and their centrality dependence, the transverse mass spectra for identified charged hadrons are presented here. From former studies at lower beam energies, it is known that the invariant differential cross sections in  $p + p$ ,  $p + A$ , and  $A + A$  collisions generally show a shape of an exponential in  $m_T - m_0$  (see Section 1.2.1). For an  $m_T$  spectrum with an exponential shape, one can parameterize it as follows:

$$\frac{1}{2\pi m_T} \frac{d^2N}{dm_T dy} = \frac{1}{2\pi T(T + m_0)} \cdot A \cdot \exp\left(-\frac{m_T - m_0}{T}\right), \quad (5.1)$$

where  $T$  is referred to as the inverse slope parameter, and  $A$  is a normalization parameter which contains information on  $dN/dy$ . In Figure 5.5,  $m_T$  distributions for  $\pi^\pm$ ,  $K^\pm$ ,  $p$  and  $\bar{p}$  for central 0–5% (top panels), mid-central 40–50% (middle panels) and peripheral 60–92% (bottom panels) collisions are shown. The spectra for positive particles are on the left and for negative particles are on the right. The solid lines overlaid on each spectra are the fit results using Eq. 5.1. The error bars are statistical only. As seen in Figure 5.5, all the  $m_T$  spectra display an exponential shape in the low  $m_T$  region. However, at higher  $m_T$ , the spectra become less steep, which corresponds to a power-law behavior in  $p_T$ . Thus, the inverse slope parameter in Eq. 5.1 depends on the fitting range. In this analysis, the fits cover the range  $0.2 – 1.0 \text{ GeV}/c^2$  for pions and  $0.1 – 1.0 \text{ GeV}/c^2$  for kaons, protons, and anti-protons in  $m_T - m_0$ . The low  $m_T$  region ( $m_T - m_0 < 0.2 \text{ GeV}/c^2$ ) for pions is excluded from the fit to eliminate the contributions from resonance decays. The inverse slope parameters for each particle species in the three centrality bins are summarized in Figure 5.6 and in Table 5.2. The inverse slope parameters increase with increasing particle mass in all centrality bins. This increase for central collisions is more rapid for heavier particles.

Such a behavior was derived, under certain conditions, by E. Schnedermann *et al.* [13] for central collisions and by T. Csörgő *et al.* [76] for non-central heavy-ion collisions:

$$T = T_0 + m\langle u_t \rangle^2, \quad (5.2)$$

where  $T_0$  is a freeze-out temperature and  $\langle u_t \rangle$  is a measure of the strength of the (average radial) transverse flow. The dotted lines in Figure 5.6 represent a linear fit of the results from each centrality bin as a function of mass using Eq. 5.2. The fit parameters for positive and negative particles are shown in Table 5.2. It indicates, that the linear extrapolation of the slope parameter  $T(m)$  to zero mass has the same intercept parameters  $T_0$  in all the

centrality classes, indicating that the freeze-out temperature is approximately independent of the centrality. On the other hand,  $\langle u_t \rangle$ , the strength of the average transverse flow is increasing with increasing centrality, supporting the hydrodynamic picture.

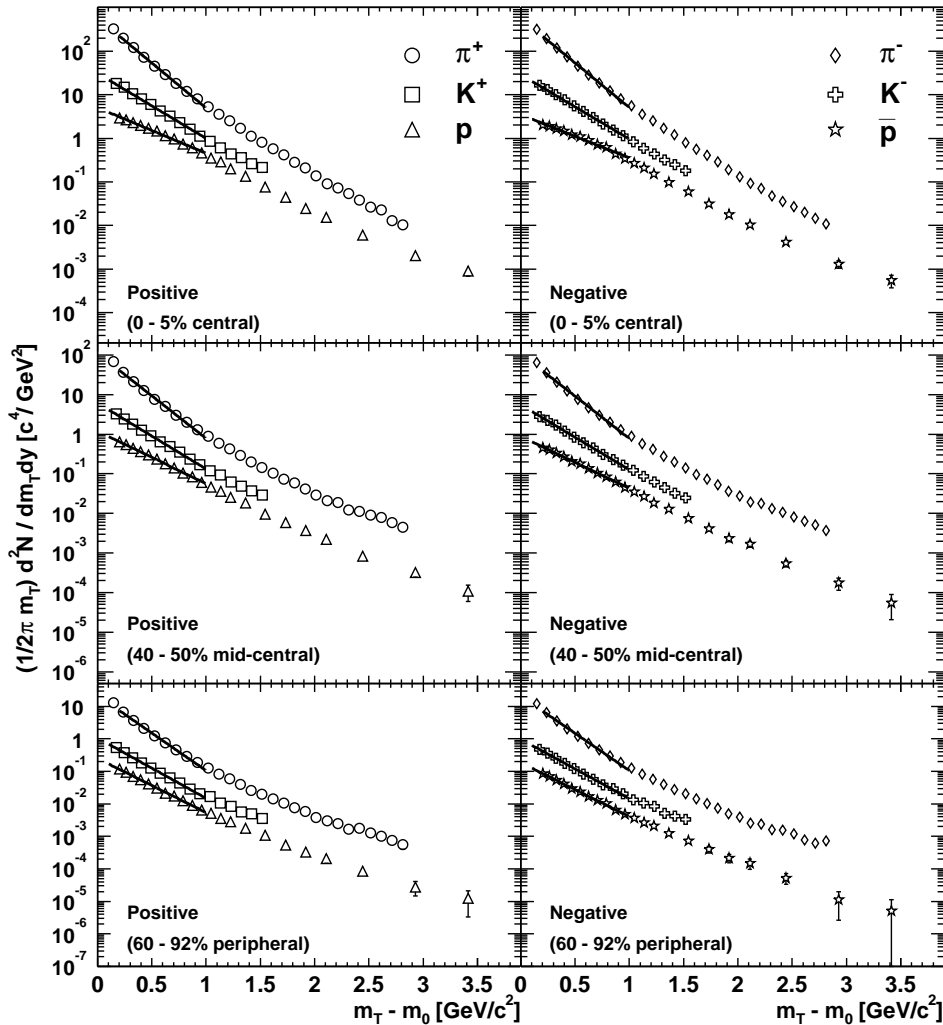


Figure 5.5: Transverse mass distributions for  $\pi^\pm$ ,  $K^\pm$ , protons and anti-protons for central 0–5% (top panels), mid-central 40–50% (middle panels) and peripheral 60–92% (bottom panels) in Au+Au collisions at  $\sqrt{s_{\text{NN}}} = 200$  GeV. The lines on each spectra are the fitted results using  $m_T$  exponential function. The fit ranges are  $0.2 - 1.0 \text{ GeV}/c^2$  for pions and  $0.1 - 1.0 \text{ GeV}/c^2$  for kaons, protons, and anti-protons in  $m_T - m_0$ . The error bars are statistical errors only.

	$\pi^+$	$K^+$	$p$	$T_0^{(+)}$	$\langle u_t \rangle^{(+)}$
0–5%	$210.2 \pm 0.8$	$290.2 \pm 2.2$	$414.8 \pm 7.5$	$177.0 \pm 1.2$	$0.48 \pm 0.07$
40–50%	$201.9 \pm 0.8$	$260.6 \pm 2.4$	$326.3 \pm 5.9$	$179.5 \pm 1.2$	$0.40 \pm 0.07$
60–92%	$187.8 \pm 0.7$	$233.9 \pm 2.6$	$260.7 \pm 5.4$	$173.1 \pm 1.2$	$0.32 \pm 0.07$
	$\pi^-$	$K^-$	$\bar{p}$	$T_0^{(-)}$	$\langle u_t \rangle^{(-)}$
0–5%	$211.9 \pm 0.7$	$293.8 \pm 2.2$	$437.9 \pm 8.5$	$177.3 \pm 1.2$	$0.49 \pm 0.07$
40–50%	$203.0 \pm 0.7$	$265.1 \pm 2.3$	$330.5 \pm 6.4$	$179.6 \pm 1.2$	$0.41 \pm 0.07$
60–92%	$189.2 \pm 0.7$	$237.4 \pm 2.6$	$262.1 \pm 5.9$	$173.7 \pm 1.1$	$0.33 \pm 0.07$

Table 5.2: (Top) Inverse slope parameters for  $\pi$ ,  $K$ ,  $p$  and  $\bar{p}$  for the 0–5%, 40–50% and 60–92% centrality bins, in units of  $\text{MeV}/c^2$ . The errors are statistical only. (Bottom) The extracted fit parameters of the freeze-out temperature ( $T_0$ ) in units of  $\text{MeV}/c^2$  and the measure of the strength of the average radial transverse flow ( $\langle u_t \rangle$ ) using Eq. 5.2. The fit results shown here are for positive and negative particles, as denoted in the superscripts, and for three different centrality bins.

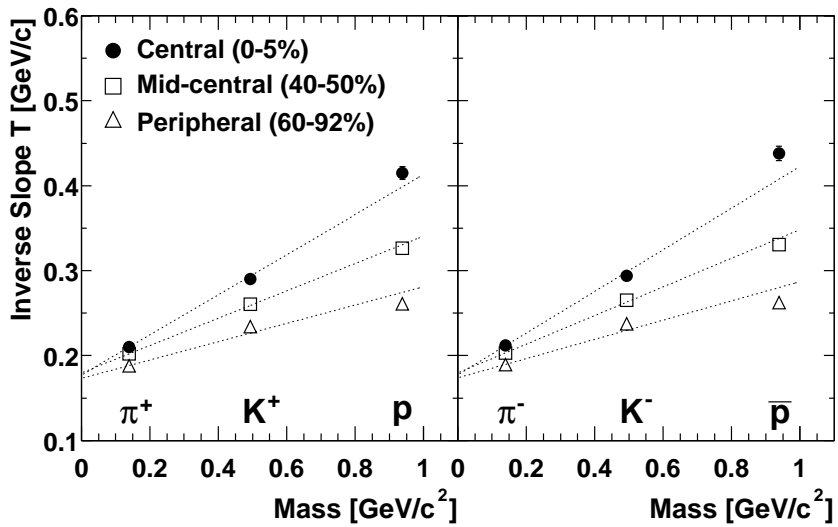


Figure 5.6: Mass and centrality dependence of inverse slope parameters  $T$  in  $m_T$  spectra for positive (left) and negative (right) particles in Au+Au collisions at  $\sqrt{s_{\text{NN}}} = 200$  GeV. The fit ranges are  $0.2 - 1.0 \text{ GeV}/c^2$  for pions and  $0.1 - 1.0 \text{ GeV}/c^2$  for kaons, protons, and anti-protons in  $m_T - m_0$ . The dotted lines represent a linear fit of the results from each centrality bin as a function of mass using Eq. 5.2.

## 5.3 Collective Expansion Model

Up to  $p_T \sim 1.5 - 2.0 \text{ GeV}/c$ , it has been found that hydrodynamic models can reproduce the data well for  $\pi^\pm, K^\pm, p$  and  $\bar{p}$  spectra at 130 GeV [73], and also at 200 GeV in Au+Au collisions [77, 79]. These models assume thermal equilibrium and that the created particles are affected by a common transverse (radial) flow velocity  $\beta_T$  and freeze-out (stop interacting) at a temperature  $T_{\text{fo}}$  with a fixed initial condition governed by the equation of state (EOS) of matter.

### 5.3.1 Blast-wave Parametrization

A sophisticated approach to understanding the particle spectra is to compare to a functional form which describes a boosted thermal source, based on relativistic hydrodynamics [13]. This is a two-parameter model, termed the “blast-wave” model, in which the surface radial flow velocity ( $\beta_T$ ) and freeze-out temperature ( $T_{\text{fo}}$ ) are extracted from the invariant cross section data according to the equation

$$\frac{dN}{m_T dm_T} \propto \int_0^R f(r) r dr m_T I_0\left(\frac{p_T \sinh \rho}{T_{\text{fo}}}\right) K_1\left(\frac{m_T \cosh \rho}{T_{\text{fo}}}\right), \quad (5.3)$$

where  $I_0$  and  $K_1$  represent modified Bessel functions with  $\rho$  being the transverse boost which depends on the radial position according to

$$\rho(r) = \tanh^{-1}(\beta_T) \cdot r/R \quad (5.4)$$

Here the parameter  $R$  is the maximum radius of the expanding source at freeze-out. The function  $f(r)$  represent the density which is taken to be uniform in this calculation (i.e.,  $f(r) = 1$ ). The radial flow velocity profile  $\beta_r(r)$  is defined as  $\beta_r(r) = \tanh \rho$  (Figure 5.7),

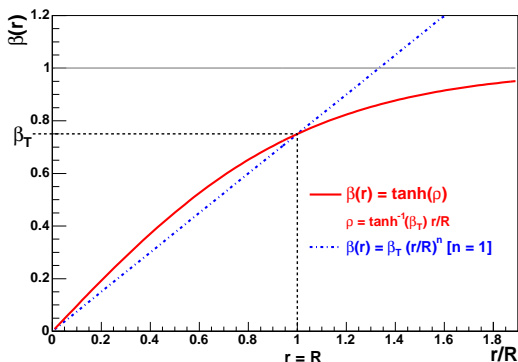


Figure 5.7: The definition of transverse flow velocity profile:  $\beta(r) = \tanh(\rho) = \tanh(\tanh^{-1} \beta_T \cdot r/R)$  : solid line (red),  $\beta(r) = \beta_T \cdot (r/R)^n$  [n=1 : dashed line (blue)]

the average of the radial flow velocity is calculated as following equation,

$$\langle \beta_T \rangle = \frac{\int_0^R \beta_r(r) r dr}{\int_0^R r dr} = \frac{\int_0^R \tanh(\rho r/R) r dr}{\int_0^R r dr} = \frac{\int_0^R \tanh(\tanh^{-1}(\beta_T)r/R) r dr}{\int_0^R r dr}. \quad (5.5)$$

### 5.3.2 Previous Studies

To study the parameter correlations, we make a grid of  $(T_{\text{fo}}, \beta_T)$  pairs and then we perform a chi-squared minimization for each particle type. The first fit attempt is performed simultaneously for the six particle species  $\pi^\pm, K^\pm, p$  and  $\bar{p}$  in the range  $(m_T - m_0) < 1.0 \text{ GeV}/c^2$ . In addition to this upper limit in the fit, the fit range for pion includes a lower limit of  $p_T > 0.5 \text{ GeV}/c$  to avoid the resonance contribution to the low- $p_T$  region.

The two-parameter  $T_{\text{fo}}$  vs  $\beta_T$  fit results obtained in this analysis for the most central 0–5% collisions are shown in Figure 5.8. The contour lines are one sigma steps. Shown in the lower panels of the figure are the  $\chi^2$  contour levels obtained from fitting each particle spectrum separately. We observed that the parameter  $T_{\text{fo}}$  and  $\beta_T$  are anti-correlated, the different particles have different proffered parameter space and different sensitivity to the parameters. For example, the heavier particles are more sensitive to the radial flow velocity than to the kinetic freeze-out temperature. The contours for the six particle species do overlap at a single common point at the  $3\sigma$  level.

To study the resonance contribution at low- $p_T$  region, we change the lower limit of  $p_T$  for pions. Figure 5.9 shows the fit results for the peripheral collisions. Figure 5.9a is  $p_T > 0.5 \text{ GeV}/c$  and Figure 5.9b is  $p_T > 0.8 \text{ GeV}/c$  for pion. Due to large contribution of resonance, the best fit values are changed by fitting range.

### 5.3.3 Proposed Analysis and Results

Since the experimental data include the decay of resonance, we add the decay of mesonic ( $\rho, \eta, \omega, K^*, \dots$ ) and baryonic ( $\Delta, \Lambda, \Sigma, \dots$ ) resonance effects as follows:

- 1) Generate resonances with the transverse momentum distribution determined by each combinations of  $T_{\text{fo}}$  and  $\beta_T$ .
- 2) Decay them using Monte Carlo simulation, and obtain  $\pi^\pm, K^\pm, p$  and  $\bar{p}$  distribution.
- 3) Merge all particles, where the particle abundance is calculated with chemical parameters ( $T_{\text{ch}} = 177 \text{ MeV}, \mu_B = 29 \text{ MeV}$ ) [67].

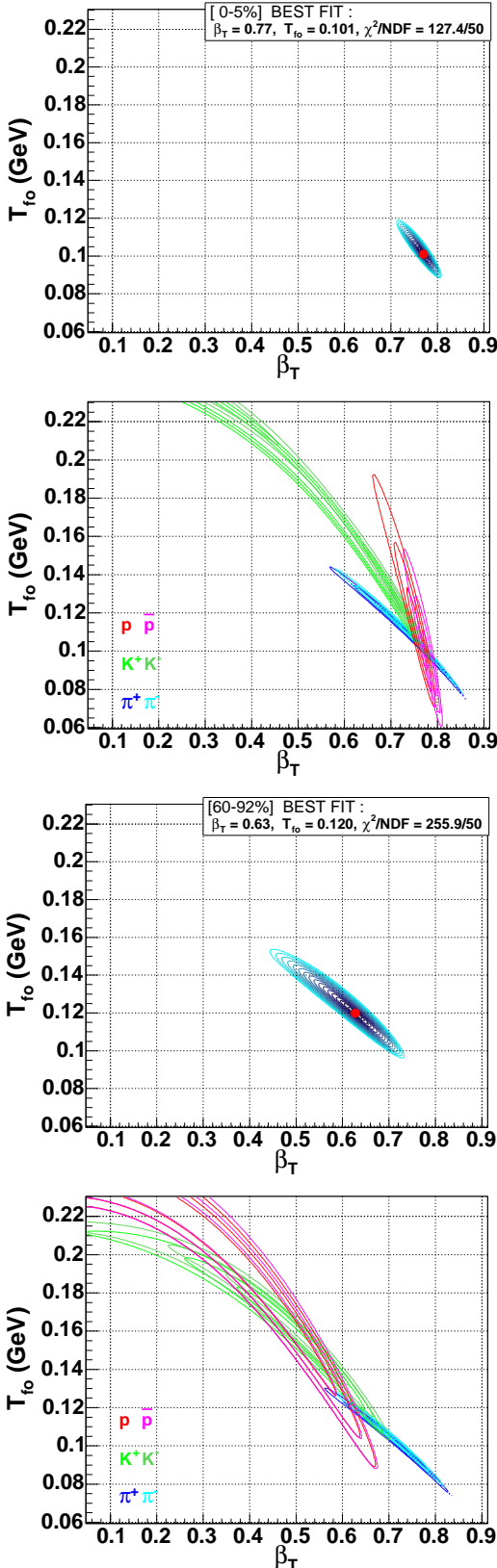


Figure 5.8: Contour plot for the most central 0-5% collisions. The contour lines are one sigma steps. The upper plot is from a simultaneous fit with the best value shown as the point. The lower plot is from independent fits for the six particle spectra.

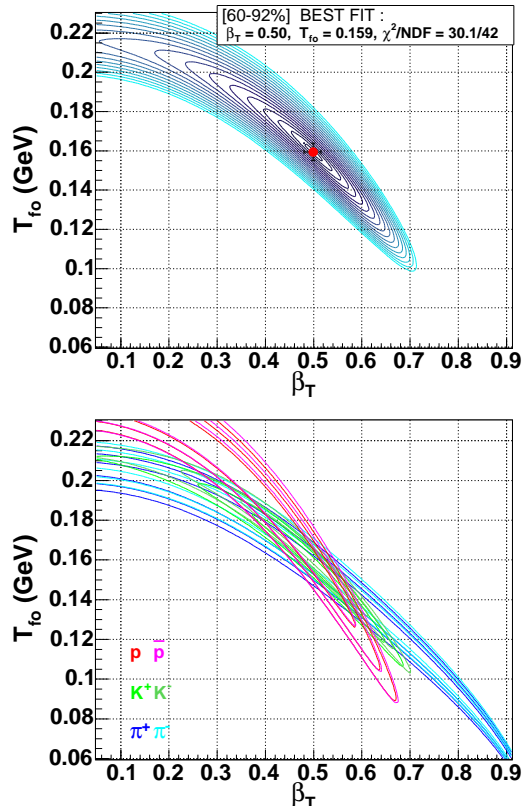


Figure 5.9: Contour plot for the most peripheral collisions. The contour lines are one sigma steps. The right plot(b) is set a lower limit of  $p_T > 0.8$  GeV/c for pion.

Figure 5.10 shows the fro-chart of model fit with resonance feed down. As shown in Figure 5.12, we now succeed in reproducing the spectrum with the freeze-out temperature  $T_{\text{fo}}$  and radial flow velocity  $\beta_T$ . The kinematics of the resonance decays result in very steeply dropping daughter pion spectra and raise considerably the total pion yield at low- $p_T$  region.

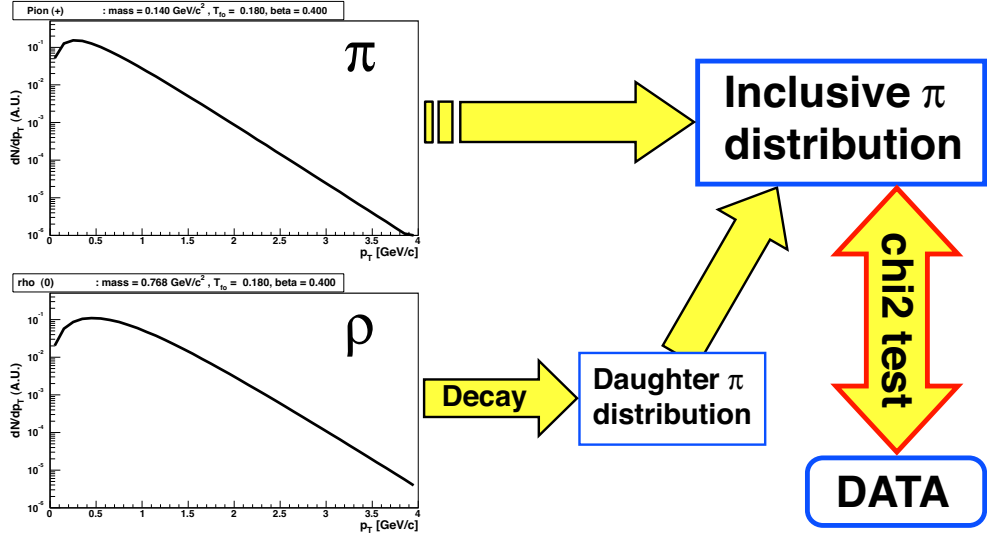


Figure 5.10: Fro-chart of model fit with resonance feed down.

The two-parameter  $T_{\text{fo}}$  vs  $\beta_T$  fit results obtained in this analysis for the most central 0–5% collisions are shown in Figure 5.13. The contour lines are one sigma steps. Shown in the lower panels of the figure are the  $\chi^2$  contour levels obtained from fitting each particle spectrum separately. The contours for the six particle species do overlap at a single common point at the  $3\sigma$  level. To find the values of the parameters at this overlap point, a simultaneous fit for the six single particle spectra ( $\pi^\pm, K^\pm$ , and  $p, \bar{p}$ ) was done which converges to a best fit value of  $T_{\text{fo}} = 107.8^{+3.7}_{-3.3}$  MeV and  $\beta_T = 0.773^{+0.0055}_{-0.0065}$ .

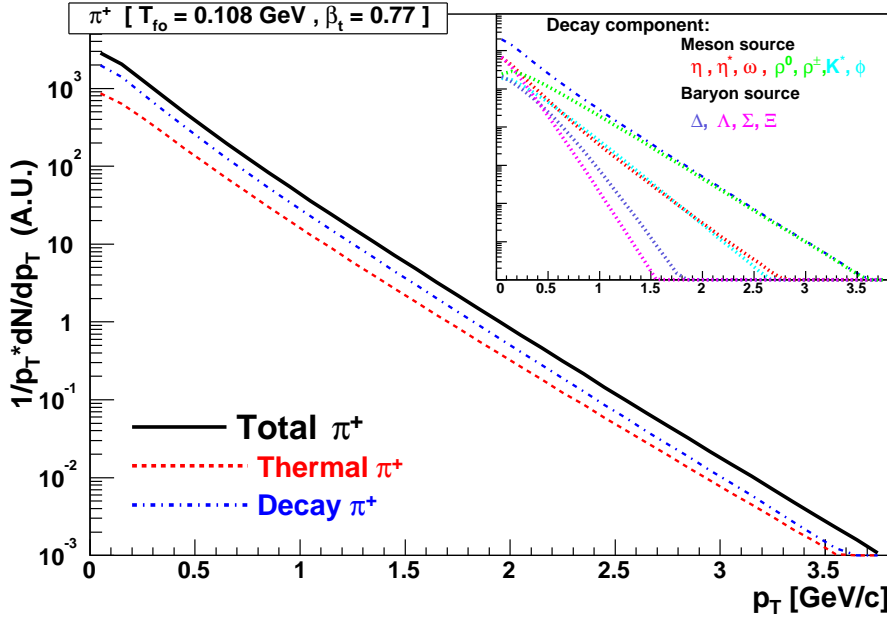


Figure 5.11: The total  $\pi^+$  spectrum from a thermal source with the temperature  $T_{\text{fo}} = 108 \text{ MeV}$  and flow velocity  $\beta_T = 0.77$ . The thermal  $\pi^+$  (dashed, red) and the decay daughter  $\pi^+$  (dash-dotted, blue) add up to the total spectrum. The upper right figure show the decay component of mesonic and baryonic resonance.

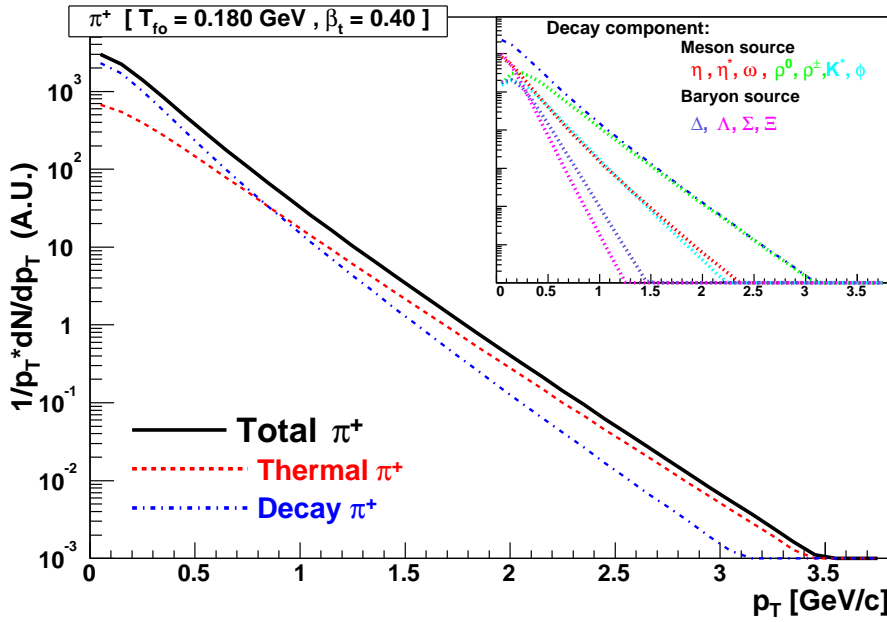


Figure 5.12: The total  $\pi^+$  spectrum from a thermal source with the temperature  $T_{\text{fo}} = 180 \text{ MeV}$  and flow velocity  $\beta_T = 0.40$ . The thermal  $\pi^+$  (dashed, red) and the decay daughter  $\pi^+$  (dash-dotted, blue) add up to the total spectrum. The upper right figure show the decay component of mesonic and baryonic resonance.

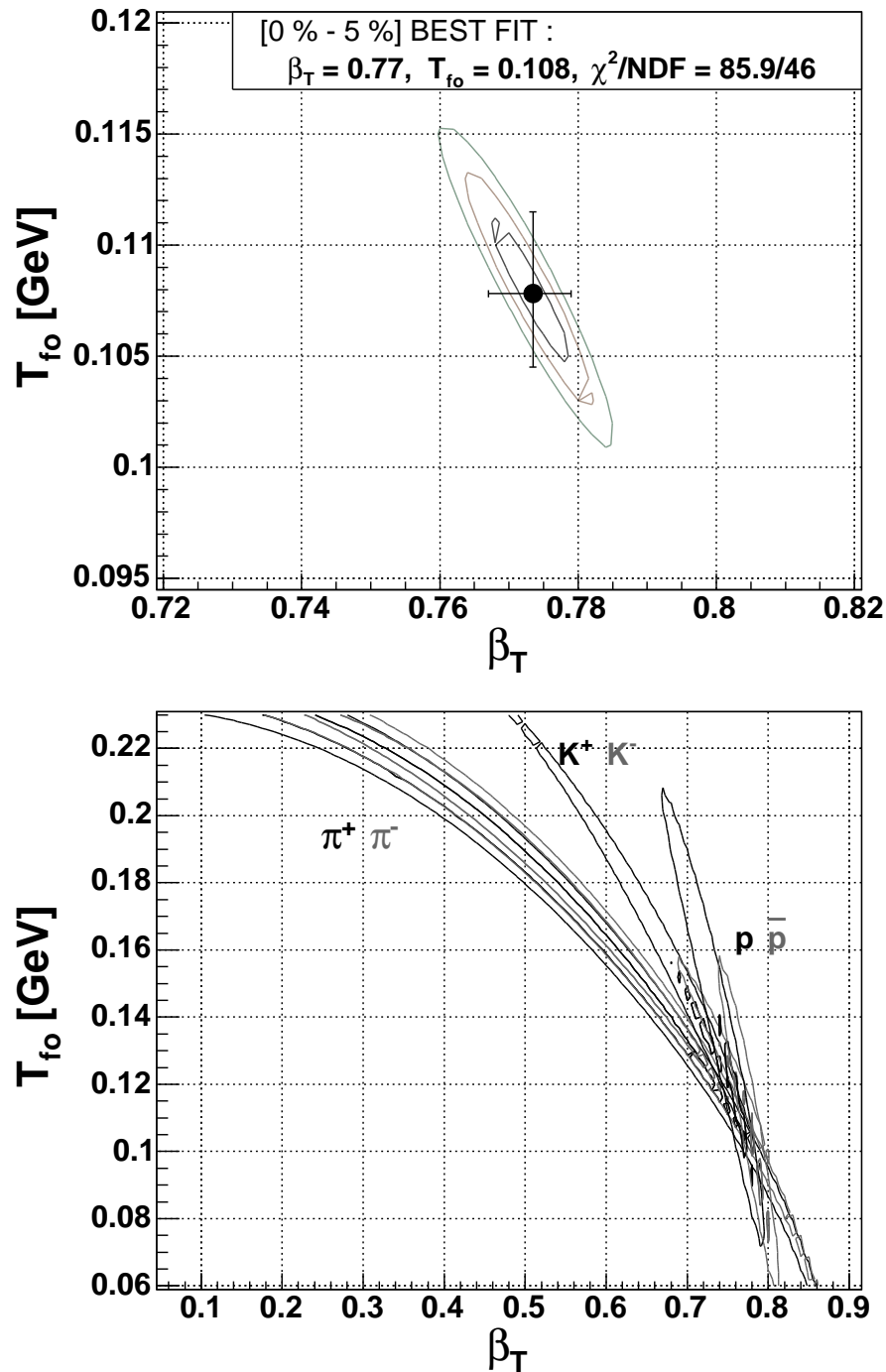


Figure 5.13: Contour plot for the most central 0-5% collisions. The contour lines are one sigma steps. The upper plot is from a simultaneous fit with the best value shown as the point. The lower plot is from independent fits for the six particle spectra.

Figure 5.14 shows  $\chi^2$  contours on the parameter space of the freeze-out temperature  $T_{\text{fo}}$  and radial flow velocity  $\langle \beta_T \rangle$  for each centrality. For the most central 0–5% collisions, we obtain freeze-out temperature  $T_{\text{fo}} = 108$  MeV and average flow velocity  $\langle \beta_T \rangle = 0.57$  (Surface flow velocity is  $\beta_T = 0.77$ ). Figure 5.15 shows the centrality dependence of the  $T_{\text{fo}}$  and  $\langle \beta_T \rangle$ . The value for  $T_{\text{fo}}$ ,  $\beta_T$  and  $\langle \beta_T \rangle$  are tabulated in Table 5.3. It is found that  $T_{\text{fo}}$  decreases and  $\beta_T$  increases from the most peripheral to mid-central collisions, and appears to saturate in the central collisions. The behavior of  $\beta_T$  is in accordance with a collective expansion picture.

Centrality	$T_{\text{fo}}$ [MeV]	$\beta_T$	$\langle \beta_T \rangle$	$\chi^2/NDF$
0- 5%	$107.8^{+3.7}_{-3.3}$	$0.773^{+0.0055}_{-0.0065}$	$0.574^{+0.0041}_{-0.0048}$	85.9/46
5-10%	$109.8^{+3.7}_{-3.3}$	$0.769^{+0.0055}_{-0.0065}$	$0.570^{+0.0041}_{-0.0048}$	75.7/46
10-15%	$113.3^{+3.2}_{-2.8}$	$0.763^{+0.006}_{-0.006}$	$0.564^{+0.0044}_{-0.0044}$	84.2/46
15-20%	$116.5^{+4.0}_{-4.0}$	$0.754^{+0.007}_{-0.007}$	$0.555^{+0.0051}_{-0.0051}$	62.6/46
20-30%	$123.0^{+3.5}_{-3.5}$	$0.738^{+0.007}_{-0.007}$	$0.541^{+0.0051}_{-0.0051}$	69.2/46
30-40%	$132^{+2}_{-2}$	$0.71^{+0.005}_{-0.005}$	$0.515^{+0.0036}_{-0.0036}$	81.7/46
40-50%	$142^{+2}_{-4}$	$0.67^{+0.01}_{-0.005}$	$0.481^{+0.0072}_{-0.0036}$	70.0/46
50-60%	$153^{+5}_{-5}$	$0.614^{+0.016}_{-0.014}$	$0.434^{+0.0113}_{-0.0099}$	59.9/46
60-70%	$163^{+7}_{-7}$	$0.555^{+0.025}_{-0.025}$	$0.388^{+0.0175}_{-0.0175}$	47.3/46
70-80%	$168^{+10}_{-10}$	$0.497^{+0.042}_{-0.037}$	$0.344^{+0.0295}_{-0.0258}$	39.7/46
80-92%	$179^{+13}_{-15}$	$0.399^{+0.071}_{-0.079}$	$0.272^{+0.0484}_{-0.0539}$	59.0/46
0-10%	$108.9^{+2.6}_{-2.4}$	$0.771^{+0.003}_{-0.004}$	$0.572^{+0.0026}_{-0.0033}$	148.0/46
60-92%	$167^{+7}_{-7}$	$0.525^{+0.025}_{-0.025}$	$0.365^{+0.0174}_{-0.0174}$	47.1/46

Table 5.3: Fitting results for each centrality

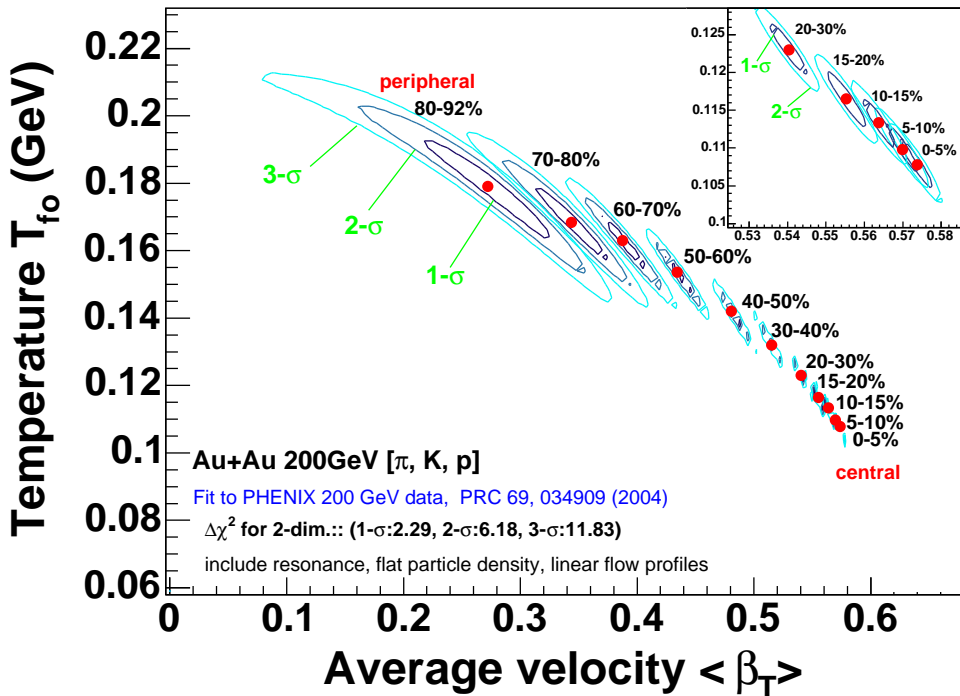


Figure 5.14: Contour plot Freeze-out temperature  $T_{\text{fo}}$  and radial flow velocity  $\beta_T$

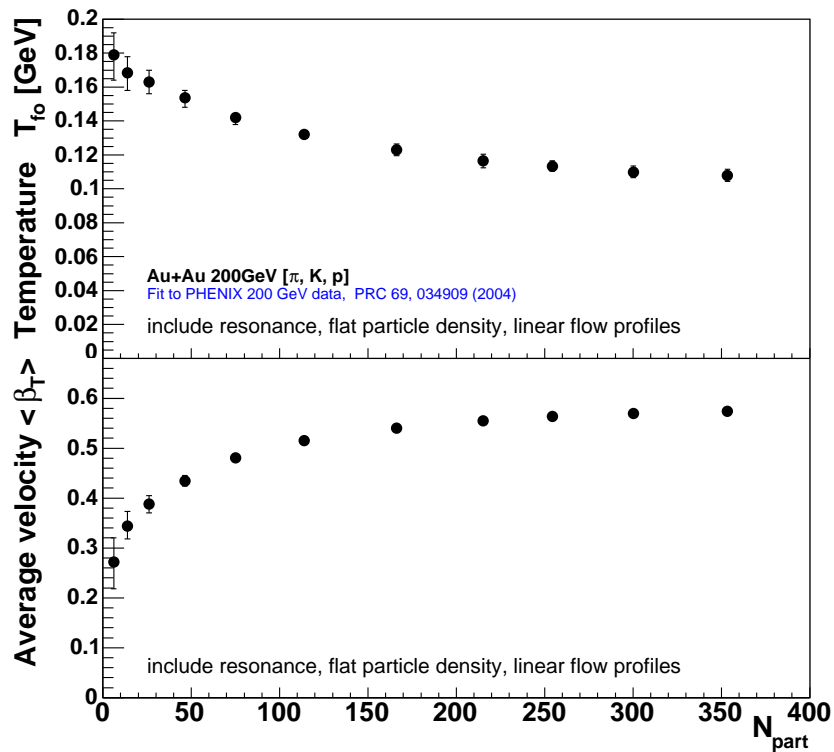


Figure 5.15: Freeze-out temperature  $T_{\text{fo}}$  (top) and radial flow velocity  $\beta_T$  (bottom) as a function of  $N_{\text{part}}$ . The error is statistical only.

The results are plotted together with the spectra in Figure 5.16. Hydrodynamical fits in the range  $(m_T - m_0) < 1\text{GeV}$  (solid line) are extrapolated over the entire transverse kinematic energy range (dashed line) for comparison to the data.

By this approach, we achieve following things,

- Unified view of transverse distribution by thermal and chemical equilibrium.
- Realize the spectrum component of thermal source and decay resonance.
- Observed strong adiabatic expansion in central collisions.

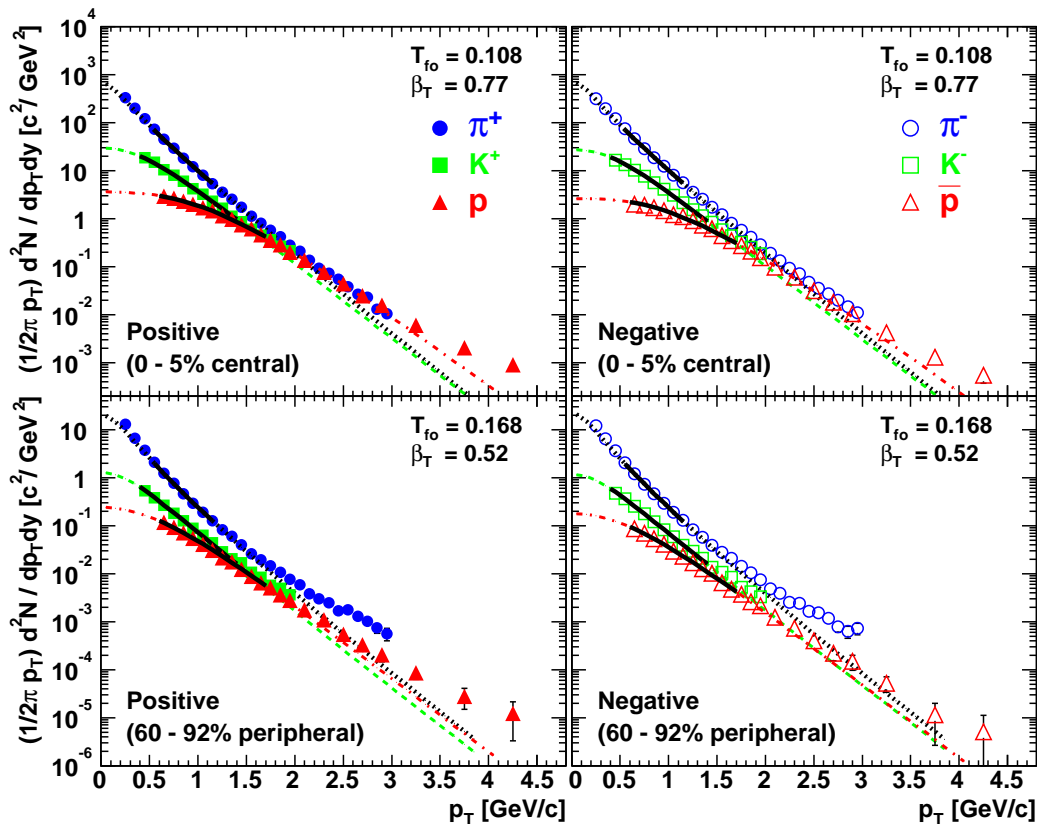


Figure 5.16: The top two figures show  $p_T$  spectra for the most central 0–5% collisions. The bottom two are for the most peripheral 60–92% collisions. Hydrodynamical fits in the range  $(m_T - m_0) < 1\text{GeV}$  (solid line) are extrapolated over the entire transverse kinematic energy range (dashed line) for comparison to the data.

## 5.4 Beyond the Thermal Behavior: Hard Component

### 5.4.1 Suppression of High $p_T$ Hadrons

As discussed in Section 1.3, the spectra of high- $p_T$  hadrons potentially provide a direct probe of the properties of the initial state in heavy-ion collision.

One of the most striking features in Au+Au collisions at RHIC is that  $\pi^0$  and non-identified hadron yields at  $p_T > 2 \text{ GeV}/c$  in central collisions are suppressed with respect to the number of nucleon-nucleon binary collisions  $N_{\text{coll}}$  scaled by  $p + p$  and peripheral Au+Au results [30, 31, 32]. Moreover, the suppression of  $\pi^0$  is stronger than that for non-identified charged hadrons [30], and the yields of protons and anti-protons in central collisions are comparable to that of pions around  $2 \text{ GeV}/c$  (see Section 5.2.1). The enhancement of the  $p/\pi$  ( $\bar{p}/\pi$ ) ratio in central collisions at intermediate  $p_T$  region ( $2.0 - 4.5 \text{ GeV}/c$ ), which was presented in Section 5.2.2, is consistent with the above observations. These results strongly suggest significant contributions of proton and anti-proton yield to the total particle composition at this intermediate  $p_T$  region.

We present here the  $N_{\text{coll}}$  scaling behavior for charged pions, kaons and protons (anti-protons) in order to quantify the particle composition at intermediate  $p_T$ . The medium modifications of hadron spectra are often quantified by the *nuclear modification factor*  $R_{AA}$  which discuss in Section 1.3.2. Figure 5.17 shows the central (0–10%) to peripheral (60–92%) ratio for  $N_{\text{coll}}$  scaled  $p_T$  spectra of  $(\bar{p} + p)/2$ , kaons, charged pions and  $\pi^0$ . We define  $R_{\text{CP}}$  as:

$$R_{\text{CP}} = \frac{\text{Yield}^{0-10\%}/\langle N_{\text{coll}}^{0-10\%} \rangle}{\text{Yield}^{60-92\%}/\langle N_{\text{coll}}^{60-92\%} \rangle}. \quad (5.6)$$

The peripheral 60–92% Au+Au spectrum is used as an approximation of the yields in  $p + p$  collisions, based on the experimental fact that the peripheral spectra scale with  $N_{\text{coll}}$  by using the yields in  $p + p$  collisions measured by PHENIX [23, 32]. Thus the meaning of the  $R_{\text{CP}}$  is expected to be the same as  $R_{AA}$ . The horizontal lines in Figure 5.17 indicate the expectations of  $N_{\text{part}}$  (dotted) and  $N_{\text{coll}}$  (dashed) scaling. The shaded bars at the end of each line represent the systematic error associated with the determination of these quantities for central and peripheral events. The error bars on charged particles are statistical errors only, and those for  $\pi^0$  are the quadratic sum of the statistical errors and the point-to-point systematic errors. The data show the  $N_{\text{part}}$  scaling behavior at low- $p_T$  region ( $p_T < 0.5 \text{ GeV}/c$ ), consistent with wounded nucleon scaling. The curves on data are calculated by blast-wave fit results and extrapolated over the entire range. This hydrodynamical behavior indicates that the ratio would continue to increase. However, the data show that  $(\bar{p} + p)/2$  reaches

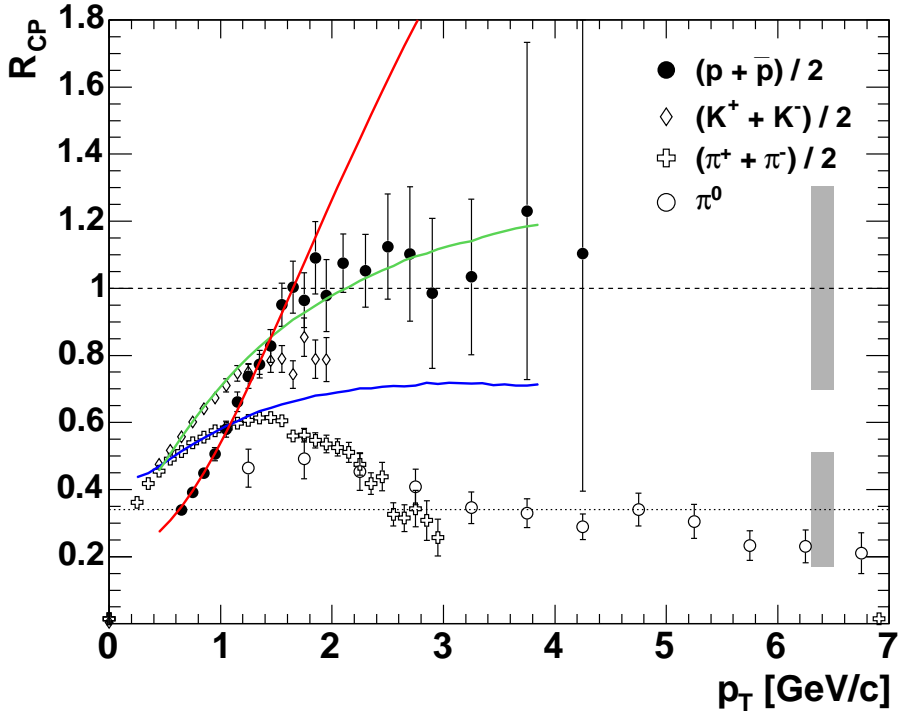


Figure 5.17: Central (0–10%) to peripheral (60–92%) ratios of binary-collision-scaled  $p_T$  spectra,  $R_{CP}$ , as a function of  $p_T$  for  $(\bar{p} + p)/2$ , charged kaons, charged pions, and  $\pi^0$  [32] in Au+Au collisions at  $\sqrt{s_{NN}} = 200$  GeV. The horizontal lines indicate the expectations of  $N_{\text{part}}$  (dotted) and  $N_{\text{coll}}$  (dashed) scaling, the shaded bars represent the systematic errors on these quantities. The curves on data are calculated by blast-wave fit results.

unity for  $p_T > 1.5$  GeV/ $c$ . It is consistent with  $N_{\text{coll}}$  scaling. The data for kaons also show the  $N_{\text{coll}}$  scaling behavior around 1.5 – 2.0 GeV/ $c$ , but the behavior is weaker than for protons. As with neutral pions [32], charged pions are also suppressed at 2 – 3 GeV/ $c$  with respect to peripheral Au+Au collisions.

Motivated by the observation that the  $(\bar{p} + p)/2$  spectra scale with  $N_{\text{coll}}$  above  $p_T = 1.5$  GeV/ $c$ , the ratio of the integrated yield between central and peripheral events (scaled by the corresponding  $N_{\text{coll}}$ ) for  $p_T > 1.5$  GeV/ $c$  are shown in Figure 5.18 as a function of  $N_{\text{part}}$ . The  $p_T$  ranges for the integration are, 1.5 – 4.5 GeV/ $c$  for  $(\bar{p} + p)/2$ , 1.5 – 2.0 GeV/ $c$  for kaons, and 1.5 – 3.0 GeV/ $c$  for charged pions. The data points are normalized to the most peripheral data point. The shaded boxes in the figure indicate the systematic errors, which include the normalization errors on the  $p_T$  spectra, the errors on the detector occupancy corrections, and the uncertainties of the  $\langle T_{\text{AuAu}} \rangle$  determination for the numerator only. Only at the most peripheral data point, the uncertainty on the denominator  $\langle T_{\text{AuAu}}^{60-92\%} \rangle$  is also

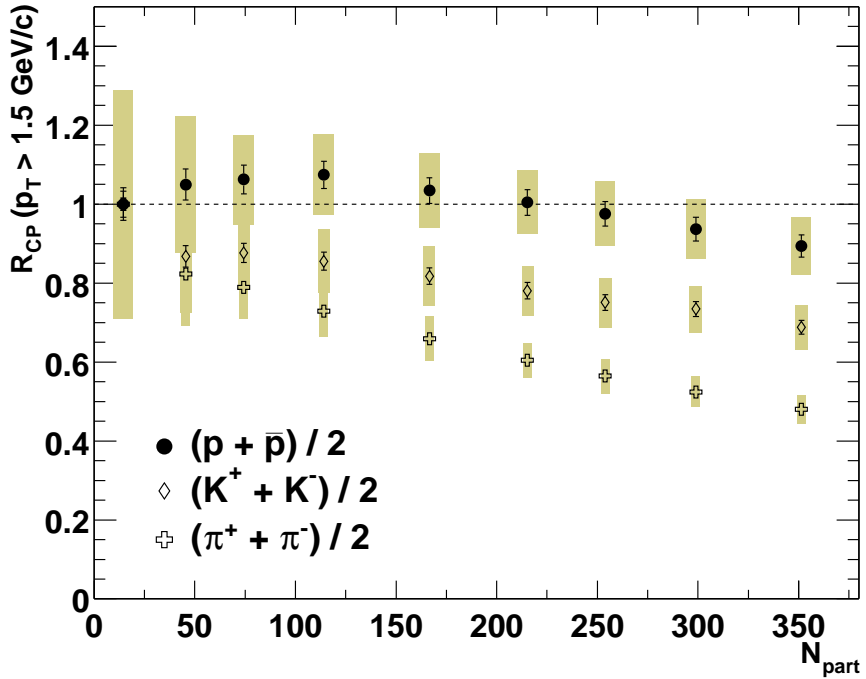


Figure 5.18: Centrality dependence of integrated  $R_{CP}$  above 1.5 GeV/c normalized to the most peripheral 60–92% value. The data shows  $R_{CP}$  for  $(\bar{p} + p)/2$ , charged kaons, and charged pions in Au+Au collisions at  $\sqrt{s_{NN}} = 200$  GeV. The error bars are statistical only. The shaded boxes represent the systematic errors (see text for details).

added. The figure shows that  $(\bar{p} + p)/2$  scales with  $N_{coll}$  for all centrality bins, while the data for charged pions show a decrease with  $N_{part}$ . The kaon data points are between the charged pions and the  $(\bar{p} + p)/2$  spectra.

### 5.4.2 Comparison with Theoretical Models: hydro+jet and recombination

The standard picture of hadron production at high momentum is the fragmentation of energetic partons. While the observed suppression of the  $\pi^0$  yield at high  $p_T$  in central collisions may be attributed to the energy loss of partons during their propagation through the hot and dense matter created in the collisions, i.e. jet quenching [17, 16], it is a theoretical challenge to explain the absence of suppression for baryons up to 4.5 GeV/c for all centralities along with the enhancement of the  $p/\pi$  ratio at  $p_T = 2 - 4$  GeV/c for central collisions.

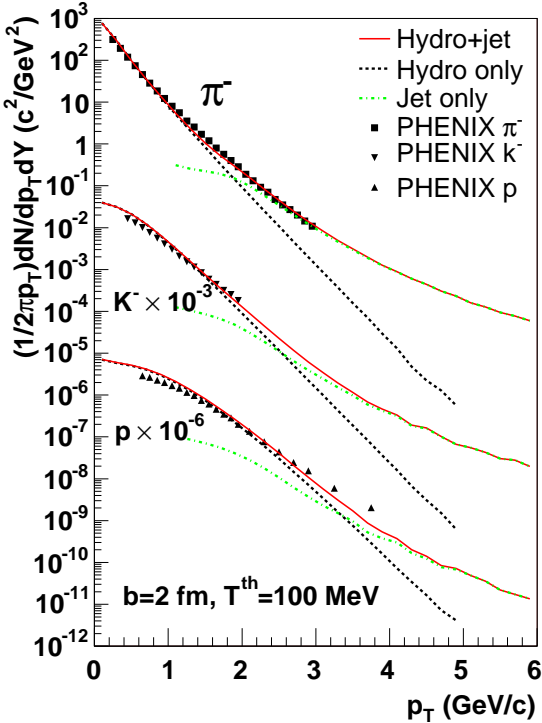


Figure 5.19: Each contribution from hydrodynamics and minijets for  $\pi^-$ ,  $K^-$ , and  $p$  in Au+Au collisions at  $\sqrt{s_{NN}} = 200$  GeV at the impact parameter of  $b = 2.0$  fm. This figure is taken from [82].

### Hydro + jet model

The large  $p/\pi$  ratio is the strong radial flow that boosts the momentum spectra of heavier particles to high- $p_T$ . These observations can be explained by the hydrodynamical model with jet fragmentation (hydro + jet model) [82].

The main feature of the hydrodynamic part in the hydro + jet model are the following: Assuming local thermal equilibrium of partonic/hadronic matter at an initial time  $\tau$ , the hydrodynamical model describe its space-time evolution. The equation of state (EOS) has a first order phase transition between the QGP phase and the hadron phase at  $T_c = 170$  MeV. The QGP phase assumed to be free gas composed quarks with  $N_f = 3$  and gluons. For the hadron phase, a partial chemical equilibrium model with chemical freeze-out temperature  $T_{ch} = 170$  MeV is employed to describe the early chemical freeze-out picture of hadronic matter. Pure hydrodynamics predicts that  $p/\pi$  ratio would continue to increase essentially up to  $p_T \rightarrow \infty$ . However, these particles cannot have a zero mean free path in the medium. Any finite mean free path and a finite volume will limit the number of  $p_T$  “kicks” a particle can receive. For this reason many of the hydrodynamic calculations are not extended into the  $p_T$  region 2–5 GeV/c. Above few  $p_T$ , hydrodynamics should fail to describe the data and jet fragmentation should dominate. The hard part in the hydro + jet model is calculated

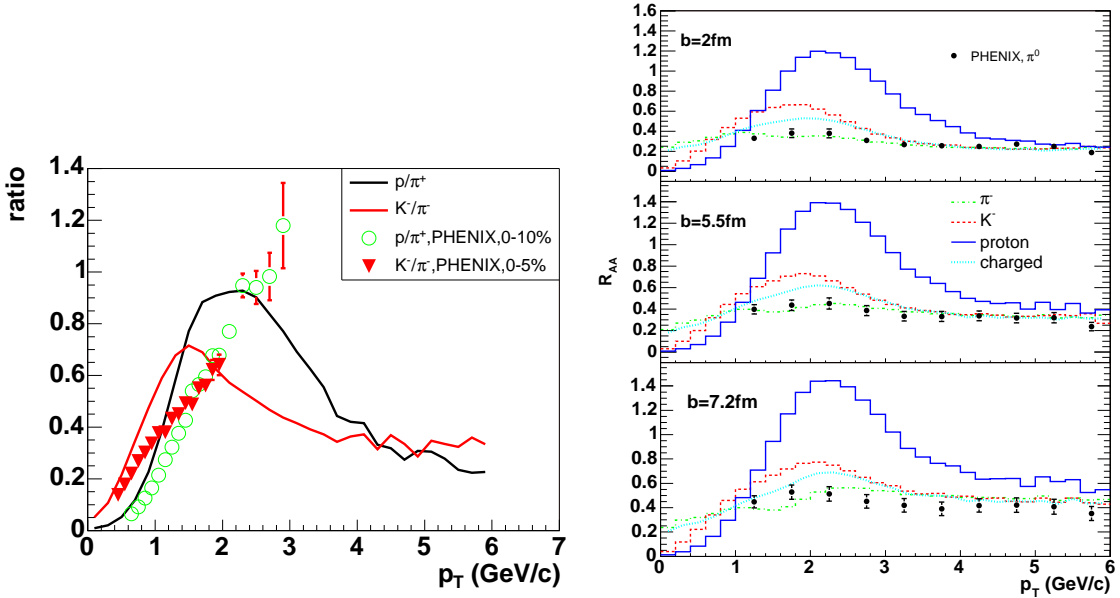


Figure 5.20: The “hydro + jet” model comparison for  $p/\pi$  ratio and  $R_{\text{CP}}$ . Left figure is the  $p/\pi$  and  $K/\pi$  ratios as a function of  $p_T$  in Au+Au collisions at impact parameter  $b = 2$  fm. Right figure is impact parameter dependence of the suppression factors  $R_{AA}$  in Au+Au collisions at  $\sqrt{s_{\text{NN}}} = 200$  GeV as a function of  $p_T$  for  $\pi^-$ ,  $K^-$ , and  $p$ . This figure are taken from [82].

using perturbative QCD. (see Section 1.3)

From this model, Figure 5.19 shows the spectra into hydro parts and minijet parts. It is seen that both soft and hard components are important for the hadron spectra in the transverse momentum of the range around  $2 \leq p_T \leq 5$  GeV/c depending on the hadron mass. Figure 5.20 shows hydro + jet model calculations compared to the  $p/\pi$ ,  $K/\pi$  ratios and  $R_{\text{CP}}$  from PHENIX. The model successfully represents the pion suppression and proton boost at low to intermediate  $p_T$  regions.

### Parton Recombination

Another possible explanation is the dominance of parton recombination at intermediate  $p_T$ , rather than by fragmentation (recombination and fragmentation model) [83, 84, 85]. In the recombination picture, three quarks or a quark/anti-quark pair in a densely populated phase space can form a baryon or meson, respectively. The amplitude for this process is determined by the hadron wave function. This process becomes important particularly at dense environment. Meson (M) is formed from recombination of a quark ( $a$ ) and an

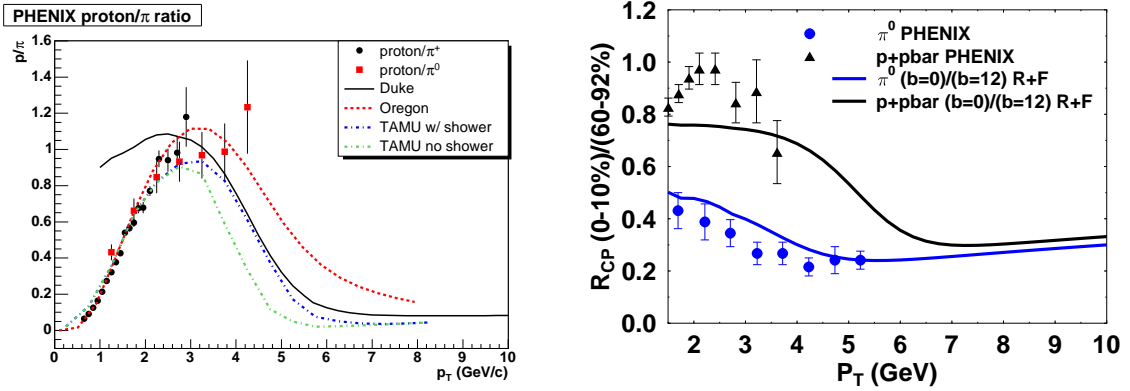


Figure 5.21: The “recombination” model comparison for  $p/\pi$  ratio and  $R_{CP}$ . Left figure is the  $p/\pi$  ratio measured by PHENIX and several comparisons to recombination models. Right figure is  $R_{CP}$  for  $\pi^0$  and protons given by the ratio of particle yields at impact parameters 3 and 12 fm. This figures are taken from [83, 86].

anti-quark ( $b$ ) and baryon (B) is formed of three quarks ( $a, b$  and  $c$ ) as, respectively

$$E \frac{d^3 N_M}{d^3 p} \propto \int dx w_a(x p_T) \bar{w}_b((1-x)p_T) |\psi_{ab}|^2, \quad (5.7)$$

$$E \frac{d^3 N_B}{d^3 p} \propto \int dx dx' w_a(x p_T) w_b(x' p_T) w_c((1-x-x')p_T) |\psi_{abc}|^2, \quad (5.8)$$

where  $w_\alpha(p_T)$  is the parton distribution,  $x$  ( $x'$ ) is the fraction of the momentum and  $\psi_{ab}$  ( $\psi_{abc}$ ) is the meson (baryon) wave function. For an equal momentum fraction, namely  $x = 1/2$  for mesons and  $x = x' = 1/3$  for baryons,

$$\frac{dN_M}{p_T dp_T} = C_M w_a(p_T/2)^2, \quad \frac{dN_B}{p_T dp_T} = C_B w_b(p_T/3)^3, \quad (5.9)$$

where  $C_M$  and  $C_B$  correspond to the coalescence probabilities for mesons and baryons, respectively.

Three essential features are predicted by recombination models. First, baryons at moderate  $p_T$  are greatly enhanced relative to mesons as their transverse momentum is the sum of three quarks rather than two. Recombination dominates over parton fragmentation in this region, because, for an exponential spectrum recombination is a more efficient means of producing particles at a particular  $p_T$ . This enhancement should return to its fragmentation values at higher  $p_T$ . In the intermediate range, all mesons should behave in a similar manner regardless of mass, as should all baryons. Secondly, recombination predicts that the collective flow of the final-state hadrons should follow the collective flow of their constituent

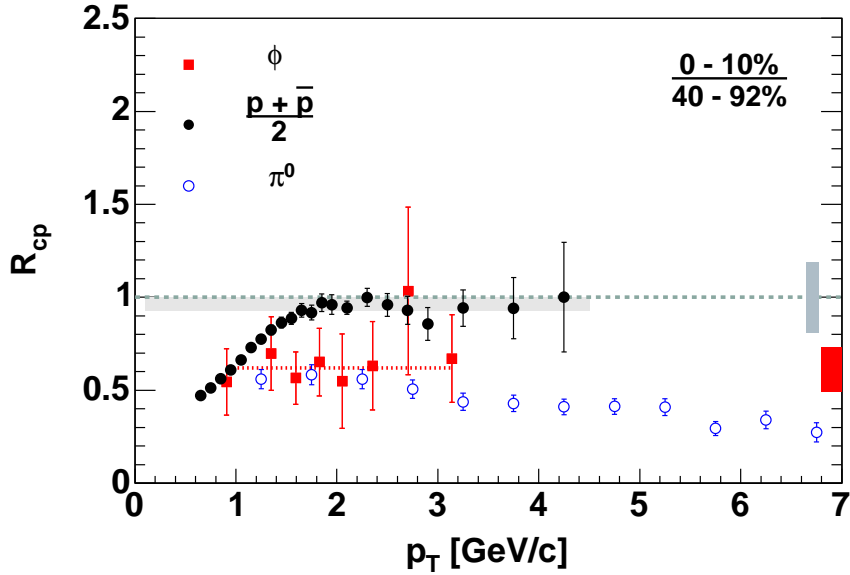


Figure 5.22: The  $R_{CP}$  of the  $\phi$  as measured in the  $KK$  channel, compared to the protons and pions for Au+Au collisions at  $\sqrt{s_{NN}} = 200$  GeV. This figure is taken from [87].

quarks. Finally, recombination causes thermal features to extend to higher transverse momentum,  $p_T \gg T_c$  than one might naively expect since the underlying thermal spectrum of the constituents gets a multiplication factor of essentially three for baryons and two for mesons. A last general feature which is true for the simplest of the models, but may not necessarily be true for more complex models, is that at intermediate  $p_T$ , recombination is the dominant mechanism for the production of hadrons—particularly of baryons.

Figure 5.21 shows several recombination model calculations compared to the  $p/\pi$  ratio and  $R_{CP}$  from PHENIX. The general features at  $p_T > 2$  GeV/c are reasonably reproduced that is the protons show a strong enhancement at moderate  $p_T$ . Since the recombination model’s essential ingredient is the number of constituent quarks in a hadron, the similarity of  $R_{CP}$  for the  $\phi$  and pions is nicely explained.

The competition between recombination and fragmentation of partons may explain the observed features. The model predicts that the effect is limited to  $p_T < 5$  GeV/c, beyond which fragmentation becomes the dominant production mechanism for all particle species.

### Comparison with the $\phi$ meson

In both theoretical models, the baryon enhancement as a function of centrality can be tuned to reproduce the apparent binary collision scaling observed in the data. An important dis-

tinction between the two models is that in one case this enhancement is mass dependent and in the other it comes from the combination of quark momenta and thus distinguishes between baryons and mesons.

We have extended our identified hadron studies to include the  $\phi$  vector meson as measured in the  $K^+K^-$  decay channel. The  $\phi$  is a meson, and is in that sense similar to the pion with a valence quark and antiquark, and yet its mass is comparable to that of the proton. Figure 5.22 shows  $R_{CP}$ , the ratio of production in central to peripheral Au+Au collisions scaled by binary collisions, for protons, pions and  $\phi$  mesons detected via its  $KK$  decay channel [87] in Au+Au collisions at  $\sqrt{s_{NN}} = 200$  GeV. The  $\phi$  follows the suppression pattern of the pions within errors, indicating that the surprising behavior of the protons is not followed by the  $\phi$ . This scaling with quark content, as opposed to mass, favors recombination models.

# Chapter 6

## Conclusions

We have presented the results of identified hadron spectra and yields in Au+Au collisions at the energy of  $\sqrt{s_{\text{NN}}} = 200$  GeV by the PHENIX experiment using the Relativistic Heavy Ion Collider (RHIC) at Brookhaven National Laboratory (BNL).

For the systematic study of hadron productions in relativistic heavy-ion collisions near mid-rapidity region, we have constructed Time-of-Flight counter and installed in PHENIX detector systems. It is designed for the good particle identification capability under the condition of high particle density and for the wide range of kinematic coverage in Au+Au collisions at RHIC. Using the data taken by the PHENIX central arm spectrometers, single particle spectra and yields are analyzed.

For single particle analysis, we have measured the transverse momentum spectra and yields for  $\pi^\pm$ ,  $K^\pm$ ,  $p$  and  $\bar{p}$  at mid-rapidity in Au+Au collisions at  $\sqrt{s_{\text{NN}}} = 200$  GeV over a broad momentum range with various centrality selections. We have observed a clear particle mass dependence of the shapes of transverse momentum spectra in central collisions below  $\sim 2$  GeV/c in  $p_T$ . Both mean transverse momenta and particle yields per participant pair increase from peripheral to mid-central and saturate at the most central collisions for all particle species. The net proton number in Au+Au central collisions at  $\sqrt{s_{\text{NN}}} = 200$  GeV is  $\sim 5$  at mid-rapidity.

We also measured the particle ratios of  $\pi^-/\pi^+$ ,  $K^-/K^+$ ,  $\bar{p}/p$ ,  $K/\pi$ ,  $p/\pi$  and  $\bar{p}/\pi$  as a function of  $p_T$  and collision centrality. The ratios of equal mass particle yields are independent of  $p_T$  and centrality within the experimental uncertainties. The ratios in central Au+Au collisions are well reproduced by the statistical thermal model with a baryon chemical potential of  $\mu_B = 29$  MeV and a chemical freeze-out temperature of  $T_{\text{ch}} = 177$  MeV. On the other hand, both  $K/\pi$  and  $p/\pi$  ( $\bar{p}/\pi$ ) ratios increase as a function of  $p_T$ . This increase

with  $p_T$  is stronger for central than for peripheral events.

The particle spectra can be well fit with a hydrodynamic-inspired parameterization to extract freeze-out temperature and radial flow velocity of the particle source. The experimental data include the decay of resonance; we added the decay of mesonic ( $\rho, \eta, \omega, K^*, \dots$ ) and baryonic ( $\Delta, \Lambda, \Sigma, \dots$ ) resonance effects which the abundance is determined by chemical parameters. The simultaneous fits of  $\pi^\pm, K^\pm, p$  and  $\bar{p}$  spectra for the most central 0–5% collisions, we have obtained freeze-out temperature  $T_{\text{fo}} = 108$  MeV and average flow velocity  $\langle \beta_T \rangle = 0.57$ . It was found that  $T_{\text{fo}}$  decreases and  $\beta_T$  increases from the most peripheral to mid-central collisions, and appears to saturate in the central collisions.

For the high- $p_T$  region, the scaling behavior of identified charged hadrons has been compared with results for neutral pions. The central-to-peripheral ratio,  $R_{\text{CP}}$ , approaches unity for  $(\bar{p} + p)/2$  from  $p_T = 1.5$  up to 4.5 GeV/c. Meanwhile, charged and neutral pions are suppressed. The ratio of integrated  $R_{\text{CP}}$  from  $p_T = 1.5$  to 4.5 GeV/c exhibits an  $N_{\text{coll}}$  scaling behavior for all centrality bins in the  $(\bar{p} + p)/2$  data, which is in contrast to the stronger pion suppression, that increases with centrality. The  $p/\pi$  and  $\bar{p}/\pi$  ratios in central events both increase with  $p_T$  up to 3 GeV/c and approach unity at  $p_T \approx 2$  GeV/c. However, in peripheral collisions these ratios saturate at the value of 0.3 – 0.4 around  $p_T = 1.5$  GeV/c.

The standard picture of hadron production at high momentum is the fragmentation of energetic partons. While the observed suppression of the  $\pi$  yield at high- $p_T$  in central collisions might be attributed to the energy loss of partons during their propagation through the hot and dense matter created in the collisions. The observed  $R_{\text{CP}}$  and  $p/\pi$  ratios in intermediate  $p_T$  region are not explained by the hydrodynamic model alone, but some of theoretical model qualitatively agree with data. These observations can be explained by the hydrodynamical model with jet fragmentation (hydro + jet model). Above few GeV  $p_T$ , hydrodynamics fail to describe the data and jet fragmentation should dominate. Another possible explanation is the dominance of parton recombination at intermediate  $p_T$ , rather than by fragmentation (recombination and fragmentation model). In the recombination picture, three quarks or a quark/anti-quark pair in a densely populated phase space can form a baryon or meson, respectively. Both theoretical models reproduce the binary collision scaling observed in the data. We have extended our identified hadron studies to include the  $\phi$  vector meson. The observed  $R_{\text{CP}}$  for  $\phi$  is similar to other mesons despite the fact that they are more massive than protons. This scaling with quark content favors recombination models.

# Appendix A

## Numerical Supplement

### A.1 Relativistic Kinematics and Variables

Here, we introduce kinematic variables used in the thesis. It is useful to describe them with Lorentz invariant variables or variables which have simple Lorentz transformation properties, because we deal with relativistic particles and system.

We take a beam line to be z-axis of a frame. For a particle which has momentum  $\mathbf{p} = (p_x, p_y, p_z)$  and mass  $m$ , we use a longitudinal momentum  $p_z$ , a transverse momentum  $p_T \equiv \sqrt{p_x^2 + p_y^2}$ , and total energy  $E = \sqrt{\mathbf{p}^2 + m^2}$ . Transverse mass  $m_T$  and rapidity  $y$  are defined as

$$m_T \equiv \sqrt{p_T^2 + m^2}, \quad y \equiv \frac{1}{2} \ln \frac{E + p_z}{E - p_z}. \quad (\text{A.1})$$

The total energy and longitudinal momentum of a particle can be easily related to its transverse mass and rapidity as

$$E = m_T \cosh y, \quad p_z = m_T \sinh y. \quad (\text{A.2})$$

On the Bjorken's space-time picture, the proper time  $\tau$  and space-time rapidity  $Y$  are defined as

$$\tau = \sqrt{t^2 - z^2}, \quad Y = \frac{1}{2} \ln \frac{t+z}{t-z}, \quad (\text{A.3})$$

$$t = \tau \cosh Y, \quad z = \tau \sinh Y. \quad (\text{A.4})$$

## A.2 Transverse Expansion

In this section, we show the actual computation of the spectra and follow the spirits of boost-invariant scenario. We employ cylindrical coordinates  $(r, \phi, z)$  where  $z$  is the coordinate along the collision axis with  $r \equiv \sqrt{x^2 + y^2} = z = 0$  being the collision point. In addition we define the longitudinal proper time,  $\tau = \sqrt{t^2 - z^2}$ . To obtain the boost invariant-solutions in a longitudinal direction, we define the transverse velocity to the following form for azimuthal symmetry

$$u^\mu = (u_t, u_r, u_\phi, u_z) = \frac{1}{\sqrt{1 - \beta_r^2}} \left( \frac{t}{\tau}, \beta_r(\tau, r), 0, \frac{z}{\tau} \right), \quad (\text{A.5})$$

where the overall factor in the right hand side is obtained from the normalization  $u^\mu u_\mu = 1$ .

We define the transverse rapidity  $\rho$  as

$$\rho = \tanh^{-1} \beta_r = \frac{1}{2} \ln \frac{1 + \beta_r}{1 - \beta_r}, \quad (\text{A.6})$$

which gives  $\cosh \rho = 1/\sqrt{1 - \beta_r^2}$  and  $\sinh \rho = \beta_r/\sqrt{1 - \beta_r^2}$ . Together with Eq.(A.4), we obtain the transverse velocity form as

$$u^\mu = (\cosh \beta \cosh Y, \sinh \beta, 0, \cosh \beta \sinh Y). \quad (\text{A.7})$$

The invariant momentum spectrum of hadrons emitted at freezeout is given by a local thermal distribution  $f(x, p)$  [88], with the freezeout temperature  $T$ , boosted by a local velocity field  $u^\mu$  at the freezeout hypersurface  $\sigma$ :

$$\begin{aligned} E \frac{d^3 N}{dp^3} &= \int_{\sigma} f(x, p) p^\mu d\sigma_\mu \\ &\approx \frac{g}{(2\pi)^3} \int e^{-u^\nu p_\nu/T} p^\mu d\sigma_\mu, \end{aligned} \quad (\text{A.8})$$

We assume that the freeze-out takes place on  $\sigma$  which is a three dimensional hypersurface specified by the cylindrical coordinates:

$$\sigma^\mu = (\sigma_t, \sigma_x, \sigma_y, \sigma_z) = (t(r, z), r \cos \phi, r \sin \phi, z) \quad (\text{A.9})$$

A normal vector  $d\sigma$  to the surface is

$$\begin{aligned} d\sigma^\mu &= \epsilon_{\mu\nu\lambda\rho} \frac{\partial \sigma^\nu}{\partial r} \frac{\partial \sigma^\lambda}{\partial \phi} \frac{\partial \sigma^\rho}{\partial z} dr d\phi dz, \\ &= \left( 1, -\frac{\partial t}{\partial r} \cos \phi, -\frac{\partial t}{\partial r} \sin \phi, -\frac{\partial t}{\partial z} \right) r dr d\phi dz. \end{aligned} \quad (\text{A.10})$$

The four-momentum of the emitted hadron may be expressed in term of the momentum-space rapidity  $y$  and the transverse mass  $m_T$

$$p^\mu = (E, p_x, p_y, p_z) = (m_T \cosh y, p_T \cos \varphi, p_T \sin \varphi, m_T \sinh y), \quad (\text{A.11})$$

we obtain

$$\begin{aligned} p^\mu d\sigma_\mu &= \left[ E - p_T \frac{\partial t}{\partial r} \cos(\phi - \varphi) - p_z \frac{\partial t}{\partial z} \right] r dr d\phi dz \\ &= \left[ m_T \cosh y - m_T \sinh y \frac{\partial t}{\partial z} - p_T \frac{\partial t}{\partial r} \cos(\phi - \varphi) \right] r dr d\phi dz. \end{aligned} \quad (\text{A.12})$$

The transverse velocity  $u^\mu$  is obtained the case of  $\phi \neq 0$ :

$$u^\mu = (u^t, u^x, u^y, u^z) = (\cosh \rho \cosh Y, \sinh \rho \cos \phi, \sinh \rho \sin \phi, \cosh \rho \sinh Y). \quad (\text{A.13})$$

Then we obtain

$$\begin{aligned} u^\mu p_\mu &= E \cosh \rho \cosh Y + p_T \sinh \rho \cos \phi \cos \varphi + p_T \sinh \rho \sin \phi \sin \varphi + p_z \cosh \rho \sinh Y \\ &= m_T \cosh \rho \cosh(Y - y) - p_T \sinh \rho \cos(\phi - \varphi) \end{aligned} \quad (\text{A.14})$$

For a local thermal distribution, The invariant cross section is

$$\begin{aligned} E \frac{d^3 N}{dp^3} &= \frac{g}{(2\pi)^3} \int e^{-u^\nu p_\nu/T} p^\mu d\sigma_\mu \\ &= \frac{g}{(2\pi)^3} \int r dr d\phi dz \left[ m_T \cosh y - m_T \sinh y \frac{\partial t}{\partial z} - p_T \frac{\partial t}{\partial r} \cos(\phi - \varphi) \right] \\ &\quad \times \exp \left( -\frac{m_T \cosh \rho}{T} \cosh(Y - y) + \frac{p_T \sinh \rho}{T} \cos(\phi - \varphi) \right) \\ &= \frac{g}{(2\pi)^2} \int r dr dz e^{-\frac{m_T \cosh \rho}{T} \cosh(Y - y)} \left[ m_T \left( \cosh y - \sinh y \frac{\partial t}{\partial z} \right) \frac{1}{2\pi} \int_0^{2\pi} e^{\frac{p_T \sinh \rho}{T} \cos(\phi - \varphi)} d\phi \right. \\ &\quad \left. - p_T \frac{\partial t}{\partial r} \frac{1}{2\pi} \int_0^{2\pi} \cos(\phi - \varphi) e^{\frac{p_T \sinh \rho}{T} \cos(\phi - \varphi)} d\phi \right] \\ &= \frac{g}{(2\pi)^2} \int r dr dz e^{-\frac{m_T \cosh \rho}{T} \cosh(Y - y)} \\ &\quad \times \left[ m_T \left( \cosh y - \sinh y \frac{\partial t}{\partial z} \right) I_0 \left( \frac{p_T \sinh \rho}{T} \right) - p_T \frac{\partial t}{\partial r} I_1 \left( \frac{p_T \sinh \rho}{T} \right) \right] \end{aligned} \quad (\text{A.15})$$

Here the integration over  $\phi$  is carried out by making use the modified Bessel functions  $I_n(\zeta)$  defined in Eq. A.20.

The transverse mass spectrum is presented in terms of the invariant cross section:

$$E \frac{d^3 N}{dp^3} = \frac{d^3 N}{m_T dm_T dy d\phi} = \frac{1}{2\pi m_T} \frac{d^2 N}{dm_T dy}, \quad (\text{A.16})$$

For the transverse mass spectrum, we integrate over  $\phi$  and  $y$ . As for the latter, we assume that the detector system has full  $y$  acceptance and shift the integration variable  $y$  to  $y - Y$ . Then the result is expressed by another modified Bessel functions  $K_n(\zeta)$  defined in Eq. A.21.

$$\begin{aligned} \frac{dN}{m_T dm_T} &= \frac{g}{2\pi} m_T \int r dr dz \int_{-\infty}^{+\infty} dy e^{-\frac{m_T \cosh \rho}{T} \cosh y} \\ &\quad \times \left[ \left( \cosh(y - Y) - \sinh(y - Y) \frac{\partial t}{\partial z} \right) I_0 \left( \frac{p_T \sinh \rho}{T} \right) - \frac{p_T}{m_T} \frac{\partial t}{\partial r} I_1 \left( \frac{p_T \sinh \rho}{T} \right) \right] \\ &= \frac{2g}{\pi} m_T \int r dr dz \left[ \left( \cosh Y - \sinh Y \frac{\partial t}{\partial z} \right) K_1 \left( \frac{m_T \cosh \rho}{T} \right) I_0 \left( \frac{p_T \sinh \rho}{T} \right) \right. \\ &\quad \left. - \frac{p_T}{m_T} \frac{\partial t}{\partial r} K_0 \left( \frac{m_T \cosh \rho}{T} \right) I_1 \left( \frac{p_T \sinh \rho}{T} \right) \right]. \end{aligned} \quad (\text{A.17})$$

Here the integration over  $y$  is carried out by making use the modified Bessel functions of the second kind  $K_n(\zeta)$  defined in Eq. A.21.

Lets us further parametrize the freeze-out hypersurface as  $t(r, z) = \sqrt{\tau^2(r) + z^2}$ . Then, we have  $\frac{\partial t}{\partial z} = z/\sqrt{\tau^2(r) + z^2}$ ,  $\frac{\partial t}{\partial r} = (d\tau/dr)/\cosh Y$ . Knowing  $dz = \tau \cosh Y dY$ , we may integrate over  $z$  to obtain

$$\begin{aligned} \frac{dN}{m_T dm_T} &= \frac{2g}{\pi} m_T Y_{max} \int_0^R r dr \tau(r) \left[ K_1 \left( \frac{m_T \cosh \rho}{T} \right) I_0 \left( \frac{p_T \sinh \rho}{T} \right) \right. \\ &\quad \left. - \frac{p_T}{m_T} \frac{d\tau}{dr} K_0 \left( \frac{m_T \cosh \rho}{T} \right) I_1 \left( \frac{p_T \sinh \rho}{T} \right) \right]. \end{aligned} \quad (\text{A.18})$$

If we further assume an instant freezer independent of  $r$  at  $\tau = \text{const}$ , the second term inside the bracket of Eq. A.18 vanishes. Then, we obtain following “blast-wave” formation.

$$\frac{dN}{m_T dm_T} \propto \int_0^R r dr m_T I_0 \left( \frac{p_T \sinh \rho}{T} \right) K_1 \left( \frac{m_T \cosh \rho}{T} \right). \quad (\text{A.19})$$

### modified Bessel function

$$I_n(\zeta) = \frac{1}{2\pi} \int_0^{2\pi} \cos n\phi \exp(\zeta \cos \phi) d\phi, \quad (\text{A.20})$$

$$K_n(\zeta) = \frac{1}{2} \int_{-\infty}^{+\infty} \cosh ny \exp(-\zeta \cosh y) dy. \quad (\text{A.21})$$

# Appendix B

## Time-of-flight Detector

PHENIX has a capability for simultaneous measurement of many different probes such as hadrons, leptons and phonons. Since hadron production in heavy ion collisions carries the basic information of the properties of the matter, it is important to measure identified hadrons in a wide range of  $p_T$ . In addition to single particle spectrum measurements, Hanbury-Brown-Twiss (HBT) correlation measurements and measurement of  $\phi$  mesons through the  $K^+K^-$  channel are also important to probe the hot and dense matter created in Au + Au collisions at RHIC. For particle identification, time-of-flight (TOF) measurements, where one compares the particle time of flight to the measured momentum of the particle, are one of the most powerful methods for separating particle species. The TOF contains 960 scintillator slats oriented along the  $r - \phi$  direction. Its timing resolution was about 100 ps. In this chapter we describe the basic design of the TOF counter, the specification of each component and the front end electronics module. Finally we present the performance of the TOF detector using data taken in the first year of RHIC operation.

### B.1 Detector Design

The PHENIX TOF system serves as a primary particle identification device for charged hadrons in PHENIX. It is designed to have about 100 ps timing resolution in order to achieve clear particle separation in the high momentum region, i.e.  $\pi/K$  separation up to 2.4 GeV/c and  $K/\text{proton}$  separation up to 4.0 GeV/c.

The TOF detector is placed at a distance of 5.06 m from the collision vertex, in between



Figure B.1: The TOF detector system mounted on the PHENIX East Arm showing 10 panels of the detector.

the Pad Chamber (PC3) and the EMCAL in the east arm of PHENIX. It is designed to cover the  $\eta$  range ( $70^\circ \leq \theta \leq 110^\circ$ ) of the central detector over  $45^\circ$  in azimuthal angle. The TOF detector consists of 10 panels of TOF walls. Figure B.1 shows a photo of the TOF detector system mounted on the east central arm in the PHENIX experimental hall. All 10 panels of the detector are seen. One TOF wall consists of 96 segments, each equipped with a plastic scintillator slat and photomultiplier tubes which are read out at both ends.

The number of segments in the TOF system is determined by minimizing the probability of two or more particles hitting a single segment. For the TOF system design the double hit probability is kept as low as possible. Assuming the charged particle rapidity density to be  $dN_{ch}/dy = 1500$ , the charged particle multiplicity on the one TOF wall is expected to

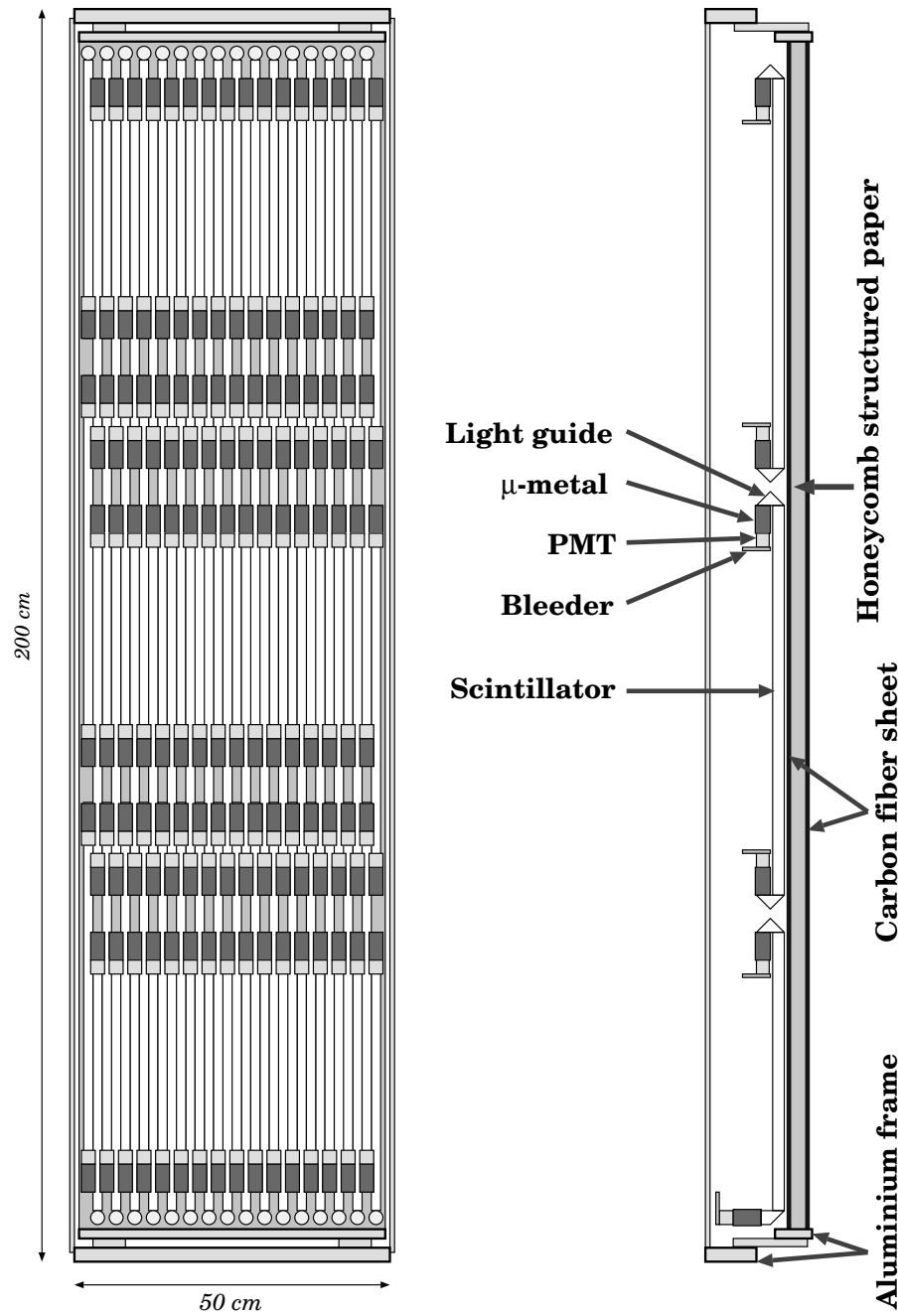


Figure B.2: Schematic diagram of the components of a single TOF panel which consists of 96 plastic scintillation counters with photomultiplier tubes at both ends, light guides and supports.

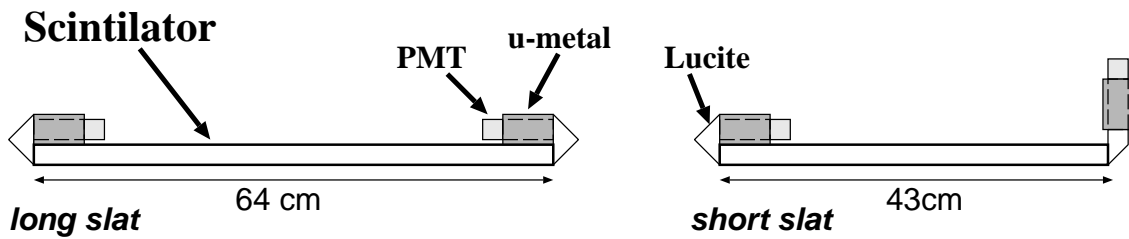


Figure B.3: Schematic diagram of the components of a plastic scintillation counters with photomultiplier tubes at both ends, light guides and supports.

be 9. In order to keep the occupancy below 10%, the segmentation is about 1000 and the required area of each segment at a distance of 5.06 m away from the vertex is  $100 \text{ cm}^2$ .

A total 10 TOF panels, 960 slats of scintillators and 1920 channels of PMTs were installed and operated at the first year of operation. The slat is oriented along the  $r - \phi$  direction and provides time and longitudinal position information of particles that hit the slat. Figure B.2 shows a schematic view of one panel of the TOF detector. It consists of 96 plastic scintillation counters with photomultiplier tubes (PMT's) at both ends, light guides and mechanical supports. Scintillator rod and light guides were wrapped with thin aluminum foil and were glued on the honeycomb board. The honeycomb boards are made of paper of a honeycomb structure sandwiched between carbon fiber sheets, which provide a “massless” rigid structure. Scintillators with two different lengths (637.7 and 433.9 mm) are assembled in an alternating fashion in order to avoid geometrical conflicts between the PMTs of neighboring slats. Each end of the scintillator slat is attached with optical glue to a  $180^\circ$  bent light guide. On both sides of one panel, the light guides are bent  $90^\circ$  so as not to conflict with the neighboring PMT's. (Figure B.3 The scintillator slats are glued on the honeycomb board which consists of carbon fiber sheet and honeycomb paper in order to reduce the amount of material but also provide the wall with sufficient mechanical strength. The signal cables are RG58C/U and the high voltage cables are GXO3173-01. The total radiation length including PMT's and cables is about 6%. Using different lengths of scintillator slats and adoption of bent light guides as described above has allowed us to achieve very small dead space between the TOF slats.

## B.2 The TOF Scintillator and Photomultiplier Tubes

The plastic scintillator used in the TOF is Bicron BC404, 1.5 cm in width and 1.5 cm in depth. It has good timing characteristics with a moderate attenuation length. The physical constants of this scintillator are given in Table B.1.

Physical constant	Value
Light output (% anthracene)	68
Wavelength of maximum emission	408 nm
Decay constant	1.8 ns
Bulk attenuation length	160 cm
Refractive index ( $n$ )	1.58

Table B.1: Characteristics of the BC404 Scintillator

The TOF system uses HAMAMATSU R3478S PMT's. These tubes have a 0.75 inch (19 mm) diameter window of borosilicate glass, an 8 stage linear-focussed dynode structure and a bialkali photocathode. The length of the tube is about 6.7 cm. The relevant physical constants of this tube are given in Table B.2. The PMT's are arranged along the direction parallel to the scintillator bar. The magnetic field expected around the TOF system is less than 10 Gauss and its direction is perpendicular to the PMT. The requirement for the  $\mu$ -metal shielding is therefore not severe. We use a 0.5-mm thick, 7.0-cm long  $\mu$ -metal shield with an internal diameter of 23 mm. The hit position in the vertical direction (along the slats) is derived from the time difference observed in the signals, read out at the two ends of the slat.

Physical constant	Value
Wavelength of maximum response	420 nm
Current amplification	$\sim 10^6$
Anode pulse rise time	1.3 ns
Electron transit time	14 ns
Transit time spread	0.36 ns
High voltage supply	-1800 Vdc



Table B.2: Characteristics of the HAMAMATSU R3478S PMT and photo.

### B.3 Front End Electronics

The front-end electronics (FEE) of the TOF are designed to sample the PMT signals at the bunch crossing frequency (9.4 MHz) of RHIC and store them during the first level trigger latency of 4.24  $\mu$ sec corresponding to 40 RHIC bunch crossings. The signal timing from the PMT is determined by a leading edge discriminator followed by a Time-to-Voltage Converter (TVC). The charge information is converted to a voltage by a Charge-to-Voltage Converter (QVC). The analog voltages from the TVC and the QVC are stored by a switched capacitor Analog Memory Unit (AMU) which stores the information during the latency and buffers up to five accepted events. The stored voltages are digitized by a 12 bit 1.25 MHz ADC. To eliminate the cross talk between adjacent channels there are two independent readout channels. One is a signal channel and the other is a reference channel which serves as an antenna for cross talk elimination. By taking the difference between the two channels, there is now no crosstalk in the output. The block diagram of TOF-FEE architecture is shown in Figure B.4.

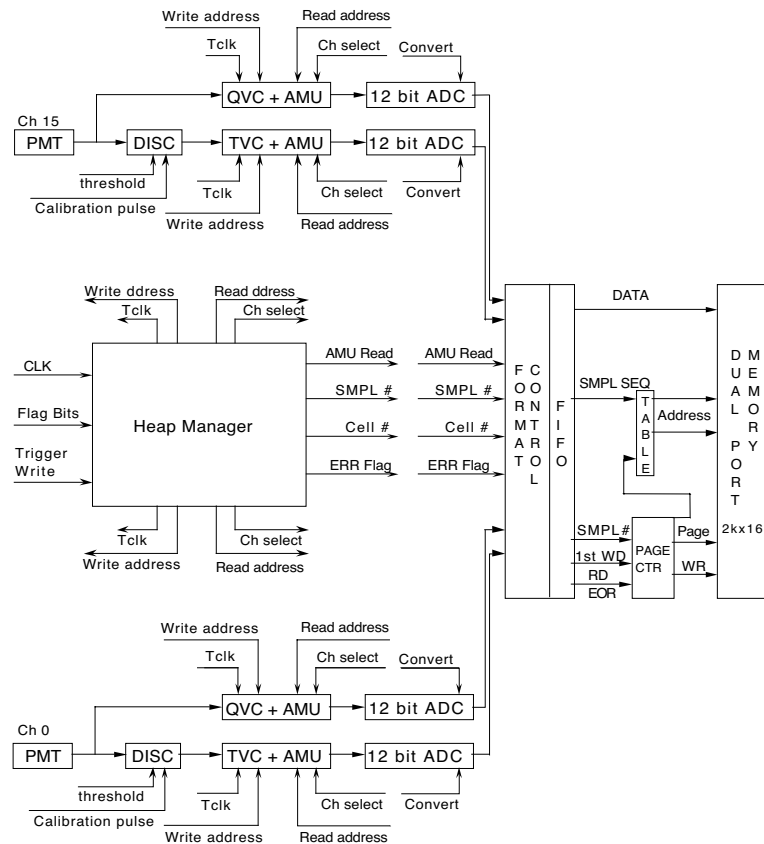


Figure B.4: The block diagram of TOF front-end electronics module.

Figure B.5 shows the time and charge measurement principle of TOF-FEE system in PHENIX. The value of the timing signal measured by TVC ( $T_{mea}$ ) is the timing difference between the discriminator's output and next beam clock.

$$T_{mea} = (T_{clk} + 106\text{ns}) - T_{TOF} \quad (\text{B.1})$$

The TVC takes 3 clock cycle (charge up, sampling reset) per valid hits. After sampling, the TVC is discharged immediately. The charge is measured by the difference of the QVC value before and after integration,

$$\text{Charge} = Q_{post} - Q_{pre}. \quad (\text{B.2})$$

The QVC takes each clock cycles. The QVC is reset regularly with external NIM pulse.

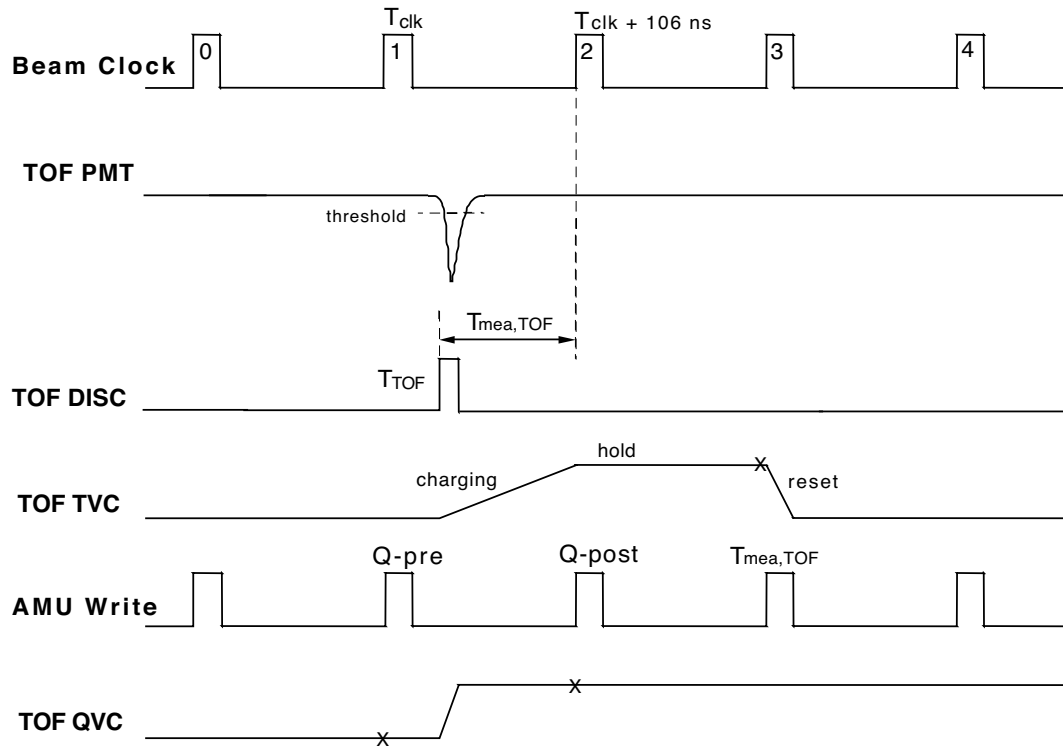


Figure B.5: Time and charge measurement principle. The timing measured by the TVC is the difference between the discriminator's output and next beam clock. The charge is measured by difference of QVC value before (Q-pre) and after integration (Q-post).

## B.4 TOF Detector Performance

Particle identification for charged hadrons is performed by combining the information from the DC, PC1, BBC and the TOF. The designed time-of-flight resolution is about 100 psec. This allows us to achieve a PID capability for high momentum particles, a  $4\sigma$   $\pi/K$  separation at momenta up to 2.4 GeV/c and a  $K/p$  separation up to 4.0 GeV/c. Figure B.6 illustrates the particle separation capabilities of the TOF system. A track is reconstructed from hits in the DC and PC1 that point to the TOF detector. In this reconstruction we use a window for TOF association adjusted so that the residuals between the projection point and the reconstructed TOF hit position is within 2.5 standard deviations. The flight-path length of the track from the event vertex to the TOF detector as calculated by the momentum reconstruction algorithm is used to correct the time-of-flight value measured by the TOF detector.

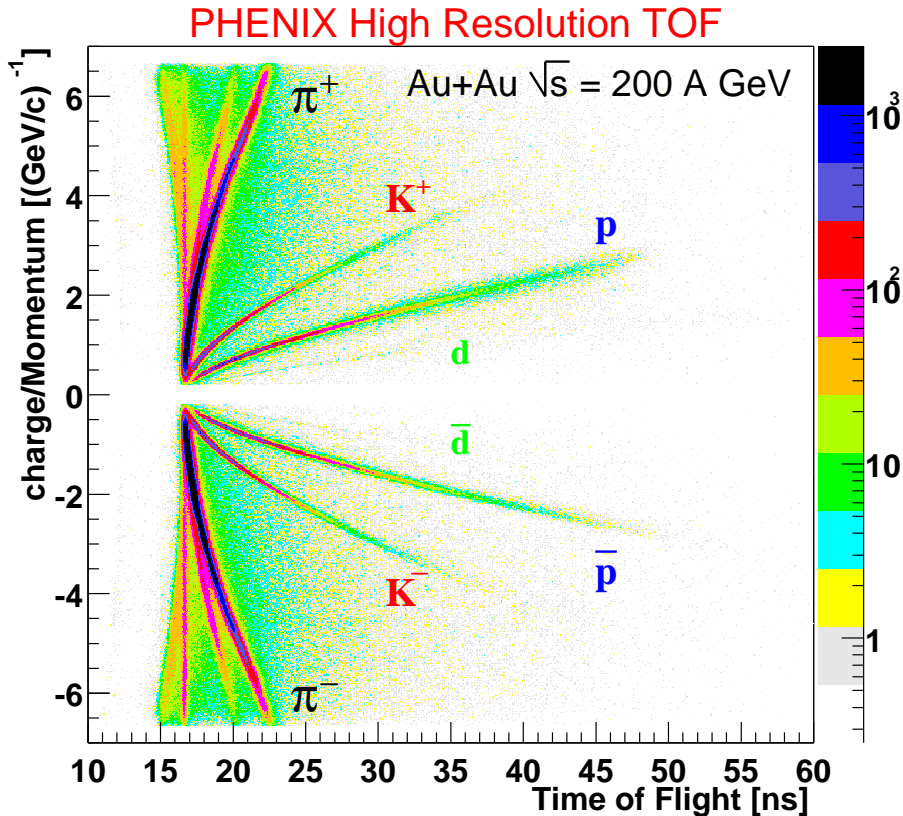


Figure B.6: Contour plot of the time-of-flight versus reciprocal momentum in minimum bias Au+Au collisions at the energy of  $\sqrt{s_{NN}} = 200$  GeV. The figure clearly demonstrates the particle identification capability using the TOF detector in the year 2001 data taking period.

Figure B.7 shows the time-of-flight resolution for various particles. For this example a momentum range of  $1.4 < p_T < 1.8 \text{ GeV}/c$  for  $\pi^+$  was used. The resulting time-of-flight resolution was  $\sigma = 96 \text{ ps}$ . Figure B.8 shows the mass-squared distribution for positive (top) and negative (bottom) charged particles integrated over all momenta. The vertical axes in these figures are in arbitrary units. The figure demonstrates that clear particle identification using the TOF was achieved in the first year of RHIC running. The timing resolution given above for the complete TOF system is achieved after slewing effect corrections and run-by-run timing offset calibrations are made.

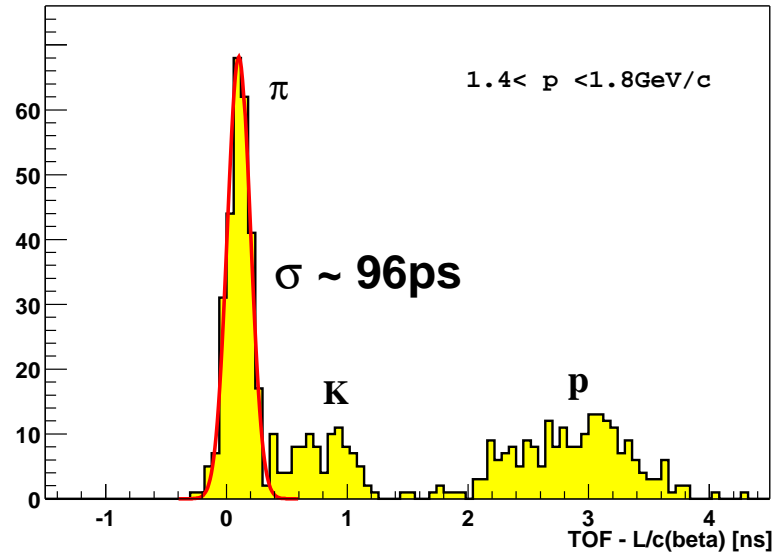


Figure B.7: The time-of-flight resolution in the transverse momentum range  $1.4 < p_T < 1.8 \text{ GeV}/c$  for positively charged pions. The overall time-of-flight resolution of 96 psec is achieved.

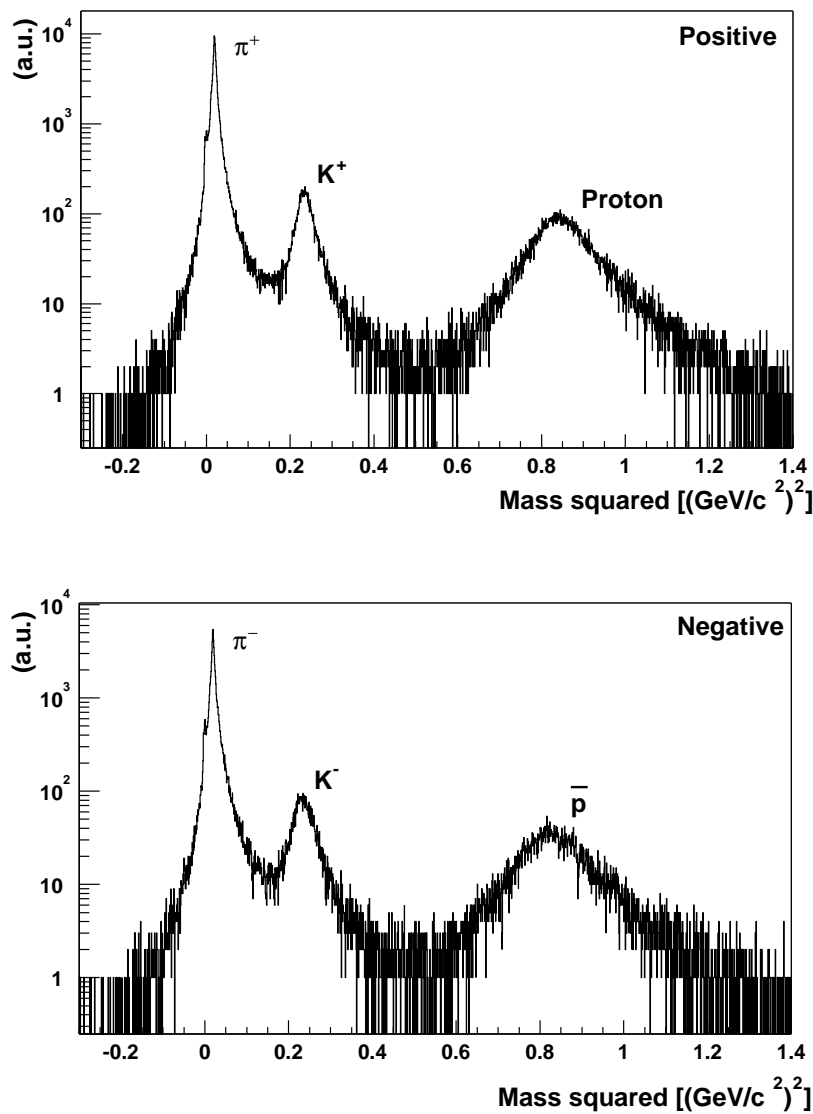


Figure B.8: Mass squared distribution for positive particles (top) and negative particles (bottom) without a momentum cutoff including all momenta. Going from left to right clear peaks for pions, kaons and protons can be seen in each panel.

## TOF construction pictures



Figure B.9: Construction at Tsukuba. [1996–1997]



Figure B.10: Construction at BNL. [1998–1999]



Figure B.11: Installed on PHENIX east central arm. August, 1999

# Appendix C

## Data Tables

### C.1 $p_T$ Spectra Data Tables

The invariant yields for  $\pi^\pm$ ,  $K^\pm$ ,  $p$  and  $\bar{p}$  in Au+Au collisions at  $\sqrt{s_{\text{NN}}} = 200$  GeV at mid-rapidity are tabulated in Tables C.1 – C.20. The data presented here are for the the minimum bias events and each centrality bin (0–5%, 5–10%, 10–15%, 15–20%, 20–30%, ..., 70–80%, 80–92%, and 60–92%). Errors are statistical only.

Table C.1: Invariant yields for  $\pi^+$  at mid-rapidity in the minimum bias, 0–5%, 5–10%, and 10–15% centrality bins, normalized to one unit rapidity. Errors are statistical only.

$p_T$ [GeV/c]	Minimum bias	0–5%	5–10%	10–15%
0.25	1.07e+02 ± 8.8e-01	3.29e+02 ± 2.7e+00	2.76e+02 ± 2.3e+00	2.39e+02 ± 2.0e+00
0.35	6.06e+01 ± 5.0e-01	1.97e+02 ± 1.6e+00	1.64e+02 ± 1.4e+00	1.39e+02 ± 1.2e+00
0.45	3.63e+01 ± 3.1e-01	1.20e+02 ± 1.1e+00	9.93e+01 ± 8.7e-01	8.41e+01 ± 7.4e-01
0.55	2.18e+01 ± 2.0e-01	7.26e+01 ± 6.7e-01	6.02e+01 ± 5.6e-01	5.08e+01 ± 4.7e-01
0.65	1.34e+01 ± 1.3e-01	4.49e+01 ± 4.5e-01	3.74e+01 ± 3.8e-01	3.16e+01 ± 3.2e-01
0.75	8.71e+00 ± 9.5e-02	2.93e+01 ± 3.3e-01	2.43e+01 ± 2.7e-01	2.05e+01 ± 2.3e-01
0.85	5.41e+00 ± 6.3e-02	1.82e+01 ± 2.2e-01	1.53e+01 ± 1.8e-01	1.29e+01 ± 1.6e-01
0.95	3.59e+00 ± 4.5e-02	1.21e+01 ± 1.6e-01	1.01e+01 ± 1.3e-01	8.56e+00 ± 1.1e-01
1.05	2.35e+00 ± 3.1e-02	7.96e+00 ± 1.1e-01	6.56e+00 ± 9.3e-02	5.56e+00 ± 8.0e-02
1.15	1.58e+00 ± 2.2e-02	5.32e+00 ± 8.0e-02	4.47e+00 ± 6.8e-02	3.72e+00 ± 5.7e-02
1.25	1.05e+00 ± 1.5e-02	3.55e+00 ± 5.7e-02	2.99e+00 ± 4.9e-02	2.51e+00 ± 4.2e-02
1.35	7.59e-01 ± 1.2e-02	2.55e+00 ± 4.5e-02	2.15e+00 ± 3.9e-02	1.81e+00 ± 3.3e-02
1.45	5.16e-01 ± 8.3e-03	1.72e+00 ± 3.3e-02	1.45e+00 ± 2.8e-02	1.23e+00 ± 2.5e-02
1.55	3.37e-01 ± 5.6e-03	1.13e+00 ± 2.3e-02	9.36e-01 ± 2.0e-02	7.93e-01 ± 1.7e-02
1.65	2.44e-01 ± 4.2e-03	8.05e-01 ± 1.8e-02	6.68e-01 ± 1.6e-02	5.78e-01 ± 1.4e-02
1.75	1.77e-01 ± 3.3e-03	5.70e-01 ± 1.4e-02	4.84e-01 ± 1.3e-02	4.19e-01 ± 1.1e-02
1.85	1.27e-01 ± 2.4e-03	4.18e-01 ± 1.2e-02	3.42e-01 ± 1.0e-02	2.99e-01 ± 9.1e-03
1.95	9.01e-02 ± 1.9e-03	2.80e-01 ± 9.0e-03	2.50e-01 ± 8.3e-03	2.07e-01 ± 7.3e-03
2.05	6.68e-02 ± 1.2e-03	2.09e-01 ± 6.1e-03	1.82e-01 ± 5.6e-03	1.56e-01 ± 5.0e-03
2.15	4.71e-02 ± 8.9e-04	1.36e-01 ± 4.8e-03	1.27e-01 ± 4.6e-03	1.05e-01 ± 4.1e-03
2.25	3.27e-02 ± 6.8e-04	9.10e-02 ± 3.8e-03	8.06e-02 ± 3.5e-03	8.05e-02 ± 3.5e-03
2.35	2.60e-02 ± 6.2e-04	7.20e-02 ± 3.6e-03	6.28e-02 ± 3.3e-03	5.78e-02 ± 3.1e-03
2.45	1.94e-02 ± 5.3e-04	5.40e-02 ± 3.2e-03	4.57e-02 ± 2.9e-03	4.06e-02 ± 2.7e-03
2.55	1.49e-02 ± 4.7e-04	3.78e-02 ± 2.8e-03	3.59e-02 ± 2.7e-03	3.18e-02 ± 2.5e-03
2.65	1.13e-02 ± 4.2e-04	2.65e-02 ± 2.5e-03	2.50e-02 ± 2.4e-03	2.44e-02 ± 2.3e-03
2.75	9.30e-03 ± 4.0e-04	2.27e-02 ± 2.5e-03	2.19e-02 ± 2.4e-03	1.83e-02 ± 2.1e-03
2.85	6.20e-03 ± 3.2e-04	1.28e-02 ± 1.9e-03	1.21e-02 ± 1.8e-03	1.30e-02 ± 1.8e-03
2.95	5.17e-03 ± 3.1e-04	1.03e-02 ± 1.8e-03	1.08e-02 ± 1.8e-03	1.04e-02 ± 1.8e-03

Table C.2: Invariant yields for  $\pi^+$  at mid-rapidity in 15–20%, 20–30%, 30–40%, and 40–50% centrality bins, normalized to one unit rapidity. Errors are statistical only.

$p_T$ [GeV/c]	15–20%	20–30%	30–40%	40–50%
0.25	2.04e+02 $\pm$ 1.7e+00	1.57e+02 $\pm$ 1.3e+00	1.07e+02 $\pm$ 8.9e-01	6.84e+01 $\pm$ 5.7e-01
0.35	1.18e+02 $\pm$ 9.9e-01	8.82e+01 $\pm$ 7.4e-01	5.86e+01 $\pm$ 4.9e-01	3.67e+01 $\pm$ 3.1e-01
0.45	7.09e+01 $\pm$ 6.2e-01	5.27e+01 $\pm$ 4.6e-01	3.46e+01 $\pm$ 3.0e-01	2.15e+01 $\pm$ 1.9e-01
0.55	4.28e+01 $\pm$ 4.0e-01	3.17e+01 $\pm$ 2.9e-01	2.06e+01 $\pm$ 1.9e-01	1.26e+01 $\pm$ 1.2e-01
0.65	2.65e+01 $\pm$ 2.7e-01	1.95e+01 $\pm$ 2.0e-01	1.26e+01 $\pm$ 1.3e-01	7.66e+00 $\pm$ 8.0e-02
0.75	1.73e+01 $\pm$ 2.0e-01	1.27e+01 $\pm$ 1.4e-01	8.29e+00 $\pm$ 9.4e-02	4.99e+00 $\pm$ 5.8e-02
0.85	1.07e+01 $\pm$ 1.3e-01	7.94e+00 $\pm$ 9.5e-02	5.10e+00 $\pm$ 6.3e-02	3.04e+00 $\pm$ 3.9e-02
0.95	7.12e+00 $\pm$ 9.6e-02	5.31e+00 $\pm$ 7.0e-02	3.38e+00 $\pm$ 4.6e-02	2.02e+00 $\pm$ 2.9e-02
1.05	4.77e+00 $\pm$ 6.9e-02	3.49e+00 $\pm$ 4.9e-02	2.22e+00 $\pm$ 3.2e-02	1.30e+00 $\pm$ 2.0e-02
1.15	3.16e+00 $\pm$ 5.0e-02	2.34e+00 $\pm$ 3.5e-02	1.50e+00 $\pm$ 2.4e-02	8.78e-01 $\pm$ 1.5e-02
1.25	2.10e+00 $\pm$ 3.6e-02	1.56e+00 $\pm$ 2.5e-02	9.99e-01 $\pm$ 1.7e-02	5.98e-01 $\pm$ 1.1e-02
1.35	1.52e+00 $\pm$ 2.9e-02	1.12e+00 $\pm$ 2.0e-02	7.17e-01 $\pm$ 1.4e-02	4.26e-01 $\pm$ 9.0e-03
1.45	1.05e+00 $\pm$ 2.2e-02	7.57e-01 $\pm$ 1.5e-02	4.98e-01 $\pm$ 1.0e-02	2.91e-01 $\pm$ 6.9e-03
1.55	6.78e-01 $\pm$ 1.5e-02	5.07e-01 $\pm$ 1.0e-02	3.24e-01 $\pm$ 7.4e-03	1.97e-01 $\pm$ 5.2e-03
1.65	4.93e-01 $\pm$ 1.2e-02	3.67e-01 $\pm$ 8.3e-03	2.31e-01 $\pm$ 5.9e-03	1.42e-01 $\pm$ 4.2e-03
1.75	3.60e-01 $\pm$ 1.0e-02	2.67e-01 $\pm$ 6.7e-03	1.69e-01 $\pm$ 4.9e-03	1.03e-01 $\pm$ 3.5e-03
1.85	2.56e-01 $\pm$ 8.2e-03	1.92e-01 $\pm$ 5.3e-03	1.22e-01 $\pm$ 3.9e-03	7.29e-02 $\pm$ 2.8e-03
1.95	1.78e-01 $\pm$ 6.6e-03	1.38e-01 $\pm$ 4.3e-03	8.80e-02 $\pm$ 3.3e-03	5.80e-02 $\pm$ 2.5e-03
2.05	1.35e-01 $\pm$ 4.6e-03	1.00e-01 $\pm$ 2.9e-03	6.67e-02 $\pm$ 2.3e-03	4.13e-02 $\pm$ 1.7e-03
2.15	1.02e-01 $\pm$ 4.0e-03	7.41e-02 $\pm$ 2.4e-03	4.90e-02 $\pm$ 1.9e-03	2.92e-02 $\pm$ 1.4e-03
2.25	6.65e-02 $\pm$ 3.1e-03	5.16e-02 $\pm$ 2.0e-03	3.58e-02 $\pm$ 1.6e-03	2.09e-02 $\pm$ 1.2e-03
2.35	5.43e-02 $\pm$ 3.0e-03	4.12e-02 $\pm$ 1.9e-03	2.84e-02 $\pm$ 1.5e-03	1.87e-02 $\pm$ 1.2e-03
2.45	3.97e-02 $\pm$ 2.6e-03	3.28e-02 $\pm$ 1.7e-03	2.27e-02 $\pm$ 1.4e-03	1.21e-02 $\pm$ 9.8e-04
2.55	2.88e-02 $\pm$ 2.4e-03	2.41e-02 $\pm$ 1.5e-03	1.70e-02 $\pm$ 1.3e-03	1.11e-02 $\pm$ 1.0e-03
2.65	2.21e-02 $\pm$ 2.2e-03	1.85e-02 $\pm$ 1.4e-03	1.40e-02 $\pm$ 1.2e-03	8.92e-03 $\pm$ 9.5e-04
2.75	1.58e-02 $\pm$ 2.0e-03	1.55e-02 $\pm$ 1.4e-03	1.20e-02 $\pm$ 1.2e-03	7.80e-03 $\pm$ 9.5e-04
2.85	1.37e-02 $\pm$ 1.9e-03	1.03e-02 $\pm$ 1.1e-03	7.69e-03 $\pm$ 9.7e-04	5.80e-03 $\pm$ 8.3e-04
2.95	1.08e-02 $\pm$ 1.8e-03	9.32e-03 $\pm$ 1.2e-03	6.39e-03 $\pm$ 9.6e-04	4.49e-03 $\pm$ 7.9e-04

Table C.3: Invariant yields for  $\pi^+$  at mid-rapidity in 50–60%, 60–70%, 70–80%, and 80–92% centrality bins, normalized to one unit rapidity. Errors are statistical only.

$p_T$ [GeV/c]	50–60%	60–70%	70–80%	80–92%
0.25	4.10e+01 $\pm$ 3.4e-01	2.19e+01 $\pm$ 1.9e-01	1.03e+01 $\pm$ 9.2e-02	5.20e+00 $\pm$ 5.0e-02
0.35	2.17e+01 $\pm$ 1.9e-01	1.13e+01 $\pm$ 1.0e-01	5.27e+00 $\pm$ 5.0e-02	2.75e+00 $\pm$ 2.8e-02
0.45	1.24e+01 $\pm$ 1.1e-01	6.37e+00 $\pm$ 6.0e-02	2.95e+00 $\pm$ 3.1e-02	1.49e+00 $\pm$ 1.8e-02
0.55	7.20e+00 $\pm$ 7.0e-02	3.65e+00 $\pm$ 3.8e-02	1.62e+00 $\pm$ 1.9e-02	8.20e-01 $\pm$ 1.1e-02
0.65	4.33e+00 $\pm$ 4.7e-02	2.18e+00 $\pm$ 2.6e-02	9.63e-01 $\pm$ 1.3e-02	4.72e-01 $\pm$ 8.1e-03
0.75	2.78e+00 $\pm$ 3.4e-02	1.36e+00 $\pm$ 1.9e-02	5.91e-01 $\pm$ 9.9e-03	2.69e-01 $\pm$ 5.9e-03
0.85	1.67e+00 $\pm$ 2.3e-02	8.36e-01 $\pm$ 1.3e-02	3.53e-01 $\pm$ 7.1e-03	1.63e-01 $\pm$ 4.4e-03
0.95	1.11e+00 $\pm$ 1.7e-02	5.29e-01 $\pm$ 9.6e-03	2.22e-01 $\pm$ 5.4e-03	1.02e-01 $\pm$ 3.4e-03
1.05	7.11e-01 $\pm$ 1.2e-02	3.51e-01 $\pm$ 7.3e-03	1.41e-01 $\pm$ 4.1e-03	6.51e-02 $\pm$ 2.6e-03
1.15	4.71e-01 $\pm$ 9.2e-03	2.21e-01 $\pm$ 5.4e-03	1.01e-01 $\pm$ 3.4e-03	4.48e-02 $\pm$ 2.2e-03
1.25	3.14e-01 $\pm$ 6.9e-03	1.51e-01 $\pm$ 4.3e-03	6.06e-02 $\pm$ 2.5e-03	2.63e-02 $\pm$ 1.6e-03
1.35	2.31e-01 $\pm$ 5.8e-03	1.10e-01 $\pm$ 3.6e-03	4.25e-02 $\pm$ 2.1e-03	2.07e-02 $\pm$ 1.5e-03
1.45	1.59e-01 $\pm$ 4.6e-03	7.17e-02 $\pm$ 2.8e-03	3.04e-02 $\pm$ 1.8e-03	1.30e-02 $\pm$ 1.1e-03
1.55	1.02e-01 $\pm$ 3.4e-03	4.72e-02 $\pm$ 2.2e-03	1.89e-02 $\pm$ 1.3e-03	8.48e-03 $\pm$ 8.8e-04
1.65	7.47e-02 $\pm$ 2.8e-03	3.50e-02 $\pm$ 1.8e-03	1.52e-02 $\pm$ 1.2e-03	7.00e-03 $\pm$ 8.1e-04
1.75	5.60e-02 $\pm$ 2.4e-03	2.63e-02 $\pm$ 1.6e-03	1.03e-02 $\pm$ 1.0e-03	5.37e-03 $\pm$ 7.1e-04
1.85	3.80e-02 $\pm$ 2.0e-03	1.92e-02 $\pm$ 1.3e-03	8.04e-03 $\pm$ 8.7e-04	3.87e-03 $\pm$ 6.0e-04
1.95	2.86e-02 $\pm$ 1.7e-03	1.41e-02 $\pm$ 1.2e-03	6.06e-03 $\pm$ 7.6e-04	2.26e-03 $\pm$ 4.6e-04
2.05	2.26e-02 $\pm$ 1.2e-03	1.12e-02 $\pm$ 8.4e-04	4.34e-03 $\pm$ 5.3e-04	1.56e-03 $\pm$ 3.1e-04
2.15	1.60e-02 $\pm$ 1.0e-03	6.73e-03 $\pm$ 6.6e-04	3.09e-03 $\pm$ 4.5e-04	1.23e-03 $\pm$ 2.8e-04
2.25	1.13e-02 $\pm$ 8.6e-04	5.46e-03 $\pm$ 5.9e-04	2.43e-03 $\pm$ 4.0e-04	8.48e-04 $\pm$ 2.3e-04
2.35	9.73e-03 $\pm$ 8.5e-04	4.42e-03 $\pm$ 5.7e-04	1.98e-03 $\pm$ 3.9e-04	8.16e-04 $\pm$ 2.5e-04
2.45	7.73e-03 $\pm$ 7.8e-04	3.27e-03 $\pm$ 5.0e-04	1.30e-03 $\pm$ 3.2e-04	3.19e-04 $\pm$ 1.6e-04
2.55	5.77e-03 $\pm$ 7.2e-04	3.38e-03 $\pm$ 5.5e-04	1.17e-03 $\pm$ 3.3e-04	5.92e-04 $\pm$ 2.3e-04
2.65	4.48e-03 $\pm$ 6.7e-04	2.82e-03 $\pm$ 5.2e-04	5.70e-04 $\pm$ 2.4e-04	3.37e-04 $\pm$ 1.8e-04
2.75	3.84e-03 $\pm$ 6.7e-04	1.72e-03 $\pm$ 4.4e-04	8.51e-04 $\pm$ 3.2e-04	4.22e-04 $\pm$ 2.2e-04
2.85	2.30e-03 $\pm$ 5.2e-04	1.35e-03 $\pm$ 4.0e-04	6.79e-04 $\pm$ 2.9e-04	1.65e-04 $\pm$ 1.4e-04
2.95	2.16e-03 $\pm$ 5.5e-04	1.16e-03 $\pm$ 4.0e-04	2.88e-04 $\pm$ 2.0e-04	1.90e-04 $\pm$ 1.6e-04

Table C.4: Invariant yields for  $\pi^-$  at mid-rapidity in the minimum bias, 0–5%, 5–10%, and 10–15% centrality bins, normalized to one unit rapidity. Errors are statistical only.

$p_T$ [GeV/c]	Minimum bias	0–5%	5–10%	10–15%
0.25	1.02e+02 $\pm$ 7.9e-01	3.15e+02 $\pm$ 2.4e+00	2.71e+02 $\pm$ 2.1e+00	2.27e+02 $\pm$ 1.8e+00
0.35	5.92e+01 $\pm$ 4.6e-01	1.94e+02 $\pm$ 1.5e+00	1.64e+02 $\pm$ 1.3e+00	1.35e+02 $\pm$ 1.1e+00
0.45	3.56e+01 $\pm$ 2.9e-01	1.19e+02 $\pm$ 9.8e-01	9.93e+01 $\pm$ 8.2e-01	8.18e+01 $\pm$ 6.8e-01
0.55	2.18e+01 $\pm$ 1.9e-01	7.37e+01 $\pm$ 6.5e-01	6.17e+01 $\pm$ 5.4e-01	5.04e+01 $\pm$ 4.5e-01
0.65	1.34e+01 $\pm$ 1.2e-01	4.57e+01 $\pm$ 4.3e-01	3.82e+01 $\pm$ 3.6e-01	3.15e+01 $\pm$ 3.0e-01
0.75	8.36e+00 $\pm$ 8.2e-02	2.86e+01 $\pm$ 2.9e-01	2.40e+01 $\pm$ 2.4e-01	1.96e+01 $\pm$ 2.0e-01
0.85	5.44e+00 $\pm$ 5.7e-02	1.86e+01 $\pm$ 2.0e-01	1.56e+01 $\pm$ 1.7e-01	1.28e+01 $\pm$ 1.4e-01
0.95	3.58e+00 $\pm$ 4.1e-02	1.22e+01 $\pm$ 1.4e-01	1.02e+01 $\pm$ 1.2e-01	8.47e+00 $\pm$ 1.0e-01
1.05	2.35e+00 $\pm$ 2.8e-02	8.02e+00 $\pm$ 1.0e-01	6.75e+00 $\pm$ 8.7e-02	5.57e+00 $\pm$ 7.2e-02
1.15	1.62e+00 $\pm$ 2.1e-02	5.55e+00 $\pm$ 7.7e-02	4.64e+00 $\pm$ 6.5e-02	3.83e+00 $\pm$ 5.5e-02
1.25	1.04e+00 $\pm$ 1.4e-02	3.53e+00 $\pm$ 5.2e-02	2.94e+00 $\pm$ 4.4e-02	2.46e+00 $\pm$ 3.8e-02
1.35	7.54e-01 $\pm$ 1.1e-02	2.55e+00 $\pm$ 4.1e-02	2.19e+00 $\pm$ 3.6e-02	1.80e+00 $\pm$ 3.0e-02
1.45	5.07e-01 $\pm$ 7.6e-03	1.71e+00 $\pm$ 3.0e-02	1.48e+00 $\pm$ 2.7e-02	1.22e+00 $\pm$ 2.2e-02
1.55	3.61e-01 $\pm$ 5.7e-03	1.20e+00 $\pm$ 2.3e-02	1.02e+00 $\pm$ 2.0e-02	8.63e-01 $\pm$ 1.8e-02
1.65	2.46e-01 $\pm$ 4.0e-03	8.02e-01 $\pm$ 1.7e-02	6.94e-01 $\pm$ 1.5e-02	5.86e-01 $\pm$ 1.3e-02
1.75	1.73e-01 $\pm$ 3.0e-03	5.65e-01 $\pm$ 1.3e-02	4.91e-01 $\pm$ 1.2e-02	4.10e-01 $\pm$ 1.0e-02
1.85	1.25e-01 $\pm$ 2.3e-03	4.05e-01 $\pm$ 1.1e-02	3.48e-01 $\pm$ 9.6e-03	3.00e-01 $\pm$ 8.5e-03
1.95	8.97e-02 $\pm$ 1.8e-03	2.85e-01 $\pm$ 8.8e-03	2.53e-01 $\pm$ 8.1e-03	2.12e-01 $\pm$ 7.1e-03
2.05	6.10e-02 $\pm$ 1.1e-03	1.89e-01 $\pm$ 5.8e-03	1.64e-01 $\pm$ 5.4e-03	1.42e-01 $\pm$ 4.8e-03
2.15	4.43e-02 $\pm$ 8.7e-04	1.32e-01 $\pm$ 4.8e-03	1.20e-01 $\pm$ 4.5e-03	1.01e-01 $\pm$ 4.0e-03
2.25	3.20e-02 $\pm$ 7.0e-04	9.24e-02 $\pm$ 4.0e-03	8.31e-02 $\pm$ 3.8e-03	7.21e-02 $\pm$ 3.4e-03
2.35	2.52e-02 $\pm$ 6.3e-04	7.07e-02 $\pm$ 3.7e-03	6.29e-02 $\pm$ 3.5e-03	5.95e-02 $\pm$ 3.3e-03
2.45	1.79e-02 $\pm$ 5.1e-04	4.71e-02 $\pm$ 3.0e-03	4.47e-02 $\pm$ 2.9e-03	3.97e-02 $\pm$ 2.7e-03
2.55	1.41e-02 $\pm$ 4.8e-04	3.50e-02 $\pm$ 2.8e-03	3.33e-02 $\pm$ 2.7e-03	3.28e-02 $\pm$ 2.7e-03
2.65	1.06e-02 $\pm$ 4.1e-04	2.69e-02 $\pm$ 2.5e-03	2.36e-02 $\pm$ 2.3e-03	2.22e-02 $\pm$ 2.2e-03
2.75	8.05e-03 $\pm$ 3.7e-04	1.99e-02 $\pm$ 2.3e-03	1.67e-02 $\pm$ 2.1e-03	1.61e-02 $\pm$ 2.0e-03
2.85	6.45e-03 $\pm$ 3.5e-04	1.45e-02 $\pm$ 2.1e-03	1.63e-02 $\pm$ 2.2e-03	1.21e-02 $\pm$ 1.9e-03
2.95	4.95e-03 $\pm$ 3.2e-04	1.08e-02 $\pm$ 1.9e-03	1.16e-02 $\pm$ 2.0e-03	1.03e-02 $\pm$ 1.8e-03

Table C.5: Invariant yields for  $\pi^-$  at mid-rapidity in 15–20%, 20–30%, 30–40%, and 40–50% centrality bins, normalized to one unit rapidity. Errors are statistical only.

$p_T$ [GeV/c]	15–20%	20–30%	30–40%	40–50%
0.25	1.95e+02 $\pm$ 1.5e+00	1.51e+02 $\pm$ 1.2e+00	1.02e+02 $\pm$ 7.9e-01	6.53e+01 $\pm$ 5.1e-01
0.35	1.13e+02 $\pm$ 9.0e-01	8.62e+01 $\pm$ 6.8e-01	5.68e+01 $\pm$ 4.5e-01	3.56e+01 $\pm$ 2.8e-01
0.45	6.86e+01 $\pm$ 5.7e-01	5.18e+01 $\pm$ 4.3e-01	3.36e+01 $\pm$ 2.8e-01	2.08e+01 $\pm$ 1.7e-01
0.55	4.22e+01 $\pm$ 3.7e-01	3.17e+01 $\pm$ 2.8e-01	2.04e+01 $\pm$ 1.8e-01	1.24e+01 $\pm$ 1.1e-01
0.65	2.61e+01 $\pm$ 2.5e-01	1.95e+01 $\pm$ 1.8e-01	1.26e+01 $\pm$ 1.2e-01	7.57e+00 $\pm$ 7.4e-02
0.75	1.63e+01 $\pm$ 1.7e-01	1.22e+01 $\pm$ 1.2e-01	7.81e+00 $\pm$ 8.0e-02	4.67e+00 $\pm$ 4.9e-02
0.85	1.06e+01 $\pm$ 1.2e-01	7.96e+00 $\pm$ 8.7e-02	5.06e+00 $\pm$ 5.7e-02	3.04e+00 $\pm$ 3.5e-02
0.95	7.01e+00 $\pm$ 8.6e-02	5.31e+00 $\pm$ 6.3e-02	3.37e+00 $\pm$ 4.1e-02	1.99e+00 $\pm$ 2.6e-02
1.05	4.68e+00 $\pm$ 6.2e-02	3.45e+00 $\pm$ 4.4e-02	2.18e+00 $\pm$ 2.9e-02	1.30e+00 $\pm$ 1.8e-02
1.15	3.19e+00 $\pm$ 4.6e-02	2.36e+00 $\pm$ 3.3e-02	1.52e+00 $\pm$ 2.2e-02	8.96e-01 $\pm$ 1.4e-02
1.25	2.05e+00 $\pm$ 3.2e-02	1.55e+00 $\pm$ 2.3e-02	9.75e-01 $\pm$ 1.5e-02	5.68e-01 $\pm$ 9.8e-03
1.35	1.49e+00 $\pm$ 2.6e-02	1.10e+00 $\pm$ 1.8e-02	7.11e-01 $\pm$ 1.2e-02	4.18e-01 $\pm$ 8.2e-03
1.45	9.90e-01 $\pm$ 1.9e-02	7.55e-01 $\pm$ 1.3e-02	4.76e-01 $\pm$ 9.2e-03	2.75e-01 $\pm$ 6.1e-03
1.55	7.11e-01 $\pm$ 1.5e-02	5.41e-01 $\pm$ 1.1e-02	3.42e-01 $\pm$ 7.4e-03	2.01e-01 $\pm$ 5.0e-03
1.65	4.85e-01 $\pm$ 1.2e-02	3.71e-01 $\pm$ 7.9e-03	2.37e-01 $\pm$ 5.7e-03	1.40e-01 $\pm$ 3.9e-03
1.75	3.43e-01 $\pm$ 9.2e-03	2.56e-01 $\pm$ 6.1e-03	1.68e-01 $\pm$ 4.5e-03	9.60e-02 $\pm$ 3.1e-03
1.85	2.38e-01 $\pm$ 7.3e-03	1.93e-01 $\pm$ 5.0e-03	1.20e-01 $\pm$ 3.7e-03	7.36e-02 $\pm$ 2.7e-03
1.95	1.74e-01 $\pm$ 6.2e-03	1.36e-01 $\pm$ 4.1e-03	8.73e-02 $\pm$ 3.1e-03	5.34e-02 $\pm$ 2.3e-03
2.05	1.16e-01 $\pm$ 4.2e-03	9.65e-02 $\pm$ 2.9e-03	6.46e-02 $\pm$ 2.2e-03	3.64e-02 $\pm$ 1.6e-03
2.15	8.98e-02 $\pm$ 3.7e-03	6.97e-02 $\pm$ 2.4e-03	4.55e-02 $\pm$ 1.9e-03	2.72e-02 $\pm$ 1.4e-03
2.25	6.55e-02 $\pm$ 3.2e-03	5.15e-02 $\pm$ 2.1e-03	3.60e-02 $\pm$ 1.7e-03	1.95e-02 $\pm$ 1.2e-03
2.35	5.02e-02 $\pm$ 2.9e-03	3.83e-02 $\pm$ 1.9e-03	2.83e-02 $\pm$ 1.6e-03	1.76e-02 $\pm$ 1.2e-03
2.45	3.62e-02 $\pm$ 2.5e-03	2.84e-02 $\pm$ 1.6e-03	1.94e-02 $\pm$ 1.3e-03	1.33e-02 $\pm$ 1.0e-03
2.55	2.55e-02 $\pm$ 2.3e-03	2.37e-02 $\pm$ 1.6e-03	1.57e-02 $\pm$ 1.3e-03	1.06e-02 $\pm$ 1.0e-03
2.65	2.01e-02 $\pm$ 2.1e-03	1.68e-02 $\pm$ 1.4e-03	1.30e-02 $\pm$ 1.2e-03	8.20e-03 $\pm$ 9.1e-04
2.75	1.57e-02 $\pm$ 1.9e-03	1.35e-02 $\pm$ 1.3e-03	1.06e-02 $\pm$ 1.1e-03	6.35e-03 $\pm$ 8.5e-04
2.85	1.30e-02 $\pm$ 1.9e-03	1.03e-02 $\pm$ 1.2e-03	8.61e-03 $\pm$ 1.1e-03	5.10e-03 $\pm$ 8.3e-04
2.95	9.44e-03 $\pm$ 1.7e-03	8.45e-03 $\pm$ 1.2e-03	6.16e-03 $\pm$ 9.8e-04	3.72e-03 $\pm$ 7.5e-04

Table C.6: Invariant yields for  $\pi^-$  at mid-rapidity in 50–60%, 60–70%, 70–80%, and 80–92% centrality bins, normalized to one unit rapidity. Errors are statistical only.

$p_T$ [GeV/c]	50–60%	60–70%	70–80%	80–92%
0.25	3.92e+01 $\pm$ 3.1e-01	2.07e+01 $\pm$ 1.7e-01	9.77e+00 $\pm$ 8.2e-02	5.03e+00 $\pm$ 4.5e-02
0.35	2.10e+01 $\pm$ 1.7e-01	1.09e+01 $\pm$ 9.0e-02	5.19e+00 $\pm$ 4.6e-02	2.67e+00 $\pm$ 2.6e-02
0.45	1.21e+01 $\pm$ 1.0e-01	6.21e+00 $\pm$ 5.5e-02	2.84e+00 $\pm$ 2.8e-02	1.45e+00 $\pm$ 1.6e-02
0.55	7.13e+00 $\pm$ 6.6e-02	3.59e+00 $\pm$ 3.5e-02	1.62e+00 $\pm$ 1.8e-02	8.13e-01 $\pm$ 1.1e-02
0.65	4.30e+00 $\pm$ 4.4e-02	2.16e+00 $\pm$ 2.4e-02	9.32e-01 $\pm$ 1.2e-02	4.54e-01 $\pm$ 7.3e-03
0.75	2.61e+00 $\pm$ 2.9e-02	1.30e+00 $\pm$ 1.6e-02	5.61e-01 $\pm$ 8.6e-03	2.70e-01 $\pm$ 5.3e-03
0.85	1.68e+00 $\pm$ 2.1e-02	8.30e-01 $\pm$ 1.2e-02	3.52e-01 $\pm$ 6.4e-03	1.59e-01 $\pm$ 3.9e-03
0.95	1.10e+00 $\pm$ 1.5e-02	5.26e-01 $\pm$ 8.7e-03	2.27e-01 $\pm$ 5.0e-03	1.07e-01 $\pm$ 3.2e-03
1.05	7.13e-01 $\pm$ 1.1e-02	3.45e-01 $\pm$ 6.6e-03	1.41e-01 $\pm$ 3.8e-03	6.63e-02 $\pm$ 2.4e-03
1.15	4.88e-01 $\pm$ 8.8e-03	2.32e-01 $\pm$ 5.2e-03	9.75e-02 $\pm$ 3.1e-03	4.46e-02 $\pm$ 2.0e-03
1.25	3.12e-01 $\pm$ 6.3e-03	1.47e-01 $\pm$ 3.8e-03	6.31e-02 $\pm$ 2.4e-03	2.65e-02 $\pm$ 1.5e-03
1.35	2.29e-01 $\pm$ 5.3e-03	1.05e-01 $\pm$ 3.2e-03	4.17e-02 $\pm$ 1.9e-03	2.02e-02 $\pm$ 1.3e-03
1.45	1.51e-01 $\pm$ 4.1e-03	7.32e-02 $\pm$ 2.6e-03	2.81e-02 $\pm$ 1.6e-03	1.28e-02 $\pm$ 1.0e-03
1.55	1.10e-01 $\pm$ 3.4e-03	5.15e-02 $\pm$ 2.2e-03	2.11e-02 $\pm$ 1.4e-03	9.27e-03 $\pm$ 8.8e-04
1.65	7.11e-02 $\pm$ 2.6e-03	3.83e-02 $\pm$ 1.8e-03	1.53e-02 $\pm$ 1.1e-03	6.56e-03 $\pm$ 7.3e-04
1.75	5.38e-02 $\pm$ 2.2e-03	2.51e-02 $\pm$ 1.4e-03	1.08e-02 $\pm$ 9.5e-04	5.14e-03 $\pm$ 6.5e-04
1.85	4.00e-02 $\pm$ 1.9e-03	1.87e-02 $\pm$ 1.2e-03	8.06e-03 $\pm$ 8.2e-04	3.51e-03 $\pm$ 5.3e-04
1.95	2.88e-02 $\pm$ 1.6e-03	1.30e-02 $\pm$ 1.1e-03	6.03e-03 $\pm$ 7.3e-04	2.70e-03 $\pm$ 4.8e-04
2.05	2.04e-02 $\pm$ 1.2e-03	8.63e-03 $\pm$ 7.4e-04	4.23e-03 $\pm$ 5.3e-04	1.40e-03 $\pm$ 3.0e-04
2.15	1.53e-02 $\pm$ 1.0e-03	6.88e-03 $\pm$ 6.7e-04	3.17e-03 $\pm$ 4.6e-04	1.25e-03 $\pm$ 2.9e-04
2.25	1.08e-02 $\pm$ 8.8e-04	4.71e-03 $\pm$ 5.7e-04	1.89e-03 $\pm$ 3.7e-04	8.66e-04 $\pm$ 2.5e-04
2.35	8.95e-03 $\pm$ 8.4e-04	4.42e-03 $\pm$ 5.8e-04	1.96e-03 $\pm$ 4.0e-04	6.65e-04 $\pm$ 2.3e-04
2.45	7.17e-03 $\pm$ 7.6e-04	3.04e-03 $\pm$ 4.9e-04	1.17e-03 $\pm$ 3.1e-04	5.61e-04 $\pm$ 2.1e-04
2.55	5.72e-03 $\pm$ 7.5e-04	2.96e-03 $\pm$ 5.3e-04	1.16e-03 $\pm$ 3.4e-04	3.79e-04 $\pm$ 1.9e-04
2.65	4.94e-03 $\pm$ 7.1e-04	2.21e-03 $\pm$ 4.7e-04	8.05e-04 $\pm$ 2.9e-04	4.14e-04 $\pm$ 2.0e-04
2.75	3.43e-03 $\pm$ 6.3e-04	1.54e-03 $\pm$ 4.2e-04	3.78e-04 $\pm$ 2.1e-04	3.34e-04 $\pm$ 2.0e-04
2.85	2.67e-03 $\pm$ 6.0e-04	1.24e-03 $\pm$ 4.1e-04	2.87e-04 $\pm$ 2.0e-04	2.85e-04 $\pm$ 2.0e-04
2.95	1.73e-03 $\pm$ 5.1e-04	1.25e-03 $\pm$ 4.3e-04	6.75e-04 $\pm$ 3.2e-04	2.04e-04 $\pm$ 1.8e-04

Table C.7: Invariant yields for  $K^+$  at mid-rapidity in the minimum bias, 0–5%, 5–10%, and 10–15% centrality bins, normalized to one unit rapidity. Errors are statistical only.

$p_T$ [GeV/c]	Minimum bias	0–5%	5–10%	10–15%
0.45	5.46e+00 ± 1.1e-01	1.83e+01 ± 3.9e-01	1.50e+01 ± 3.3e-01	1.29e+01 ± 2.8e-01
0.55	4.28e+00 ± 7.8e-02	1.48e+01 ± 2.9e-01	1.20e+01 ± 2.4e-01	9.88e+00 ± 2.0e-01
0.65	3.11e+00 ± 5.4e-02	1.05e+01 ± 2.0e-01	8.75e+00 ± 1.7e-01	7.38e+00 ± 1.4e-01
0.75	2.27e+00 ± 3.9e-02	7.97e+00 ± 1.5e-01	6.48e+00 ± 1.2e-01	5.39e+00 ± 1.0e-01
0.85	1.69e+00 ± 3.0e-02	5.96e+00 ± 1.2e-01	4.81e+00 ± 9.5e-02	4.02e+00 ± 8.1e-02
0.95	1.20e+00 ± 2.2e-02	4.19e+00 ± 8.5e-02	3.47e+00 ± 7.2e-02	2.91e+00 ± 6.1e-02
1.05	9.06e-01 ± 1.7e-02	3.20e+00 ± 6.8e-02	2.61e+00 ± 5.7e-02	2.21e+00 ± 5.0e-02
1.15	6.57e-01 ± 1.3e-02	2.31e+00 ± 5.2e-02	1.91e+00 ± 4.4e-02	1.63e+00 ± 3.9e-02
1.25	4.55e-01 ± 8.9e-03	1.64e+00 ± 3.9e-02	1.32e+00 ± 3.3e-02	1.14e+00 ± 2.9e-02
1.35	3.24e-01 ± 6.5e-03	1.13e+00 ± 2.9e-02	9.63e-01 ± 2.5e-02	7.88e-01 ± 2.2e-02
1.45	2.43e-01 ± 5.1e-03	8.52e-01 ± 2.4e-02	7.33e-01 ± 2.1e-02	6.05e-01 ± 1.8e-02
1.55	1.76e-01 ± 3.8e-03	6.03e-01 ± 1.8e-02	5.16e-01 ± 1.6e-02	4.33e-01 ± 1.4e-02
1.65	1.27e-01 ± 2.9e-03	4.43e-01 ± 1.5e-02	3.84e-01 ± 1.3e-02	3.04e-01 ± 1.1e-02
1.75	9.47e-02 ± 2.3e-03	3.61e-01 ± 1.3e-02	2.76e-01 ± 1.1e-02	2.28e-01 ± 9.3e-03
1.85	7.24e-02 ± 1.8e-03	2.64e-01 ± 1.0e-02	2.17e-01 ± 9.0e-03	1.72e-01 ± 7.7e-03
1.95	5.67e-02 ± 1.5e-03	2.12e-01 ± 9.1e-03	1.67e-01 ± 7.8e-03	1.37e-01 ± 6.9e-03

Table C.8: Invariant yields for  $K^+$  at mid-rapidity in 15–20%, 20–30%, 30–40%, and 40–50% centrality bins, normalized to one unit rapidity. Errors are statistical only.

$p_T$ [GeV/c]	15–20%	20–30%	30–40%	40–50%
0.45	1.04e+01 ± 2.3e-01	7.81e+00 ± 1.7e-01	5.11e+00 ± 1.1e-01	3.28e+00 ± 7.8e-02
0.55	8.30e+00 ± 1.7e-01	6.22e+00 ± 1.2e-01	4.06e+00 ± 8.3e-02	2.43e+00 ± 5.3e-02
0.65	6.20e+00 ± 1.2e-01	4.51e+00 ± 8.5e-02	2.89e+00 ± 5.7e-02	1.78e+00 ± 3.8e-02
0.75	4.46e+00 ± 8.8e-02	3.31e+00 ± 6.2e-02	2.07e+00 ± 4.1e-02	1.26e+00 ± 2.7e-02
0.85	3.36e+00 ± 7.0e-02	2.50e+00 ± 4.9e-02	1.60e+00 ± 3.3e-02	9.00e-01 ± 2.1e-02
0.95	2.40e+00 ± 5.2e-02	1.74e+00 ± 3.6e-02	1.08e+00 ± 2.4e-02	6.46e-01 ± 1.6e-02
1.05	1.81e+00 ± 4.2e-02	1.31e+00 ± 2.8e-02	8.42e-01 ± 2.0e-02	4.82e-01 ± 1.3e-02
1.15	1.29e+00 ± 3.2e-02	9.60e-01 ± 2.2e-02	6.01e-01 ± 1.5e-02	3.48e-01 ± 1.0e-02
1.25	8.82e-01 ± 2.4e-02	6.54e-01 ± 1.6e-02	4.22e-01 ± 1.1e-02	2.34e-01 ± 7.5e-03
1.35	6.60e-01 ± 1.9e-02	4.68e-01 ± 1.2e-02	2.99e-01 ± 8.7e-03	1.70e-01 ± 5.9e-03
1.45	4.91e-01 ± 1.5e-02	3.50e-01 ± 9.9e-03	2.22e-01 ± 7.2e-03	1.20e-01 ± 4.8e-03
1.55	3.55e-01 ± 1.2e-02	2.59e-01 ± 7.9e-03	1.63e-01 ± 5.8e-03	9.25e-02 ± 4.0e-03
1.65	2.62e-01 ± 1.0e-02	1.88e-01 ± 6.3e-03	1.14e-01 ± 4.6e-03	6.22e-02 ± 3.1e-03
1.75	1.92e-01 ± 8.3e-03	1.34e-01 ± 5.1e-03	8.52e-02 ± 3.8e-03	4.81e-02 ± 2.7e-03
1.85	1.48e-01 ± 7.0e-03	1.04e-01 ± 4.2e-03	6.58e-02 ± 3.2e-03	3.66e-02 ± 2.3e-03
1.95	1.14e-01 ± 6.1e-03	8.21e-02 ± 3.7e-03	4.87e-02 ± 2.7e-03	2.91e-02 ± 2.0e-03

Table C.9: Invariant yields for  $K^+$  at mid-rapidity in 50–60%, 60–70%, 70–80%, and 80–92% centrality bins, normalized to one unit rapidity. Errors are statistical only.

$p_T$ [GeV/c]	50–60%	60–70%	70–80%	80–92%
0.45	1.93e+00 $\pm$ 5.0e-02	9.56e-01 $\pm$ 2.9e-02	4.06e-01 $\pm$ 1.7e-02	1.88e-01 $\pm$ 1.1e-02
0.55	1.36e+00 $\pm$ 3.3e-02	6.72e-01 $\pm$ 2.0e-02	2.89e-01 $\pm$ 1.2e-02	1.48e-01 $\pm$ 7.8e-03
0.65	1.01e+00 $\pm$ 2.4e-02	4.81e-01 $\pm$ 1.4e-02	1.88e-01 $\pm$ 8.0e-03	1.02e-01 $\pm$ 5.6e-03
0.75	6.82e-01 $\pm$ 1.7e-02	3.40e-01 $\pm$ 1.1e-02	1.24e-01 $\pm$ 5.8e-03	5.88e-02 $\pm$ 3.9e-03
0.85	4.77e-01 $\pm$ 1.3e-02	2.33e-01 $\pm$ 8.1e-03	9.39e-02 $\pm$ 4.8e-03	3.87e-02 $\pm$ 3.0e-03
0.95	3.51e-01 $\pm$ 1.0e-02	1.69e-01 $\pm$ 6.4e-03	5.66e-02 $\pm$ 3.5e-03	2.99e-02 $\pm$ 2.5e-03
1.05	2.54e-01 $\pm$ 8.2e-03	1.19e-01 $\pm$ 5.1e-03	4.40e-02 $\pm$ 3.0e-03	2.07e-02 $\pm$ 2.0e-03
1.15	1.80e-01 $\pm$ 6.4e-03	7.84e-02 $\pm$ 3.9e-03	3.12e-02 $\pm$ 2.4e-03	1.64e-02 $\pm$ 1.7e-03
1.25	1.28e-01 $\pm$ 5.1e-03	5.43e-02 $\pm$ 3.1e-03	2.07e-02 $\pm$ 1.9e-03	7.94e-03 $\pm$ 1.1e-03
1.35	8.53e-02 $\pm$ 3.9e-03	3.85e-02 $\pm$ 2.5e-03	1.38e-02 $\pm$ 1.5e-03	6.53e-03 $\pm$ 9.9e-04
1.45	6.40e-02 $\pm$ 3.3e-03	2.94e-02 $\pm$ 2.1e-03	1.34e-02 $\pm$ 1.4e-03	5.70e-03 $\pm$ 9.2e-04
1.55	4.73e-02 $\pm$ 2.7e-03	2.10e-02 $\pm$ 1.8e-03	6.85e-03 $\pm$ 1.0e-03	2.84e-03 $\pm$ 6.4e-04
1.65	3.39e-02 $\pm$ 2.2e-03	1.60e-02 $\pm$ 1.5e-03	5.62e-03 $\pm$ 8.9e-04	2.67e-03 $\pm$ 6.1e-04
1.75	2.31e-02 $\pm$ 1.8e-03	1.04e-02 $\pm$ 1.2e-03	4.19e-03 $\pm$ 7.6e-04	1.85e-03 $\pm$ 5.0e-04
1.85	1.72e-02 $\pm$ 1.5e-03	8.75e-03 $\pm$ 1.1e-03	3.39e-03 $\pm$ 6.7e-04	2.09e-03 $\pm$ 5.2e-04
1.95	1.53e-02 $\pm$ 1.4e-03	6.49e-03 $\pm$ 9.2e-04	2.75e-03 $\pm$ 6.1e-04	1.16e-03 $\pm$ 3.9e-04

Table C.10: Invariant yields for  $K^-$  at mid-rapidity in the minimum bias, 0–5%, 5–10%, and 10–15% centrality bins, normalized to one unit rapidity. Errors are statistical only.

$p_T$ [GeV/c]	Minimum bias	0–5%	5–10%	10–15%
0.45	4.87e+00 $\pm$ 9.3e-02	1.64e+01 $\pm$ 3.4e-01	1.36e+01 $\pm$ 2.8e-01	1.12e+01 $\pm$ 2.4e-01
0.55	3.88e+00 $\pm$ 6.7e-02	1.31e+01 $\pm$ 2.4e-01	1.09e+01 $\pm$ 2.0e-01	8.91e+00 $\pm$ 1.7e-01
0.65	2.96e+00 $\pm$ 4.9e-02	1.01e+01 $\pm$ 1.8e-01	8.57e+00 $\pm$ 1.5e-01	6.94e+00 $\pm$ 1.3e-01
0.75	2.20e+00 $\pm$ 3.6e-02	7.69e+00 $\pm$ 1.4e-01	6.27e+00 $\pm$ 1.1e-01	5.14e+00 $\pm$ 9.5e-02
0.85	1.59e+00 $\pm$ 2.6e-02	5.61e+00 $\pm$ 1.0e-01	4.55e+00 $\pm$ 8.4e-02	3.82e+00 $\pm$ 7.2e-02
0.95	1.14e+00 $\pm$ 1.9e-02	4.11e+00 $\pm$ 7.7e-02	3.36e+00 $\pm$ 6.5e-02	2.76e+00 $\pm$ 5.4e-02
1.05	8.50e-01 $\pm$ 1.5e-02	3.03e+00 $\pm$ 6.0e-02	2.53e+00 $\pm$ 5.2e-02	2.05e+00 $\pm$ 4.3e-02
1.15	5.96e-01 $\pm$ 1.0e-02	2.11e+00 $\pm$ 4.4e-02	1.79e+00 $\pm$ 3.8e-02	1.44e+00 $\pm$ 3.2e-02
1.25	4.29e-01 $\pm$ 7.8e-03	1.53e+00 $\pm$ 3.4e-02	1.25e+00 $\pm$ 2.9e-02	1.05e+00 $\pm$ 2.5e-02
1.35	3.23e-01 $\pm$ 6.2e-03	1.15e+00 $\pm$ 2.8e-02	9.45e-01 $\pm$ 2.4e-02	8.03e-01 $\pm$ 2.1e-02
1.45	2.32e-01 $\pm$ 4.6e-03	8.42e-01 $\pm$ 2.2e-02	6.97e-01 $\pm$ 1.9e-02	5.62e-01 $\pm$ 1.6e-02
1.55	1.67e-01 $\pm$ 3.4e-03	5.86e-01 $\pm$ 1.7e-02	4.97e-01 $\pm$ 1.5e-02	4.16e-01 $\pm$ 1.3e-02
1.65	1.21e-01 $\pm$ 2.6e-03	4.42e-01 $\pm$ 1.4e-02	3.82e-01 $\pm$ 1.2e-02	2.93e-01 $\pm$ 1.0e-02
1.75	8.78e-02 $\pm$ 2.0e-03	3.17e-01 $\pm$ 1.1e-02	2.64e-01 $\pm$ 9.6e-03	2.11e-01 $\pm$ 8.2e-03
1.85	6.76e-02 $\pm$ 1.6e-03	2.52e-01 $\pm$ 9.4e-03	2.10e-01 $\pm$ 8.4e-03	1.61e-01 $\pm$ 7.0e-03
1.95	5.10e-02 $\pm$ 1.3e-03	1.83e-01 $\pm$ 7.9e-03	1.53e-01 $\pm$ 7.1e-03	1.22e-01 $\pm$ 6.1e-03

Table C.11: Invariant yields for  $K^-$  at mid-rapidity in 15–20%, 20–30%, 30–40%, and 40–50% centrality bins, normalized to one unit rapidity. Errors are statistical only.

$p_T$ [GeV/c]	15–20%	20–30%	30–40%	40–50%
0.45	9.24e+00 ± 2.0e-01	7.05e+00 ± 1.5e-01	4.60e+00 ± 9.9e-02	2.79e+00 ± 6.4e-02
0.55	7.61e+00 ± 1.5e-01	5.62e+00 ± 1.0e-01	3.68e+00 ± 7.1e-02	2.25e+00 ± 4.7e-02
0.65	5.78e+00 ± 1.1e-01	4.29e+00 ± 7.7e-02	2.74e+00 ± 5.1e-02	1.69e+00 ± 3.4e-02
0.75	4.33e+00 ± 8.1e-02	3.22e+00 ± 5.8e-02	2.04e+00 ± 3.8e-02	1.19e+00 ± 2.5e-02
0.85	3.13e+00 ± 6.0e-02	2.29e+00 ± 4.2e-02	1.49e+00 ± 2.9e-02	8.47e-01 ± 1.8e-02
0.95	2.23e+00 ± 4.5e-02	1.61e+00 ± 3.1e-02	1.04e+00 ± 2.1e-02	6.04e-01 ± 1.4e-02
1.05	1.70e+00 ± 3.7e-02	1.21e+00 ± 2.5e-02	7.74e-01 ± 1.7e-02	4.49e-01 ± 1.1e-02
1.15	1.17e+00 ± 2.7e-02	8.78e-01 ± 1.9e-02	5.39e-01 ± 1.3e-02	3.11e-01 ± 8.4e-03
1.25	8.58e-01 ± 2.1e-02	6.29e-01 ± 1.4e-02	3.87e-01 ± 9.9e-03	2.25e-01 ± 6.8e-03
1.35	6.26e-01 ± 1.7e-02	4.76e-01 ± 1.2e-02	2.97e-01 ± 8.3e-03	1.64e-01 ± 5.5e-03
1.45	4.56e-01 ± 1.4e-02	3.41e-01 ± 9.2e-03	2.09e-01 ± 6.5e-03	1.21e-01 ± 4.5e-03
1.55	3.25e-01 ± 1.1e-02	2.50e-01 ± 7.3e-03	1.43e-01 ± 5.0e-03	8.71e-02 ± 3.7e-03
1.65	2.36e-01 ± 8.9e-03	1.72e-01 ± 5.7e-03	1.07e-01 ± 4.2e-03	6.17e-02 ± 3.0e-03
1.75	1.83e-01 ± 7.4e-03	1.29e-01 ± 4.6e-03	7.79e-02 ± 3.4e-03	4.42e-02 ± 2.4e-03
1.85	1.29e-01 ± 6.0e-03	1.01e-01 ± 4.0e-03	5.84e-02 ± 2.8e-03	3.24e-02 ± 2.0e-03
1.95	1.05e-01 ± 5.5e-03	7.67e-02 ± 3.4e-03	4.31e-02 ± 2.4e-03	2.46e-02 ± 1.8e-03

Table C.12: Invariant yields for  $K^-$  at mid-rapidity in 50–60%, 60–70%, 70–80%, and 80–92% centrality bins, normalized to one unit rapidity. Errors are statistical only.

$p_T$ [GeV/c]	50–60%	60–70%	70–80%	80–92%
0.45	1.73e+00 ± 4.3e-02	8.11e-01 ± 2.5e-02	3.89e-01 ± 1.6e-02	1.82e-01 ± 9.9e-03
0.55	1.25e+00 ± 2.9e-02	6.37e-01 ± 1.8e-02	2.80e-01 ± 1.1e-02	1.37e-01 ± 7.1e-03
0.65	9.30e-01 ± 2.1e-02	4.43e-01 ± 1.3e-02	1.83e-01 ± 7.5e-03	1.02e-01 ± 5.4e-03
0.75	6.59e-01 ± 1.6e-02	3.16e-01 ± 9.5e-03	1.40e-01 ± 5.9e-03	6.21e-02 ± 3.8e-03
0.85	4.65e-01 ± 1.2e-02	2.31e-01 ± 7.4e-03	8.42e-02 ± 4.2e-03	3.81e-02 ± 2.7e-03
0.95	3.22e-01 ± 9.0e-03	1.56e-01 ± 5.7e-03	5.67e-02 ± 3.2e-03	2.57e-02 ± 2.1e-03
1.05	2.32e-01 ± 7.2e-03	1.09e-01 ± 4.5e-03	4.26e-02 ± 2.7e-03	1.73e-02 ± 1.7e-03
1.15	1.60e-01 ± 5.5e-03	7.06e-02 ± 3.4e-03	2.98e-02 ± 2.1e-03	1.32e-02 ± 1.4e-03
1.25	1.15e-01 ± 4.4e-03	5.72e-02 ± 2.9e-03	1.84e-02 ± 1.6e-03	9.79e-03 ± 1.2e-03
1.35	8.85e-02 ± 3.8e-03	3.67e-02 ± 2.3e-03	1.59e-02 ± 1.5e-03	7.78e-03 ± 1.0e-03
1.45	5.83e-02 ± 3.0e-03	2.38e-02 ± 1.8e-03	1.12e-02 ± 1.2e-03	4.22e-03 ± 7.5e-04
1.55	4.60e-02 ± 2.5e-03	1.89e-02 ± 1.6e-03	7.86e-03 ± 1.0e-03	3.92e-03 ± 7.1e-04
1.65	3.05e-02 ± 2.0e-03	1.53e-02 ± 1.4e-03	6.44e-03 ± 9.0e-04	2.92e-03 ± 6.0e-04
1.75	2.07e-02 ± 1.6e-03	1.00e-02 ± 1.1e-03	3.65e-03 ± 6.6e-04	1.27e-03 ± 3.9e-04
1.85	1.84e-02 ± 1.5e-03	7.82e-03 ± 9.5e-04	2.81e-03 ± 5.8e-04	1.44e-03 ± 4.1e-04
1.95	1.46e-02 ± 1.3e-03	6.14e-03 ± 8.6e-04	2.12e-03 ± 5.1e-04	1.30e-03 ± 4.0e-04

Table C.13: Invariant yields for protons at mid-rapidity in the minimum bias, 0–5%, 5–10%, and 10–15% centrality bins, normalized to one unit rapidity. Errors are statistical only.

$p_T$ [GeV/c]	Minimum bias	0–5%	5–10%	10–15%
0.65	9.51e-01 $\pm$ 2.7e-02	2.90e+00 $\pm$ 9.3e-02	2.44e+00 $\pm$ 8.0e-02	2.09e+00 $\pm$ 6.9e-02
0.75	8.47e-01 $\pm$ 2.4e-02	2.65e+00 $\pm$ 8.5e-02	2.24e+00 $\pm$ 7.3e-02	1.87e+00 $\pm$ 6.2e-02
0.85	7.08e-01 $\pm$ 2.0e-02	2.28e+00 $\pm$ 7.3e-02	1.91e+00 $\pm$ 6.3e-02	1.60e+00 $\pm$ 5.3e-02
0.95	6.06e-01 $\pm$ 1.8e-02	2.00e+00 $\pm$ 6.6e-02	1.66e+00 $\pm$ 5.5e-02	1.41e+00 $\pm$ 4.8e-02
1.05	5.05e-01 $\pm$ 1.5e-02	1.68e+00 $\pm$ 5.7e-02	1.43e+00 $\pm$ 4.9e-02	1.16e+00 $\pm$ 4.1e-02
1.15	4.23e-01 $\pm$ 1.3e-02	1.46e+00 $\pm$ 5.1e-02	1.22e+00 $\pm$ 4.3e-02	9.85e-01 $\pm$ 3.6e-02
1.25	3.30e-01 $\pm$ 1.0e-02	1.16e+00 $\pm$ 4.2e-02	9.51e-01 $\pm$ 3.5e-02	7.92e-01 $\pm$ 3.0e-02
1.35	2.71e-01 $\pm$ 8.8e-03	9.72e-01 $\pm$ 3.7e-02	7.96e-01 $\pm$ 3.1e-02	6.55e-01 $\pm$ 2.6e-02
1.45	2.04e-01 $\pm$ 6.7e-03	7.42e-01 $\pm$ 2.9e-02	6.09e-01 $\pm$ 2.5e-02	5.07e-01 $\pm$ 2.1e-02
1.55	1.68e-01 $\pm$ 5.8e-03	6.05e-01 $\pm$ 2.5e-02	5.08e-01 $\pm$ 2.2e-02	4.21e-01 $\pm$ 1.9e-02
1.65	1.25e-01 $\pm$ 4.4e-03	4.55e-01 $\pm$ 2.0e-02	3.77e-01 $\pm$ 1.7e-02	3.02e-01 $\pm$ 1.4e-02
1.75	9.38e-02 $\pm$ 3.4e-03	3.51e-01 $\pm$ 1.6e-02	2.76e-01 $\pm$ 1.4e-02	2.29e-01 $\pm$ 1.2e-02
1.85	7.50e-02 $\pm$ 2.8e-03	2.85e-01 $\pm$ 1.4e-02	2.28e-01 $\pm$ 1.2e-02	1.79e-01 $\pm$ 1.0e-02
1.95	5.37e-02 $\pm$ 2.1e-03	1.99e-01 $\pm$ 1.1e-02	1.61e-01 $\pm$ 9.3e-03	1.36e-01 $\pm$ 8.2e-03
2.10	3.71e-02 $\pm$ 9.4e-04	1.35e-01 $\pm$ 5.0e-03	1.12e-01 $\pm$ 4.4e-03	9.18e-02 $\pm$ 3.8e-03
2.30	2.15e-02 $\pm$ 5.9e-04	7.69e-02 $\pm$ 3.5e-03	6.73e-02 $\pm$ 3.2e-03	5.39e-02 $\pm$ 2.7e-03
2.50	1.21e-02 $\pm$ 4.2e-04	4.39e-02 $\pm$ 2.5e-03	3.67e-02 $\pm$ 2.2e-03	3.05e-02 $\pm$ 2.0e-03
2.70	7.26e-03 $\pm$ 2.8e-04	2.44e-02 $\pm$ 1.8e-03	2.27e-02 $\pm$ 1.7e-03	1.78e-02 $\pm$ 1.5e-03
2.90	4.17e-03 $\pm$ 1.9e-04	1.54e-02 $\pm$ 1.4e-03	1.16e-02 $\pm$ 1.2e-03	1.04e-02 $\pm$ 1.1e-03
3.25	1.70e-03 $\pm$ 8.3e-05	5.98e-03 $\pm$ 5.5e-04	5.17e-03 $\pm$ 5.0e-04	4.04e-03 $\pm$ 4.3e-04
3.75	5.79e-04 $\pm$ 4.4e-05	2.05e-03 $\pm$ 3.1e-04	1.68e-03 $\pm$ 2.8e-04	1.45e-03 $\pm$ 2.5e-04
4.25	2.21e-04 $\pm$ 2.7e-05	8.96e-04 $\pm$ 2.2e-04	7.04e-04 $\pm$ 1.9e-04	4.70e-04 $\pm$ 1.5e-04

Table C.14: Invariant yields for protons at mid-rapidity in 15–20%, 20–30%, 30–40%, and 40–50% centrality bins, normalized to one unit rapidity. Errors are statistical only.

$p_T$ [GeV/c]	15–20%	20–30%	30–40%	40–50%
0.65	1.76e+00 $\pm$ 6.0e-02	1.37e+00 $\pm$ 4.4e-02	9.68e-01 $\pm$ 3.2e-02	6.31e-01 $\pm$ 2.2e-02
0.75	1.59e+00 $\pm$ 5.4e-02	1.24e+00 $\pm$ 4.0e-02	8.52e-01 $\pm$ 2.9e-02	5.39e-01 $\pm$ 1.9e-02
0.85	1.34e+00 $\pm$ 4.6e-02	1.02e+00 $\pm$ 3.3e-02	7.06e-01 $\pm$ 2.4e-02	4.33e-01 $\pm$ 1.6e-02
0.95	1.16e+00 $\pm$ 4.1e-02	8.90e-01 $\pm$ 2.9e-02	5.79e-01 $\pm$ 2.0e-02	3.60e-01 $\pm$ 1.4e-02
1.05	9.75e-01 $\pm$ 3.5e-02	7.41e-01 $\pm$ 2.5e-02	4.83e-01 $\pm$ 1.7e-02	2.96e-01 $\pm$ 1.2e-02
1.15	8.38e-01 $\pm$ 3.1e-02	6.27e-01 $\pm$ 2.2e-02	3.93e-01 $\pm$ 1.5e-02	2.33e-01 $\pm$ 9.7e-03
1.25	6.47e-01 $\pm$ 2.5e-02	4.83e-01 $\pm$ 1.8e-02	3.09e-01 $\pm$ 1.2e-02	1.77e-01 $\pm$ 7.9e-03
1.35	5.35e-01 $\pm$ 2.2e-02	3.93e-01 $\pm$ 1.5e-02	2.46e-01 $\pm$ 1.0e-02	1.40e-01 $\pm$ 6.7e-03
1.45	4.04e-01 $\pm$ 1.8e-02	2.90e-01 $\pm$ 1.2e-02	1.89e-01 $\pm$ 8.3e-03	1.05e-01 $\pm$ 5.4e-03
1.55	3.33e-01 $\pm$ 1.6e-02	2.42e-01 $\pm$ 1.0e-02	1.49e-01 $\pm$ 7.1e-03	8.39e-02 $\pm$ 4.7e-03
1.65	2.60e-01 $\pm$ 1.3e-02	1.80e-01 $\pm$ 8.1e-03	1.10e-01 $\pm$ 5.6e-03	6.02e-02 $\pm$ 3.7e-03
1.75	1.86e-01 $\pm$ 1.0e-02	1.36e-01 $\pm$ 6.6e-03	8.52e-02 $\pm$ 4.7e-03	4.64e-02 $\pm$ 3.1e-03
1.85	1.51e-01 $\pm$ 8.9e-03	1.08e-01 $\pm$ 5.7e-03	6.68e-02 $\pm$ 4.0e-03	3.64e-02 $\pm$ 2.7e-03
1.95	1.06e-01 $\pm$ 6.9e-03	7.98e-02 $\pm$ 4.5e-03	4.72e-02 $\pm$ 3.2e-03	2.53e-02 $\pm$ 2.1e-03
2.10	7.41e-02 $\pm$ 3.3e-03	5.63e-02 $\pm$ 2.1e-03	3.32e-02 $\pm$ 1.5e-03	1.82e-02 $\pm$ 1.0e-03
2.30	4.46e-02 $\pm$ 2.4e-03	3.19e-02 $\pm$ 1.5e-03	1.96e-02 $\pm$ 1.1e-03	9.61e-03 $\pm$ 7.2e-04
2.50	2.52e-02 $\pm$ 1.7e-03	1.79e-02 $\pm$ 1.1e-03	1.07e-02 $\pm$ 7.8e-04	5.83e-03 $\pm$ 5.5e-04
2.70	1.55e-02 $\pm$ 1.3e-03	1.08e-02 $\pm$ 8.0e-04	6.78e-03 $\pm$ 6.1e-04	3.73e-03 $\pm$ 4.4e-04
2.90	8.35e-03 $\pm$ 9.5e-04	6.05e-03 $\pm$ 5.8e-04	4.10e-03 $\pm$ 4.7e-04	2.20e-03 $\pm$ 3.3e-04
3.25	3.51e-03 $\pm$ 3.9e-04	2.54e-03 $\pm$ 2.4e-04	1.64e-03 $\pm$ 1.9e-04	8.36e-04 $\pm$ 1.3e-04
3.75	1.18e-03 $\pm$ 2.2e-04	8.20e-04 $\pm$ 1.3e-04	5.66e-04 $\pm$ 1.1e-04	3.25e-04 $\pm$ 7.8e-05
4.25	4.64e-04 $\pm$ 1.4e-04	3.07e-04 $\pm$ 8.3e-05	1.93e-04 $\pm$ 6.4e-05	1.07e-04 $\pm$ 4.7e-05

Table C.15: Invariant yields for protons at mid-rapidity in 50–60%, 60–70%, 70–80%, and 80–92% centrality bins, normalized to one unit rapidity. Errors are statistical only.

$p_T$ [GeV/c]	50–60%	60–70%	70–80%	80–92%
0.65	3.82e-01 $\pm$ 1.5e-02	2.04e-01 $\pm$ 9.7e-03	9.09e-02 $\pm$ 5.9e-03	4.96e-02 $\pm$ 4.2e-03
0.75	3.25e-01 $\pm$ 1.3e-02	1.65e-01 $\pm$ 8.1e-03	7.04e-02 $\pm$ 4.9e-03	3.79e-02 $\pm$ 3.4e-03
0.85	2.60e-01 $\pm$ 1.1e-02	1.27e-01 $\pm$ 6.5e-03	5.41e-02 $\pm$ 4.0e-03	2.62e-02 $\pm$ 2.7e-03
0.95	2.08e-01 $\pm$ 9.1e-03	1.00e-01 $\pm$ 5.5e-03	4.11e-02 $\pm$ 3.3e-03	2.06e-02 $\pm$ 2.3e-03
1.05	1.61e-01 $\pm$ 7.5e-03	7.43e-02 $\pm$ 4.5e-03	3.14e-02 $\pm$ 2.8e-03	1.54e-02 $\pm$ 1.9e-03
1.15	1.24e-01 $\pm$ 6.2e-03	5.88e-02 $\pm$ 3.8e-03	2.40e-02 $\pm$ 2.3e-03	8.08e-03 $\pm$ 1.3e-03
1.25	9.20e-02 $\pm$ 5.0e-03	3.98e-02 $\pm$ 3.0e-03	1.68e-02 $\pm$ 1.9e-03	6.94e-03 $\pm$ 1.2e-03
1.35	7.34e-02 $\pm$ 4.4e-03	3.41e-02 $\pm$ 2.7e-03	1.21e-02 $\pm$ 1.6e-03	5.84e-03 $\pm$ 1.1e-03
1.45	4.98e-02 $\pm$ 3.3e-03	2.41e-02 $\pm$ 2.2e-03	9.02e-03 $\pm$ 1.3e-03	3.61e-03 $\pm$ 8.1e-04
1.55	4.43e-02 $\pm$ 3.1e-03	1.69e-02 $\pm$ 1.8e-03	6.98e-03 $\pm$ 1.1e-03	2.19e-03 $\pm$ 6.3e-04
1.65	3.29e-02 $\pm$ 2.6e-03	1.30e-02 $\pm$ 1.5e-03	4.57e-03 $\pm$ 9.0e-04	1.36e-03 $\pm$ 4.8e-04
1.75	2.37e-02 $\pm$ 2.1e-03	9.76e-03 $\pm$ 1.3e-03	3.81e-03 $\pm$ 8.0e-04	1.40e-03 $\pm$ 4.8e-04
1.85	1.80e-02 $\pm$ 1.8e-03	7.16e-03 $\pm$ 1.1e-03	2.56e-03 $\pm$ 6.6e-04	8.09e-04 $\pm$ 3.7e-04
1.95	1.24e-02 $\pm$ 1.4e-03	5.34e-03 $\pm$ 9.1e-04	2.04e-03 $\pm$ 5.7e-04	8.46e-04 $\pm$ 3.6e-04
2.10	9.33e-03 $\pm$ 7.2e-04	3.47e-03 $\pm$ 4.2e-04	1.34e-03 $\pm$ 2.7e-04	4.08e-04 $\pm$ 1.5e-04
2.30	4.86e-03 $\pm$ 5.0e-04	2.28e-03 $\pm$ 3.4e-04	6.06e-04 $\pm$ 1.8e-04	2.88e-04 $\pm$ 1.2e-04
2.50	3.01e-03 $\pm$ 3.9e-04	9.91e-04 $\pm$ 2.2e-04	3.91e-04 $\pm$ 1.4e-04	2.19e-04 $\pm$ 1.0e-04
2.70	1.66e-03 $\pm$ 2.9e-04	6.31e-04 $\pm$ 1.7e-04	2.37e-04 $\pm$ 1.1e-04	1.12e-04 $\pm$ 7.4e-05
2.90	1.03e-03 $\pm$ 2.2e-04	4.62e-04 $\pm$ 1.5e-04	1.06e-04 $\pm$ 7.3e-05	3.22e-05 $\pm$ 4.0e-05
3.25	4.01e-04 $\pm$ 8.7e-05	1.66e-04 $\pm$ 5.5e-05	6.73e-05 $\pm$ 3.6e-05	2.02e-05 $\pm$ 2.0e-05
3.75	1.45e-04 $\pm$ 5.2e-05	5.72e-05 $\pm$ 3.2e-05	2.13e-05 $\pm$ 1.9e-05	2.89e-06 $\pm$ 7.7e-06
4.25	4.94e-05 $\pm$ 3.2e-05	2.40e-05 $\pm$ 2.2e-05	1.02e-05 $\pm$ 1.5e-05	2.43e-06 $\pm$ 6.7e-06

Table C.16: Invariant yields for anti-protons at mid-rapidity in the minimum bias, 0–5%, 5–10%, and 10–15% centrality bins, normalized to one unit rapidity. Errors are statistical only.

$p_T$ [GeV/c]	Minimum bias	0–5%	5–10%	10–15%
0.65	6.73e-01 $\pm$ 2.0e-02	2.00e+00 $\pm$ 6.8e-02	1.73e+00 $\pm$ 6.0e-02	1.48e+00 $\pm$ 5.2e-02
0.75	6.16e-01 $\pm$ 1.8e-02	1.89e+00 $\pm$ 6.2e-02	1.61e+00 $\pm$ 5.4e-02	1.34e+00 $\pm$ 4.6e-02
0.85	5.28e-01 $\pm$ 1.5e-02	1.67e+00 $\pm$ 5.4e-02	1.42e+00 $\pm$ 4.7e-02	1.19e+00 $\pm$ 4.1e-02
0.95	4.52e-01 $\pm$ 1.3e-02	1.47e+00 $\pm$ 4.8e-02	1.25e+00 $\pm$ 4.2e-02	1.05e+00 $\pm$ 3.6e-02
1.05	3.65e-01 $\pm$ 1.1e-02	1.21e+00 $\pm$ 4.1e-02	1.04e+00 $\pm$ 3.6e-02	8.82e-01 $\pm$ 3.1e-02
1.15	3.19e-01 $\pm$ 9.7e-03	1.10e+00 $\pm$ 3.9e-02	9.28e-01 $\pm$ 3.4e-02	7.39e-01 $\pm$ 2.8e-02
1.25	2.53e-01 $\pm$ 7.9e-03	8.90e-01 $\pm$ 3.3e-02	7.47e-01 $\pm$ 2.8e-02	6.15e-01 $\pm$ 2.4e-02
1.35	2.01e-01 $\pm$ 6.5e-03	7.24e-01 $\pm$ 2.8e-02	6.08e-01 $\pm$ 2.4e-02	4.88e-01 $\pm$ 2.0e-02
1.45	1.66e-01 $\pm$ 5.6e-03	6.12e-01 $\pm$ 2.5e-02	5.01e-01 $\pm$ 2.1e-02	4.09e-01 $\pm$ 1.8e-02
1.55	1.22e-01 $\pm$ 4.1e-03	4.43e-01 $\pm$ 1.9e-02	3.69e-01 $\pm$ 1.6e-02	3.04e-01 $\pm$ 1.4e-02
1.65	9.61e-02 $\pm$ 3.4e-03	3.46e-01 $\pm$ 1.6e-02	3.00e-01 $\pm$ 1.4e-02	2.43e-01 $\pm$ 1.2e-02
1.75	7.19e-02 $\pm$ 2.7e-03	2.70e-01 $\pm$ 1.3e-02	2.17e-01 $\pm$ 1.1e-02	1.84e-01 $\pm$ 9.9e-03
1.85	5.57e-02 $\pm$ 2.1e-03	2.07e-01 $\pm$ 1.1e-02	1.68e-01 $\pm$ 9.5e-03	1.45e-01 $\pm$ 8.4e-03
1.95	4.04e-02 $\pm$ 1.7e-03	1.53e-01 $\pm$ 9.2e-03	1.19e-01 $\pm$ 7.7e-03	1.02e-01 $\pm$ 6.9e-03
2.10	2.61e-02 $\pm$ 7.3e-04	9.75e-02 $\pm$ 4.2e-03	7.95e-02 $\pm$ 3.7e-03	6.64e-02 $\pm$ 3.2e-03
2.30	1.54e-02 $\pm$ 4.8e-04	5.99e-02 $\pm$ 3.1e-03	4.59e-02 $\pm$ 2.7e-03	3.87e-02 $\pm$ 2.4e-03
2.50	8.66e-03 $\pm$ 3.4e-04	3.16e-02 $\pm$ 2.2e-03	2.69e-02 $\pm$ 2.0e-03	2.29e-02 $\pm$ 1.8e-03
2.70	4.79e-03 $\pm$ 2.2e-04	1.79e-02 $\pm$ 1.6e-03	1.46e-02 $\pm$ 1.4e-03	1.19e-02 $\pm$ 1.2e-03
2.90	2.91e-03 $\pm$ 1.6e-04	1.04e-02 $\pm$ 1.2e-03	8.43e-03 $\pm$ 1.1e-03	7.25e-03 $\pm$ 9.6e-04
3.25	1.16e-03 $\pm$ 6.7e-05	4.14e-03 $\pm$ 4.7e-04	3.55e-03 $\pm$ 4.3e-04	3.02e-03 $\pm$ 3.8e-04
3.75	3.71e-04 $\pm$ 3.5e-05	1.29e-03 $\pm$ 2.5e-04	1.30e-03 $\pm$ 2.5e-04	1.09e-03 $\pm$ 2.2e-04
4.25	1.35e-04 $\pm$ 2.1e-05	5.44e-04 $\pm$ 1.7e-04	3.98e-04 $\pm$ 1.4e-04	3.57e-04 $\pm$ 1.3e-04

Table C.17: Invariant yields for anti-protons at mid-rapidity in 15–20%, 20–30%, 30–40%, and 40–50% centrality bins, normalized to one unit rapidity. Errors are statistical only.

$p_T$ [GeV/c]	15–20%	20–30%	30–40%	40–50%
0.65	1.25e+00 $\pm$ 4.5e-02	9.68e-01 $\pm$ 3.2e-02	6.98e-01 $\pm$ 2.4e-02	4.51e-01 $\pm$ 1.7e-02
0.75	1.16e+00 $\pm$ 4.1e-02	8.94e-01 $\pm$ 2.9e-02	6.35e-01 $\pm$ 2.2e-02	4.06e-01 $\pm$ 1.5e-02
0.85	1.02e+00 $\pm$ 3.5e-02	7.83e-01 $\pm$ 2.5e-02	5.21e-01 $\pm$ 1.8e-02	3.37e-01 $\pm$ 1.3e-02
0.95	8.85e-01 $\pm$ 3.1e-02	6.61e-01 $\pm$ 2.2e-02	4.42e-01 $\pm$ 1.5e-02	2.70e-01 $\pm$ 1.0e-02
1.05	7.26e-01 $\pm$ 2.6e-02	5.25e-01 $\pm$ 1.8e-02	3.54e-01 $\pm$ 1.3e-02	2.05e-01 $\pm$ 8.4e-03
1.15	6.43e-01 $\pm$ 2.5e-02	4.63e-01 $\pm$ 1.6e-02	2.99e-01 $\pm$ 1.2e-02	1.79e-01 $\pm$ 7.7e-03
1.25	4.99e-01 $\pm$ 2.0e-02	3.65e-01 $\pm$ 1.4e-02	2.33e-01 $\pm$ 9.5e-03	1.37e-01 $\pm$ 6.4e-03
1.35	4.11e-01 $\pm$ 1.8e-02	2.88e-01 $\pm$ 1.1e-02	1.80e-01 $\pm$ 7.8e-03	1.03e-01 $\pm$ 5.2e-03
1.45	3.40e-01 $\pm$ 1.5e-02	2.41e-01 $\pm$ 1.0e-02	1.42e-01 $\pm$ 6.7e-03	8.40e-02 $\pm$ 4.6e-03
1.55	2.45e-01 $\pm$ 1.2e-02	1.77e-01 $\pm$ 7.8e-03	1.06e-01 $\pm$ 5.3e-03	6.14e-02 $\pm$ 3.6e-03
1.65	1.90e-01 $\pm$ 1.0e-02	1.43e-01 $\pm$ 6.7e-03	8.53e-02 $\pm$ 4.6e-03	4.50e-02 $\pm$ 3.0e-03
1.75	1.45e-01 $\pm$ 8.4e-03	1.02e-01 $\pm$ 5.2e-03	6.32e-02 $\pm$ 3.8e-03	3.49e-02 $\pm$ 2.6e-03
1.85	1.20e-01 $\pm$ 7.4e-03	7.97e-02 $\pm$ 4.4e-03	4.76e-02 $\pm$ 3.1e-03	2.66e-02 $\pm$ 2.2e-03
1.95	8.41e-02 $\pm$ 6.0e-03	5.83e-02 $\pm$ 3.7e-03	3.56e-02 $\pm$ 2.7e-03	1.84e-02 $\pm$ 1.8e-03
2.10	5.22e-02 $\pm$ 2.8e-03	3.90e-02 $\pm$ 1.7e-03	2.30e-02 $\pm$ 1.3e-03	1.27e-02 $\pm$ 8.8e-04
2.30	3.19e-02 $\pm$ 2.1e-03	2.24e-02 $\pm$ 1.2e-03	1.34e-02 $\pm$ 9.2e-04	7.39e-03 $\pm$ 6.6e-04
2.50	1.83e-02 $\pm$ 1.5e-03	1.22e-02 $\pm$ 9.0e-04	7.78e-03 $\pm$ 6.9e-04	4.11e-03 $\pm$ 4.8e-04
2.70	9.79e-03 $\pm$ 1.1e-03	6.65e-03 $\pm$ 6.4e-04	4.66e-03 $\pm$ 5.2e-04	2.30e-03 $\pm$ 3.5e-04
2.90	6.28e-03 $\pm$ 8.7e-04	4.33e-03 $\pm$ 5.1e-04	2.57e-03 $\pm$ 3.8e-04	1.67e-03 $\pm$ 3.0e-04
3.25	2.55e-03 $\pm$ 3.4e-04	1.64e-03 $\pm$ 2.0e-04	1.05e-03 $\pm$ 1.5e-04	5.44e-04 $\pm$ 1.1e-04
3.75	8.03e-04 $\pm$ 1.9e-04	5.39e-04 $\pm$ 1.1e-04	2.59e-04 $\pm$ 7.3e-05	1.75e-04 $\pm$ 5.9e-05
4.25	2.92e-04 $\pm$ 1.2e-04	1.74e-04 $\pm$ 6.3e-05	1.12e-04 $\pm$ 4.9e-05	5.56e-05 $\pm$ 3.5e-05

Table C.18: Invariant yields for anti-protons at mid-rapidity in 50–60%, 60–70%, 70–80%, and 80–92% centrality bins, normalized to one unit rapidity. Errors are statistical only.

$p_T$ [GeV/c]	50–60%	60–70%	70–80%	80–92%
0.65	2.84e-01 $\pm$ 1.2e-02	1.58e-01 $\pm$ 8.1e-03	6.22e-02 $\pm$ 4.7e-03	3.55e-02 $\pm$ 3.4e-03
0.75	2.50e-01 $\pm$ 1.1e-02	1.25e-01 $\pm$ 6.6e-03	5.43e-02 $\pm$ 4.0e-03	2.77e-02 $\pm$ 2.8e-03
0.85	1.89e-01 $\pm$ 8.3e-03	9.50e-02 $\pm$ 5.2e-03	4.16e-02 $\pm$ 3.3e-03	2.06e-02 $\pm$ 2.2e-03
0.95	1.58e-01 $\pm$ 7.1e-03	7.38e-02 $\pm$ 4.3e-03	3.13e-02 $\pm$ 2.7e-03	1.56e-02 $\pm$ 1.8e-03
1.05	1.19e-01 $\pm$ 5.8e-03	5.50e-02 $\pm$ 3.5e-03	2.12e-02 $\pm$ 2.1e-03	1.01e-02 $\pm$ 1.4e-03
1.15	9.60e-02 $\pm$ 5.1e-03	4.34e-02 $\pm$ 3.1e-03	1.73e-02 $\pm$ 1.9e-03	7.94e-03 $\pm$ 1.2e-03
1.25	7.11e-02 $\pm$ 4.1e-03	3.19e-02 $\pm$ 2.5e-03	1.22e-02 $\pm$ 1.5e-03	6.05e-03 $\pm$ 1.1e-03
1.35	5.31e-02 $\pm$ 3.4e-03	2.40e-02 $\pm$ 2.1e-03	9.65e-03 $\pm$ 1.3e-03	4.08e-03 $\pm$ 8.4e-04
1.45	4.43e-02 $\pm$ 3.1e-03	1.90e-02 $\pm$ 1.9e-03	7.69e-03 $\pm$ 1.2e-03	3.31e-03 $\pm$ 7.6e-04
1.55	3.13e-02 $\pm$ 2.4e-03	1.28e-02 $\pm$ 1.4e-03	4.43e-03 $\pm$ 8.5e-04	2.02e-03 $\pm$ 5.6e-04
1.65	2.39e-02 $\pm$ 2.1e-03	9.29e-03 $\pm$ 1.2e-03	3.09e-03 $\pm$ 7.0e-04	1.70e-03 $\pm$ 5.2e-04
1.75	1.79e-02 $\pm$ 1.7e-03	6.92e-03 $\pm$ 1.0e-03	2.79e-03 $\pm$ 6.6e-04	1.21e-03 $\pm$ 4.3e-04
1.85	1.28e-02 $\pm$ 1.4e-03	5.66e-03 $\pm$ 9.3e-04	1.27e-03 $\pm$ 4.4e-04	7.33e-04 $\pm$ 3.3e-04
1.95	1.00e-02 $\pm$ 1.3e-03	3.93e-03 $\pm$ 7.8e-04	1.54e-03 $\pm$ 4.9e-04	7.92e-04 $\pm$ 3.5e-04
2.10	6.03e-03 $\pm$ 5.9e-04	2.58e-03 $\pm$ 3.8e-04	6.91e-04 $\pm$ 2.0e-04	3.59e-04 $\pm$ 1.4e-04
2.30	3.46e-03 $\pm$ 4.4e-04	1.37e-03 $\pm$ 2.7e-04	5.66e-04 $\pm$ 1.8e-04	2.03e-04 $\pm$ 1.1e-04
2.50	2.04e-03 $\pm$ 3.4e-04	7.56e-04 $\pm$ 2.0e-04	2.85e-04 $\pm$ 1.3e-04	1.35e-04 $\pm$ 8.5e-05
2.70	1.20e-03 $\pm$ 2.5e-04	3.92e-04 $\pm$ 1.4e-04	2.26e-04 $\pm$ 1.1e-04	2.67e-05 $\pm$ 3.8e-05
2.90	6.21e-04 $\pm$ 1.8e-04	2.92e-04 $\pm$ 1.2e-04	1.40e-04 $\pm$ 8.8e-05	8.76e-06 $\pm$ 2.2e-05
3.25	2.61e-04 $\pm$ 7.3e-05	1.10e-04 $\pm$ 4.7e-05	3.63e-05 $\pm$ 2.8e-05	9.16e-06 $\pm$ 1.4e-05
3.75	6.52e-05 $\pm$ 3.6e-05	2.77e-05 $\pm$ 2.3e-05	5.76e-06 $\pm$ 1.1e-05	
4.25	4.82e-05 $\pm$ 3.2e-05	1.23e-05 $\pm$ 1.6e-05	2.71e-06 $\pm$ 8.1e-06	

Table C.19: Invariant yields for  $\pi^\pm$  and  $K^\pm$  at mid-rapidity in 60–92% centrality bin, normalized to one unit rapidity. Errors are statistical only.

$p_T$ [GeV/c]	$\pi^+$	$\pi^-$	$K^+$	$K^-$
0.25	1.28e+01 ± 1.1e-01	1.21e+01 ± 9.5e-02		
0.35	6.61e+00 ± 5.7e-02	6.42e+00 ± 5.2e-02		
0.45	3.71e+00 ± 3.4e-02	3.59e+00 ± 3.1e-02	5.35e-01 ± 1.5e-02	4.74e-01 ± 1.3e-02
0.55	2.09e+00 ± 2.1e-02	2.06e+00 ± 1.9e-02	3.83e-01 ± 9.7e-03	3.62e-01 ± 8.8e-03
0.65	1.24e+00 ± 1.4e-02	1.21e+00 ± 1.3e-02	2.66e-01 ± 6.8e-03	2.50e-01 ± 6.2e-03
0.75	7.63e-01 ± 9.6e-03	7.31e-01 ± 8.4e-03	1.81e-01 ± 4.9e-03	1.78e-01 ± 4.6e-03
0.85	4.64e-01 ± 6.6e-03	4.60e-01 ± 5.9e-03	1.26e-01 ± 3.7e-03	1.21e-01 ± 3.4e-03
0.95	2.93e-01 ± 4.8e-03	2.95e-01 ± 4.3e-03	8.85e-02 ± 2.9e-03	8.21e-02 ± 2.5e-03
1.05	1.91e-01 ± 3.5e-03	1.89e-01 ± 3.2e-03	6.34e-02 ± 2.3e-03	5.80e-02 ± 2.0e-03
1.15	1.26e-01 ± 2.6e-03	1.28e-01 ± 2.5e-03	4.35e-02 ± 1.8e-03	3.91e-02 ± 1.5e-03
1.25	8.15e-02 ± 2.0e-03	8.12e-02 ± 1.8e-03	2.87e-02 ± 1.4e-03	2.94e-02 ± 1.3e-03
1.35	5.96e-02 ± 1.7e-03	5.71e-02 ± 1.5e-03	2.03e-02 ± 1.1e-03	2.07e-02 ± 1.0e-03
1.45	3.95e-02 ± 1.3e-03	3.91e-02 ± 1.2e-03	1.68e-02 ± 9.7e-04	1.35e-02 ± 8.2e-04
1.55	2.56e-02 ± 9.7e-04	2.81e-02 ± 9.7e-04	1.06e-02 ± 7.5e-04	1.05e-02 ± 7.0e-04
1.65	1.96e-02 ± 8.4e-04	2.07e-02 ± 8.1e-04	8.39e-03 ± 6.5e-04	8.47e-03 ± 6.2e-04
1.75	1.44e-02 ± 7.1e-04	1.41e-02 ± 6.5e-04	5.68e-03 ± 5.2e-04	5.15e-03 ± 4.6e-04
1.85	1.07e-02 ± 6.0e-04	1.04e-02 ± 5.6e-04	4.91e-03 ± 4.7e-04	4.15e-03 ± 4.1e-04
1.95	7.68e-03 ± 5.1e-04	7.42e-03 ± 4.8e-04	3.59e-03 ± 4.1e-04	3.29e-03 ± 3.7e-04
2.05	5.87e-03 ± 3.6e-04	4.87e-03 ± 3.3e-04		
2.15	3.78e-03 ± 2.9e-04	3.87e-03 ± 3.0e-04		
2.25	2.99e-03 ± 2.6e-04	2.55e-03 ± 2.5e-04		
2.35	2.47e-03 ± 2.5e-04	2.41e-03 ± 2.6e-04		
2.45	1.68e-03 ± 2.1e-04	1.63e-03 ± 2.1e-04		
2.55	1.77e-03 ± 2.3e-04	1.54e-03 ± 2.3e-04		
2.65	1.28e-03 ± 2.1e-04	1.18e-03 ± 2.0e-04		
2.75	1.02e-03 ± 2.0e-04	7.74e-04 ± 1.7e-04		
2.85	7.49e-04 ± 1.7e-04	6.23e-04 ± 1.7e-04		
2.95	5.61e-04 ± 1.6e-04	7.27e-04 ± 1.9e-04		

Table C.20: Invariant yields for protons and anti-protons at mid-rapidity in 60–92% centrality bin, normalized to one unit rapidity. Errors are statistical only.

$p_T$ [GeV/c]	$p$	$\bar{p}$
0.65	1.17e-01 $\pm$ 4.8e-03	8.63e-02 $\pm$ 3.8e-03
0.75	9.26e-02 $\pm$ 3.9e-03	7.00e-02 $\pm$ 3.1e-03
0.85	7.01e-02 $\pm$ 3.1e-03	5.31e-02 $\pm$ 2.5e-03
0.95	5.48e-02 $\pm$ 2.6e-03	4.07e-02 $\pm$ 2.0e-03
1.05	4.10e-02 $\pm$ 2.1e-03	2.92e-02 $\pm$ 1.6e-03
1.15	3.09e-02 $\pm$ 1.7e-03	2.32e-02 $\pm$ 1.4e-03
1.25	2.16e-02 $\pm$ 1.3e-03	1.70e-02 $\pm$ 1.1e-03
1.35	1.77e-02 $\pm$ 1.2e-03	1.27e-02 $\pm$ 9.4e-04
1.45	1.25e-02 $\pm$ 9.4e-04	1.02e-02 $\pm$ 8.3e-04
1.55	8.85e-03 $\pm$ 7.8e-04	6.51e-03 $\pm$ 6.2e-04
1.65	6.42e-03 $\pm$ 6.3e-04	4.76e-03 $\pm$ 5.2e-04
1.75	5.08e-03 $\pm$ 5.5e-04	3.69e-03 $\pm$ 4.5e-04
1.85	3.58e-03 $\pm$ 4.6e-04	2.60e-03 $\pm$ 3.7e-04
1.95	2.79e-03 $\pm$ 3.9e-04	2.11e-03 $\pm$ 3.4e-04
2.10	1.77e-03 $\pm$ 1.8e-04	1.23e-03 $\pm$ 1.5e-04
2.30	1.08e-03 $\pm$ 1.4e-04	7.22e-04 $\pm$ 1.2e-04
2.50	5.42e-04 $\pm$ 9.5e-05	3.97e-04 $\pm$ 8.5e-05
2.70	3.32e-04 $\pm$ 7.4e-05	2.17e-04 $\pm$ 6.2e-05
2.90	2.04e-04 $\pm$ 5.8e-05	1.49e-04 $\pm$ 5.2e-05
3.25	8.58e-05 $\pm$ 2.3e-05	5.24e-05 $\pm$ 1.9e-05
3.75	2.76e-05 $\pm$ 1.3e-05	1.14e-05 $\pm$ 8.7e-06
4.25	1.24e-05 $\pm$ 9.1e-06	5.08e-06 $\pm$ 6.1e-06

## C.2 Particle Ratio Data Tables

The ratios of anti-particle/particle measured as a function of  $p_T$  (Tables C.21–C.27) and centrality (Tables C.36–C.42) at  $\sqrt{s_{\text{NN}}} = 200$  GeV in Au+Au collisions are tabulated. The ratios of  $K/\pi$  (Tables C.28–C.31) and  $p/\pi$  (Table C.32–C.35) as a function of  $p_T$  are also tabulated.

Table C.21:  $\pi^-/\pi^+$  vs.  $p_T$  Central (0-5%)

$p_T$ [GeV/c]	$\pi^-/\pi^+$	Stat. Err	Sys. Err
0.25	0.957466	0.0108386	0.055533
0.35	0.985735	0.0113168	0.0571726
0.45	0.988715	0.01189	0.0573455
0.55	1.0152	0.0129776	0.0588814
0.65	1.01614	0.0140238	0.0589363
0.75	0.974639	0.0146318	0.0565291
0.85	1.02419	0.0165982	0.059403
0.95	1.01075	0.0178344	0.0586234
1.05	1.00777	0.0190503	0.0584508
1.15	1.04431	0.0213183	0.0605703
1.25	0.994569	0.0216472	0.057685
1.35	1.00098	0.0239656	0.0580567
1.45	0.991924	0.0256721	0.0575316
1.55	1.06993	0.0301215	0.0620559
1.65	0.996205	0.0309089	0.0577799
1.75	0.990885	0.0342661	0.0574713
1.85	0.969285	0.0371367	0.0562185
1.95	1.01774	0.0454356	0.059029
2.05	0.900701	0.0383941	0.0522406
2.15	0.969844	0.0492246	0.056251
2.25	1.0149	0.0616524	0.0588643
2.35	0.981962	0.0713501	0.0569538
2.45	0.872258	0.0761743	0.050591
2.55	0.926298	0.101928	0.0537253
2.65	1.01643	0.13417	0.0589528
2.75	0.876785	0.138999	0.0508535
2.85	1.12719	0.23259	0.0653769
2.95	1.04642	0.26209	0.0606926

Table C.22:  $\pi^-/\pi^+$  vs.  $p_T$  Peripheral (60-92%)

$p_T$ [GeV/c]	$\pi^-/\pi^+$	Stat. Err	Sys. Err
0.25	0.94893	0.010933	0.055038
0.35	0.970338	0.011472	0.0562796
0.45	0.970189	0.0121975	0.056271
0.55	0.986006	0.0134646	0.0571884
0.65	0.978866	0.0148279	0.0567742
0.75	0.958889	0.0163472	0.0556156
0.85	0.990725	0.0190215	0.0574621
0.95	1.00815	0.0221512	0.058473
1.05	0.990833	0.0246458	0.0574683
1.15	1.02042	0.0290904	0.0591843
1.25	0.995222	0.0325835	0.0577229
1.35	0.957329	0.0364374	0.0555251
1.45	0.991001	0.0437177	0.057478
1.55	1.0956	0.0561949	0.0635448
1.65	1.05152	0.0609568	0.0609881
1.75	0.975835	0.0662536	0.0565984
1.85	0.972191	0.0757114	0.0563871
1.95	0.966195	0.0895788	0.0560393
2.05	0.830706	0.0763071	0.0481809
2.15	1.02233	0.111425	0.0592954
2.25	0.853348	0.110786	0.0494942
2.35	0.976019	0.143371	0.0566091
2.45	0.97344	0.17686	0.0564595
2.55	0.873141	0.172251	0.0506422
2.65	0.916944	0.216275	0.0531827
2.75	0.757713	0.22604	0.0439474
2.85	0.831459	0.29699	0.0482246
2.95	1.2959	0.511151	0.0751624

Table C.23:  $K^-/K^+$  vs.  $p_T$  Central (0-5%)

$p_T$ [GeV/c]	$K^-/K^+$	Stat. Err	Sys. Err
0.45	0.898844	0.0267777	0.052133
0.55	0.889577	0.0238841	0.0515954
0.65	0.959843	0.0247583	0.0556709
0.75	0.965118	0.0248376	0.0559769
0.85	0.941609	0.024992	0.0546133
0.95	0.980866	0.0270415	0.0568902
1.05	0.947405	0.0276913	0.0549495
1.15	0.916562	0.0280294	0.0531606
1.25	0.933744	0.0303916	0.0541572
1.35	1.0187	0.0356997	0.0590848
1.45	0.987732	0.0375261	0.0572885
1.55	0.971392	0.0404556	0.0563407
1.65	0.996458	0.0451965	0.0577945
1.75	0.876869	0.0430984	0.0508584
1.85	0.954324	0.0514233	0.0553508
1.95	0.86042	0.0524042	0.0499044

Table C.24:  $K^-/K^+$  vs.  $p_T$  Peripheral (60-92%)

$p_T$ [GeV/c]	$K^-/K^+$	Stat. Err	Sys. Err
0.45	0.886941	0.0335849	0.0514426
0.55	0.945889	0.0332914	0.0548616
0.65	0.941417	0.033292	0.0546022
0.75	0.985671	0.0366679	0.0571689
0.85	0.961988	0.0391291	0.0557953
0.95	0.9272	0.0416124	0.0537776
1.05	0.914415	0.0461903	0.0530361
1.15	0.897972	0.0510247	0.0520824
1.25	1.02589	0.0659854	0.0595018
1.35	1.02059	0.0750557	0.0591942
1.45	0.803198	0.0673834	0.0465855
1.55	0.991018	0.0957383	0.0574791
1.65	1.00874	0.106742	0.0585068
1.75	0.906489	0.116425	0.0525763
1.85	0.845204	0.116963	0.0490219
1.95	0.91656	0.14709	0.0531605

Table C.25:  $\bar{p}/p$  vs.  $p_T$  Central (0-5%)

$p_T$ [GeV/c]	$\bar{p}/p$	Stat. Err	Sys. Err
0.65	0.68951	0.0321448	0.0427496
0.75	0.712713	0.0328213	0.0441882
0.85	0.73101	0.0334939	0.0453226
0.95	0.736244	0.0342573	0.0456471
1.05	0.719409	0.0343607	0.0446034
1.15	0.755606	0.0374725	0.0468475
1.25	0.76989	0.0398593	0.0477332
1.35	0.745183	0.0403655	0.0462013
1.45	0.825053	0.0467199	0.0511533
1.55	0.731295	0.0438201	0.0453403
1.65	0.761274	0.048314	0.047199
1.75	0.770284	0.0523973	0.0477576
1.85	0.725194	0.0531511	0.044962
1.95	0.77025	0.0624643	0.0477555
2.1	0.724176	0.0413287	0.0448989
2.3	0.778882	0.0538694	0.0482907
2.5	0.719541	0.065372	0.0446115
2.7	0.736885	0.0854318	0.0456869
2.9	0.670069	0.0983822	0.0415443
3.25	0.692255	0.101403	0.0429198
3.75	0.627522	0.156272	0.0389064
4.25	0.607027	0.23984	0.0376357

Table C.26:  $\bar{p}/p$  vs.  $p_T$  Peripheral (60-92%)

$p_T$ [GeV/c]	$\bar{p}/p$	Stat. Err	Sys. Err
0.65	0.739699	0.0444199	0.0458613
0.75	0.755839	0.046385	0.046862
0.85	0.756991	0.0485329	0.0469334
0.95	0.743343	0.0506493	0.0460872
1.05	0.710274	0.0526111	0.044037
1.15	0.751543	0.06116	0.0465956
1.25	0.787698	0.0715585	0.0488373
1.35	0.72142	0.0719526	0.044728
1.45	0.814944	0.0906561	0.0505265
1.55	0.734908	0.0949341	0.0455643
1.65	0.741776	0.109148	0.0459901
1.75	0.725716	0.117763	0.0449944
1.85	0.726744	0.139112	0.0450581
1.95	0.757069	0.160937	0.0469383
2.1	0.693528	0.111093	0.0429987
2.3	0.669031	0.137209	0.0414799
2.5	0.732649	0.202738	0.0454242
2.7	0.654012	0.238308	0.0405488
2.9	0.726441	0.327224	0.0450394
3.25	0.611011	0.277024	0.0378827
3.75	0.411293	0.369192	0.0255001
4.25	0.409961	0.575587	0.0254176

Table C.27:  $\bar{p}/p$  vs.  $p_T$  (Minimum Bias)

$p_T$ [GeV/c]	$\bar{p}/p$	Stat. Err	Sys. Err
0.65	0.707462	0.0288444	0.0608418
0.75	0.726951	0.0294881	0.0625178
0.85	0.745031	0.0299795	0.0640726
0.95	0.746203	0.0304332	0.0641734
1.05	0.723701	0.0301031	0.0622383
1.15	0.752394	0.0324272	0.0647059
1.25	0.76649	0.0340711	0.0659181
1.35	0.741634	0.0340348	0.0637805
1.45	0.814023	0.0382622	0.070006
1.55	0.724222	0.0351452	0.0622831
1.65	0.771602	0.0382693	0.0663577
1.75	0.765792	0.0397655	0.0658581
1.85	0.743242	0.0400783	0.0639188
1.95	0.751736	0.0423895	0.0646493
2.1	0.702342	0.0265656	0.0604014
2.3	0.714374	0.0297922	0.0614362
2.5	0.714924	0.0377343	0.0614834
2.7	0.659917	0.0402772	0.0567529
2.9	0.696633	0.0504722	0.0599104
3.25	0.680084	0.051579	0.0584872
3.75	0.639874	0.0767322	0.0550292
4.25	0.609606	0.120051	0.0524261

Table C.28:  $K^+/\pi^+$  vs.  $p_T$  Central (0-5%)

$p_T$ [GeV/c]	$K^+/\pi^+$	Stat. Err	Sys. Err
0.45	0.152121	0.00354289	0.00943151
0.55	0.203336	0.004379	0.0126068
0.65	0.2336	0.00495461	0.0144832
0.75	0.271772	0.00591241	0.0168499
0.85	0.327879	0.00748147	0.0203285
0.95	0.347032	0.00835229	0.021516
1.05	0.401574	0.0102534	0.0248976
1.15	0.433756	0.0117113	0.0268929
1.25	0.460921	0.013201	0.0285771
1.35	0.442816	0.013679	0.0274546
1.45	0.494649	0.0165727	0.0306683
1.55	0.536572	0.0195863	0.0332675
1.65	0.550532	0.0219767	0.034133
1.75	0.6339	0.0275176	0.0393018
1.85	0.631001	0.030144	0.039122
1.95	0.758117	0.040729	0.0470033

Table C.29:  $K^+/\pi^+$  vs.  $p_T$  Peripheral (60-92%)

$p_T$ [GeV/c]	$K^+/\pi^+$	Stat. Err	Sys. Err
0.45	0.14439	0.00413693	0.00895216
0.55	0.183178	0.00499529	0.011357
0.65	0.21435	0.00594108	0.0132897
0.75	0.236847	0.00705893	0.0146845
0.85	0.272119	0.00894806	0.0168714
0.95	0.302603	0.0110048	0.0187614
1.05	0.331629	0.0135421	0.020561
1.15	0.346321	0.016	0.0214719
1.25	0.351324	0.0186808	0.0217821
1.35	0.340854	0.0205096	0.0211329
1.45	0.424388	0.0282166	0.0263121
1.55	0.415043	0.0330855	0.0257327
1.65	0.427335	0.0375954	0.0264948
1.75	0.393658	0.0411178	0.0244068
1.85	0.461005	0.0515587	0.0285823
1.95	0.467455	0.0616281	0.0289822

Table C.30:  $K^-/\pi^-$  vs.  $p_T$  Central (0-5%)

$p_T$ [GeV/c]	$K^-/\pi^-$	Stat. Err	Sys. Err	$p_T$ [GeV/c]	$K^-/\pi^-$	Stat. Err	Sys. Err
0.45	0.138294	0.00306037	0.00857422	0.45	0.132	0.00366525	0.00818401
0.55	0.178175	0.00365361	0.0110469	0.55	0.175725	0.00458762	0.010895
0.65	0.220657	0.00444585	0.0136808	0.65	0.206149	0.00550014	0.0127813
0.75	0.269118	0.00547838	0.0166853	0.75	0.243462	0.00682683	0.0150946
0.85	0.301443	0.00636934	0.0186894	0.85	0.264226	0.0081088	0.016382
0.95	0.336772	0.00747096	0.0208799	0.95	0.278304	0.00953729	0.0172548
1.05	0.377519	0.00893147	0.0234062	1.05	0.306052	0.0118645	0.0189752
1.15	0.380694	0.00950161	0.023603	1.15	0.304764	0.013309	0.0188954
1.25	0.432732	0.0115535	0.0268294	1.25	0.362152	0.0176737	0.0224534
1.35	0.450657	0.0131162	0.0279408	1.35	0.363378	0.0206725	0.0225294
1.45	0.492559	0.0155036	0.0305387	1.45	0.343963	0.0232365	0.0213257
1.55	0.487155	0.0168376	0.0302036	1.55	0.375425	0.0281166	0.0232763
1.65	0.550671	0.0207976	0.0341416	1.65	0.409949	0.0338501	0.0254168
1.75	0.56096	0.0233132	0.0347795	1.75	0.365684	0.0369236	0.0226724
1.85	0.621261	0.0283973	0.0385182	1.85	0.400789	0.0451788	0.0248489
1.95	0.640928	0.034013	0.0397375	1.95	0.443441	0.057764	0.0274933

Table C.31:  $K^-/\pi^-$  vs.  $p_T$  Peripheral (60-92%)Table C.32:  $p/\pi^+$  vs.  $p_T$  Central (0-5%)

$p_T$ [GeV/c]	$p/\pi^+$	Stat. Err	Sys. Err	$p_T$ [GeV/c]	$p/\pi^+$	Stat. Err	Sys. Err
0.65	0.0646409	0.00217313	0.00555912	0.65	0.0940895	0.00397164	0.00809169
0.75	0.0904598	0.00308416	0.00777954	0.75	0.121414	0.00536262	0.0104416
0.85	0.125508	0.00430889	0.0107937	0.85	0.151096	0.00701646	0.0129942
0.95	0.165361	0.00584442	0.014221	0.95	0.187395	0.00932005	0.016116
1.05	0.211399	0.00772416	0.0181803	1.05	0.214704	0.0115865	0.0184645
1.15	0.274289	0.0103891	0.0235888	1.15	0.245723	0.0145912	0.0211322
1.25	0.325878	0.0128933	0.0280255	1.25	0.264227	0.017631	0.0227235
1.35	0.381552	0.0159602	0.0328135	1.35	0.296344	0.0216266	0.0254856
1.45	0.430832	0.0188002	0.0370516	1.45	0.315437	0.0259637	0.0271276
1.55	0.538133	0.025122	0.0462794	1.55	0.345492	0.0330717	0.0297123
1.65	0.565018	0.0279089	0.0485915	1.65	0.326856	0.0351717	0.0281096
1.75	0.61537	0.0327739	0.0529218	1.75	0.352425	0.0418389	0.0303086
1.85	0.683019	0.0392303	0.0587397	1.85	0.335835	0.0470085	0.0288818
1.95	0.711554	0.0452083	0.0611936	1.95	0.363426	0.0564291	0.0312547
2.1	0.783806	0.0340629	0.0674073	2.1	0.368314	0.0410877	0.031675
2.3	0.94554	0.0525536	0.0813164	2.3	0.39638	0.0566075	0.0340887
2.5	0.96017	0.0713159	0.0825746	2.5	0.314617	0.0620752	0.0270571
2.7	0.992269	0.10206	0.0853351	2.7	0.288419	0.0740105	0.024804
2.9	1.3365	0.193417	0.114939	2.9	0.312786	0.105493	0.0268996

Table C.33:  $p/\pi^+$  vs.  $p_T$  Peripheral (60-92%)

Table C.34:  $\bar{p}/\pi^-$  vs.  $p_T$  Central (0-5%)

$p_T$ [GeV/c]	$\bar{p}/\pi^-$	Stat. Err	Sys. Err	$p_T$ [GeV/c]	$\bar{p}/\pi^-$	Stat. Err	Sys. Err
0.65	0.0438624	0.00154061	0.00377217	0.65	0.0711005	0.00322222	0.00611465
0.75	0.0661495	0.00227585	0.00568886	0.75	0.0957039	0.00439192	0.00823054
0.85	0.0895809	0.00308156	0.00770396	0.85	0.115449	0.00556397	0.0099286
0.95	0.120451	0.00421958	0.0103588	0.95	0.138172	0.00711537	0.0118828
1.05	0.150909	0.00544851	0.0129782	1.05	0.153909	0.00869701	0.0132362
1.15	0.198459	0.00753499	0.0170675	1.15	0.180976	0.0113154	0.0155639
1.25	0.25226	0.0100549	0.0216944	1.25	0.20913	0.0145976	0.0179852
1.35	0.284048	0.0119089	0.0244282	1.35	0.223318	0.0173994	0.0192053
1.45	0.358354	0.0159144	0.0308184	1.45	0.259398	0.0225333	0.0223082
1.55	0.367812	0.0172667	0.0316319	1.55	0.231749	0.0233536	0.0199304
1.65	0.431772	0.0218059	0.0371324	1.65	0.230575	0.0267238	0.0198294
1.75	0.47837	0.0261426	0.0411398	1.75	0.262094	0.0340199	0.0225401
1.85	0.511018	0.0304075	0.0439475	1.85	0.251047	0.0381667	0.0215901
1.95	0.53852	0.0362572	0.0463127	1.95	0.284765	0.0490566	0.0244898
2.1	0.611174	0.0301507	0.0525609	2.1	0.281321	0.0378904	0.0241936
2.3	0.736463	0.0458647	0.0633359	2.3	0.291385	0.0514544	0.0250591
2.5	0.7719	0.0666452	0.0663834	2.5	0.250272	0.0590408	0.0215234
2.7	0.769071	0.0884184	0.0661401	2.7	0.223266	0.0710798	0.0192009
2.9	0.821256	0.132828	0.070628	2.9	0.219691	0.0875284	0.0188935

Table C.36:  $\pi^-/\pi^+$  vs.  $N_{\text{part}}$ 

$N_{\text{part}}$	$\pi^-/\pi^+$	Stat. Err	Sys. Err
351.4	0.984201	0.0049369	0.0570837
299	0.997229	0.00500613	0.0578393
253.9	0.968558	0.00486565	0.0561764
215.3	0.96293	0.00484265	0.0558499
166.6	0.977273	0.00488647	0.0566819
114.2	0.969567	0.00486067	0.0562349
74.4	0.964838	0.00486577	0.0559606
45.5	0.967325	0.00494973	0.0561048
25.7	0.958872	0.00507733	0.0556146
13.4	0.964984	0.00553412	0.0559691
6.3	0.971025	0.00625725	0.0563194

Table C.37:  $K^-/K^+$  vs.  $N_{\text{part}}$ 

$N_{\text{part}}$	$K^-/K^+$	Stat. Err	Sys. Err
351.4	0.933841	0.00796795	0.0541627
299	0.94272	0.00820853	0.0546778
253.9	0.920505	0.00815443	0.0533893
215.3	0.925989	0.00838429	0.0537074
166.6	0.927478	0.00799809	0.0537937
114.2	0.932175	0.00848459	0.0540662
74.4	0.917311	0.00908818	0.0532041
45.5	0.923619	0.010479	0.0535699
25.7	0.916084	0.0128362	0.0531329
13.4	0.981581	0.0195033	0.0569317
6.3	0.968334	0.025965	0.0561634

Table C.38:  $\bar{p}/p$  vs.  $N_{\text{part}}$ 

$N_{\text{part}}$	$\bar{p}/p$	Stat. Err	Sys. Err
351.4	0.731953	0.0116658	0.062948
299	0.742626	0.0121516	0.0638659
253.9	0.7426	0.012443	0.0638636
215.3	0.749601	0.0129325	0.0644657
166.6	0.738992	0.0116483	0.0635533
114.2	0.744046	0.0125436	0.063988
74.4	0.746218	0.0138783	0.0641747
45.5	0.756393	0.0163038	0.0650498
25.7	0.759773	0.0203813	0.0653405
13.4	0.73962	0.0284461	0.0636073
6.3	0.737784	0.0363725	0.0634495

**Table C.39:**  $K^+/\pi^+$  vs.  $N_{\text{part}}$ 

$N_{\text{part}}$	$K^+/\pi^+$	Stat. Err	Sys. Err
351.4	0.171047	0.00123418	0.0106049
299	0.167582	0.00122603	0.0103901
253.9	0.165128	0.0012238	0.0102379
215.3	0.160557	0.00121019	0.00995452
166.6	0.158613	0.00114938	0.00983403
114.2	0.152447	0.00115294	0.00945169
74.4	0.146874	0.00118405	0.00910616
45.5	0.139298	0.00125364	0.00863646
25.7	0.129979	0.00140097	0.00805872
13.4	0.112338	0.00168682	0.00696493
6.3	0.108754	0.00216993	0.00674277

**Table C.40:**  $K^-/\pi^-$  vs.  $N_{\text{part}}$ 

$N_{\text{part}}$	$K^-/\pi^-$	Stat. Err	Sys. Err
351.4	0.162295	0.00109956	0.0100623
299	0.158422	0.00109179	0.00982218
253.9	0.156935	0.00109615	0.00972998
215.3	0.154397	0.00109677	0.00957263
166.6	0.150532	0.00103039	0.00933295
114.2	0.146568	0.00104445	0.00908719
74.4	0.139639	0.00106893	0.0086576
45.5	0.133004	0.00114346	0.00824624
25.7	0.124179	0.0012917	0.00769911
13.4	0.11427	0.00162492	0.00708472
6.3	0.108453	0.00206464	0.00672408

**Table C.41:**  $p/\pi^+$  vs.  $N_{\text{part}}$ 

$N_{\text{part}}$	$p/\pi^+$	Stat. Err	Sys. Err
351.4	0.064502	0.000751529	0.00399912
299	0.0642273	0.00076539	0.00398209
253.9	0.0626094	0.000760693	0.00388179
215.3	0.061324	0.000764915	0.00380209
166.6	0.0621517	0.000720009	0.00385341
114.2	0.0616229	0.00075611	0.00382062
74.4	0.0599168	0.000798928	0.00371484
45.5	0.0583358	0.000890211	0.00361682
25.7	0.0550752	0.00102933	0.00341466
13.4	0.0505031	0.00132667	0.00313119
6.3	0.0519336	0.00170869	0.00321988

**Table C.42:**  $\bar{p}/\pi^-$  vs.  $N_{\text{part}}$ 

$N_{\text{part}}$	$\bar{p}/\pi^-$	Stat. Err	Sys. Err
351.4	0.0479703	0.0005745	0.00297416
299	0.0478294	0.000587613	0.00296542
253.9	0.0480031	0.000604115	0.00297619
215.3	0.0477381	0.000617567	0.00295976
166.6	0.0469977	0.000554593	0.00291386
114.2	0.0472895	0.000595914	0.00293195
74.4	0.0463404	0.000644667	0.0028731
45.5	0.0456153	0.000732573	0.00282815
25.7	0.0436395	0.000870989	0.00270565
13.4	0.0387085	0.00110982	0.00239993
6.3	0.0394592	0.00147087	0.00244647

# Appendix D

## PHENIX Collaboration List

S.S. Adler,<sup>5</sup> S. Afanasiev,<sup>17</sup> C. Aidala,<sup>5</sup> N.N. Ajitanand,<sup>43</sup> Y. Akiba,<sup>20,38</sup> J. Alexander,<sup>43</sup> R. Amirikas,<sup>12</sup> L. Aphecetche,<sup>45</sup> S.H. Aronson,<sup>5</sup> R. Averbeck,<sup>44</sup> T.C. Awes,<sup>35</sup> R. Azmoun,<sup>44</sup> V. Babintsev,<sup>15</sup> A. Baldissari,<sup>10</sup> K.N. Barish,<sup>6</sup> P.D. Barnes,<sup>27</sup> B. Bassalleck,<sup>33</sup> S. Bathe,<sup>30</sup> S. Batsouli,<sup>9</sup> V. Baublis,<sup>37</sup> A. Bazilevsky,<sup>39,15</sup> S. Belikov,<sup>16,15</sup> Y. Berdnikov,<sup>40</sup> S. Bhagavatula,<sup>16</sup> J.G. Boissevain,<sup>27</sup> H. Borel,<sup>10</sup> S. Borenstein,<sup>25</sup> M.L. Brooks,<sup>27</sup> D.S. Brown,<sup>34</sup> N. Bruner,<sup>33</sup> D. Bucher,<sup>30</sup> H. Buesching,<sup>30</sup> V. Bumazhnov,<sup>15</sup> G. Bunce,<sup>5,39</sup> J.M. Burward-Hoy,<sup>26,44</sup> S. Butsyk,<sup>44</sup> X. Camard,<sup>45</sup> J.-S. Chai,<sup>18</sup> P. Chand,<sup>4</sup> W.C. Chang,<sup>2</sup> S. Chernichenko,<sup>15</sup> C.Y. Chi,<sup>9</sup> J. Chiba,<sup>20</sup> M. Chiu,<sup>9</sup> I.J. Choi,<sup>52</sup> J. Choi,<sup>19</sup> R.K. Choudhury,<sup>4</sup> T. Chujo,<sup>5</sup> V. Cianciolo,<sup>35</sup> Y. Cobigo,<sup>10</sup> B.A. Cole,<sup>9</sup> P. Constantin,<sup>16</sup> D.G. d'Enterria,<sup>45</sup> G. David,<sup>5</sup> H. Delagrange,<sup>45</sup> A. Denisov,<sup>15</sup> A. Deshpande,<sup>39</sup> E.J. Desmond,<sup>5</sup> O. Dietzsch,<sup>41</sup> O. Drapier,<sup>25</sup> A. Drees,<sup>44</sup> K.A. Drees,<sup>5</sup> R. du Rietz,<sup>29</sup> A. Durum,<sup>15</sup> D. Dutta,<sup>4</sup> Y.V. Efremenko,<sup>35</sup> K. El Chenawi,<sup>49</sup> A. Enokizono,<sup>14</sup> H. En'yo,<sup>38,39</sup> S. Esumi,<sup>48</sup> L. Ewell,<sup>5</sup> D.E. Fields,<sup>33,39</sup> F. Fleuret,<sup>25</sup> S.L. Fokin,<sup>23</sup> B.D. Fox,<sup>39</sup> Z. Fraenkel,<sup>51</sup> J.E. Frantz,<sup>9</sup> A. Franz,<sup>5</sup> A.D. Frawley,<sup>12</sup> S.-Y. Fung,<sup>6</sup> S. Garpman,<sup>29,\*</sup> T.K. Ghosh,<sup>49</sup> A. Glenn,<sup>46</sup> G. Gogiberidze,<sup>46</sup> M. Gonin,<sup>25</sup> J. Gosset,<sup>10</sup> Y. Goto,<sup>39</sup> R. Granier de Cassagnac,<sup>25</sup> N. Grau,<sup>16</sup> S.V. Greene,<sup>49</sup> M. Grosse Perdekamp,<sup>39</sup> W. Guryn,<sup>5</sup> H.-Å. Gustafsson,<sup>29</sup> T. Hachiya,<sup>14</sup> J.S. Haggerty,<sup>5</sup> H. Hamagaki,<sup>8</sup> A.G. Hansen,<sup>27</sup> E.P. Hartouni,<sup>26</sup> M. Harvey,<sup>5</sup> R. Hayano,<sup>8</sup> X. He,<sup>13</sup> M. Heffner,<sup>26</sup> T.K. Hemmick,<sup>44</sup> J.M. Heuser,<sup>44</sup> M. Hibino,<sup>50</sup> J.C. Hill,<sup>16</sup> W. Holzmann,<sup>43</sup> K. Homma,<sup>14</sup> B. Hong,<sup>22</sup> A. Hoover,<sup>34</sup> T. Ichihara,<sup>38,39</sup> V.V. Ikonnikov,<sup>23</sup> K. Imai,<sup>24,38</sup> L.D. Isenhower,<sup>1</sup> M. Ishihara,<sup>38</sup> M. Issah,<sup>43</sup> A. Isupov,<sup>17</sup> B.V. Jacak,<sup>44</sup> W.Y. Jang,<sup>22</sup> Y. Jeong,<sup>19</sup> J. Jia,<sup>44</sup> O. Jinnouchi,<sup>38</sup> B.M. Johnson,<sup>5</sup> S.C. Johnson,<sup>26</sup> K.S. Joo,<sup>31</sup> D. Jouan,<sup>36</sup> S. Kametani,<sup>8,50</sup> N. Kamihara,<sup>47,38</sup> J.H. Kang,<sup>52</sup> S.S. Kapoor,<sup>4</sup> K. Katou,<sup>50</sup> S. Kelly,<sup>9</sup> B. Khachaturov,<sup>51</sup> A. Khanzadeev,<sup>37</sup> J. Kikuchi,<sup>50</sup> D.H. Kim,<sup>31</sup> D.J. Kim,<sup>52</sup> D.W. Kim,<sup>19</sup> E. Kim,<sup>42</sup> G.-B. Kim,<sup>25</sup> H.J. Kim,<sup>52</sup> E. Kistenev,<sup>5</sup> A. Kiyomichi,<sup>48</sup> K. Kiyoyama,<sup>32</sup> C. Klein-Boesing,<sup>30</sup> H. Kobayashi,<sup>38,39</sup> L. Kochenda,<sup>37</sup> V. Kochetkov,<sup>15</sup> D. Koehler,<sup>33</sup> T. Kohama,<sup>14</sup> M. Kopytine,<sup>44</sup> D. Kotchetkov,<sup>6</sup> A. Kozlov,<sup>51</sup> P.J. Kroon,<sup>5</sup> C.H. Kuberg,<sup>1,27</sup> K. Kurita,<sup>39</sup> Y. Kuroki,<sup>48</sup> M.J. Kweon,<sup>22</sup> Y. Kwon,<sup>52</sup> G.S. Kyle,<sup>34</sup> R. Lacey,<sup>43</sup> V. Ladygin,<sup>17</sup> J.G. Lajoie,<sup>16</sup> A. Lebedev,<sup>16,23</sup> S. Leckey,<sup>44</sup> D.M. Lee,<sup>27</sup> S. Lee,<sup>19</sup> M.J. Leitch,<sup>27</sup> X.H. Li,<sup>6</sup> H. Lim,<sup>42</sup> A. Litvinenko,<sup>17</sup> M.X. Liu,<sup>27</sup> Y. Liu,<sup>36</sup> C.F. Maguire,<sup>49</sup> Y.I. Makdisi,<sup>5</sup> A. Malakhov,<sup>17</sup> V.I. Manko,<sup>23</sup> Y. Mao,<sup>7,38</sup> G. Martinez,<sup>45</sup> M.D. Marx,<sup>44</sup> H. Masui,<sup>48</sup> F. Matathias,<sup>44</sup> T. Matsumoto,<sup>8,50</sup> P.L. McGaughey,<sup>27</sup> E. Melnikov,<sup>15</sup> F. Messer,<sup>44</sup> Y. Miake,<sup>48</sup> J. Milan,<sup>43</sup> T.E. Miller,<sup>49</sup> A. Milov,<sup>44,51</sup> S. Mioduszewski,<sup>5</sup> R.E. Mischke,<sup>27</sup> G.C. Mishra,<sup>13</sup> J.T. Mitchell,<sup>5</sup> A.K. Mohanty,<sup>4</sup> D.P. Morrison,<sup>5</sup> J.M. Moss,<sup>27</sup> F. Mühlbacher,<sup>44</sup> D. Mukhopadhyay,<sup>51</sup> M. Muniruzzaman,<sup>6</sup> J. Murata,<sup>38,39</sup> S. Nagamiya,<sup>20</sup> J.L. Nagle,<sup>9</sup> T. Nakamura,<sup>14</sup> B.K. Nandi,<sup>6</sup> M. Nara,<sup>48</sup> J. Newby,<sup>46</sup> P. Nilsson,<sup>29</sup> A.S. Nyanin,<sup>23</sup>

J. Nystrand,<sup>29</sup> E. O'Brien,<sup>5</sup> C.A. Ogilvie,<sup>16</sup> H. Ohnishi,<sup>5,38</sup> I.D. Ojha,<sup>49,3</sup> K. Okada,<sup>38</sup> M. Ono,<sup>48</sup>  
V. Onuchin,<sup>15</sup> A. Oskarsson,<sup>29</sup> I. Otterlund,<sup>29</sup> K. Oyama,<sup>8</sup> K. Ozawa,<sup>8</sup> D. Pal,<sup>51</sup> A.P.T. Palounek,<sup>27</sup>  
V.S. Pantuev,<sup>44</sup> V. Papavassiliou,<sup>34</sup> J. Park,<sup>42</sup> A. Parmar,<sup>33</sup> S.F. Pate,<sup>34</sup> T. Peitzmann,<sup>30</sup>  
J.-C. Peng,<sup>27</sup> V. Peresedov,<sup>17</sup> C. Pinkenburg,<sup>5</sup> R.P. Pisani,<sup>5</sup> F. Plasil,<sup>35</sup> M.L. Purschke,<sup>5</sup>  
A. Purwar,<sup>44</sup> J. Rak,<sup>16</sup> I. Ravinovich,<sup>51</sup> K.F. Read,<sup>35,46</sup> M. Reuter,<sup>44</sup> K. Reygers,<sup>30</sup> V. Riabov,<sup>37,40</sup>  
Y. Riabov,<sup>37</sup> G. Roche,<sup>28</sup> A. Romana,<sup>25</sup> M. Rosati,<sup>16</sup> P. Rosnet,<sup>28</sup> S.S. Ryu,<sup>52</sup> M.E. Sadler,<sup>1</sup>  
N. Saito,<sup>38,39</sup> T. Sakaguchi,<sup>8,50</sup> M. Sakai,<sup>32</sup> S. Sakai,<sup>48</sup> V. Samsonov,<sup>37</sup> L. Sanfratello,<sup>33</sup> R. Santo,<sup>30</sup>  
H.D. Sato,<sup>24,38</sup> S. Sato,<sup>5,48</sup> S. Sawada,<sup>20</sup> Y. Schutz,<sup>45</sup> V. Semenov,<sup>15</sup> R. Seto,<sup>6</sup> M.R. Shaw,<sup>1,27</sup>  
T.K. Shea,<sup>5</sup> T.-A. Shibata,<sup>47,38</sup> K. Shigaki,<sup>14,20</sup> T. Shiina,<sup>27</sup> C.L. Silva,<sup>41</sup> D. Silvermyr,<sup>27,29</sup>  
K.S. Sim,<sup>22</sup> C.P. Singh,<sup>3</sup> V. Singh,<sup>3</sup> M. Sivertz,<sup>5</sup> A. Soldatov,<sup>15</sup> R.A. Soltz,<sup>26</sup> W.E. Sondheim,<sup>27</sup>  
S.P. Sorensen,<sup>46</sup> I.V. Sourikova,<sup>5</sup> F. Staley,<sup>10</sup> P.W. Stankus,<sup>35</sup> E. Stenlund,<sup>29</sup> M. Stepanov,<sup>34</sup>  
A. Ster,<sup>21</sup> S.P. Stoll,<sup>5</sup> T. Sugitate,<sup>14</sup> J.P. Sullivan,<sup>27</sup> E.M. Takagui,<sup>41</sup> A. Taketani,<sup>38,39</sup> M. Tamai,<sup>50</sup>  
K.H. Tanaka,<sup>20</sup> Y. Tanaka,<sup>32</sup> K. Tanida,<sup>38</sup> M.J. Tannenbaum,<sup>5</sup> P. Tarján,<sup>11</sup> J.D. Tepe,<sup>1,27</sup>  
T.L. Thomas,<sup>33</sup> J. Tojo,<sup>24,38</sup> H. Torii,<sup>24,38</sup> R.S. Towell,<sup>1</sup> I. Tserruya,<sup>51</sup> H. Tsuruoka,<sup>48</sup> S.K. Tuli,<sup>3</sup>  
H. Tydesjö,<sup>29</sup> N. Tyurin,<sup>15</sup> H.W. van Hecke,<sup>27</sup> J. Velkovska,<sup>5,44</sup> M. Velkovsky,<sup>44</sup> L. Villatte,<sup>46</sup>  
A.A. Vinogradov,<sup>23</sup> M.A. Volkov,<sup>23</sup> E. Vznuzdaev,<sup>37</sup> X.R. Wang,<sup>13</sup> Y. Watanabe,<sup>38,39</sup> S.N. White,<sup>5</sup>  
F.K. Wohn,<sup>16</sup> C.L. Woody,<sup>5</sup> W. Xie,<sup>6</sup> Y. Yang,<sup>7</sup> A. Yanovich,<sup>15</sup> S. Yokkaichi,<sup>38,39</sup> G.R. Young,<sup>35</sup>  
I.E. Yushmanov,<sup>23</sup> W.A. Zajc,<sup>9,†</sup> C. Zhang,<sup>9</sup> S. Zhou,<sup>7,51</sup> L. Zolin,<sup>17</sup>

## (PHENIX Collaboration)

<sup>1</sup>Abilene Christian University, Abilene, TX 79699, USA<sup>2</sup>Institute of Physics, Academia Sinica, Taipei 11529, Taiwan<sup>3</sup>Department of Physics, Banaras Hindu University, Varanasi 221005, India<sup>4</sup>Bhabha Atomic Research Centre, Bombay 400 085, India<sup>5</sup>Brookhaven National Laboratory, Upton, NY 11973-5000, USA<sup>6</sup>University of California - Riverside, Riverside, CA 92521, USA<sup>7</sup>China Institute of Atomic Energy (CIAE), Beijing, People's Republic of China<sup>8</sup>Center for Nuclear Study, Graduate School of Science, University of Tokyo, 7-3-1 Hongo, Bunkyo, Tokyo  
113-0033, Japan<sup>9</sup>Columbia University, New York, NY 10027 and Nevis Laboratories, Irvington, NY 10533, USA<sup>10</sup>Dapnia, CEA Saclay, Bat. 703, F-91191, Gif-sur-Yvette, France<sup>11</sup>Debrecen University, H-4010 Debrecen, Egyetem tér 1, Hungary<sup>12</sup>Florida State University, Tallahassee, FL 32306, USA<sup>13</sup>Georgia State University, Atlanta, GA 30303, USA<sup>14</sup>Hiroshima University, Kagamiyama, Higashi-Hiroshima 739-8526, Japan<sup>15</sup>Institute for High Energy Physics (IHEP), Protvino, Russia<sup>16</sup>Iowa State University, Ames, IA 50011, USA<sup>17</sup>Joint Institute for Nuclear Research, 141980 Dubna, Moscow Region, Russia<sup>18</sup>KAERI, Cyclotron Application Laboratory, Seoul, South Korea<sup>19</sup>Kangnung National University, Kangnung 210-702, South Korea<sup>20</sup>KEK, High Energy Accelerator Research Organization, Tsukuba-shi, Ibaraki-ken 305-0801, Japan<sup>21</sup>KFKI Research Institute for Particle and Nuclear Physics (RMKI), H-1525 Budapest 114, POBox 49,  
Hungary<sup>22</sup>Korea University, Seoul, 136-701, Korea<sup>23</sup>Russian Research Center "Kurchatov Institute", Moscow, Russia<sup>24</sup>Kyoto University, Kyoto 606, Japan<sup>25</sup>Laboratoire Leprince-Ringuet, Ecole Polytechnique, CNRS-IN2P3, Route de Saclay, F-91128, Palaiseau,  
France<sup>26</sup>Lawrence Livermore National Laboratory, Livermore, CA 94550, USA<sup>27</sup>Los Alamos National Laboratory, Los Alamos, NM 87545, USA<sup>28</sup>LPC, Université Blaise Pascal, CNRS-IN2P3, Clermont-Fd, 63177 Aubiere Cedex, France<sup>29</sup>Department of Physics, Lund University, Box 118, SE-221 00 Lund, Sweden

- <sup>30</sup>Institut fuer Kernphysik, University of Muenster, D-48149 Muenster, Germany  
<sup>31</sup>Myongji University, Yongin, Kyonggido 449-728, Korea  
<sup>32</sup>Nagasaki Institute of Applied Science, Nagasaki-shi, Nagasaki 851-0193, Japan  
<sup>33</sup>University of New Mexico, Albuquerque, NM, USA  
<sup>34</sup>New Mexico State University, Las Cruces, NM 88003, USA  
<sup>35</sup>Oak Ridge National Laboratory, Oak Ridge, TN 37831, USA  
<sup>36</sup>IPN-Orsay, Universite Paris Sud, CNRS-IN2P3, BP1, F-91406, Orsay, France  
<sup>37</sup>PNPI, Petersburg Nuclear Physics Institute, Gatchina, Russia  
<sup>38</sup>RIKEN (The Institute of Physical and Chemical Research), Wako, Saitama 351-0198, JAPAN  
<sup>39</sup>RIKEN BNL Research Center, Brookhaven National Laboratory, Upton, NY 11973-5000, USA  
<sup>40</sup>St. Petersburg State Technical University, St. Petersburg, Russia  
<sup>41</sup>Universidade de São Paulo, Instituto de Física, Caixa Postal 66318, São Paulo CEP05315-970, Brazil  
<sup>42</sup>System Electronics Laboratory, Seoul National University, Seoul, South Korea  
<sup>43</sup>Chemistry Department, Stony Brook University, SUNY, Stony Brook, NY 11794-3400, USA  
<sup>44</sup>Department of Physics and Astronomy, Stony Brook University, SUNY, Stony Brook, NY 11794, USA  
<sup>45</sup>SUBATECH (Ecole des Mines de Nantes, CNRS-IN2P3, Université de Nantes) BP 20722 - 44307, Nantes, France  
<sup>46</sup>University of Tennessee, Knoxville, TN 37996, USA  
<sup>47</sup>Department of Physics, Tokyo Institute of Technology, Tokyo, 152-8551, Japan  
<sup>48</sup>Institute of Physics, University of Tsukuba, Tsukuba, Ibaraki 305, Japan  
<sup>49</sup>Vanderbilt University, Nashville, TN 37235, USA  
<sup>50</sup>Waseda University, Advanced Research Institute for Science and Engineering, 17 Kikui-cho, Shinjuku-ku, Tokyo 162-0044, Japan  
<sup>51</sup>Weizmann Institute, Rehovot 76100, Israel  
<sup>52</sup>Yonsei University, IPAP, Seoul 120-749, Korea

# Bibliography

- [1] F. Karsch, Lect. Notes Phys. **583** 209 (2002), hep-lat/0106019; F. Karsch, E. Laermann and A. Peikert, Phys. Lett. **B478**, 447 (2000).
- [2] T. Matsui and H. Satz, Phys. Lett. **B178**, 416 (1986).
- [3] T. Matsui, Z. Phys. **C38**, 245 (1988).
- [4] D. H. Rischke, NPA**610**, 88c (1996).
- [5] S. Margetis, K. Šafařík and O. V. Baillie Ann. Rev. Nucl. Part. Sci. **50**, 299 (2000), J. Rafelski Phys. Lett. **B262**, 333 (1991).
- [6] R. J. Glauber and G. Matthiae, Nucl. Phys. **B21**, 135 (1970)
- [7] E. Fermi, Prog. Theor. Phys. **5**, 570 (1950).
- [8] E. L. Feinberg, Sov. Phys. Usp. **14**, 455 (1972).
- [9] E. V. Shuryak, Sov. J. Nucl. Phys. **20**, 295 (1975).
- [10] K. Yagi, T. Hatsuda and Y. Miake, “Quark-Gluon Plasma: An Ultimate State of Matter”, Cambridge Univ. Pr., in press.
- [11] I. G. Bearden *et al.*, Phys. Rev. Lett. **78**, 2080 (1997).
- [12] T. Csörgő and B. Lörstad, Phys. Rev. **C54**, 1390 (1996).
- [13] E. Schnedermann, J. Sollfrank, and U. Heinz, Phys. Rev. **C48**, 2462 (1993)
- [14] S. Esumi, S. Chapman, H. van Hecke, and N. Xu, Phys. Rev. **C55**, R2163 (1997)
- [15] P. Braun-Munzinger, I. Heppe, J. Stachel, Phys. Lett. **B465**, 15 (1999).

- [16] M. Gyulassy and M. Plümer, Phys. Lett. **B243**, 432 (1990); R. Baier *et al.*, Phys. Lett. **B345**, 277 (1995).
- [17] X. N. Wang and M. Gyulassy, Phys. Rev. Lett. **68**, 1480 (1992); X. N. Wang, Phys. Rev. **C58**, 2321 (1998).
- [18] R. Baier, D. Schiff, and B. G. Zakharov, Ann. Rev. Nucl. Part. Sci. **50**, 37 (2000).
- [19] R. Baier, Y. L. Dokshitzer, A. H. Mueller, and D. Schiff, J. High Energy Phys. **9**, 33 (2001), hep-ph0106347.
- [20] X. N. Wang, Phys. Rev. **C63**, 054902 (2001).
- [21] X. N. Wang, Nucl. Phys. **A715**, 775c (2003).
- [22] J. F. Owens *et al.*, Phys. Rev. **D18**, 1501 (1978).
- [23] PHENIX Collaboration, S. S. Adler *et al.*, Phys. Rev. Lett. **91**, 241803 (2003).
- [24] B. A. Kniehl *et al.*, Nucl. Phys. **B597**, 337 (2001).
- [25] S. Kretzer, Phys. Rev. **D62**, 054001 (2000).
- [26] D. Antreasyan *et al.*, Phys. Rev. **D19**, 764 (1979).
- [27] J. Cronin *et al.*, Phys. Rev. **D11**, 3105 (1975).
- [28] D. Antreasyan *et al.*, Phys. Rev. **D19**, 764 (1979).
- [29] J. J. Aubert *et al.*, Phys. Lett. **B123**, 275 (1983); R. G. Arnold *et al.*, Phys. Rev. Lett. **52**, 727 (1984).
- [30] PHENIX Collaboration, K. Adcox *et al.*, Phys. Rev. Lett. **88**, 022301 (2002).
- [31] PHENIX Collaboration, K. Adcox *et al.*, Phys. Lett. **B561**, 82 (2003).
- [32] PHENIX Collaboration, S. S. Adler *et al.*, Phys. Rev. Lett. **91**, 072301 (2003).
- [33] PHENIX Collaboration, S. S. Adler *et al.*, Phys. Rev. **C69**, 034910 (2004).
- [34] BCMOR Collaboration, A.L.S. Angelis *et al.*, Phys. Lett. **B185**, 213 (1987).
- [35] E. Wang and X. N. Wang, Phys. Rev. **C64**, 034901 (2001) and references therein.

- [36] D. Kharzeev, E. Levin and L. McLerran, Phys. Lett. **B561**, 93 (2003).
- [37] K. Gallmeister, C. Greiner and Z. Xu, Phys. Rev. **C67**, 044905 (2003).
- [38] PHENIX Collaboration, S. S. Adler *et al.*, Phys. Rev. Lett. **91**, 072303 (2003).
- [39] PHENIX Collaboration, S. S. Adler *et al.*, Phys. Rev. Lett. **91**, 172301 (2003).
- [40] PHENIX Collaboration, S. S. Adler *et al.*, Phys. Rev. **C69**, 034909 (2004).
- [41] M. Harrison *et al.*, Nucl. Instrum. Methods **A499**, 235 (2003).
- [42] H. Hahn *et al.*, Nucl. Instrum. Methods **A499**, 245 (2003).
- [43] PHENIX Conceptual Design Report (CDR), Jan. 1993; S. Nagamiya, Nucl. Phys. **A566**, 287c (1994).
- [44] K. Adcox *et al.*, Nucl. Instrum. Methods **A499**, 469 (2003).
- [45] S. H. Aronson *et al.*, Nucl. Instrum. Methods **A499**, 480 (2003).
- [46] M. Allen *et al.*, Nucl. Instrum. Methods **A499**, 549 (2003).
- [47] C. Adler *et al.*, Nucl. Instrum. Methods **A470**, 488 (2001).
- [48] K. Adcox *et al.*, Nucl. Instrum. Methods **A499**, 489 (2003).
- [49] M. Aizawa *et al.*, Nucl. Instrum. Methods **A499**, 508 (2003).
- [50] L. Aphecetche *et al.*, Nucl. Instrum. Methods **A499**, 521 (2003).
- [51] H. Akikawa *et al.*, Nucl. Instrum. Methods **A499**, 537 (2003).
- [52] PHENIX Collaboration, K. Adcox *et al.*, Phys. Rev. Lett. **87**, 052301 (2001).
- [53] PHENIX Collaboration, K. Adcox *et al.*, Phys. Rev. Lett. **89**, 092302 (2002).
- [54] GEANT 3.21, CERN program library.
- [55] X. N. Wang and M. Gyulassy, Phys. Rev. **D44**, 3501 (1991), version 1.35.
- [56] J. T. Mitchell *et al.*, Nucl. Instrum. Methods **A482**, 491 (2002).
- [57] P. Christiansen for the BRAHMS Collaboration, nucl-ex/0212002.

- [58] STAR Collaboration, C. Adler *et al.*, Phys. Rev. Lett. **86**, 4778 (2001).
- [59] STAR Collaboration, J. Adams *et al.*, Phys. Rev. Lett. **90**, 119903 (2003).
- [60] STAR Collaboration, C. Adler *et al.*, Phys. Lett. **B595**, 143 (2004).
- [61] STAR Collaboration, J. Adams *et al.*, Phys. Lett. **B567**, 167 (2003).
- [62] PHOBOS Collaboration, B. B. Back *et al.*, Phys. Rev. Lett. **87**, 102301 (2001).
- [63] BRAHMS Collaboration, I. G. Bearden *et al.*, Phys. Rev. Lett. **87**, 112305 (2001).
- [64] PHOBOS Collaboration, B. B. Back *et al.*, Phys. Rev. **C67**, 021901(R) (2003).
- [65] BRAHMS Collaboration, I. G. Bearden *et al.*, Phys. Rev. Lett. **90**, 102301 (2003).
- [66] STAR Collaboration, J. Adams *et al.*, Phys. Rev. Lett. **92**, 012301 (2004).
- [67] P. Braun-Munzinger, D. Magestro, K. Redlich, and J. Stachel, Phys. Lett. **B518**, 41 (2001).
- [68] P. Braun-Munzinger and J. Stachel, J. Phys **G28**, 1971 (2002).
- [69] P. Braun-Munzinger, K. Redlich, and J. Stachel, nucl-th/0304013
- [70] S. Ejiri, *et al.*, Nucl. Phys. **B119**, 538 (2003), hep-lat/0209012; C. Schmidt, *et al.*, Nucl. Phys. **B119**, 517 (2003), hep-lat/0209009. (LATTICE 2002 Symposium Proceedings)
- [71] Z. Fodor and S. D. Katz, Phys. Lett. **B534**, 87 (2002).
- [72] PHENIX Collaboration, K. Adcox *et al.*, Phys. Rev. Lett. **88**, 242301 (2002).
- [73] PHENIX Collaboration, K. Adcox *et al.*, Phys. Rev. **C69**, 024904 (2004).
- [74] B. Alper *et al.*, Nucl. Phys. **B100**, 237 (1975).
- [75] DELPHI Collaboration, P. Abreu *et al.*, Eur. Phys. J. **C17**, 207 (2000).
- [76] T. Csörgő, S. V. Akkelin, Y. Hama, B. Lukács and Y. M. Sinyukov, Phys. Rev. **C67**, 034904 (2003).
- [77] P.F. Kolb and R. Rapp, Phys. Rev. **C67**, 044903 (2003).

- [78] W. Broniowski and W. Florkowski, Phys. Rev. Lett. **87**, 272302 (2001); W. Broniowski and W. Florkowski, Phys. Rev. **C65**, 064905 (2002).
- [79] D. Teaney, J. Lauret, and E. V. Shuryak, nucl-th/0110037; D. Teaney, J. Lauret, and E. V. Shuryak, Phys. Rev. Lett. **86**, 4783 (2001).
- [80] P. F. Kolb, U. Heinz, P. Huovinen, K. J. Eskola, and K. Tuominen, Nucl. Phys. **A696**, 197 (2001); P. Huovinen, P. Huovinen, U. Heinz, P. V. Ruuskanen and S. A. Voloshin, Phys. Lett. **B503**, 58 (2001).
- [81] U. Heinz and P. Kolb, Nucl. Phys. **A702**, 269 (2002).
- [82] T. Hirano and Y. Nara, Phys. Rev. **C69**, 034908 (2004); Phys. Rev. **C66**, 041901(R) (2002)
- [83] R. J. Fries, B. Müller, C. Nonaka and S. A. Bass, Phys. Rev. Lett. **90**, 202303 (2003); Phys. Rev. **C68**, 044902 (2003).
- [84] R. C. Hwa and C. B. Yang, Phys. Rev. **C67**, 034902 (2003); Phys. Rev. **C70**, 024905 (2004).
- [85] V. Greco, C. M. Ko and P. Lévai, Phys. Rev. Lett. **90**, 202302 (2003)
- [86] PHENIX Collaboration, K. Adcox *et al.*, submitted to Nucl. Phys. **A**, nucl-ex/0410003.
- [87] PHENIX Collaboration, S. S. Adler *et al.*, submitted to Phys. Rev. **C**, nucl-ex/0410012.
- [88] F. Cooper and G. Frye, Phys. Rev. **D10**, 186 (1974).
- [89] J. D. Bjorken, Phys. Rev. **D27**, 140 (1983).